Bangor University

DOCTOR OF PHILOSOPHY

The derivation of suspended sediment concentrations in the Irish Sea from in situ and remotely-sensed ocean colour

Binding, Caren

Award date:
2003

Awarding institution:
Bangor University

Link to publication

The derivation of suspended sediment concentrations in the Irish Sea from *in situ* and remotely-sensed ocean colour

By

Caren E. Binding, B.Sc., M.Sc.
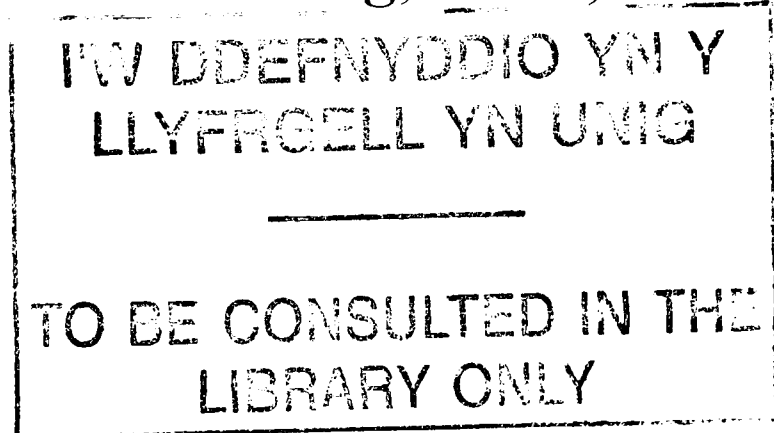
A thesis in partial fulfilment of the requirements of the University of Wales for the degree of Doctor of Philosophy

May 2003

University of Wales Bangor
School of Ocean Sciences
Menai Bridge
Anglesey
Wales
LL59 5AB

ABSTRACT

This study was conducted with the aim of developing an algorithm for the retrieval of suspended sediment concentrations in the Irish Sea from ocean colour imagery obtained from the Sea-viewing Wide Field-of-view Sensor (SeaWiFS). *In situ* measurements of irradiance reflectance were collected at wavelengths coincident with the SeaWiFS sensor, enabling an assessment of the way suspended sediments and other optically active constituents affect ocean colour in the region.

It was found that the measurement of single band reflectance, rather than variations in colour through reflectance ratios, is the most reliable method for the derivation of suspended sediments in the Irish Sea. A simple algorithm utilising a strong empirical relationship between reflectance at 665 nm (R_{665}) and mineral suspended sediment (MSS) concentrations enables the prediction of MSS concentrations with an average uncertainty of less than 22%.

Detailed analysis of the inherent optical properties of suspended sediments shows that much of the variability in the MSS-reflectance relationship can be attributed to variations in the specific scattering coefficient for MSS, b^*_{MSS}. Accounting for these variations in particle scattering through inverse modelling is shown to reduce the uncertainty in MSS predictions to less than 14%. In the Irish Sea, variations in b^*_{MSS} are attributed to differences in particle properties such as grain size, particle composition and the backscattering probability. A method is presented that enables the prediction of b^*_{MSS} from spectral reflectance with an average uncertainty of less than 24%.

The above techniques are applied to two independent data sets of ocean colour as an algorithm validation exercise. A time series of optical and water quality observations in the Menai Strait shows that b^*_{MSS} exhibits a seasonal pattern, with a minimum in the summer months. This seasonality in b^*_{MSS} is attributed to the flocculation of particles in the summer months as a result of both an increase in organic matter and a decrease in wind-induced turbulence. Application of the simple reflectance algorithm to the Menai Strait data series results in consistently underestimated MSS concentrations, suggesting that the particles here are less efficient scatterers than those in the Irish Sea. Accounting for variations in particle scattering efficiencies through inverse modelling considerably improves the accuracy of the MSS concentrations predicted in the Menai Strait, particularly in the summer months.

The application of the reflectance model to SeaWiFS imagery of the Irish Sea reproduces accurately known regions of high turbidity with MSS concentrations that are in good agreement with those measured *in situ* from a moored transmissometer. Processed images provide a valuable time series of maps detailing the seasonal distributions of suspended sediment in the Irish Sea.

LIST OF CONTENTS

Chapter Four – Results: The Development of an Algorithm for the Retrieval of Suspended Sediments from *in situ* Ocean Colour

Chapter Five – Results: The Effect of Variable Particle Scattering Properties on Simple Reflectance Algorithms

Chapter Six: Results - Algorithm Validation in the Menai Strait and Results from SeaWiFS Satellite Imagery

LIST OF FIGURES

Chapter Five: Results - The Effect of Variable Particle Scattering Properties on Simple Reflectance Algorithms

Chapter Six: Results - Algorithm Validation in the Menai Strait and Results from SeaWiFS Satellite Imagery

Chapter Seven – Summary & Conclusions

LIST OF TABLES

Chapter Six: Results - Algorithm Validation in the Menai Strait and Results from SeaWiFS Satellite Imagery

THESIS STRUCTURE

Chapter One   *Introduction, Rationale and Project Objectives*
Describes the motivation behind the study from environmental, ecological and socio-economical perspectives. Specific aims of the study are presented.

Chapter Two   *Background Relating to Ocean Optical Theory and the Remote Sensing of Suspended Sediments*
Provides background information relevant to the fields of ocean optics and remote sensing, with particular emphasis on the optical properties and remote sensing of suspended sediments.

Chapter Three   *An Introduction to the Study Region and Details of the Adopted Methodology and Sampling Strategy*
Presents a brief description of the study region followed by details of the methodology adopted for both field and laboratory techniques.

Chapter Four   *Results: The Development of an Algorithm for the Retrieval of Suspended Sediments from in situ Ocean Colour Data*
Includes the preliminary analysis of measured inherent and apparent optical properties. Various reflectance parameters are assessed for the development of an algorithm to derive mineral sediment concentrations from ocean colour information. Application of a reflectance model enables the comparison of *in situ* observations with optical theory.

Chapter Five   *Results: The Effect of Variable Particle Scattering Properties on Simple Reflectance Algorithms*
Presents results relating to the effect of variable particle scattering efficiency on reflectance including an assessment of the factors determining particle scattering efficiency. A method is proposed for the preliminary estimation of particle scattering properties which may improve the accuracy of reflectance based algorithms.

Chapter Six   *Results - Algorithm Validation in the Menai Strait and Results from SeaWiFS Satellite Imagery*
Techniques developed in chapters Four and Five are applied to a time series of *in situ* ocean colour observations in the Menai Strait as an algorithm validation exercise. Algorithms are then applied to SeaWiFS ocean colour imagery to present maps of suspended sediments in the Irish Sea.

Chapter Seven   *Summary and Conclusions*
The main conclusions of the study are presented and the implications for future research are discussed. Recommendations for further work are outlined.

ACKNOWLEDGEMENTS

☺☺☺☺☺☺☺☺☺☺☺☺☺☺☺☺☺☺☺☺☺☺☺☺☺☺☺☺☺☺☺☺☺☺☺☺☺☺☺

Chapter One

Introduction, Rationale and Project Objectives

CHAPTER ONE: INTRODUCTION, RATIONALE AND PROJECT OBJECTIVES

This short chapter aims to describe the motivation behind the study in terms of the environmental, economic and social importance of suspended sediment observations in coastal and shelf seas and the role that remote sensing of ocean colour can play in monitoring sediment concentrations. Specific aims of the study are presented in section 1.2.

1.1   Introduction and Rationale

Suspended Particulate Matter (SPM) is diverse in both origin and composition. It can include mineral particles and organic matter as well as materials of anthropogenic origin. The mineral component of SPM consists mainly of quartz, feldspars and clay minerals that are supplied to the marine environment through the combined processes of river discharge, shore erosion, bottom re-suspension and the deposition of wind-blown sediments (Eisma, 1993). Organic matter consists of both living organisms (phytoplankton, zooplankton) and organic detritus (largely decomposition products of phytoplankton and zooplankton cells and faecal debris) and can sometimes account for the majority of the total SPM concentration in highly productive areas. In addition, some planktonic organisms form calcium carbonate (coccolithophores, foraminifera) particles, which can make a considerable contribution to total SPM in the open ocean. In the Irish Sea, the combination of relatively shallow waters and strong tidal currents means that SPM is dominated by the inorganic mineral fraction (Simpson and Brown, 1987; Bowers *et al.*, 1996), most of which is re-suspended from the bottom or delivered to the coastal regions through major river systems such as the Mersey and Severn.

The concentrations, spatial and temporal distributions, and transport of suspended particles in the marine environment are of considerable interest in terms of water quality monitoring, pollutant dispersal and primary productivity. Consequently, the ability to make reliable measurements of SPM is of substantial economic, social and ecological importance. Suspended sediments are most predominant in the coastal zone and shelf seas, areas which are also a major resource for human populations. With over 60% of the global population living in the coastal zone, coastal resources

have been excessively exploited compared with the much greater area of open ocean (table 1.1). Subsequent coastal developments inevitably lead to considerable modification of the sources, distributions and ultimate fate of sediments.

Activities such as dredging may result in damage to benthic ecosystems through shading or smothering, and the remobilisation of contaminated materials (Wakemann *et al.*, 1975; Moore, 1977). Many contaminants adsorb onto sediment surfaces, which act as carriers and ultimately remove pollutants from the water column through deposition (Duursma and Smies, 1982). Contaminants such as heavy metals, radioactive elements and organic compounds stored in sediments may, therefore, be released back into the water column by coastal developments. In recent years, the potential role of an increasingly stormy climate in re-suspending pollutants has also been highlighted (Irish Sea Forum Report; Concerns for the Irish Sea's Environment, February 2000). It is feasible, therefore, that the spatial distribution, transport, sources and sinks of contaminants, and their biological uptake into the food web, may be linked to the suspended sediment dynamics. In these cases, the monitoring of sediment transport and fluxes in estuarine and coastal regions provides great scope for more effective coastal zone management (Jay *et al.*, 1997; Robinson *et al.*, 1998).

Table 1.1: Coastal Zone Statistics (from Parslow *et al.*, 2000)

• 60% of human population
• 66% of the world's largest cities
• 8% of ocean surface
• 14% of global ocean primary production
• 90% of world fish catch
• 75-90% of global sink of suspended river load

Recreational and tourism activities are concentrated in the coastal zone and depend on the maintenance of high water quality. Water transparency and colour strongly affect our perception of water quality. Consequently, established environmental directives requiring the monitoring of coastal water quality now include transparency, water colour and suspended solids as water quality indicators (e.g.

Bathing Water Quality, 76/160/EEC; Shellfish Water Quality, 79/923/EEC; Urban Waste Treatment, 91/271/EEC).

The delivery of nutrients to the coastal zone, through river runoff or upwelling events, creates regions of high productivity in shelf seas and consequently, these areas provide a disproportionate share of the world's fisheries catch (Parslow *et al.*, 2000). However, SPM plays a major role in the vertical attenuation of light in shelf and coastal seas, regulating phytoplankton productivity by limiting the light available for photosynthesis (Tett, 1990). In recent years there have been suggestions that shelf seas are becoming more turbid, as a consequence of eutrophication effects (Bonsdorff *et al.*, 1997) and increasing storminess associated with climate change (Alexandersson *et al.*, 2000). If this trend was to continue over long timescales, increased turbidity could lead to considerable reductions in the biological productivity of coastal and shelf sea waters, with detrimental effects on fisheries and benthic communities. Concerns about increased turbidity and associated ecological impacts in estuarine and coastal waters have been the focus of many recent efforts relating satellite observations to *in situ* constituents affecting light attenuation in the water column (Woodruff *et al.*, 1999). The ability to monitor suspended sediments may, therefore, have implications not only in understanding and modelling primary productivity in turbid shelf seas but also in explaining long term fluctuations in primary productivity, fisheries and the global carbon cycle. Such monitoring should be carried out at appropriate spatial and temporal scales if human and environmental impacts on coastal and shelf seas are to be managed and mitigated.

The measurement of SPM over large areas using the conventional method of water sample filtration is time-consuming, expensive, and has limited spatial and temporal sampling coverage. More importantly, discrete samples do not fully represent the spatial heterogeneity of suspended sediment concentrations, particularly in the dynamic coastal and shelf sea environments. In contrast, optical instruments (measuring beam transmittance or scattering) can provide detailed profiles or transects of sediment distributions that cannot be obtained through water filtrations alone. Moored optical instruments for determining turbidity and sediment concentrations are useful for near-continuous monitoring but offer information only for a single point, giving little insight to spatial variability. Satellite sensors provide

an alternative, synoptic and economic method for assessing the spatial variability of suspended sediments in natural waters. Remote sensing is a monitoring technique that is of increasing importance in coastal and marine environmental management and protection, especially where access is difficult or the area to be covered is large.

In the coastal zone, an obvious distinction can often be seen between the colour of shallow waters, in which sediments are easily re-suspended, and that of neighbouring deeper waters. This is also evident where turbid river waters discharge into clearer coastal waters and where human activity results in the re-suspension of sediment from the bottom (see figure 1.1).

(a)

(b)

Figure 1.1: Aerial photographs of a) the mouth of the Conwy Estuary, showing increased turbidity associated with coastal re-suspension of suspended sediments and b) the Menai Strait where trawling activity leads to localised re-suspension of bottom sediments. Photographs courtesy of the NERC Airborne Remote Sensing Facility (Site 03/01 Menai Strait, 8th May 2001).

It is this principle of colour change that enables the study of sediment concentrations from remotely sensed images of ocean colour. In 1978, the National Aeronautics and Space Administration (NASA) launched the first satellite sensor devoted to the study of ocean colour, the Coastal Zone Color Scanner (CZCS), which opened the door to the application of these simple observations to remotely sensed ocean colour imagery. Now, a new generation of ocean colour sensors is operational, offering improved capabilities with respect to spectral resolution and radiometric sensitivity and resulting in detailed spectral information more suited to the optical complexity of natural waters (Sathyendranath, 2000).

The intrinsic colour of the ocean is determined by scattering and absorption of visible light within the water body (Gordon *et al.*, 1975; Morel and Prieur, 1977). Although there may be many additional parameters of more minor importance, the colour of natural waters can be practically determined from three main optically active constituents; phytoplankton, mineral sediments and dissolved organic matter, in addition to pure water itself (Morel and Prieur, 1977). The link between these constituents and observed ocean colour can be studied in terms of forward and inverse modelling (figure 1.2), by incorporating both inherent and apparent optical properties of the water body.

Inherent optical properties (IOPs) were defined by Preisendorfer (1961) as those properties of the aquatic medium itself, such as absorption and scattering, whose values depend only upon the medium and are independent of the prevailing radiance distribution. In contrast, apparent optical properties (AOPs) are dependent upon the light field within the medium but are also largely a function of the composition of the water and thus are related to the inherent optical properties. The forward modelling problem uses the concentrations and IOPs of the various substances present in the water column to determine their effect on ocean colour. The inverse modelling problem is the retrieval of these water quality parameters from satellite measured ocean colour and requires the interpretation of the spectral signature in terms of the water's optical properties, which in turn can be related to concentrations of dissolved and particulate matter.
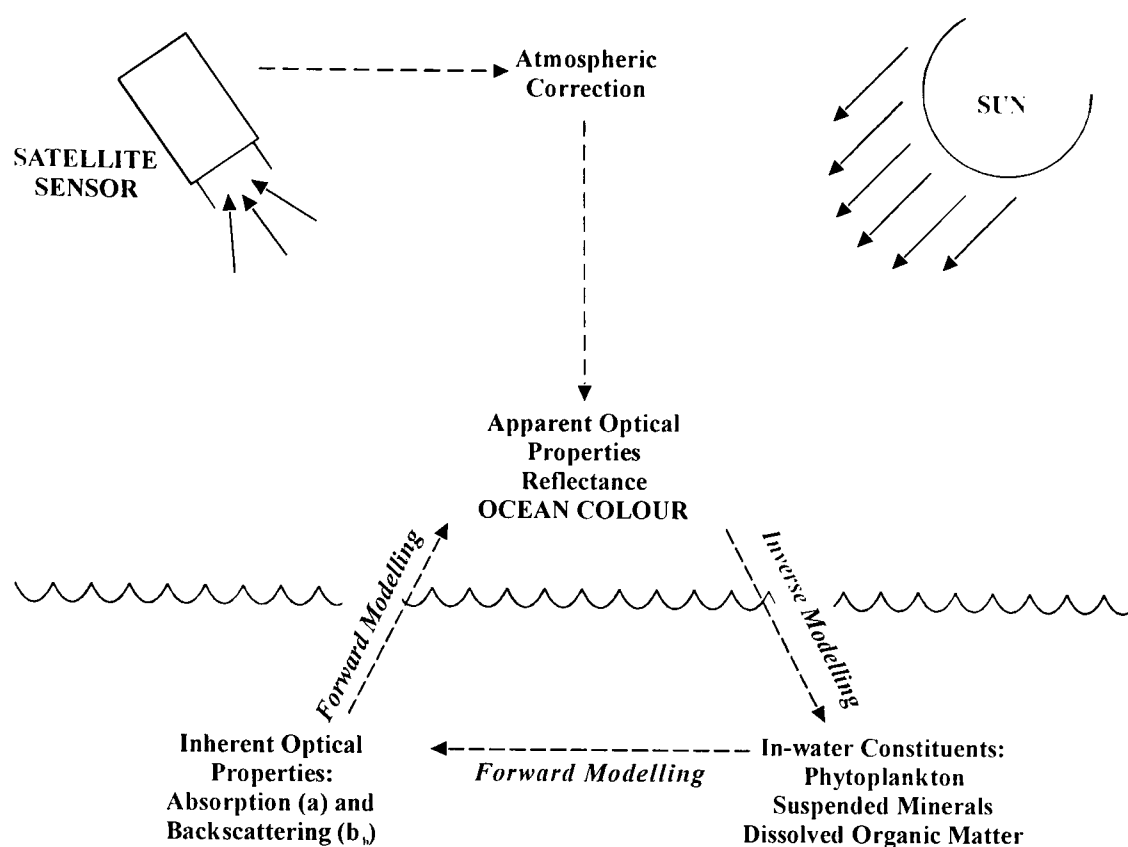
Figure 1.2:   Relationships between remotely sensed ocean colour, AOPs, IOPs and in-water constituents.

The complex nature of many natural waters has led to many classification schemes aimed at separating waters into 'types' defined by their optical properties. The most frequently adopted classification is that first introduced by Morel and Prieur (1977) whereby waters are classified as either Case 1 or Case 2. Case 1 waters are those where the optical properties are principally determined by phytoplankton and their associated co-varying organic material. Case 2 waters are influenced not just by phytoplankton but also by other substances that vary independently of phytoplankton, in particular suspended minerals and dissolved organic matter.

Case 1 waters are considered to encompass over 90% of the world oceans (Sathyendranath, 2000). To date, remote sensing of ocean colour has focussed largely on these relatively simple Case 1 waters and comparatively little work has been carried out in the optically more complex Case 2 waters, such as the Irish Sea. Even though only a small part of the earth's water surface falls into the Case 2 water category, it is an important fraction that includes most coastal and inland water bodies. Consequently, optical properties and the remote sensing of Case 2 waters have received increased attention in recent years.

The assumptions underlying the definition of Case 1 waters means that optical properties of these waters can be modelled simply as a function of chlorophyll concentration. This has led to success in the use of ocean colour algorithms for chlorophyll retrieval and advances in estimates of primary productivity in Case 1 waters (Longhurst *et al.*, 1995; Behrenfeld and Falkowski, 1997). Algorithms incorporating reflectance ratios have been traditionally adopted for estimating chlorophyll concentrations from ocean colour information. A blue/green ratio is commonly used, representing the shift in water colour from blue to green with increasing chlorophyll concentration (Gordon and Morel, 1983). However, it is well recognised that the standard algorithms for retrieval of chlorophyll break down in Case 2 waters, where other constituents complicate the optical signal (Mitchelson *et al.*, 1986; Brown and Simpson, 1990). Brown and Simpson (1990) were able to show empirically that the relationship between the blue/green ratio and chlorophyll concentration changed in response to changes in the concentration of inorganic sediments. Platt and Sathyendranath (1988) also showed that estimates of water-column primary productivity are extremely sensitive to light attenuation by substances other than phytoplankton. This means that in order to make accurate estimates of chlorophyll, and therefore primary productivity, in shelf seas it may be necessary to have an independent estimate of the sediment concentration.

There have been numerous studies over the years attempting to derive SPM concentrations from remotely sensed ocean colour, with many of the above applications in mind. Early research relied on the coincident measurement of SPM concentrations with satellite overpasses (Ritchie and Cooper, 1988; Lathrop *et al.*, 1991). This technique was open to several sources of error in particular the lack of spatial coverage and errors introduced through water mass advection and sub-pixel variability. The use of *in situ* radiometric measurements to obtain empirical relationships between SPM and ocean colour enables the reduction of much of this uncertainty. Recently, effort has turned to a more thorough understanding of the optical properties of the parameters of interest and the development of optical models to derive concentrations of the in-water constituents (Forget *et al.*, 1999; Moore *et al.*, 1999; Doxaran *et al.*, 2002a). Whilst this has resulted in some degree of success, effort is still required to reduce the level of uncertainty in retrieved parameter concentrations.

There has been little agreement to date between published suspended sediment algorithms (Mitchelson-Jacob, 1999), either in their form, or wavelength selection. This has been attributed to many factors including variations in the range of MSS concentrations for which the algorithm was derived for, variations in particle properties such as size, shape or mineralogy, as well as errors incurred through the presence of co-varying in-water constituents such as chlorophyll and yellow substance (Novo *et al.*, 1989). These algorithms have been applicable to a range of ocean colour sensors, from CZCS (e.g. Clark *et al.* 1980; Simpson and Brown, 1987), and Landsat (e.g. Ritchie and Cooper, 1988) to the currently operating SeaWiFS (Tassan, 1994; Wernand *et al.*, 1998). Much of this literature, however, relates to ocean colour sensors that are no longer in operation (algorithms are rarely interchangeable due to differences in spectral wavebands). As a result of all these factors, reliable algorithms are currently limited to season- and site-specific examples. Mitchelson-Jacob (1999) tested 18 existing suspended sediment algorithms on SeaWiFS imagery of the European continental shelf. None of those algorithms tested were able to derive realistic distributions or concentrations of suspended sediments for this region.

1.2   Main Objectives of the Study

The ultimate aim of the study was to successfully derive suspended sediment concentrations from ocean colour satellite imagery of the Irish Sea. To reach this, a number of specific objectives were set:

- To obtain *in situ* measurements of ocean colour in waters containing a range of suspended sediment, chlorophyll and yellow substance concentrations.

- To develop an algorithm for the retrieval of suspended sediment concentrations from this ocean colour information.

- To test results against known optical theory.

- To validate the algorithm using an independent dataset.

- To apply the algorithm to SeaWiFS ocean colour imagery to produce maps of suspended sediment in the Irish Sea.

1.3   Publications and Presentations

During this period of research, results have been presented at conferences through both poster and oral presentations and within the School of Ocean Sciences through departmental seminars. Early results on the development of an SPM algorithm for the Irish Sea (some of which are presented in Chapter Four) have been peer-reviewed and published in the *International Journal of Remote Sensing*. A further study, developing a method for measuring salinity from remotely sensed ocean colour, although not directly related to the subject of this thesis, was published from the same data-set.

Binding, C. E. and Mitchelson-Jacob, E. G. 2000. SPM algorithms for SeaWiFS imagery of Case 2 waters. Poster presented at Oceans from Space, Venice 2000.

Binding, C. E. and Bowers, D. G. 2003. Measuring the salinity of the Clyde Sea from remotely sensed ocean colour. *Estuarine, Coastal and Shelf Science*, in press.

Binding, C. E., Bowers, D. G. and Mitchelson-Jacob, E.G. 2003. An algorithm for the retrieval of suspended sediment concentrations in the Irish Sea from SeaWiFS ocean colour satellite imagery. *International Journal of Remote Sensing*, in press.

Binding, C. E., Bowers, D. G. and Mitchelson-Jacob, E. G. 2002. The retrieval of suspended sediments from ocean colour satellite imagery. Paper presented at the Challenger Society for Marine Science, Plymouth, 9-13 September 2002.

Chapter Two

Background Relating to Ocean Optical Theory and the Remote Sensing of Suspended Sediments

CHAPTER TWO: BACKGROUND RELATING TO OCEAN OPTICAL THEORY AND THE REMOTE SENSING OF SUSPENDED SEDIMENTS

2.1   Introduction

This chapter aims to introduce the optical theory used during this period of research and to describe how this theory is relevant in the remote sensing of ocean colour, with particular emphasis on the effect of suspended particulate material. Section 2.2 defines the fundamental parameters involved in the study of ocean optics, describing the relationships between the inherent and apparent optical properties. Section 2.3 describes the effect of various in-water constituents (dissolved and particulate) on ocean colour. This leads to a section on the remote sensing of ocean colour and details of the SeaWiFS ocean colour satellite sensor. Finally, section 2.4 provides a review of the remote sensing of suspended sediments, including the assessment of previously published algorithms.

2.2   Properties of Light

Light of wavelength λ is composed of a stream of photons, each of which possess a specific energy hc/λ where h is Planck's constant (6.626×10^{-34} J s) and c is the speed of light (2.998×10^{8} ms^{-1}). The wavelength of light is determined by $\lambda = c/f$ where f is the photon's frequency. The human eye is sensitive only to electromagnetic radiation in the visible spectrum, that is wavelengths ranging from 400 nm to 700 nm, and it is this wavelength range that is measured in the remote sensing of ocean colour. The following sections describe the primary optical parameters measured in optical and remote sensing studies. For the most part, definitions are taken from the key texts on marine optics; Jerlov (1976), Kirk (1994) and Mobley (1994).

2.2.1   Ocean Optical Theory

The fundamental radiometric parameters of interest in ocean optics are derived from the spectral radiance and irradiance. Radiance, irradiance, and all terms derived from them, are wavelength dependent, exhibiting considerable variation across the visible spectrum. Consequently, these parameters are expressed with respect to particular wavelengths, for example, downwelling irradiance is typically denoted as $E_d(\lambda)$, with

the relevant wavelength in parentheses.

The radiant flux, Φ, is the rate of flow of light energy, expressed in W (J s^{-1}). The radiant intensity, I (W sr^{-1}), is defined as the radiant flux per unit solid angle in a specified direction.

Radiance, L, for wavelength λ and at depth z, is defined as the radiant flux per unit solid angle ω in a given direction per unit projected area in that direction (equation 2.1 and figure 2.1).

$$L(\lambda,z) = \frac{d^2\Phi}{dS\cos\theta\,d\omega} \qquad (\mu W\,cm^{-2}\,nm^{-1}\,sr^{-1}) \qquad (2.1)$$
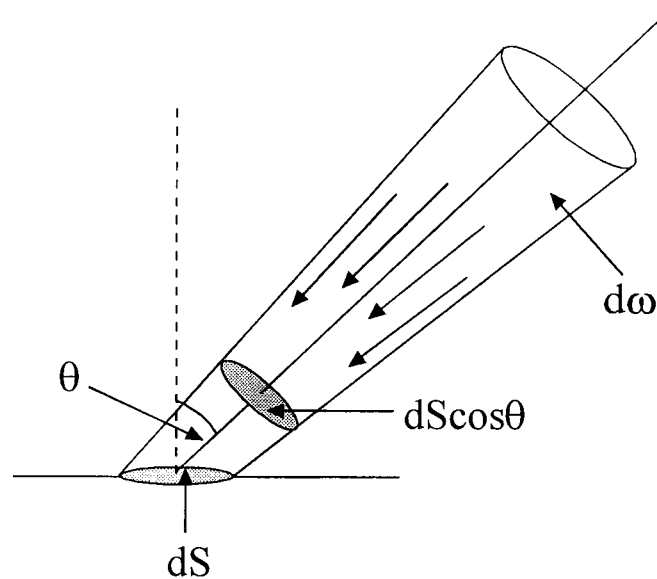
Figure 2.1: Definition of radiance, L, incident on area dS at a zenith angle θ. The radiant flux passes perpendicularly to dScosθ, the projected area of dS.

Irradiance, E, is the total radiant flux (Φ) intercepted by an area (A) of a given plane surface (E=Φ/A). Irradiance does not specify the direction in which the radiation is travelling, but integrates the total flux over an entire hemisphere of directions. A flux passing downwards through the water column is referred to as the downwelling irradiance, E_d, whilst that travelling up through the water column is the upwelling irradiance, E_u. The total downward irradiance at a surface is therefore obtained by integrating radiance with respect to the solid angle over the whole of the upper hemisphere (equation 2.2).

$$E_d(\lambda, z) = \int_{2\pi} L(\theta, \phi) \cos\theta \, d\omega \qquad (\mu W \, cm^{-2} \, nm^{-1}) \qquad (2.2)$$

where θ and ϕ define the zenith and azimuthal angles of the incident radiance.

Similarly, total upward irradiance is given by equation 2.3. The equation is made negative in order to allow for the fact that $\cos\theta$ is negative for $90° < \theta < 180°$.

$$E_u = -\int_{-2\pi} L(\theta, \phi) \cos\theta \, d\omega \qquad (\mu W \, cm^{-2} \, nm^{-1}) \qquad (2.3)$$

As the angle of the radiant flux to the irradiance sensor changes, the area of the collector upon which light impinges also changes. To compensate for this, the response of the irradiance sensor should be proportional to the cosine of the angle θ. When a detector is equally sensitive to photons travelling in any direction, it measures scalar irradiance, E_0, which is independent of the angle of incidence and is measured as the integral of the radiance distribution at a point over all directions about that point (equation 2.4).

$$E_0 = \int_{4\pi} L(\theta, \phi) \, d\omega \qquad (\mu W \, cm^{-2} \, nm^{-1}) \qquad (2.4)$$

Collecting all downward travelling photons in this way gives the downwelling scalar irradiance, E_{0d}, measured as the integral of radiance over all directions on the upper hemisphere (2π). Likewise, collecting all upward travelling photons in the same manner would result in the measurement of the upwelling scalar irradiance, E_{0u} (integrating over the lower hemisphere, -2π).

2.2.2   Inherent and Apparent Optical Properties

Optical properties of an aquatic medium were conveniently categorised by Preisendorfer (1961) into inherent and apparent optical properties. Inherent optical properties (IOPs) are intrinsic properties of the aquatic medium itself, whose values depend only upon the medium and are independent of the prevailing radiance distribution. In contrast, apparent optical properties (AOPs) are dependent upon the light field within the medium and, therefore, vary to some extent with solar altitude

and depth, but are also largely a function of the composition of the water and thus are related to the inherent optical properties. Inherent optical properties of a water body include the absorption, scattering and beam attenuation coefficients (a, b and c respectively) and the volume scattering function (β). Commonly used apparent optical properties are the irradiance reflectance, diffuse attenuation coefficient and average cosine.

Inherent Optical Properties (IOPs)

Absorption, Scattering and Beam Attenuation Coefficients

Absorption is the process by which molecules of water and other constituents capture photons, causing the molecule to gain energy corresponding to the energy of the incident photon (Kirk, 1994). Absorption results in the attenuation of light. Scattering is a process that causes the deviation of light from a rectilinear propagation, resulting in alterations to the angular distribution of the light field. Scattering may make downwelling photons travel more obliquely, thus increasing their pathlength and consequently their rate of absorption per unit vertical distance travelled (Kirk, 1991). Scattering is caused both by the water itself and by particles, more details of which are discussed in section 2.3. The beam attenuation coefficient, describes the combined effect of absorption and scattering and represents the diminution of light with increasing distance traversed.

Figure 2.2 describes a volume of water of thickness Δr, illuminated by a collimated beam of monochromatic light of total radiant power $\Phi_i(\lambda)$. A proportion (Φ_a,λ), of the incident power is absorbed within the volume of water, whilst some (Φ_s,λ), is scattered out of the beam of light at an angle Ψ. The remainder (Φ_t,λ), is transmitted through the volume with no change in direction.
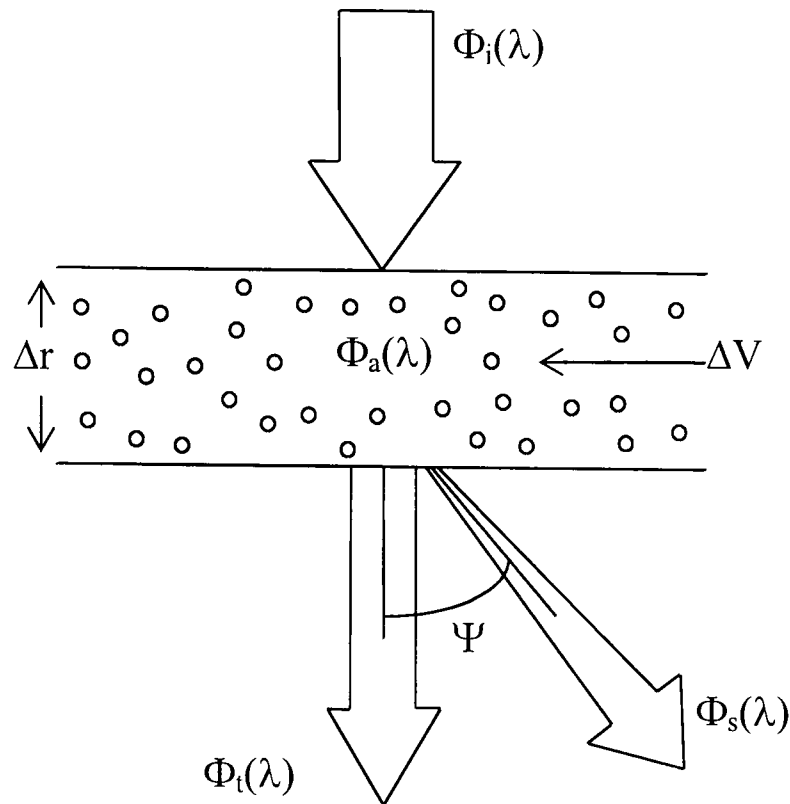
Figure 2.2: Diagrammatic representation of inherent optical properties. Reproduced from Mobley (1994).

The spectral absorbance, $A(\lambda)$, is the fraction of incident power that is absorbed within the defined volume of water.

$$A(\lambda) = \frac{\Phi_a(\lambda)}{\Phi_i(\lambda)} \tag{2.5}$$

From this, the absorption coefficient, $a(\lambda)$, is defined as the total absorbance per unit distance of the medium.

$$a(\lambda) = \frac{\Phi_a(\lambda)}{\Phi_i(\lambda)} \bigg/ \Delta r \qquad (\mathrm{m}^{-1}) \tag{2.6}$$

Similarly, the spectral scatterance, $B(\lambda)$, is the fraction of incident power that is scattered out of the beam.

$$B(\lambda) = \frac{\Phi_s(\lambda)}{\Phi_i(\lambda)} \tag{2.7}$$

and the scattering coefficient, $b(\lambda)$, is defined as the total scatterance per unit distance of the medium.

$$b(\lambda) = \frac{\Phi_b(\lambda)}{\Phi_i(\lambda)} \Big/ \Delta r \qquad\qquad (m^{-1}) \qquad\qquad (2.8)$$

In the same way, the spectral transmittance, $T(\lambda)$, is the proportion of incident power that is transmitted through the medium, whilst the spectral beam attenuation coefficient, $c(\lambda)$ is defined simply as the sum of the absorption and scattering coefficients ($c = a + b$).

In their definition as inherent optical properties of sea water, a, b and c are dependent on the various constituents present in the water. It is therefore possible to identify the contribution that each constituent in the water makes to the total absorption, scattering and attenuation coefficients. This is done by separating, for example, the total absorption coefficient into individual contributions from pure water, phytoplankton pigments (C), suspended sediment (MSS) and yellow substance (YS). According to the Lambert-Beer law, all inherent optical properties are additive over the constituents of the medium (Kirk, 1994). Absorption can therefore be written as:

$$a = a_{Water} + a_C + a_{MSS} + a_{YS} \qquad\qquad (2.9)$$

Another form of the Lambert-Beer law is that the inherent optical property due to any constituent of the medium is proportional to the concentration of that constituent such that:

$$a = a_w + \sum (a_i{}^* C_i) \qquad\qquad (2.10)$$

where a_w is the absorption by water and $a_i{}^*$ and C_i are the specific absorption coefficient and concentration of constituent i respectively.

Equation 2.9 can, therefore, be expressed in terms of both the specific absorption coefficients, a^* (expressed per unit of concentration) and the total concentration of

the individual constituent, expressed in square brackets:

$$a = a_{Water} + [C]a^*_C + [MSS]a^*_{MSS} + [YS]a^*_{YS}$$ (2.11)

Similar expressions can be written for the specific scattering coefficients, although since yellow substance does not contribute to scattering the expression would consist only of scattering due to water, phytoplankton and suspended sediments.

Volume Scattering Function

The effect of the scattering process on the light field is dependent not only on the total scattering coefficient but also on the directional properties of the scattered flux. The volume scattering function specifies the angular distribution of scattering as the amount of scattering per unit angle. It is defined as that fraction of the radiant intensity, dI, which is scattered in a given direction per unit incident irradiance per unit volume (equation 2.12).

$$\beta = \frac{dI}{EdV} \qquad (m^{-1}\,sr^{-1}) \qquad (2.12)$$

The integral of β over all directions gives the total scattering coefficient (equation 2.13).

$$b = \int_{4\pi} \beta(\theta)d\omega \qquad (m^{-1}) \qquad (2.13)$$

The total scattering coefficient can subsequently be partitioned into its forward (b_f) and backward (b_b) components by integrating over scattering angles from 0 to 2π and 2π to 4π respectively.

The volume scattering function, β, is often normalised to total scattering to give scattering per unit angle relative to total scattering and is referred to as the scattering phase function ($\tilde{\beta} = \beta / b$). For the majority of natural waters, particularly the more turbid waters, the volume scattering function has much the same shape, despite large variations in the total scattering. An accurate data set of β which has been found

applicable to all but very clear oceanic waters was obtained by Petzold (1972) for coastal waters of San Diego Harbour. Phillips and Kirk (1984) claimed that it is valid for most waters because the shape of the volume scattering function is insensitive to turbidity for scattering coefficients greater than 0.1 m^{-1}.

Apparent Optical Properties (AOPs)

Irradiance Reflectance

As with many optical parameters, the following are described with respect to specific wavelengths and depths. Each parameter is defined with these variables in parentheses, whereby z defines the depth and λ the wavelength to which the parameter refers. Many parameters are defined either just above or just below the air sea interface. In these cases, z is replaced by 0^+, denoting above water, or 0^-, denoting below water. The most common AOP used in remote sensing is the irradiance reflectance, defined as the ratio of spectral upwelling to downwelling irradiances just below the air-sea interface (equation 2.14).

$$R(0^-,\lambda) = \frac{E_u(0^-,\lambda)}{E_d(0^-,\lambda)} \qquad (2.14)$$

Often, E_u is not measured and consequently L_u is substituted (Gordon and Morel, 1983) using the relationship $E_u(0^-,\lambda) = \pi L_u(0^-,\lambda)$. The use of π in this relationship assumes complete isotropy of the upward irradiance in the underwater light field, and alters equation 2.14 to:

$$R(0^-,\lambda) = \frac{L_u(0^-,\lambda)\pi}{E_d(0^-,\lambda)} \qquad (2.15)$$

There has, however, been uncertainty over the use of π in this relationship since the light field in natural waters is almost certainly not isotropic. Austin (1974) described how a quantity Q (that is the ratio of upwelling irradiance to upwelling radiance, E_u/L_u) should be used to describe the directional structure of the upwelling radiant field, with a value of near 5. More recently, Loisel and Morel (2001) suggested that Q may vary between π and 2π in highly absorbing waters (b/a<1) and showed that.

even in very turbid waters, the upward radiance field is not isotropic and remains sun-angle dependent.

The spectral remote sensing reflectance, R_{RS} is defined as:

$$R_{RS}(0^+,\lambda) = \frac{L_W(0^+,\lambda)}{E_d(0^+,\lambda)} \qquad (sr^{-1}) \qquad (2.16)$$

where $L_w(0^+,\lambda)$ is the water-leaving radiance just above the sea surface.

A number of authors have used the relationships in equations 2.17a and 2.17b to convert from measurements just below the sea surface (0^-) to those measured by the satellite, just above the sea surface (0^+). In these equations, 0.54 is the mean coefficient summarising the effect of internal reflection of the upwelling flux during transmission through the interface and 0.96 accounts for the loss of the downwelling flux by reflection at the air-sea interface (Austin, 1974; Gordon *et al.*, 1983).

$$L_w(0^+,\lambda) = 0.54L_u(0^-,\lambda) \qquad (2.17a)$$

$$E_d(0^-,\lambda) = 0.96E_d(0^+,\lambda) \qquad (2.17b)$$

Diffuse Attenuation Coefficient

Radiance and irradiance decrease approximately exponentially with depth as a function of the diffuse attenuation coefficient, K. This is expressed in equation 2.18 relating to the downwelling irradiance and therefore the downwelling diffuse attenuation coefficient.

$$E_d(z,\lambda) = E_d(0^-,\lambda)e^{-K_d z} \qquad (m^{-1}) \qquad (2.18)$$

where $E_d(z,\lambda)$ is the downwelling irradiance at depth z and wavelength λ and $E_d(0^-,\lambda)$ is the downwelling irradiance just beneath the surface.

The beam attenuation coefficient, $c(\lambda)$, is defined in terms of the radiant power lost from a single collimated beam of photons. In contrast, the diffuse attenuation

coefficient, $K_d(\lambda)$, is defined with respect to the decreasing ambient downwelling irradiance (E_d) with depth and comprises photons travelling in all directions, not just in a collimated light field.

Average Cosines

The Gershun equation (equation 2.19) provides a simple relationship between the IOPs and the AOPs. The equation relates the diffuse attenuation coefficient, K, to the absorption coefficient, a, using the average cosine of the angle the photons make with the vertical within the water column, μ, (Jerlov, 1976).

$$K = (1/\mu)a \qquad (2.19)$$

The average cosines for upwelling, downwelling and total irradiance provide a way of specifying the angular structure of a light field. The average cosine for downwelling light, μ_d, at any point is the average value of the cosine of the zenith angle of all the downwelling photons in a volume. It can be calculated as the plane downwelling irradiance divided by the total downwelling scalar irradiance (equation 2.20)

$$\mu_d(z,\lambda) = \frac{E_d(z,\lambda)}{E_{0d}(z,\lambda)} \qquad (2.20)$$

Likewise, the spectral upwelling average cosine relates the upwelling irradiances. The average cosine for total light is the average value of the cosine of the zenith angle of all the photons in the volume and can be given by the net downward irradiance divided by the scalar irradiance:

$$\mu = \frac{\overline{E}}{E_0} = \frac{E_d - E_u}{E_0} \qquad (2.21)$$

Upper and lower limits of μ are 1.0 and -1.0 respectively, whereby for $\mu = 1$, photons are travelling vertically down.

2.2.3 Relationships between IOPs and AOPs

The complexity of the underwater light field is such that there is no analytical expression by which apparent optical properties can be directly calculated from given values of the inherent optical properties (Kirk, 1981a). However, since IOPs specify the probability of events happening to photons, (i.e. the scattering and absorption coefficients specify the probability that a photon will be scattered or absorbed by a medium), they provide the information that is needed for the Monte Carlo method. The Monte Carlo method is a technique in which the fate of large numbers of photons is followed and an average behaviour calculated. It is this method that was adopted by Gordon *et al.* (1975) in their pioneering work investigating the relationships between the inherent and apparent optical properties of the ocean. Their work resulted in the expression of the irradiance reflectance, R, in terms of absorption (a) and backscattering (b$_b$) coefficients which can be simplified (Jerlov, 1976) to

$$R = f b_b / a \qquad\qquad (2.22)$$

where f is a function of the illumination conditions (solar angles and proportions of direct to diffuse light), atmospheric turbidity and surface roughness (Morel and Gentili, 1996).

Kirk (1981a) found a linear relationship between R and b$_b$/a with the sun at zenith, represented by the expression $R = 0.328 b_b / a$. This is in good agreement with the relationship $R = 0.33 b_b / a$ obtained by Gordon *et al.* (1975), and used by Morel and Prieur (1977) in their analysis of the reasons for variations in ocean colour. Whereas the work of Gordon *et al.* (1975) and Morel and Prieur (1977) was concerned with Case 1 waters, Kirk (1981a, 1981b, 1984, 1991) studied turbid coastal and inland waters where the ratio of scattering to absorption, b/a was up to 30. The work of Kirk described below, combined with that of Petzold (1972), may therefore be applicable to the turbid waters of the Irish Sea.

Kirk (1991) found that for most water types, under vertically incident light, the relationship between b$_b$/a and R was not strongly affected by the shape of the volume

scattering function. By assuming a volume scattering function the same as that measured by Petzold (1972), the relationship between R and b_b/a (equation 2.22) can be studied simply in terms of its dependence on the angular structure of the light field. The fixed nature of this relationship is the basis of the method of estimating the total scattering and absorption coefficients from irradiance measurements.

Since apparent optical properties are affected by the angular structure of the light field within the water, it is reasonable to expect the relationship between IOPs and AOPs to depend on the angular structure of the light field incident on the water surface, i.e. to vary both with solar altitude and the proportion of direct and diffuse solar radiation. Kirk (1981a) found that for zenith angles of 45° and 60°, the constant relating b_b/a to R increased to 0.391 and 0.449 respectively. Using Monte Carlo simulations, Kirk (1984) investigated the manner in which this relationship varies with solar altitude. The constant in equation 2.22 was found to be linearly proportional to the zenith angle of incidence, rising from 0.346 for vertically incident light, to 0.57 for light at grazing incidence. This allowed the formulation of equation 2.23, relating the irradiance reflectance R to b_b/a whilst also accounting for variations in the surface light field through μ_0, the average cosine of the angle the photons make with the vertical just beneath the surface.

$$R = (0.975 - 0.629\mu_0)b_b / a \qquad (2.23)$$

For all natural waters, the shape of the volume scattering function is such that there is more forward scattering than backward. As the angle of incidence increases, so more of the forward scattered light becomes upward scattering rather than downward, this explaining why reflectance increases with increasing zenith angle (Kirk, 1989).

Equation 2.23 relates to conditions under a clear sky and therefore direct light. Kirk (1984) also studied this relationship under overcast conditions and showed that with the average value of μ_0 as 0.856, equation 2.23 can be re-written as $R = 0.427b_b/a$.

In a Monte Carlo study of underwater light fields in turbid waters (b/a up to 30), Kirk (1981, 1984) found that K_d could be related to a and b according to equation 2.24.

$$K_d = \frac{1}{\mu_0}\left(a^2 + G(\mu_0)ab\right)^{1/2} \tag{2.24}$$

where $G(\mu_0)$ is a constant that depends on the angular structure of the underwater light field. As the zenith angle of incidence increases (i.e. the solar altitude decreases), the value of $G(\mu_0)$ decreases according to equation 2.25.

$$G(\mu_0) = 0.425\mu_0 - 0.19 \tag{2.25}$$

K_d can therefore be expressed as an explicit function of μ_0, a and b

$$K_d = \frac{1}{\mu_0}\left(a^2 + (0.425\mu_0 - 0.19)ab\right)^{1/2} \tag{2.26}$$

In these calculations, K_d is the average K_d throughout the euphotic zone (the layer in which downward irradiance is reduced to 1% of the subsurface value).

Kirk (1984) showed that for waters where b/a~1, the angle of incidence created variations in K_d of up to 40%. As scattering was increased, with b/a approaching 10, the variability was reduced to 12%. Therefore K_d is less sensitive to solar altitude in highly scattering waters than in predominantly absorbing waters.

Although the conditions in these earlier studies would cover most oceanic and coastal environments (b/a up to 30 and R up to 24%), Kirk (1994) tested the applicability of this relationship to highly turbid waters where b/a reached as high as 200. In the range b/a 2-200, $G(\mu_0)$ varied only from 0.233 to 0.264 and all relationships were indistinguishable up to b/a of 70. Therefore equation 2.26 should satisfactorily describe the dependence of K_d on scattering and absorption even in extremely turbid waters.

Equations 2.23 and 2.26 provide a simple method of calculating the absorption and scattering coefficients from the apparent optical properties R and K_d (Kirk, 1981b) and have been used for this purpose by numerous authors (e.g. Phillips and Kirk, 1984; Weidemann and Bannister, 1986; Gallegos et al., 1990; Bowers and

Mitchelson-Jacob, 1996). This method was applied to data for Lake Pend Oreille (Kirk, 1981b) and gave values of b differing by only 5% from those that were calculated by subtracting the absorption coefficient from the beam attenuation coefficient.

2.3   The Composition and Optical Properties of Natural Waters

The inherent optical properties of natural waters are determined by the concentrations of dissolved and particulate matter, in addition to the effects of the water itself.   The following sections describe the optical properties of the primary constituents influencing ocean colour. Whilst it is acknowledged that factors such as detritus, bacteria and zooplankton may have minor effects on reflectance and ocean colour, this study is limited to dealing with the effects of dissolved organic material (yellow substance), phytoplankton, mineral suspended sediments and pure water.

2.3.1   Pure Water

Absorption

Pure water absorbs only very weakly in the blue and green regions of the spectrum and increases towards the longer wavelengths. At 650 nm, a 1 metre layer of pure water will absorb around 35% of the incident light (Kirk, 1994), whilst at 800 nm, all light is absorbed within 50 centimetres of the surface.

The absorption spectrum of pure water has been measured by many researchers (see Smith and Baker, 1981 and Sogandares and Fry, 1997, for reviews). Most show considerable agreement at wavelengths greater than 600 nm. This is because firstly, absorption at longer wavelengths is large and thus easier to measure and secondly because scattering by water becomes smaller compared with absorption. As the wavelength decreases to shorter visible and near-UV wavelengths there is increasing uncertainty in the measurements of absorption with published absorption data in the 400-500 nm range varying by almost an order of magnitude. Inconsistencies in published absorption spectra are probably caused by a combination of both experimental error and unknown sample purity (Sogandares and Fry, 1997).

Smith and Baker (1981) published measurements of absorption in the clearest natural waters for the range 200 nm to 800 nm and these values have been used routinely in

studies of marine and freshwater optics. More recently, Buiteveld *et al.* (1994), Sogandares and Fry (1997) and Pope and Fry (1997) provided detailed measurements of the absorption spectra of the purest water available, using techniques that are free from the effects of scattering

Scattering

Morel (1974) reviewed both theory and observations pertaining to scattering by water. Similar to the Rayleigh theory for gases, scattering by water is considered to be caused by the random motion of molecules resulting in fluctuations in molecule density. The presence of various ions in sea water (Cl^-, Na^+ etc.) results in increased scattering by up to 30%. Scattering is also known to be temperature, salinity and pressure dependent; scattering decreases with decreasing temperature or increasing pressure because of a reduction in the small-scale density fluctuations.

The directional scattering by water molecules was modelled by Morel (1974) and is given by:

$$\beta_W(\theta) = \beta_W(90°)(1 + 0.835\cos^2\theta) \qquad (m^{-1}\ sr^{-1}) \qquad (2.27)$$

Equation 2.27 shows that the volume scattering function of pure water has a minimum at 90° and increases symmetrically with increasing and decreasing angles ($\beta(180°) = \beta(0°)$). Therefore, for pure water, scattering in the backward direction is equal to that in the forward direction, and thus $b_b/b=0.5$. Values of scattering coefficients for pure water at intervals throughout the visible spectrum are presented in Morel (1974) and Smith and Baker (1981) and Buiteveld *et al.* (1994).

Scattering of pure sea water has a wavelength dependence of $\lambda^{-4.32}$ (Morel, 1974) resulting in the preferential scattering of blue light. The combination of the dominant absorption at long wavelengths described above and the dominant scattering at shorter wavelengths results in the characteristic blue colour of clear ocean waters.

2.3.2 Mineral Suspended Sediments (MSS)

Absorption

Most literature documenting the absorption properties of particulate matter relate to phytoplankton, with comparatively little evidence available describing inorganic particles. The frequently used quantitative filter technique (see Chapter Three for details) has enabled some estimates of absorption by mineral suspended sediments (MSS) to be made (Davies-Colley, 1983; Bowers *et al.*, 1996). Bowers *et al.* (1996) observed that the absorption spectra of inorganic particles collected on filters consistently showed an exponential decrease with increasing wavelength, with the absorption coefficient at a single wavelength being proportional to the concentration of mineral suspended sediments (MSS). Davies-Colley (1983) and Gallegos *et al.* (1990) found that total particulate material had an absorption spectrum that was the sum of that of chlorophyll and an exponential spectrum. Davies-Colley attributed the exponential spectrum to the chemical adsorption of yellow substance by the inorganic particles, since dissolved organic matter (yellow substance) is known to exhibit such an exponential decay (see section 2.3.4). Bricaud and Stramski (1990) studied the spectral absorption of particulates on filters and observed the exponential increase in absorption due to detrital matter with decreasing wavelength. The range of the exponents found was from 0.0024 to 0.017 for Peruvian upwelling waters and 0.008 to 0.015 for Sargasso Sea waters.

Scattering

Particulate matter is the most significant contributor to scattering in natural waters (Kullenberg, 1974). Even the clearest of natural waters contain sufficient particulate matter to alter the way in which light is scattered compared to scattering in pure water. The scattering behaviour of particles can be described by Mie theory in terms of three phenomena; diffraction, refraction and reflection (figure 2.3). Diffraction is dependent on the size and shape of the particle and determines the amount of forward scattering, whereas refraction and reflection depend on the particle composition (i.e. refractive index) and determine the extent to which light is backscattered (Kullenberg, 1974).
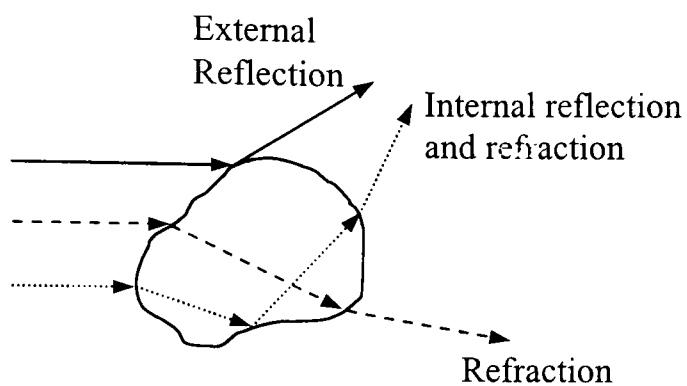
Figure 2.3: Processes of scattering by particles.

A particle will scatter a fraction of the radiant flux that depends on the scattering cross-section of the particle. The scattering cross section of a particle is not the same as the geometric cross section (that is πr^2 for a spherical particle) as it is possible for the particle to perturb the light field beyond its physical boundary (Kirk, 1994). The amount of scattering decreases as the ratio of particle volume to cross-sectional area increases (Van de Hulst, 1957; Baker and Lavelle, 1984), hence for a fixed mass, larger particles are less effective at scattering light than smaller particles.

Mie theory predicts that for particles larger than the wavelength of light, most of the total scattering is in the forward direction, resulting in a volume scattering function (scattering in a given direction) that becomes highly peaked at small angles. The most extensively cited measurements of scattering are those made by Petzold (1972) for waters ranging from the turbid water of San Diego Harbour to the clear waters of the Bahama Islands. These measurements showed very little variation in the shape of the volume scattering function in different waters, such that a typical phase function is now frequently assumed. The ratio of b_b/b showed some variation in Petzold's data that may be attributed to variations in particle composition. Values of b_b/b ranged from 0.044 for clear ocean waters (compared with 0.5 for pure water) to 0.019 for more turbid waters.

Refractive indices of oceanic particles range from about 1 to 1.26 (relative to seawater). Living cells have lower indices than mineral particles (in the range 1.02 – 1.07) because of their relatively high water content (40 to 80%) (Morel, 1987; Twardowski *et al.*, 2001). Refractive indices of inorganic particles are generally higher; the common oceanic minerals ranging from 1.14 to 1.26 (Jerlov, 1976; Twardowski *et al.*, 2001).

2.3.3 Phytoplankton

Absorption

Phytoplankton cells are strong absorbers of visible light and therefore play a major role in determining the absorption properties of natural waters. Work on the absorption properties of phytoplankton have been based both on laboratory cultures (e.g. Bricaud *et al.*, 1983) and on phytoplankton populations as they occur naturally (Keifer and SooHoo, 1982; Kishino *et al.*, 1985; Bricaud and Stramski, 1990).

The method, initiated by Yentsch (1962), of measuring the absorption properties of phytoplankton cells by concentrating them on glass fibre filters is now widely used for both culture and natural phytoplankton assemblages, enabling estimates of chlorophyll-specific absorption coefficients (absorption per unit concentration of chlorophyll, a^*_c). Bricaud *et al.* (1995) found a^*_c values to decrease uniformly from oligotrophic to eutrophic waters, spanning over one order of magnitude (0.18 to 0.01 m^2 mg^{-1}) at the blue absorption peak. There is a great deal of inter- and intra-species variability in spectral absorption by phytoplankton as a result of changes in pigment composition, pigment packaging within cells, cell size and physiological state (Morel and Prieur, 1977; Prieur and Sathyendranath, 1981; Hoepffner and Sathyendranath, 1992). Hoepffner and Sathyendranath (1992) examined the variability in shape and amplitude of the specific absorption spectra of phytoplankton in relation to such differences in pigment composition. Regardless of the large variability observed, there are a number of characteristic optical properties of phytoplankton populations. Absorption by chlorophyll is characterised by strong absorption bands in the blue and red parts of the spectrum; peaking at 430 and 662 nm respectively for chlorophyll *a*. Over the rest of the spectrum, absorption decreases with increasing wavelength, with very little absorption in the green, resulting in the characteristic green colouring of waters rich in phytoplankton.

Scattering

In addition to their absorbing properties, phytoplankton cells may also contribute to the total scattering behaviour of a water body. The scattering properties of phytoplankton have shown considerable variability between species that can be accounted for by variations in cell size, and the refractive and absorptive properties of the cell material (Morel, 1987). For example, some diatoms and coccolithophores

in which a substantial proportion of the total biomass consists of mineralised cell walls or scales, are known to be intense scatterers of light (Morel, 1987).

The specific scattering coefficient for phytoplankton (b^{*}_{c}) is defined as that part of the total scattering coefficient that is due to the presence of phytoplankton, normalised to a unit of pigment concentration. Morel (1987) presented estimated b^{*}_{c} for 22 species of marine phytoplankton grown in batch cultures ranging from 0.06 to 6.0 m^2 mg^{-1}. Weidemann and Bannister (1986) found a range of b^{*}_{c} of 0.05-0.15 m^2 mg^{-1} in Irondequoit Bay, (Lake Ontario) whilst Bricaud et al. (1983) saw a range of 0.08 to 0.62 m^2 mg^{-1} for four phytoplankton species grown in batch cultures.

According to theoretical predictions, algal cells must exhibit spectrally selective scattering (Morel and Bricaud, 1981). Some studies show the influence of cell absorptive properties on scattering, whereby total scattering was clearly depressed near the absorption bands (Latimer and Robinowitch, 1959; Bricaud et al., 1983). Featureless spectral attenuation (where c = a + b) also implies that spectral variations in absorption must be compensated for by those in scattering (Bricaud et al. 1983).

Like mineral particles, algal cells have a scattering phase function which strongly peaks at small angles, resulting in preferential scattering in the forward direction (Stramski and Morel, 1990). The backscattering probability (b_b/b) of algal cells has been found to be much lower than that of mineral particles. Bricaud et al. (1983) showed theoretical estimates to be consistent with experimental values of 6×10^{-4} to 1.3×10^{-2}. These are compared with the equivalent ratio of 0.019 for mineral particles. These differences in the backscattering probability are a consequence of the low refractive index of algal cells compared with mineral particles as described in section 2.3.2.

2.3.4   Dissolved Organic Matter (DOM)

Dissolved organic matter in natural waters originates predominantly from humic and fulvic materials of terrestrial origin (allochthonic DOM), produced from soil leaching and the decomposition of terrestrial vegetation (Chester, 1990). Alochthonic DOM is transported to coastal seas through fresh water run-off from the land. To a lesser extent, but nevertheless significant particularly in the marine environment, dissolved

organic matter is also a product of the bacterial decomposition of phytoplanktonic cells (autochthonic DOM). When phytoplankton cells decompose, the organic matter is chemically transformed through microbial action to form carbon dioxide, inorganic nitrogen, sulphur and phosphorus compounds. The decomposition process also results in the formation of a variety of complex polymers known as humic substances, the water soluble components of which comprise dissolved organic carbon in the forms of fulvic and humic acids.

As a consequence of its freshwater origin, coastal and inland waters often exhibit high concentrations of alochthonic DOM. In the Baltic Sea, a region largely affected by freshwater discharges, Bricaud *et al.* (1981) observed yellow substance absorption at 440 nm of 4.2 m^{-1}. Even higher concentrations may be found in inland waters; Kirk (1976) observed values as high as 8 m^{-1} in Australian lake and river waters. In contrast, concentrations of DOM in oceanic waters are generally considerably lower; typical concentrations being less than 0.1 m^{-1} (Kirk, 1994).

Dissolved organic matter plays an important role in marine optics and has thus been studied extensively over the years, both in terms of its inherent optical properties (Kalle, 1966; Bricaud *et al.*, 1981, Witte *et al.*, 1982) and more recently in terms of remote sensing applications (Bowers *et al.*, 2000; Siddorn *et al.*, 2001; Binding and Bowers, 2003). DOM does not have a significant impact on the scattering properties of water but does considerably affect absorption. The absorption properties of DOM are well documented and show strong absorption in the UV and the blue end of the visible spectrum, decreasing exponentially towards longer wavelengths. The spectral shape of DOM absorption, combined with the absorption properties of pure water, results in the yellow appearance of waters with high concentrations of DOM. In coastal and inland waters where land discharge is important, yellow substance is often the predominant factor affecting ocean colour, resulting in a green, or even brown, appearance when present in sufficient concentration (Bricaud *et al.*, 1981; Bowers *et al.*, 2000). As a result of this effect on ocean colour, these dissolved organic compounds are collectively called Gelbstoff and are also referred to as yellow substance and Gilvin.

Because of its strong absorption of blue light, the concentration of yellow substance

is expressed as its absorption at 440 nm ($a_{YS(440)}$). The spectral dependence of the absorption coefficient of yellow substance can be represented by equation 2.28.

$$a_{YS}(\lambda) = a_{YS(440)}e^{[-S(\lambda-440)]} \qquad (2.28)$$

where S is a wavelength-independent slope parameter. The value of S exhibits some regional variability, with known values varying between 0.011 and 0.021 (Kirk, 1994). Carder *et al.* (1989) observed S of 0.0194 and 0.011 for the Mississippi plume and the Gulf of Mexico respectively.

2.4   Remote sensing of Ocean Colour

2.4.1   Introduction

This section aims to give a very brief overview of satellite remote sensing of ocean colour, before going into details of the SeaWiFS sensor specifications. Section 2.4.3 presents a short review of published algorithms developed for the remote sensing of suspended sediment concentrations.

The era of viewing colour from space was initiated with the 1972 launch of the first in the Landsat series of Multispectral Scanner (MSS) sensors. Although used successfully for land, estuarine and coastal applications, the broad wavebands, high spatial resolution and long repeat cycle render this series of sensors unsuitable for most oceanic applications. The first satellite sensor devoted principally to the observation of ocean colour was the Coastal Zone Color Scanner (CZCS) launched in 1978 on board NASA's Nimbus-7 satellite. The purpose of the CZCS project was to obtain a better understanding of the temporal and spatial distribution of phytoplankton biomass and primary production, and a better understanding of the processes regulating the growth of phytoplankton (Hovis *et al.*, 1980). The CZCS ceased operation in 1986 and ten years passed before another ocean colour sensor became available. The Ocean Colour and Temperature Sensor (OCTS) was launched in November 1996 by the National Space Development Agency of Japan (NASDA) on board the Advanced Earth Observation Satellite (ADEOS). This sensor, however, provided ocean colour data for only seven months when in June 1997 the satellite lost power.

In August 1997, NASA launched the Sea-viewing Wide Field-of-view Sensor (SeaWiFS) sensor, designed as a follow-on sensor from the CZCS and now providing global ocean colour imagery every two days. The SeaWiFS sensor specifications and product availability will be described in more detail in the sections below. Since the launch of SeaWiFS, there have been a number of increasingly sophisticated ocean colour missions such as MERIS and MODIS, bringing with them great potential in the future of ocean colour studies, particularly in the more complex Case 2 waters.

Passive systems for the remote sensing of ocean colour make use of a sensor, with pre-selected wavebands in the visible and near infra-red domains of the electromagnetic spectrum, which scans the earth surface during daylight hours. Of the upwelling flux reaching the sensor, more than 80% may have an atmospheric origin (Morel, 1980). Therefore, accurate atmospheric correction of colour imagery is critical in order to obtain valuable information on the optical properties of the water body itself. The current atmospheric correction algorithm for SeaWiFS, developed by Gordon and Wang (1994), assumes that the ocean is a black surface at two near infra-red bands (765nm and 865nm). That is to say that absorption by water is strong enough to consider negligible water-leaving radiance. These two bands are therefore used to estimate the atmospheric effects, which can then be extrapolated into the visible wavelengths. Fine-tuning of this algorithm has resulted in the reduction of the error in the SeaWiFS-measured radiances to ~0.5% in Case 1 waters (Gordon, 1998).

On elimination of atmospheric effects, the remaining signal includes a measure of the water-leaving radiance that can then be related to the optical properties of the water and thus can be analysed to derive quantitative information on the type of substances in the water and their concentrations. Increased knowledge of the inherent optical properties of these substances has led to improvements in the ability to extract water quality parameters from spectral remote sensing data through inverse modelling techniques.

Satellite-derived images provide the only synoptic views of ocean colour and ocean colour derivable parameters, over wide areas of the world's oceans. However, the

inability of such sensors to penetrate cloud, combined with a polar orbit, means that ocean colour observations suffer from reduced temporal coverage, particularly at temperate latitudes.

2.4.2 The Sea-viewing Wide Field-of-view Sensor (SeaWiFS)

SeaWiFS was developed by Orbital Sciences Corporation (OSC) and was launched on board the SeaStar spacecraft on August 1st 1997. The satellite was launched into a 705 km circular, sun-synchronous polar orbit, providing a spatial resolution of 1.1 km and daily coverage with an equatorial crossing time of 12:00. The SeaWiFS sensor has six visible wavebands centred at 412, 443, 490, 510, 555 and 670 nm, each with a 20 nm bandwidth (table 2.1). A further two wavebands centred at 765 and 865 nm provide information for atmospheric corrections.

The purpose of the SeaWiFS project is to provide data on ocean colour that can be used to study the magnitude and variability of chlorophyll and primary production by marine phytoplankton, and to determine the distribution and timing of spring blooms. A further goal is the assessment of the ocean's role in the global carbon cycle and the exchange of other critical elements and gases between the atmosphere and the ocean (Hooker et al. 1992).

Table 2.1: SeaWiFS sensor characteristics.

Band	Centre λ (nm)	Bandwidth (nm)	Proposed Application
1	412	20	Yellow substance and detrital pigments
2	443	20	Chlorophyll absorption maximum
3	490	20	Chlorophyll and other pigments
4	510	20	Suspended sediment, red tides
5	555	20	Chlorophyll absorption minimum
6	670	20	Chlorophyll absorption
7	765	40	Vegetation, cloud, oxygen absorption, atmosphere corrections
8	865	40	Vegetation, water vapour, atmosphere corrections

Spatial Resolution: 1.1 km LAC, 4.5 km GAC

Swath Width: 2800 km

SeaWiFS Data Products

The first step in SeaWiFS data processing is to produce raw radiance data for each wavelength interval detected by the satellite sensor. These are the Level-1A products and contain all the Level-0 data (raw radiance counts from all bands as well as spacecraft and instrument telemetry) plus calibration and navigation data. Level-1A products are provided for two primary data types: global-area coverage (GAC) and local-area coverage (LAC). GAC provide lower resolution imagery for larger scale studies; data are sub-sampled from full resolution data with every fourth pixel of a scan line and every fourth scan line recorded for each swath.

Algorithms are then used to remove the effect of the atmosphere and to account for solar angle variations. This data can be combined in algorithms to produce Level-2 data which includes parameters such as pigment concentrations and the diffuse attenuation coefficient. In addition, 16 flags are associated with each pixel indicating a variety of potential causes of error for that pixel. Flags include atmospheric correction failure, sun glint, shallow water, cloud or ice, coccolithophores, high aerosol concentration and a chlorophyll algorithm failure.

A further stage of processing results in Level-3 data, in which Level-2 data is combined statistically into bins containing all the data from a certain region and presented as daily, weekly, monthly, or annual composites.

2.4.3 Retrieval of Suspended Sediments from Ocean Colour Remote Sensing

Of all the studies recognised, relating to the effect of suspended sediments on reflectance, two common features were identified; firstly, the increase in reflectance with increasing sediment load, and secondly, a shift in the peak of spectral reflectance towards longer wavelengths. In Landsat imagery of Kenyan coastal waters, Brakel (1984) showed that high concentrations of sediment could be retrieved from band 4 (700-800 nm), whilst for gradually lower concentrations, the 600-700 and 500-600 bands were more sensitive. In agreement, Topliss (1986) showed that increasing concentrations of suspended sediment were associated with a migration of the *in situ* peak in spectral reflectance towards longer wavelengths such that concentrations greater than 100 mg l^{-1} pushed the spectral response past 700 nm. The study recommended that concentrations greater than 1000 mg l^{-1} should be

monitored outside the visible spectrum, since the peak spectral response was evident in the near infra-red. Topliss suggested that ultra high sediment concentrations should approach the known spectral response of mud, which exhibits strong spectral response past the visible domain (Lyzenga, 1978). This spectral feature of turbid waters has also been documented in more recent studies (Bukata et al., 1997; Han, 1997; Forget et al., 1999). Doxaran et al. (2002a) showed that in the Gironde Estuary, for SPM concentrations from 35 to 250 mg l^{-1}, the wavelength of maximum reflectance increased between 550 and 700 nm. Beyond 250 mg l^{-1}, reflectance at these wavelengths saturated but increased between 750 and 950 nm for concentrations up to 1800 mg l^{-1}. Saturation at any wavelength occurs because reflectance is not linearly related to sediment concentration, but increases to an environmentally determined asymptote (Holyer, 1978; Curran and Novo, 1988; Doxaran et al., 2002a).

Some of the variations in spectral signatures of turbid waters have been attributed to changes in particle characteristics such as grain size, particle composition and scattering efficiency. Novo et al. (1989, 1991) suggested the relationship between suspended sediments and reflectance was dependent on sediment type and showed the difference between reflective properties of red silt and white clay. Laboratory results showed that for fine white sediment, the visible reflectance increased across the entire visible spectrum, whilst for red silts the increase was more pronounced in the red region. Simpson and Brown (1987) showed that with increasing organic matter, the sensitivity of reflectance to changes in total SPM decreases, with a corresponding increase in the slope of the SPM-Reflectance relationship. They suggested that the organic component played a critical role in determining the efficiency with which the particulate load is able to reflect light.

Holyer (1978) deduced that it was particle size rather than colour or texture that was the main factor relating suspended sediment concentrations to optical measurements. Early studies showed that the reflectance of dry sediment increased with decreasing grain size (Myers and Allen, 1968) and the same has been observed for sediments suspended in water (Moore, 1977; Holyer, 1978). In tank experiments, Moore et al. (1999) showed that the relationship between reflectance and sediment concentration varied between different sediment types and grain size. They also showed that by

using colour ratios (R_{865}/R_{775}), the spread in the data could be reduced. Han and Rundquist (1996) presented results that showed that as suspended sediment concentrations increased, reflectance from finer soils increased faster than that from coarser soils, whilst with both soil types, the wavelength of peak reflectance increased towards longer wavelengths.

With increasing knowledge of the inherent optical properties of water quality parameters, it has become increasingly popular to use optical models as a method of analysing ocean colour information (Forget *et al.*, 1999; Moore *et al.*, 1999; Doxaran *et al.*, 2002a). Doxaran *et al.* (2002a) showed through modelling that reflectance is highly sensitive to variations in both grain size and composition and encouraged the use of colour ratios to reduce algorithm sensitivity to these parameters.

The literature contains numerous attempts at estimating suspended sediment concentrations from remotely sensed reflectance in a variety of marine, coastal and freshwater environments. Studies have shown that sediments can be quantitatively mapped (with varying degrees of accuracy) from aircraft-mounted (Curran *et al.*, 1987; Robinson *et al.*, 1998) and satellite-mounted ocean colour sensors. The algorithms used, however, are as diverse as the environments they attempt to describe. Table 2.2 presents a selection of previously published algorithms for the retrieval of suspended sediment concentrations using a variety of ocean colour sensors. This is by no means an exhaustive review but aims simply to demonstrate the diversity of algorithms available. Most algorithms utilise the fact that sediment-laden waters generally show increased reflectance, either in terms of absolute reflectance (at a single wavelength) or spectral differences in reflectance (using colour ratios). There has, however, been little agreement on either the form of the algorithm or the optimum wavelength for use in these algorithms. Much of this may be due to the diversity of satellite sensors available over the years, with large variations in the available spectral characteristics.

The substantial inconsistency between studies may also be attributed to environmental variables, such as differences in the range of sediment concentrations, particle size distributions, particle mineralogy, the presence of chlorophyll and/or dissolved organic matter. In addition, there may be considerable differences in

adopted methodology, in terms of radiometric field measurements (instrument specifications, calibration and deployment), measurement of suspended sediments (differences in measured quantities, accuracy of laboratory methodology, sample variability) and techniques in data processing and analysis.

Clark *et al.* (1980) suggested that a simple reflectance ratio (R_{440}/R_{510}) would be suitable for estimating concentrations of total SPM in the Gulf of Mexico. This study however, was based on low inorganic sediment concentrations, where SPM co-varied with chlorophyll. Although this ratio was satisfactory for Case 1 waters it may not be suitable for Case 2 waters where the correlations between C and SPM may be space and time dependent as a result of, for example, river discharges and bottom re-suspension of inorganic sediments. Tassan and Sturm (1986) showed distinct relationships between chlorophyll and SPM for different coastal regions of the Adriatic Sea.

A further source of error may be due to vertical, spatial and temporal variability of sediment concentrations, particularly in some of the earlier algorithm developments that relied on the coincidence of field measurements with satellite overpasses for the derivation of relationships between the spectral reflectance and SPM concentrations (e.g. Collins and Pattiaratchi, 1984; Ritchie and Cooper, 1988; Lathrop *et al.*, 1991). Time differences between the satellite overpass and *in situ* observations may lead to considerable errors due to advection. Validation of satellite imagery through spot field measurements also introduces the problem of sub-pixel variability. There may be considerable spatial variability in sediment concentrations within a single pixel, particularly in the dynamic coastal and estuarine environments. By adopting *in situ* observations of ocean colour to directly relate changes in ocean colour to in-water constituents, providing more accurate relationships between water quality parameters and both the inherent and apparent optical properties, the potential problems of sub-pixel variability are removed.

In recent years, there has been growing interest in the optics of the more complex Case 2 waters and in the retrieval of SPM concentrations. Advances have been made in ocean colour using optical modelling but still there are no globally applicable ocean colour algorithms with acceptable retrieval accuracy. Recent work has

attempted to derive SPM concentrations and fluxes from estuaries (Robinson *et al.*, 1998; Moore *et al.*, 1999). These studies obtained SPM concentrations accurate to within 50% but this was for a single site at a single point in time. Effort is now required to firstly reduce the uncertainty in estimated concentrations and secondly investigate further the multi-region and seasonal application of such algorithms.

These previously published algorithms provide site-specific predictions of water quality parameters with reasonable accuracy but are limited in their universal application. To test the accuracy with which these algorithms could determine sediment concentrations in regions other than where they were derived, Mitchelson-Jacob (1999) applied a selection of algorithms to SeaWiFS imagery of the Irish Sea. Results showed an extensive range of derived sediment concentrations, with few deriving even reasonable concentrations and distributions of sediments in the Irish Sea. There is, therefore, at present, no ocean colour algorithm that can accurately determine sediment concentrations in the Irish Sea.

Table 2.2: A selection of published algorithms for the retrieval of SPM concentrations from ocean colour.

Satellite Sensor	Wavebands Adopted	Algorithm Form	Region of Study	Reference
Airborne TM	450-520, 520-600, 605-625	$\text{Log S} = AX_1+BX_2-CX_3-D$	Bristol Channel, UK	Collins and Pattiaratchi (1984)
Airborne ATM	420-450, 450-520, 520-605	$\text{Log S}=A+BX$	Yorkshire Coast, UK	Curran et al. (1987)
CZCS	440/550, 440/520, 520/550	$\text{Log S}=\log A+B\log X$	Gulf of Mexico	Clark et al. (1980)
CZCS	550/750	$S=e^{(A-2X)}$	Bay of Fundy	Amos and Topliss (1985)
CZCS	$[550\text{-}670]^a[520/550]^b$	$\text{Log S}=A+B\log(X)$	Adriatic Sea	Tassan and Sturm (1986)
CZCS	550	Linear	Irish sea	Simpson and Brown (1987)
CZCS	550	$\text{LogS} = A+B\log(X)$	Model results	Tassan (1988)
CZCS	520	Linear	Irish Sea	Weeks and Simpson (1991)
CZCS	440, 550, 670	$\text{Log S} = A +B[(X_2\text{-}X_3)^C/(X_1/X_2)]$	Mediterranean Sea	Mayo et al. (1993)
Landsat ERTS	700-800	Linear	Mississippi Lakes	Ritchie et al. (1976)
Landsat MSS	Band 3	Linear	Moon Lake, Mississippi	Ritchie and Cooper (1988)
Landsat TM	Bands 2/3	$\text{Log S} = AX+BX^2+C$	Bay of Fundy	Topliss et al. (1990)
Landsat TM	660/485	$S = A\exp^{(BX)}$	Lake Michigan	Lathrop et al. (1991)
Landsat TM	450-520	Linear	East Anglia, UK	Baban (1994, 1997)
Landsat TM	570, 670	$\text{LogS} = A+B\log(X)$		Tassan (1997)
SeaWiFS	$[555+670]/[490/555]^{1/2}$	$\text{Log S}=A+B\log(X)$	Mediterranean Sea	Tassan (1994)
SeaWiFS	555	$X=AS\text{-}B$	Gironde Estuary, France	Froidefond et al. (1998)
SeaWiFS	412, 670	$S=AX_2/X_1$	North Sea	Wernand et al. (1998)
CASI	509/668	$S=AX^B$	Humber Estuary, UK	Robinson et al. (1998)
MERIS/CASI	865/775	Inverse Modelled	Humber Estuary, UK	Moore et al. (1999)
SPOT	500-590/790-890	$S=A\log(X)\text{-}B$	Gironde Estuary, France	Doxaran et al. (2002a)

Chapter Three

An Introduction to the Study Region and Details of the Adopted Methodology and Sampling Strategy

CHAPTER THREE: AN INTRODUCTION TO THE STUDY REGION AND DETAILS OF THE ADOPTED METHODOLOGY AND SAMPLING STRATEGY

3.1   Introduction

This chapter details the methodology used in both data collection and initial data processing. Described first, is a brief introduction to the study region. This is followed by details of the sampling programme undertaken for both research cruises and local sampling. Section 3.3 provides instrument specifications and details of the calibration and deployment of the optical sensors used in this study. Laboratory techniques for the biogeochemical analysis of water samples are outlined in section 3.5. Section 3.6 describes the procedure for calculating the key inherent and apparent optical properties from the optical profiles. The procedures undertaken in satellite image processing are not included in this chapter but are described in full in the relevant results chapter (Chapter Six). Where possible, the adopted methodology was that recommended by the SeaWiFS Project in the NASA Ocean Optics Protocols for Satellite Ocean Colour Sensor Validation (Mueller and Fargion, 2002). However, this was not always practical due to time, space and equipment restraints. Moreover, as the SeaWiFS project is based primarily on bio-optical studies in open ocean environments, and in the absence of recommended practice, some of the methods described here have been adapted to suit the more turbid shelf sea environment under study.

3.2   Study Regions

The Irish Sea is a semi-enclosed sea with the northern boundary determined by a line joining Larne and Stranraer and the southern boundary joining Carnsore Point to St David's Head (see figure 3.1). It is connected to Atlantic waters by both the North Channel and St George's Channel in the south. The Irish Sea is approximately 400 km from North to South and its maximum width, just south of the Isle of Man, is 225 km.

The bathymetry of the Irish Sea basin is presented in figure 3.2a. To the west, there is a deep trough running from the North Channel to St George's Channel in the south, with depths frequently greater than 100 m. The path of the trough is impeded by a number

of highs off Dublin and the Wicklows (Orford, 1989). Some of the deepest waters of the Irish Sea are in the North Channel, with depths up to 270 m. In contrast, the bathymetry of the eastern Irish Sea is dominated by shallow bays, in particular Cardigan Bay and Liverpool Bay, with water depths generally less than 40 m.
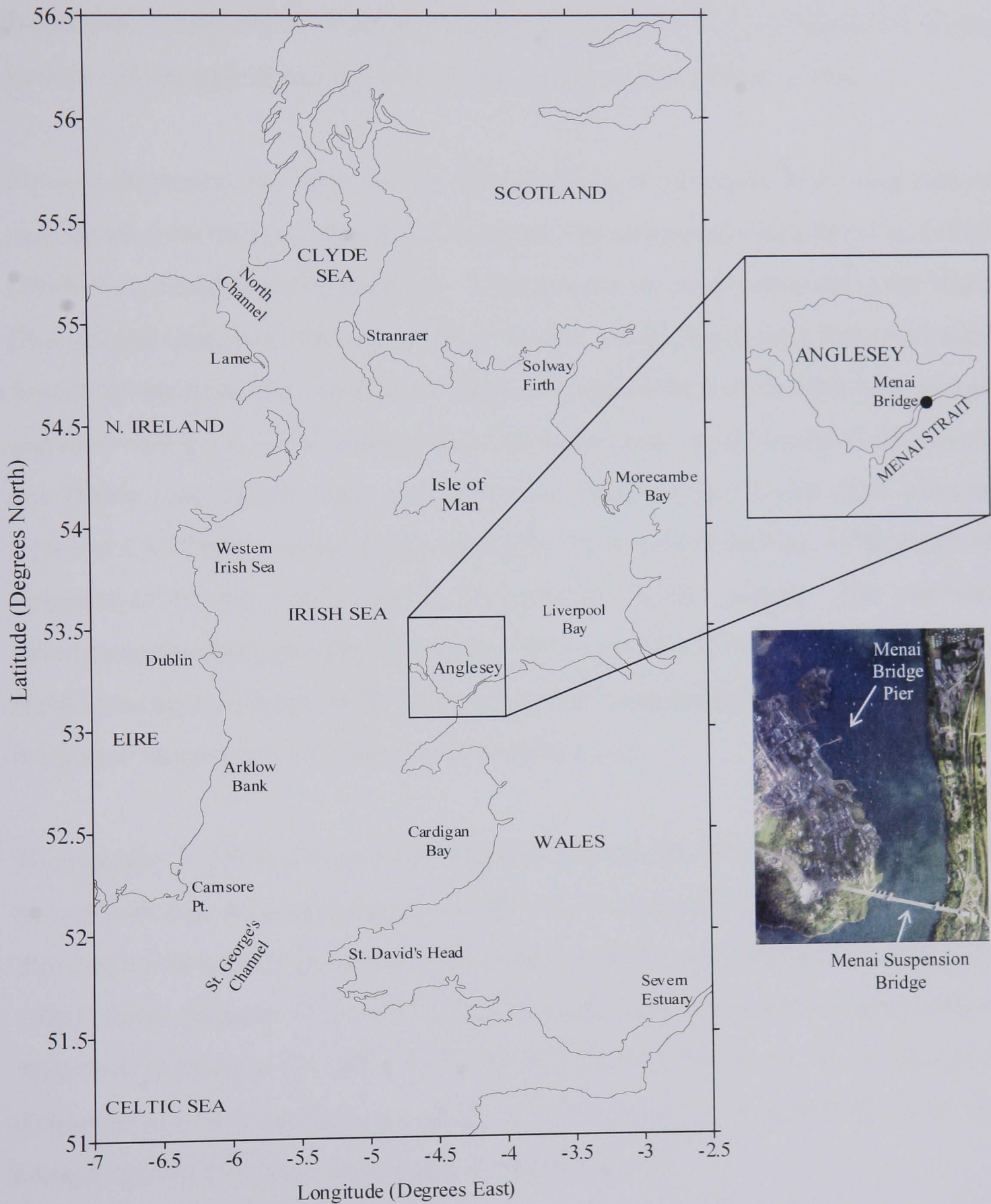
Figure 3.1: Study area location map with expanded areas showing the location of the Menai Strait sampling.

The physical oceanography of the Irish Sea is dominated by tidally driven water movements, with the tide entering the Irish Sea through both St George's Channel and the North Channel. Most of the tidal variations in this area are generated by the M_2 and S_2 components of the Atlantic Ocean tides (Robinson, 1979). The M_2 component forms the semi-diurnal cycle where the time between consecutive high waters is 12 hours and 25 minutes, whilst the S_2 component drives the fortnightly spring/neap cycle where spring tides are approximately twice as large as neap tides (Orford, 1989).

Figure 3.2b presents the mean tidal current amplitude as estimated from a tidal current and elevation model developed at the Proudman Oceanographic Laboratory (see Elliott (1991) for a description of the model). Amphidromic points are observed in the North Channel and along the Irish coast south of Arklow which play a major role in the tidal forcing of the Irish Sea, resulting in regions of high tidal current velocities in both regions (> 1.0 m s^{-1}). Tidal currents then reduce drastically in the western Irish Sea off the Down coast where high tidal elevations result in the lowest tidal currents (< 0.1 m s^{-1}). Further zones of high amplitude tidal currents include off the coast of Anglesey (> 1.2 m s^{-1}) and in the St. George's and North Channels. The non-tidal circulation of the Irish Sea was investigated by Hunter (1972) who suggested there was a residual northward current in St. George's Channel, an anticlockwise gyre south west of the Isle of Man and a clockwise gyre in Liverpool Bay.

The majority (~70%) of fresh water input to the Irish Sea through rivers is from the eastern Irish Sea; discharges from the rivers Dee, Mersey and Ribble within Liverpool Bay and the Solway Firth making the greatest contributions (Irish Sea Study Group, 1990). River discharge from the Irish coast is small; almost as much is discharged into Waterford Harbour as the sum of all other Irish sources. There are also considerable discharges of fresh water into the margins of the Irish Sea, for example from the Bristol Channel (River Severn) and the Clyde Sea (River Clyde).

As a consequence of the considerable depth variations, highly variable tides and to a lesser extent, localised fresh water inputs, the Irish Sea is frequently divided into regions of stratified and well-mixed waters. These regime changes result in the presence of

persistent shelf sea fronts, particularly in the western Irish Sea, Liverpool Bay, Celtic Sea and Clyde Sea (Simpson and Hunter, 1974; Pingree and Griffiths; 1978; Simpson, 1981). The level of water column stability is determined by the competing factors of stirring mechanisms (predominantly tidal stirring) and stabilising factors of surface heating and freshwater. Figure 3.2c shows the distribution of the stratification parameter, h/u^3, which has been used to define regions of stratified and well-mixed conditions (Pingree and Griffiths, 1978; Simpson, 1981). These features are in turn responsible for much of the variability in productivity over the Irish Sea with the onset and break-down of stratification determining the timing of the spring and autumnal phytoplankton blooms.

The Menai Strait is a narrow sea-channel separating the island of Anglesey from the mainland of north Wales. Approximately 25 km in length, the Strait is about 200 metres wide at its narrowest point with a maximum width of 2 km. Water depths in the Menai Strait are generally less than 15 m and there are large expanses of shallow inter-tidal mudflats and sand banks, such as Traeth Lafan at the north-east entrance and Traeth Melynog at the south-west, near Caernarfon.

The tidal range in the Menai Strait averages at 6.5 m on spring tides and 3.5 m on neap tides. Evidence of tidal current asymmetry in the Menai Strait indicates that the south westerly flowing tidal current is typically stronger than that flowing to the north-east. Consequently, there is a residual flow towards the south-west, which has been attributed to differences in the tidal ranges between the north-east and south-west ends of the Strait (Harvey, 1968). This strong tidal influence (currents reaching 1.5 m s^{-1}) and shallow waters ensure that the Menai Strait is vertically mixed at all times and is well flushed with water from the Irish Sea.

Numerous freshwater streams enter the Menai Strait but none produce sufficient flow to cause significant fluctuations in the salinity. Water entering the Menai Strait from the north-east is generally less saline than that at the south western approaches because of the influence of the Liverpool Bay region of freshwater influence.
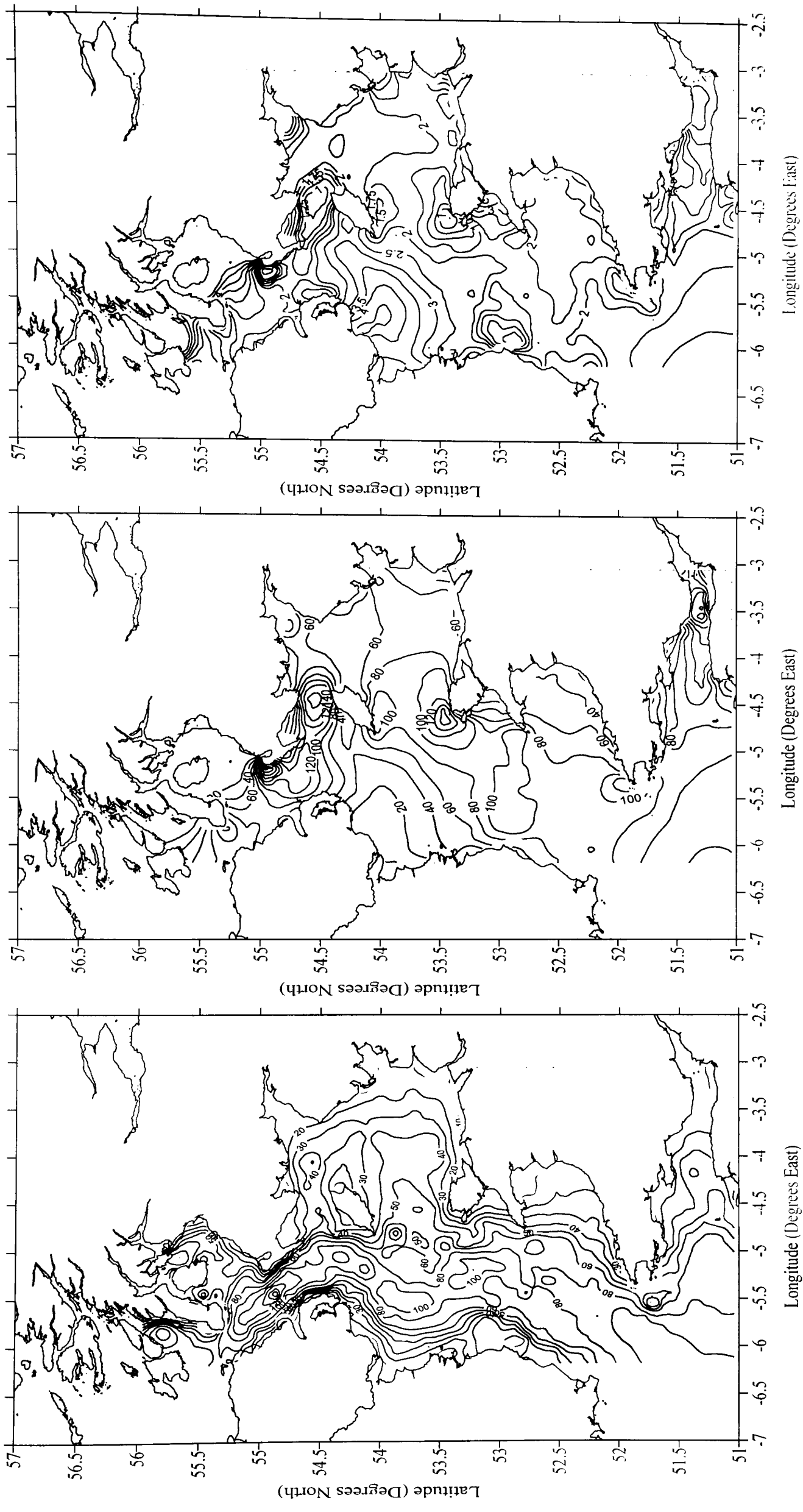
Figure 3.2: Maps of the Irish Sea showing a) bathymetry (m), b) mean tidal current amplitudes (cm s^{-1}) and c) the stratification parameter, h/u^3 (m^{-2})

3.3   Sampling Schedule

3.3.1   Research Cruises

In total, 10 cruises were carried out between March 2000 and November 2001, on board the University of Wales Bangor's *R. V. Prince Madog*. Table 3.1 provides dates and locations of all research cruises undertaken for this study. Cruises aimed to visit sites of contrasting environmental conditions to obtain a range of optical properties. Stations ranged from the clear, summer stratified waters of the Celtic Sea and Western Irish Sea, to the tidally well-mixed and turbid stations around Anglesey and Liverpool Bay (see figure 3.3 for station locations). The Clyde Sea and adjacent sea lochs provided chlorophyll and yellow substance dominated waters.

Table 3.1: Details of research cruises undertaken.

Dates	Region of Study	No. of Stations
27-30 Mar 2000	Celtic Sea	6
15-25 May 2000	Clyde Sea	22
14-15 June 2000	Celtic Sea	7
17-20 July 2000	Liverpool Bay/Irish Sea	25
4-6 Sept 2000	Irish Sea	11
10-11 Nov 2000	Anglesey	4
23-27 Apr 2001	Clyde Sea	19
6-10 Aug 2001	Liverpool Bay/Irish Sea	22
22-23 Oct 2001	Eastern Irish Sea	17
26-30 Nov 2001	Anglesey	23
Total = 38 Days		Total = 156 Stations

3.3.2   Menai Strait Time Series

In addition to the ship-borne measurements described above, sampling was undertaken in the Menai Strait, forming an eight month time-series of optical and water quality measurements. It was hoped that weekly samples could be obtained to form a complete annual time-series, however, the need for the radiometer during research cruises, inaccessibility to the sampling site, occasional instrument failure and re-calibration periods meant that this was not possible. The time series presented runs from March 8th

to November 2nd 2001 with samples obtained at intervals ranging from one day to two weeks. Radiometer profiles and water samples were obtained from Menai Bridge pier at 12 noon and processed immediately on return to the laboratory.
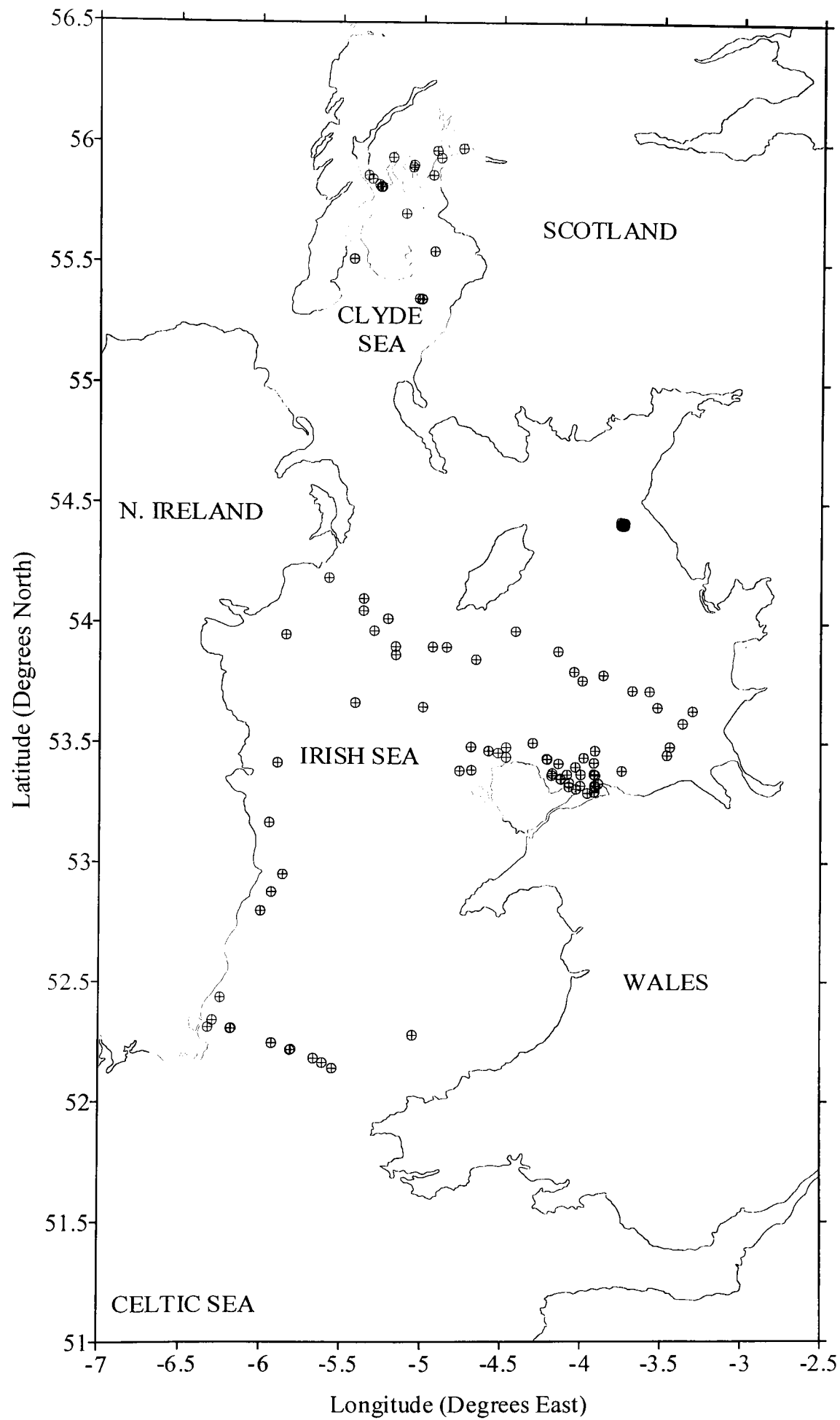
Figure 3.3: Map showing region of study where ⊕ mark station locations.

3.4   Spectral Radiometer Measurements

3.4.1   Radiometer Specifications

The underwater light field was characterised using a Profiling Reflectance Radiometer (PRR600; Biospherical Instruments Inc.). This enabled the simultaneous measurement of upwelling radiance (L_u) and downwelling irradiance (E_d) at wavelengths coincident with the SeaWiFS visible wavebands. A deck-based radiometer (PRR610) measured incident downwelling irradiance (E_s) above the sea surface at the same wavelengths, enabling the normalisation of profiles to surface light conditions (see figure 3.4).

Incident Surface Irradiance
(E_s) Collector (PRR610)

Downwelling Irradiance
(E_d) Collector

Upwelling Radiance
(L_u) Sensor

PRR600 at the surface,
measuring E_u
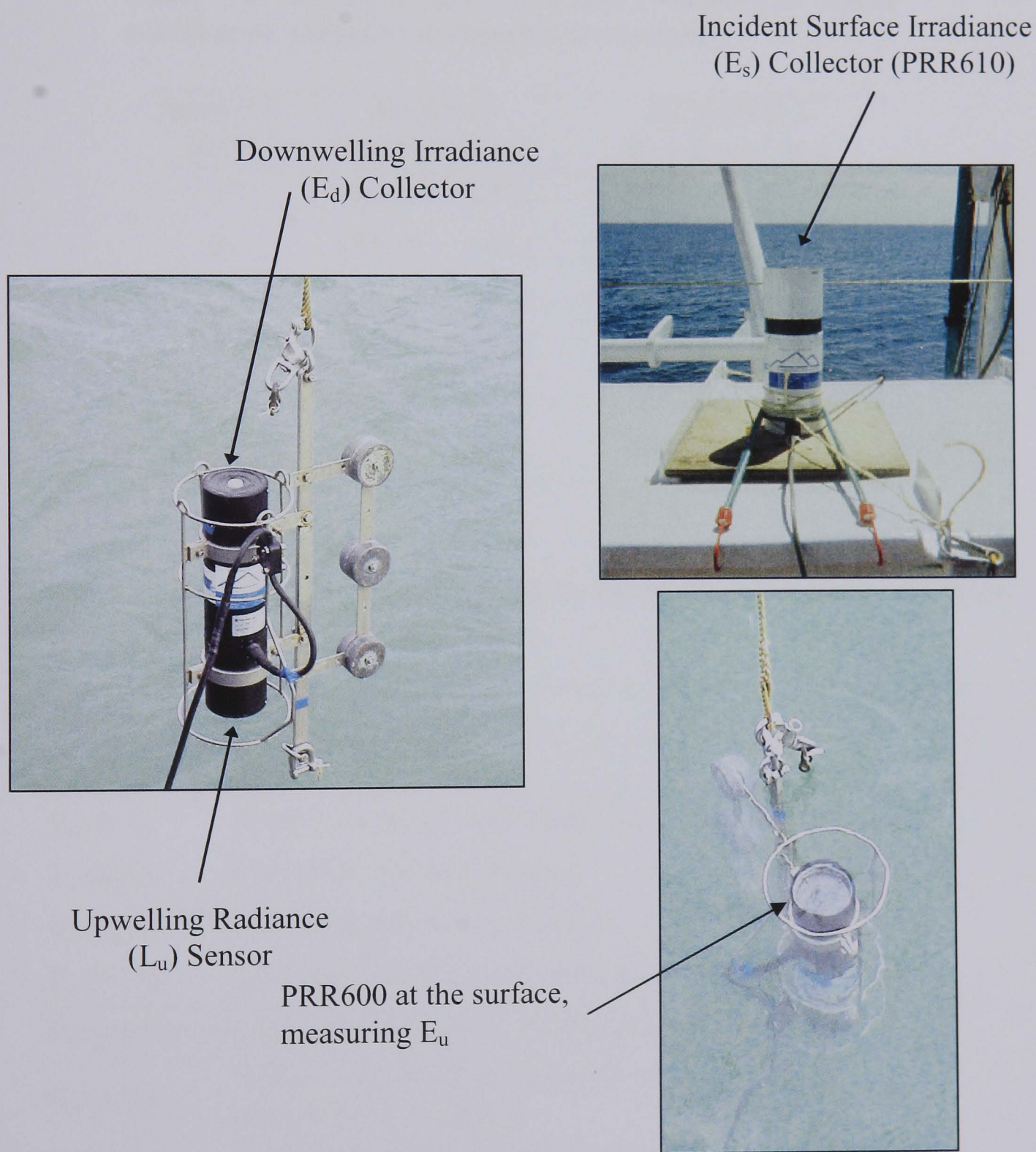
Figure 3.4: Photographs of the PRR600 and PRR610 during deployment from the *R. V. Prince Madog*.

The radiance sensor had a 10° field of view (FOV) in water. Filter photodetectors in the irradiance collector and the radiance sensor had a narrow band spectral response (10 nm Full Width at Half Maximum) with centre wavelengths designed to match the SeaWiFS channels (see table 3.2 for waveband selection). The profiling radiometer was also equipped with a temperature transducer, pressure sensor, tilt and roll sensors and a broad band PAR (photosynthetically available radiation) sensor. Table 3.3 presents those properties measured by the PRR600 and the parameters derived from the profile data.

Table 3.2: Details of SeaWiFS and PRR600/610 visible wavebands (centre wavelengths in brackets).

SeaWiFS Band	SeaWiFS Waveband (nm)	PRR600/610 Waveband (nm)
1	402-422 (412)	407-417 (412)
2	433-453 (443)	438-448 (443)
3	480-500 (490)	485-495 (490)
4	500-520 (510)	505-515 (510)
5	545-565 (555)	550-560 (555)
6	660-680 (670)	660-670 (665)

Table 3.3: Optical properties measured by the PRR600/PRR610 and those derived from the *in situ* measurements.

Parameters measured by PRR600/610:		
Symbol	Description	Unit
$E_d (z, \lambda)$	Downwelling spectral irradiance	$\mu W\ cm^{-2} nm^{-1}$
$L_u (z, \lambda)$	Upwelling spectral radiance	$\mu W\ cm^{-2} nm^{-1}\ sr^{-1}$
$E_u (z, \lambda)$	Upwelling spectral irradiance	$\mu W\ cm^{-2} nm^{-1}$
$E_s (0^+, \lambda)$	Surface incident spectral irradiance	$\mu W\ cm^{-2} nm^{-1}$
Parameters derived from PRR600/610 measurements:		
$K_d (z, \lambda)$	Diffuse attenuation coefficient for downwelling irradiance	m^{-1}
$R (z, \lambda)$	Irradiance reflection coefficient	%
$a (z, \lambda)$	Spectral absorption coefficient	m^{-1}
$b (z, \lambda)$	Spectral scattering coefficient	m^{-1}

3.4.2 Radiometer Calibration

Full calibration of the PRR600 and PRR610 radiometers was carried out at the Plymouth Marine Laboratory. Calibration facilities enabled the calibration of instruments to SeaWiFS specifications using standard lamps traceable to NIST (National Institute of Standards and Technology). SeaWiFS specifications (Mueller and Fargion, 2002) require that radiometers have bands with centre wavelengths matching those in table 3.2 to within ± 1 nm for 410 and 443 nm and within ± 2 nm for all other wavebands. Bandwidths should be 10 nm ± 2 nm FWHM (Full Width at Half Maximum). The minimum requirement for absolute radiometric data to be used in the SeaWiFS validation is for repeatable calibrations within less than 5% variability.

Spectral Bandpass Characterisation

A scanning monochromatic light source was used to obtain the centre wavelengths and wavebands of the two radiometers. All wavebands were found to fall within the SeaWiFS requirements apart from band 2 (443 nm) where the centre wavelengths had drifted by 2.3 and 4.3 nm for E_d and E_s respectively. The bandwidths also fell within the requirements of 10 ± 2 nm with the exception again of the 443 nm channel of the E_s collector. No leakage between spectral bands was evident.

Absolute Radiometric Calibration

Irradiance collectors were calibrated against a NIST traceable secondary standard lamp of known spectral irradiance. Calibration constants obtained for the E_d collector showed less than 5% variation from the previous calibration (carried out by Biospherical Instruments in 1998) therefore meeting SeaWiFS requirements. Calibration of the surface irradiance collector (E_s) identified small changes in the 443 and 490 nm bands that may be attributed to the drift in spectral sensitivity identified in the spectral characterisation.

An integrating sphere with an exit port of sufficient size to fill the FOV of the radiance sensor was used for the radiometric calibration of the radiance sensor. Calibration constants were found to vary considerably (up to 40%) from those obtained in a previous calibration carried out in 1998. These discrepancies may be attributed to differences in

calibration methodologies; Biospherical Instruments used a standard lamp with a reflective plaque. For this reason, rather than measuring L_u/E_d to derive radiance or remote sensing reflectances, the decision was made to measure the irradiance reflectance, E_u/E_d, thus eliminating any uncertainties in instrument calibration. Measurement of irradiance rather than radiance reflectance also enables the study of the relationship between R and the IOPs with greater accuracy, since no assumptions are required regarding the directional properties of the light field (Kirk, 1994).

3.4.3   Radiometer Measurement Protocols

Radiometer Deployment

The radiometer was deployed from the A-frame of the *R. V. Prince Madog* with the stern facing the sun to avoid any perturbations to the light field from the ship structure. The instrument was held at the surface at the beginning of each cast to equilibrate with the ambient water temperature and then lowered at approximately 0.5 m s^{-1}, allowing a minimum of 5 readings per metre during a profile. Optical profiles were made to at least the depth at which downward irradiance was reduced to 1% of the surface values, corresponding to the bottom of the euphotic zone, or 4.6 optical depths (Kirk, 1994).

Vertical profiles of upwelling irradiance (E_u) were measured by inverting the PRR600 frame and profiling the instrument upside down on a second profile, immediately after the first. During both profiles, the PRR610 was secured to a point on the ship free from shading and obstruction, enabling the simultaneous measurement of incident downwelling irradiance, E_s. This was used to correct the underwater profiles for variations in surface light conditions. Optical measurements were restricted by ambient light levels and were thus only carried out up to four hours either side of noon. In winter, the window of acceptable lighting was reduced, limiting the number of stations visited.

Depth Offset Adjustments

The recorded depth must be adjusted for the distance between the irradiance and radiance sensors and the pressure transducer so that the given depth is that at which the optical properties are actually measured. The full length of the PRR600 is 42 cm and the

pressure transducer is located 14 cm from the radiance sensor (28 cm from the irradiance collector). Although this is only a small offset, it may be significant in turbid waters where the attenuation coefficient is high. During the processing of optical profiles, the depth measurements were therefore corrected by adding or subtracting the relevant distance.

Instrument Dark Readings

The dark current of optical instruments is often temperature dependent (Mueller and Fargion, 2002). Each optical profile was therefore accompanied by a measurement of the instrument dark current. It was not possible to determine a dark current reading during a cast therefore an average dark reading was taken prior to the profile and was subtracted from the measured light field during data processing.

Surface Incident Irradiance

Variable atmospheric conditions, especially cloud cover, lead directly to variations in the underwater light field and a correction must be applied to enable accurate estimates of optical properties from radiance and irradiance profiles. Corrections were made to the underwater light field using measurements of above water spectral downwelling irradiance, $E_s(\lambda)$ as measured by the PRR610. Assuming that the transmission of E_s through the surface does not vary with time, then the underwater profile can be normalised to the surface light field simply by dividing the underwater irradiances by E_s.

3.5   Ancillary Measurements

3.5.1   Hydrographic Data

Vertical profiles of water temperature and salinity extending over the entire water column were obtained at every station from CTD casts carried out immediately before the optical profiles. In addition, a 25 cm pathlength transmissometer (SeaTech) and a WETStar fluorometer (WETLabs), both mounted on the CTD frame, provided simultaneous profiles of beam transmittance and chlorophyll fluorescence. These profiles, viewed in real time, provided valuable information on the water column structure during the interpretation of optical profiles.

3.5.2   Secchi Depth

Secchi depth measurements were made for a real-time estimate of water transparency and a crude estimate of K_d. Poole and Atkins (1929) made the empirical observation that the secchi depth was approximately inversely proportional to the vertical attenuation coefficient. The secchi depth was measured using a horizontal white disk, about 30 cm in diameter. The disk was lowered into the water column until it was no longer visible, then pulled back to the surface slowly until visible again. The secchi depth was recorded as the depth at which the disk re-appeared into sight.

3.5.3   General Station Observations

A number of additional measurements and observations were made for station identification and to provide a useful assessment of data quality.

> Date and time of each instrument cast (start and end)
>
> Station position (Latitude and Longitude)
>
> Sea state (swell and wave height)
>
> Sky state (percentage cloud cover, cloud type, diffuse or direct light, precipitation etc.)
>
> Wind speed and direction
>
> Ship's orientation relative to the sun
>
> Changes in surface light conditions during and/or between optical profiles

3.6   Biogeochemical Analysis of Water Samples

3.6.1   Water Sample Collection

SeaWiFS protocols for satellite ocean colour validation (Mueller and Fargion, 2002) recommend duplicate samples be taken from 12 discrete depths, with at least three in the first optical depth. In the turbid waters of the Irish Sea, however, this sampling procedure was not feasible. For remote sensing purposes, the penetration depth of light in the sea is defined as the depth above which 90% of the total radiance originates. Gordon and McCluney (1975) showed that a good estimate of this depth is given by $1/K_d$. Using this effective remote sensing depth of one attenuation length, the reflectance measured at the surface was calculated as originating from depths up to a

maximum of 2.47 metres at 665 nm during the entire study. Furthermore. the fluorescence and transmittance profiles obtained from the CTD casts showed no significant variability in readings within this first attenuation depth. This enabled the assumption that surface concentrations were fully representative of conditions within the first attenuation depth and water samples were taken at the surface only.

3.6.2   Fluorometric Measurement of Chlorophyll *a* and Phaeopigments

This method of chlorophyll analysis is based on the fluorescence of algal pigments at red wavelengths when they are excited by blue light, and is used extensively to provide an estimate of algal biomass. More recently, the recommended procedure for pigment analysis is HPLC (High Performance Liquid Chromatography) which results in a lower uncertainty in the measured chlorophyll and phaeopigment concentrations, since compounds are physically separated and quantified. This method, however, is very time-consuming and since this study was interested primarily in suspended sediment it was not thought necessary to evaluate pigment composition in this way. Fluorometry rather than spectrophotometry was chosen because the increased sensitivity of fluorescence measurements enables smaller volumes to be filtered, an important factor in very turbid waters. SeaWiFS protocols for the fluorometric determination of chlorophyll *a* and phaeopigment concentrations are based on the key references of Yentsch and Menzel (1963) and Strickland and Parsons (1972), with just a few modifications.

As soon as possible after collection, water samples were filtered through 47 mm diameter Whatman GF/F glass fibre filters of 0.7μm pore size. Volumes of water filtered varied depending on water turbidity but generally, one litre was sufficient for chlorophyll analysis. Samples were not pre-filtered to remove large zooplankton as this may exclude large or chain-forming phytoplankton. Instead, tweezers were used to remove large zooplankton from filters after filtration. Triplicate samples were filtered at all stations in order to allow some assessment of sample variability.

Filters were folded in half with the filtered halves facing in and wrapped in labelled aluminium foil parcels. Samples were stored frozen and analysed as soon as possible

after cruises. Filters were placed in centrifuge tubes with 10 ml of 90% acetone and pigments were allowed to extract for 24 hours whilst refrigerated in the dark. The extract was then analysed using a Turner design bench fluorometer for the determination of chlorophyll a and phaeopigment concentrations. Each extracted sample was placed in the fluorometer and the fluorescence signal (f_b^*) was recorded. At this stage, the fluorescence by phaeopigments makes a significant contribution to f_b^*. This was corrected for by acidifying the extract with 10% hydrochloric acid, which converts all the chlorophyll to phaeopigments. The extract was mixed by inverting the tube before recording the acidified fluorescence signal (f_a^*). The fluorescence signals of both a 90% acetone blank (B_b) and an acidified acetone blank (B_a) were also measured.

The sample fluorescences were then corrected using the appropriate blank readings (B_a and B_b) and instrument ranges (R):

$$f_b = \frac{(f_b^* - B_b)}{R} \qquad\qquad (3.1)$$

$$f_a = \frac{(f_a^* - B_a)}{R} \qquad\qquad (3.2)$$

The concentrations of chlorophyll a [Chl] and phaeopigments [Phaeo] were calculated according to equations 3.3 and 3.4.

$$[Chl] = K_f(f_b - f_a)V_{ex} / V_{filt} \qquad (\mu g \, l^{-1}) \qquad\qquad (3.3)$$

$$[Phaeo] = K_f(H_f f_a - f_b)V_{ex}/V_{filt} \qquad (\mu g \, l^{-1}) \qquad\qquad (3.4)$$

where V_{ex} and V_{filt} are the extract volume (millilitres) and the sample volume filtered (litres) respectively. The calibration constants K_f and H_f were determined during the calibration of the fluorometer against a spectrophotometrically determined chlorophyll standard.

The similarity between the absorption spectrum of chlorophyll a and phaeopigments means that it is common practise to use the sum of chlorophyll a and phaeopigments and is referred to as phytoplankton pigments, denoted C (Gordon and Morel, 1983).

3.6.3   Spectrophotometric Measurement of Yellow Substance

Absorption due to yellow substance is a routine optical measurement, with well-established protocols. Methods carried out in this study are as those described by Bricaud *et al.* (1981). Seawater samples were collected and particulate matter removed by filtration through 0.2 μm pore size Nuclepore membrane filters. Samples were processed using all-glass filtering apparatus in order to minimise contamination by organic material. The filtrate was stored in amber-coloured glass bottles to protect from photo-degradation during sample storage and refrigerated for no more than one week before analysis.

Prior to analysis, samples were warmed to room temperature since the absorption by water is strongly temperature dependent, particularly at red and near infrared wavelengths (Pegau and Zanefeld, 1993). The absorption spectra were then measured in a 10 cm glass cuvette using a dual-beam Shimadzu UV 1601 spectrophotometer, with distilled water as a reference. Spectra were measured at 1 nm resolution between 375 nm and 750 nm.

The absorption coefficient at 440 nm ($a_{YS(440)}$) was used to represent the concentration of yellow substance (Kirk, 1994), as calculated from equation 3.5.

$$a_{YS(440)} = 2.303(OD_{440}\text{-}OD_{750})/0.1 \qquad (m^{-1}) \qquad\qquad (3.5)$$

where OD_{440} and OD_{750} are the optical densities, or absorbances, measured at 440 nm and 750 nm respectively. The factor 2.303 converts from base 10 to base e logarithms. The absorbance at 750 nm is subtracted to correct for scattering by fine particles, and the denominator of 0.1 is the cell pathlength in metres.

3.6.4   Gravimetric Measurement of Total Suspended Sediments (TSS)

The concentration of Total Suspended Sediment (TSS) was measured gravimetrically according to methods outlined by Strickland and Parsons (1972). SeaWiFS protocols were not followed on this occasion as they only describe the measurement of total suspended matter using filters that are not combustible. In this study, knowledge of the organic and inorganic components of TSS (as separated during combustion) is important, therefore, methodology alternative to that of Mueller and Fargion (2002) is proposed.

Filter Preparation

Filter preparation was required prior to sampling to remove some sources of error identified in the gravimetric measurement of TSS. Whatman GF/F filters of 47 mm diameter and $0.7\mu m$ pore size were washed with distilled water and then combusted for 3 hours at $500°C$ to remove any loose particulate material. This small, but significant, amount of particulate matter could affect the measurement of TSS in a number of ways; particles may block pores on the filter, increasing the retention of the filters and thus leading to an overestimate of TSS concentrations. An alternative argument would be that these particles would contribute to the initial weight of the filter, which may then be removed in the filtration process, thus resulting in an underestimated TSS concentration.

Preliminary experiments to perfect the technique showed that for duplicate samples, the standard deviation of the mean TSS concentration was reduced from 5.45 to 0.45 by adopting the above filter preparation. Average TSS concentrations were reduced, implying that the filters are less retentive following this treatment. This would agree with the theory that this filter preparation removes loose particles on the filter, creating more uniform pore sizes and reducing variability between samples. Following preparatory treatment, filters were weighed using a 5 d.p. balance measuring to ± 0.1 mg (giving initial weight W_o) and placed in labelled aluminium trays and sealable bags for storage.

Sample Filtration

Water samples were first shaken to avoid particle flocculation, ensuring all material was

kept in uniform suspension. Water samples were filtered, as soon as possible after collection, through the pre-weighed filters and washed with 200 ml of distilled water to remove dissolved salts. Triplicate samples were filtered at all stations to give an idea of sample variability. The volume of sample filtered (V_f) depended on the sediment loading, ranging from 500 ml in the most turbid waters to 3 litres in the clearer waters. This ensured that regardless of water clarity, there was sufficient sediment retention to allow consistent weight determination. The filter was removed using flat bladed tweezers, taking great care not to tear the filter and was then returned to the labelled aluminium tray and sealed bag. Samples were stored frozen until further processing to avoid growth or degradation of the organic fraction of TSS. On return to the laboratory, filters were dried for one hour at 75°C before being weighed, giving the dry filter weight W_d. Filters were then combusted at 500°C for three hours to burn off all organic matter and re-weighed to give the burnt filter weight W_b. Because of their hygroscopic nature, samples were stored in sealed plastic bags in a desiccator containing dry silica gel following the drying and combustion stages to avoid unaccounted weight gain.

Concentrations of total suspended sediment (TSS), the inorganic fraction or mineral suspended sediment (MSS) and the organic fraction or organic suspended sediment (OSS) were then calculated according to equations 3.6, 3.7 and 3.8 respectively.

$$TSS = (W_d\text{-}W_0)/V_f \qquad (mg\ l^{-1}) \qquad\qquad (3.6)$$

$$MSS = (W_b\text{-}W_0)/V_f \qquad (mg\ l^{-1}) \qquad\qquad (3.7)$$

$$OSS = TSS\text{-}MSS \qquad\quad\ (mg\ l^{-1}) \qquad\qquad (3.8)$$

3.6.5 Quantitative Filter Technique Measurement of Particulate Absorption

The quantitative filter technique was pioneered by Yentsch (1962) and is now used routinely to quantify the contributions of individual constituents to the total absorption coefficients in the UV and visible regions of the spectrum. The technique involves the filtration of a water sample, retaining particulate matter on a filter pad, which is then scanned in a spectrophotometer to measure the light transmitted through the sample. There has been considerable effort aimed at developing protocols that provide the most accurate estimate of particle absorption (Mueller and Fargion, 2002). The most widely

used method is based on the methanol extraction as first demonstrated by Kishino *et al.* (1985). After scanning and recording the absorption spectrum of the full sample, methanol is used to bleach the phytoplankton pigments. Re-scanning and subtracting this spectrum from the full absorption spectrum produces the phytoplankton spectral absorption. Having removed the effect of phytoplankton, the remaining absorption is that due to both inorganic sediment and organic detritus. Solvent extraction presents significant limitations because firstly, some pigment types such as phycobilins are not extractable and secondly, the procedure is ineffective with some phytoplankton species, for example Chlorophycaea, whose thick cell wall hinders solvent penetration (Bricaud and Stramski, 1990).

Because in this study the primary interest lies in the optical properties of inorganic sediments, it was thought necessary to separate the absorption due to detrital matter and inorganic sediment. For the most part, studies to date have focussed on the identification of phytoplankton absorption spectra (Kishino *et al.*, 1985; Bricaud and Stramski, 1990; Bricaud *et al.*, 1995) and at present there are no well-established protocols for determining the absorption coefficient for inorganic particles. Bowers *et al.* (1996) removed all organic matter by combustion to determine the absorption properties of inorganic sediments and it was this method, with a few modifications, that was adopted in this study.

Seawater samples were filtered through pre-weighed GF/F filters and stored in aluminium trays in the freezer until further analysis. The spectral absorption analyses were carried out using a dual beam Shimadzu UV1601 spectrophotometer. Filters were placed on microscope slides and held, using small magnets, over the exit port of the spectrophotometer. Sample absorbance, or optical density (OD), was measured from 400 to 750 nm using a filter wetted with filtered seawater as a reference blank. The sample filters and the blank filter were then rinsed with distilled water to remove salts and combusted at 500°C for three hours to burn off all the organic material. Sample filters were weighed to determine the sediment mass-concentration as described in section 3.6.4 before re-scanning to obtain the absorption spectra for the inorganic component of TSS.

Historically, it has been assumed that particle absorption at 750 nm is negligible ($OD_{(750)}$ representing the loss of light due to scattering) and should be used as a null point correction. Although it is certainly true that phytoplankton cells do not absorb light at 750 nm, it may not be the case for inorganic or detrital material. Correcting for scattering in this way also assumes that scattering is constant across the spectrum. If scattering increases with shorter wavelengths as demonstrated by Gould and Arnone (1998) and Binding (1999), this would over-estimate absorption at shorter wavelengths. In this study, absorption by MSS at 750nm was set equal to that of the total absorption at the same wavelength, thus assuming that absorption by the organic fraction OSS (consisting of phytoplankton and detrital matter) at that wavelength was negligible. It is acknowledged that this assumption may introduce some error in the estimate of phytoplankton absorption, however, it was not possible in this study to isolate the absorption due to detrital matter.

It is known that the absorption as measured on filters over-estimates the absorption coefficient as would be observed *in situ* because of the diffuse nature of the light passing through the filtered sample. Multiple scattering of light within the filter increases the average pathlength of light, thus increasing the potential for absorption (Butler, 1962). This effect was corrected for by including a pathlength amplification factor, β (equation 3.9, after Cleveland and Weidemann (1993)) which converts the optical density of particles as measured on the filter paper (OD_f) to an optical density that would be measured if particles were in suspension (OD_s).

$$OD_s(\lambda) = 0.378OD_f(\lambda) + 0.523OD_f(\lambda)^2 \qquad (3.9)$$

The absorption coefficient (a_s) of the particulate material in suspension was calculated from:

$$a_s(\lambda) = 2.303OD_s(\lambda)/l_s \qquad (m^{-1}) \qquad (3.10)$$

where $OD_s(\lambda)$ is the optical density at wavelength λ as calculated from equation 3.9 and the factor 2.303 changes the base of the logs from 10 to e. The geometric absorption

pathlength (l_s) of the filtered material in suspension is given by $l_s = V_f/A_f$ where V_f is the volume of water filtered and A_f is the clearance area of the filter calculated from the diameter of the soiled part of each filter. l_s gives the length scale the particles would occupy in suspension in a cylinder of cross section A_f, thus converting OD to a measure of absorption per metre.

Phytoplankton pigment and mineral sediment specific absorption coefficients (absorption per unit concentration, a^*_C and a^*_{MSS} respectively) were obtained by regressing the relevant absorption coefficient against the concentrations of [C] and [MSS] such that:

$$a_C(\lambda) = a^*_C (\lambda)[C] \qquad\qquad (m^2\ mg^{-1}) \qquad\qquad (3.11)$$

and

$$a_{MSS}(\lambda) = a^*_{MSS}(\lambda)[MSS] \qquad (m^2\ g^{-1}) \qquad\qquad (3.12)$$

Each regression was repeated at 10 nm intervals between 400 and 750 nm to determine the spectral shape of a^*_C and a^*_{MSS}.

3.7   Calculating Inherent and Apparent Optical Properties

Using the theory outlined in Chapter Two, data from the PRR600 enabled the calculation of two key apparent optical properties; the irradiance reflectance just below the surface, $R(0^-,\lambda)$ and the diffuse attenuation coefficient for downwelling irradiance, K_d (z,λ). Sections 3.7.1 and 3.7.2 describe the data processing required to derive these parameters.

3.7.1   Irradiance Reflectance

Profiles of upwelling and downwelling irradiance were corrected for length offsets and dark current readings as described in the previous sections. Because of surface waves, it was not possible to accurately measure the near-surface underwater light field. The shallowest reliable readings typically occur at depths ranging from 0.5 to 2 m (Mueller

and Fargion, 2002), depending on surface conditions. Fluctuations associated with surface waves were removed from the profile and data was extrapolated upward to the sea surface. The log of the normalised irradiances (E_d/E_s and E_u/E_s) were plotted against depth and extrapolated to the surface by means of least square linear regression. The intercept at depth zero was taken to be the upwelling, or downwelling, irradiance just beneath the surface. Irradiance reflectance just beneath the surface, $R(0^-,\lambda)$, was then calculated as the ratio $E_u(0^-,\lambda)/E_d(0^-,\lambda)$. Normalising irradiance profiles to E_s corrects for both variations in surface light conditions during a profile and for differences in conditions between the two profiles.

3.7.2 Diffuse Attenuation Coefficient

A plot of the log of E_d against depth provides K_d as the slope of a linear fit to the data, so that:

$$K_d(z,\lambda) = -\left[\frac{d\ln[E_d(z,\lambda)]}{dz}\right] \qquad (m^{-1}) \qquad (3.13)$$

As for calculations of reflectance, normalising profiles of E_d to surface irradiance, E_s, corrects for variations in surface light conditions throughout the profile.

Before discussing the interpretation and importance of the spectral reflectance measured in this study, the potential sources of error in the *in situ* measurement of reflectance will be examined briefly. Shallow attenuation depths may lead to inaccuracies in measured reflectance because in turbid waters, or when measuring in the red portion of the spectrum where absorption by water is large, the extrapolation of *in situ* reflectance measurements to the surface may be difficult (Mueller and Austin, 1995). This however, was overcome by profiling at a rate slow enough to ensure sufficient data for accurate extrapolation.

A problem highlighted in ocean optics measurements is that of instrument self-shading (Gordon and Ding, 1992). In this study, the ratio of $E_d(0^-)/E_s(0^-)$ just below the surface was taken as a quality control for each profile. If E_d as measured by the underwater

profiler was equal to E_s measured above the water by the deck reference unit and extrapolated to below the sea surface ($E_d/E_s = 1$) then there was no shading, either by the instrument itself or by the structure of the ship. This is particularly important in the calculation of the diffuse attenuation coefficient, where the rate at which the underwater irradiance decreases is normalised to the surface irradiance. Stations were included in further processing providing the value of E_d/E_s was $1 \pm 10\%$. If there was noticeable distortion in any profiles due to unavoidable shading occurrences then that station was excluded from the data set. Only 12 stations out of a total of 156 were excluded from the data analysis.

3.7.3   Total Absorption and Scattering Coefficients

Total scattering (b) and absorption (a) coefficients were estimated from the radiometer profiles using the relationships derived by Kirk (1981; 1984) from the Monte Carlo technique (see Chapter Two). The functions required to estimate a and b are presented in equations 3.14 and 3.15.

$$R = C(\mu_0)b_b / a \qquad (3.14)$$

where $C(\mu_0) = 0.975 - 0.629\mu_0$

$$K_d = \frac{1}{\mu_0}(a^2 + G(\mu_0)ab)^{1/2} \qquad (3.15)$$

where $G(\mu_0) = 0.425\mu_0 - 0.19$

Assuming the ratio b_b/b to be the same as that observed by Petzold (1972), and calculating μ_0 for each profile as described in section 3.7.4, total scattering and absorption coefficients for all wavebands can be calculated simply in terms of R and K_d. Figure 3.5 shows contours of R and K in a-b space as estimated from the above relationships (for $\mu_0 = 0.85$), providing an example look-up table for obtaining IOPs from known AOPs and vice versa.
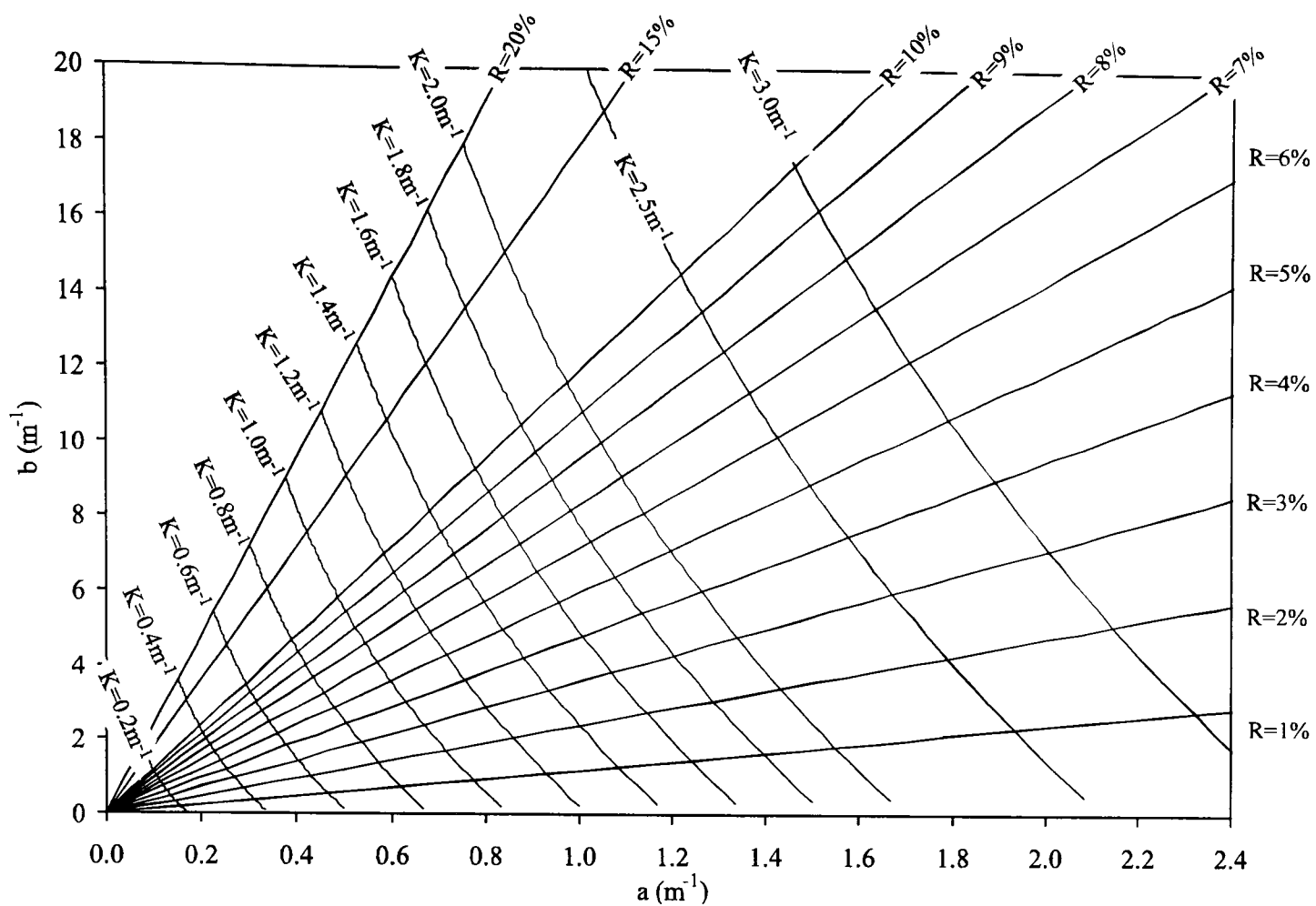
Figure 3.5: Look-up table for estimating absorption and scattering coefficients from known R and K_d, as calculated using functions from Kirk (1981) and $\mu_0 = 0.85$.

3.7.4 Average Cosines

Equations 3.14 and 3.15 show that the relationships between IOPs and AOPs are a function of μ_0, the average cosine of the angle the photons make with the vertical just beneath the surface. This parameter is related to the directional properties of the irradiance above the sea surface and therefore depends on the solar elevation (β), which varies with both time of day and time of year and can be calculated with knowledge of the solar declination (δ) and latitude. At each optical station, the value of μ_0 and thus $C(\mu_0)$ was calculated from equations 3.16 to 3.18, to enable the determination of absorption and scattering coefficients as shown in section 3.7.3.

Solar declination (that is the angle through which the earth is tilted towards the sun) was calculated for each sampling day from equation 3.16 as derived by Spencer (1971).

$$\delta = 0.39637 - 22.9133\cos\psi + 4.02543\sin\psi - 0.3872\cos2\psi + 0.052\sin2\psi \qquad (3.16)$$

where ψ is the date expressed as an angle ($\psi = 360d / 365$; d ranges from 0 on Jan 1st to 364 on Dec 31st). The solar declination is zero at the spring and autumn equinoxes and varies from +23° 27' to – 23° 27' at summer and winter solstice respectively.

With knowledge of the solar declination and the latitude, γ, the solar elevation, β, was calculated according to equation 3.17.

$$\sin\beta = \sin\gamma \, \sin\delta - \cos\gamma \, \cos\delta \, \cos\tau \qquad (3.17)$$

where τ is the time of day expressed as an angle ($\tau = 360t / 24$) and t is the time in hours after midnight.

Given the solar elevation β, the solar zenith angle above the surface (θ_a) is simply 90°–β. Snell's law (equation 3.18) was then used to account for refraction at the air/sea interface to obtain a value of θ_w, the angle the photons make with the vertical beneath the surface, and thus μ_0 and $C(\mu_0)$.

$$\frac{\sin\theta_a}{\sin\theta_w} = \frac{n_w}{n_a} \qquad (3.18)$$

where n_w and n_a are the refractive indices of water and air respectively. A value of 1.33 can be reasonably assumed for n_w/n_a.

The value of μ_0 below the sea surface is also affected by the proportion of diffuse to direct light incident on the surface. At each station, a measure of surface light conditions was recorded simply as a percentage cloud cover. Light was assumed to be 100 % diffuse under overcast conditions and 100 % direct under a clear sky. For diffuse skylight, an average μ_0 was calculated over 5° increments of incident light. For a station where there was 50 % cloud cover, μ_0 was calculated as the average of 50 % direct light and 50 % diffuse light. To demonstrate the variability of μ_0, figure 3.6 presents $C(\mu_0)$ for noon sun at a latitude of 53°, varying as a function of both time of year and surface light conditions.

Whilst equation 3.14 shows that for zenith sun, $R = 0.346b_b/a$, figure 3.6 illustrates that for a latitude of 53°, $C(\mu_0)$ has a value of 0.448 for diffuse light and varies over the year from 0.39 to 0.54 for direct light.
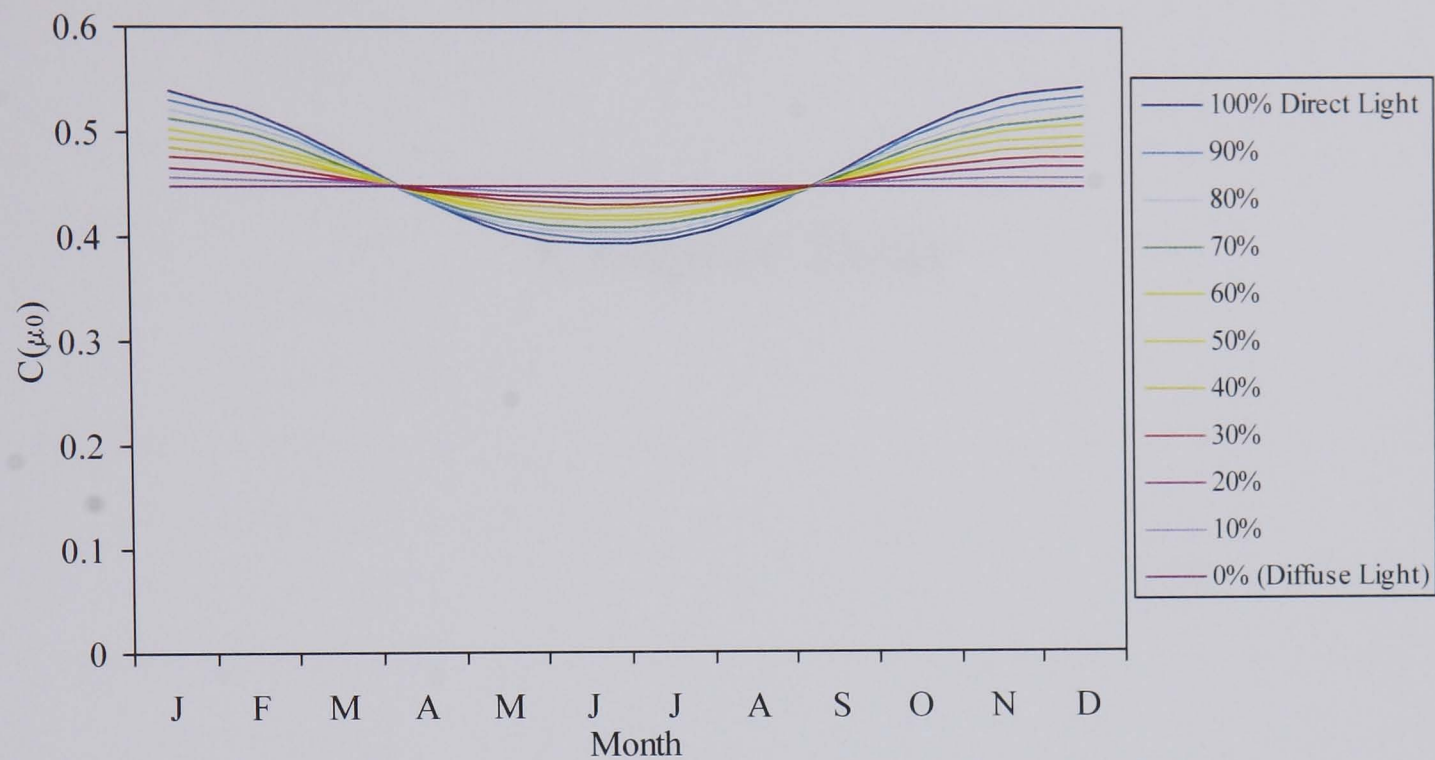
Figure 3.6: The annual variation of $C(\mu_0)$ at a latitude of 53° for varying proportions of direct to diffuse light incident at the sea surface.

Chapter Four

The Development of an Algorithm for the Retrieval of Suspended Sediments from *in situ* Ocean Colour

CHAPTER FOUR: THE DEVELOPMENT OF AN ALGORITHM FOR THE RETRIEVAL OF SUSPENDED SEDIMENTS FROM *IN SITU* OCEAN COLOUR

4.1   Introduction

This chapter presents results that have enabled a preliminary assessment of the way in which suspended sediments and other optically active constituents affect ocean colour in the Irish Sea. This assessment was carried out initially by considering the inherent and apparent optical properties, either measured directly or inferred through accepted optical relationships. Identification of the absorption and scattering properties of dissolved and particulate matter allowed a more informed analysis of the spectral reflectance signatures observed in the Irish Sea. A simple algorithm for the retrieval of mineral sediment concentrations was developed based on measurements of the irradiance reflectance at 665 nm. A reflectance model based on the derived absorption and scattering properties was then used to evaluate observations against known optical theory and was further used to assess the effects of other optically active constituents on the relationship between reflectance and MSS.

4.2   Inherent Optical Properties

Before an algorithm for the determination of sediment concentrations from ocean colour could be derived, it was necessary to understand the way in which both dissolved and particulate matter influenced ocean colour in the study region. Such information was obtained by measuring the inherent optical properties of phytoplankton (C), mineral suspended sediments (MSS) and yellow substance (YS). Absorption coefficients for C, MSS and YS were measured spectrophotometrically on filtered seawater samples. No instrumentation was available routinely for the direct measurement of scattering, therefore, scattering coefficients for C and MSS were obtained from theoretical computations of total scattering.

4.2.1   Absorption

Figure 4.1 presents the specific absorption coefficients (absorption per unit concentration) for yellow substance (a^*_{YS}), mineral suspended sediments (a^*_{MSS}) and phytoplankton pigments (chlorophyll *a* plus phaeopigments, a^*_C) at 10 nm intervals

in the spectral range between 400 nm and 750 nm. Particulate absorption spectra were measured on filters with concentration ranges of C and MSS of 0.34 - 2.8 µg l^{-1} and 0.85 - 9.6 mg l^{-1} respectively. Yellow substance concentrations ranged from 0.028 to 0.41 m^{-1}.
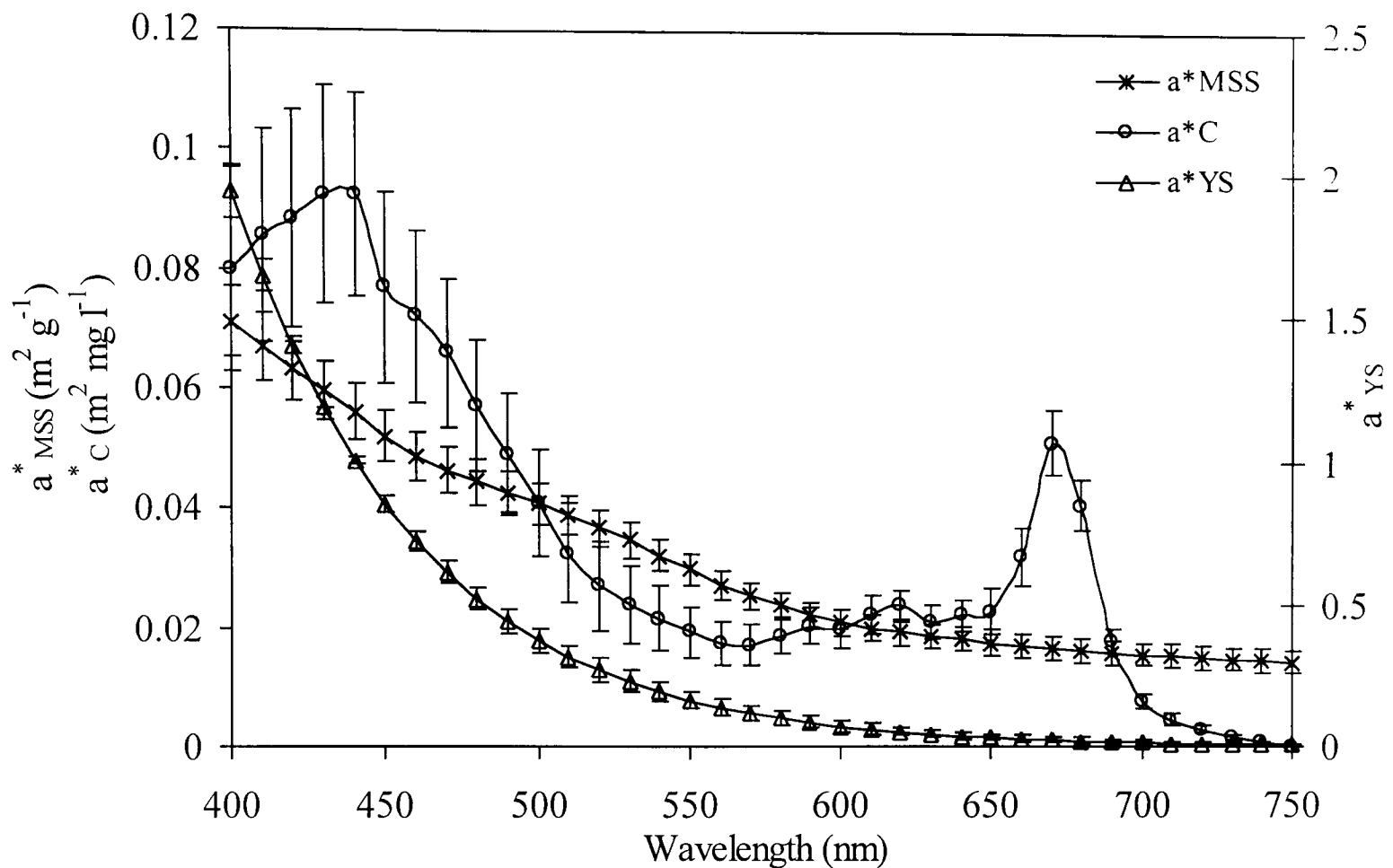
Figure 4.1: Spectral variation of specific absorption coefficients for yellow substance (YS), mineral suspended sediments (MSS) and phytoplankton pigments (C). Error bars indicate ± 2 standard errors.

The spectral variation of yellow substance absorption displayed the characteristic exponential increase with decreasing wavelength, as represented by equation 4.1

$$a_{YS}(\lambda) = a_{YS}(\lambda^*)e^{[-S(\lambda-\lambda^*)]}$$

(4.1)

where $a_{YS}(\lambda^*)$ is the absorption by yellow substance at a reference wavelength λ^*, in this case 440 nm. The coefficient describing the exponential slope, S, had a mean value of 0.0165 with a standard error of the mean of 0.0009.

Absorption by mineral sediments, normalised to a unit concentration of MSS (a$^*_{MSS}$) displayed a near constant value at red wavelengths. Absorption then increased with

decreasing wavelength in accordance with equation 4.2.

$$a^*_{MSS}(\lambda) = \alpha \lambda^2 - \beta\lambda + \gamma \qquad (R^2 = 99.7\%, p=0.00) \qquad (4.2)$$

where $\alpha = 5.6\times10^{-7} \pm 2\times10^{-8}$, $\beta = 8.03\times10^{-4} \pm 1.78\times10^{-5}$ and $\gamma = 0.3 \pm 0.005$.

Again, the small standard errors associated with this relationship suggest there was little variability in the inherent colour of MSS in this study region. This is in agreement with observations of the filtered MSS samples; whilst the intensity of colour varied with the concentration of MSS, all MSS filters appeared the same red/brown in colour.

Absorption by phytoplankton pigments (a^*_C) showed a typical absorption spectrum for chlorophyll a, with absorption peaks at 430 and 670 nm and a minimum at green wavelengths. The error bars in figure 4.1 show that the variability in a^*_C is considerably greater than that of a^*_{YS} and a^*_{MSS}, particularly at shorter wavelengths.

It is known that the absorption coefficient of particles on filters is overestimated and a path length amplification factor, β, was applied to convert the absorption coefficient of particles on the filter to that of particles in suspension. However, the correction adopted in this study (that of Cleveland and Weidemann, 1993), was derived for Case 1 waters where phytoplankton dominated the particulate matter. It can be expected that the presence of mineral particles, which are characterised by high refractive indices relative to phytoplankton and, therefore, high backscattering coefficients, may result in an underestimation of the β-factor using the method of Cleveland and Weidemann (1993). This would result in an overestimate in the derived absorption coefficients in this study.

Using the relationships between the IOPs and R and K_d (described in Chapter Two, after Kirk, 1981, 1984), an estimate of *in situ* absorption from the PRR600 data allowed the calculation of specific absorption coefficients for both MSS and C by carrying out multiple regressions of MSS and C concentrations on absorption after correcting for the influence of yellow substance and pure water. Figure 4.2 presents

$a^*{}_C$ and $a^*{}_{MSS}$ at each waveband along with the corresponding spectral absorption obtained from the quantitative filter technique for comparison. Whilst the absorption coefficients estimated from K_d and R show similar spectral variation to those measured on filters, the magnitudes of the coefficients are significantly lower. This is in agreement with the suggestion that the chosen β-factor may result in the overestimation of the filter-retrieved absorption coefficients.
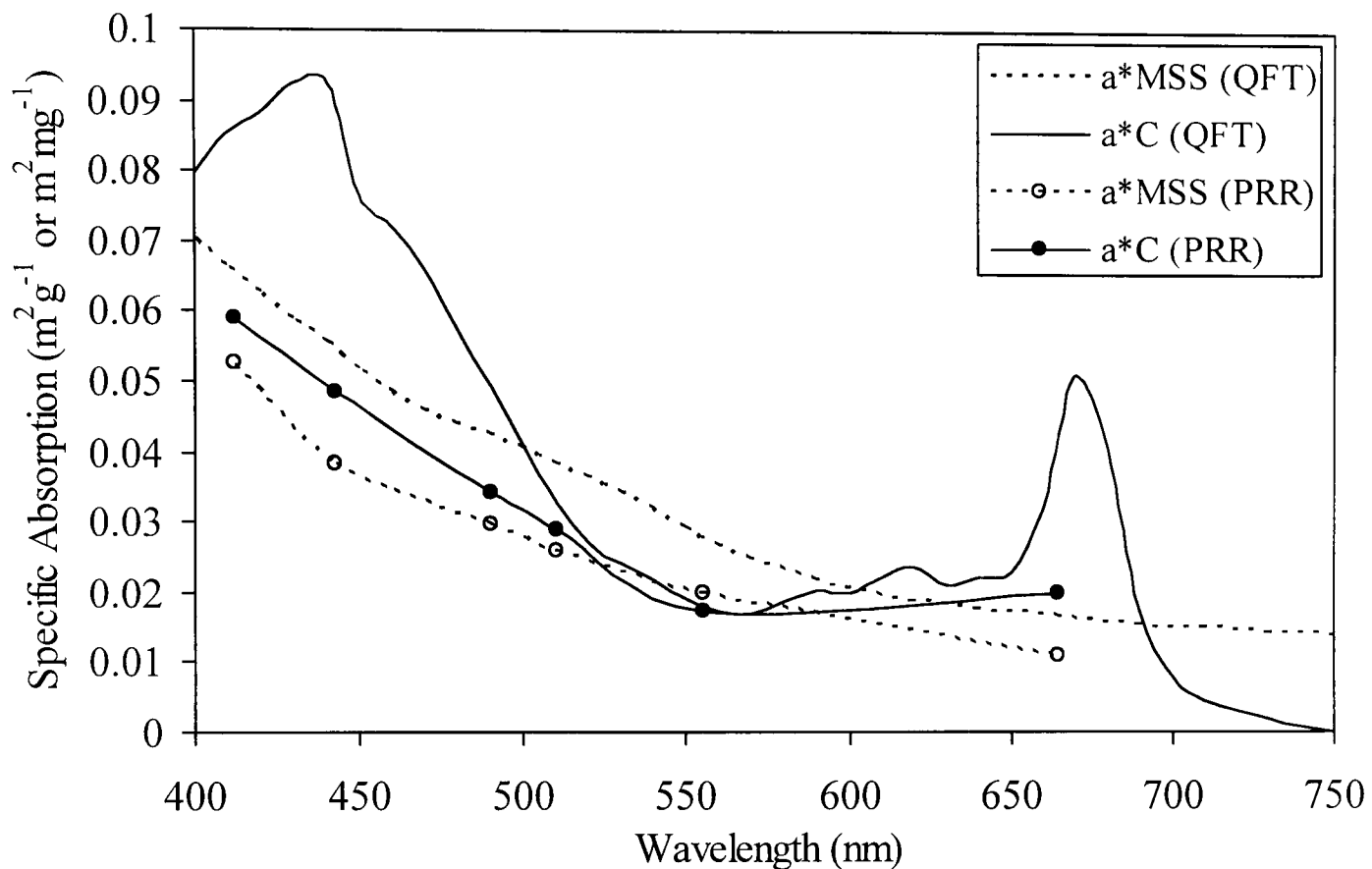
Figure 4.2: Specific absorption coefficients for C ($a^*{}_C$) and MSS ($a^*{}_{MSS}$) estimated for each of the PRR600 wavebands (PRR) and the spectral absorption from the quantitative filter technique (QFT).

On the last two research cruises carried out in this study, an AC-9 reflective tube absorption meter (WET Labs, Inc.) was available and provided independent *in situ* measurements of total absorption coefficients. The AC-9 obtained concurrent measurements of the spectral transmittance and absorption of water over nine wavelengths. Using a 25 cm pathlength, the instrument provided a method for determining the absorption (a) and beam attenuation (c) coefficients. Scattering was accounted for by using a reflective tube that reflected all scattered photons into the detector. A comparison of the absorption coefficients measured using the AC-9 and those determined from Kirk's expressions is presented in figure 4.3. The close agreement of the absorption measurements from the AC-9 and those derived from

irradiance confirms the accuracy of Kirk's method. Uncertainty in the scattering correction of the AC-9 measurements has been found to result in the slight overestimation of absorption that increases as the ratio of b to a increases (Piskozub *et al.*, 2001). There is some evidence in figure 4.3 that the AC-9 may overestimate absorption at high values.
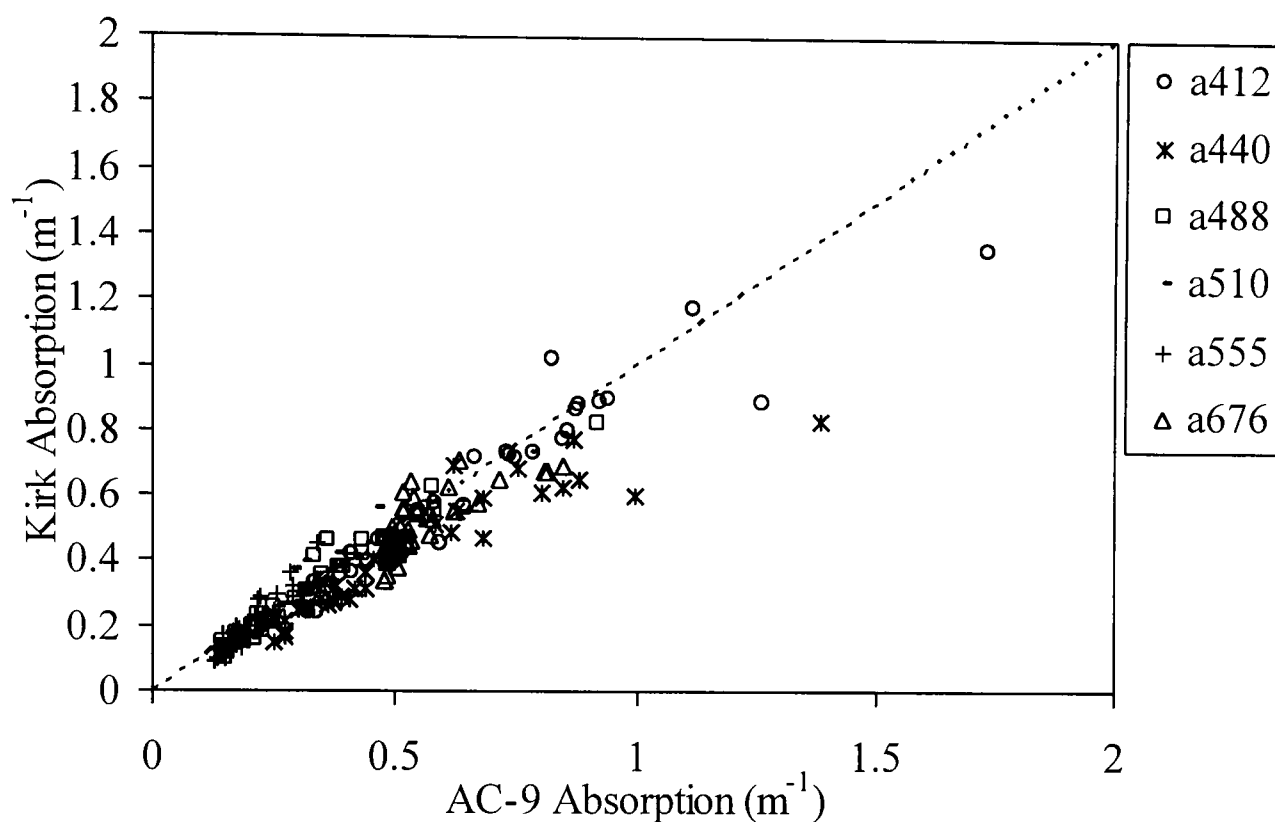
Figure 4.3: Comparison of absorption coefficients as estimated from the method of Kirk (1984) and as measured using the AC-9.

These independent determinations of the absorption coefficients enabled the assessment of measurement accuracy of the quantitative filter technique. Whilst in this study, measuring absorption on filters provided valuable results on the spectral shape of absorption coefficients, further work is needed to ensure confidence in the absolute values of a^*_C and a^*_{MSS}. The correct assessment of the absorption coefficient of natural organic and inorganic matter using the quantitative filter technique requires that the problem of estimating the β-factor be solved for coastal waters. Because of the uncertainty in the filter-retrieved absorption coefficients and the good agreement between the absorption coefficients obtained from the PRR600 and the AC-9, it was felt that the PRR600 would provide the more reliable estimates of a^*_{MSS} and a^*_C for use later in the study.

4.2.2 Scattering

Total scattering coefficients were calculated using relationships between a, b and K_d and R (Kirk, 1981; 1984). Total scattering coefficients ranged from a minimum of 0.06 m^{-1} in the red to a maximum of 10.5 m^{-1} in the green. Knowledge of the total absorption and scattering coefficients revealed that the majority of waters sampled in the region of study were scattering dominated, with calculated values of the scattering to absorption ratio, b/a, ranging from 1.4 to 20.5 at 555 nm. Even at 665 nm, where absorption by water is strong, over half of the waters sampled resulted in b/a > 1. In addition, a strong positive relationship between R_{665} and K_{d665}, the diffuse attenuation coefficient, ($K_{d665} = 0.08R_{665} + 0.51$, $R^2 = 78.0\%$) confirms the importance of scattering relative to absorption in these waters. The positive intercept in this relationship is the consequence of the strong absorption by water.

It was assumed that yellow substance did not contribute to scattering and thus specific scattering coefficients for MSS and C could be obtained by multiple regressions of b on C and MSS for all wavelengths (table 4.1). MSS-specific scattering coefficients ranged from 0.32 to 0.45 m^2 g^{-1} across the spectrum and showed preferential scattering at green wavelengths. Results in table 4.1 suggest that phytoplankton have no significant effect on scattering; the large standard errors associated with b^*_C indicate that there can be little confidence in these results. Furthermore, removing C from the regression results in little loss of the explained variance in b^*_{MSS}. However, phytoplankton cells are known to have significant scattering properties (Bricaud *et al.*, 1983; Morel, 1987). It is suggested that in this study, the contribution of phytoplankton scattering to total scattering is simply overwhelmed by scattering from high concentrations of mineral sediment.

An attempt was made to quantify the scattering properties of phytoplankton by dealing with only those stations where organic matter dominated the total suspended particulate concentration. Regression analyses were carried out for stations where MSS/TSS was less than 40%. On removal of sediment dominated stations, the scattering effect of phytoplankton could be isolated; the resulting b^*_C are presented in table 4.2. Results appear to suggest that phytoplankton are considerably less efficient at scattering light than mineral particles are, with b^*_C ranging from 0.022 to 0.032 m^2 mg^{-1}. However, in comparable units, b^*_C is 30 m^2 g^{-1}, which, compared

with b^*_{MSS}, suggests that for equal masses, phytoplankton may well scatter more light than mineral particles. Nevertheless, grams of chlorophyll per m^3 are rarely measured in nature, therefore, the total scattering by phytoplankton will usually be very much lower than that by mineral particles.

Table 4.1: Specific scattering coefficients for mineral suspended sediments (b^*_{MSS}) and phytoplankton (b^*_C).

Multiple Regression:

Wavelength (nm)	b^*_{MSS} $(m^2 g^{-1})$	S.E. $(m^2 g^{-1})$	p-value	b^*_C $(m^2 mg^{-1})$	S.E. $(m^2 mg^{-1})$	p-value	R^2 (%)
412	0.3182	0.0099	0.00	0.0059	0.0161	0.37	89.1
443	0.3489	0.0109	0.00	0.1178	0.0177	0.506	89.1
490	0.4408	0.0137	0.00	0.0228	0.0222	0.306	89.2
510	0.4425	0.0136	0.00	0.0261	0.0221	0.241	89.3
555	0.4541	0.0140	0.00	0.0317	0.0228	0.167	89.2
665	0.4106	0.0191	0.00	0.0324	0.0191	0.093	90.5

Removing C from the regression:

Wavelength (nm)	b^*_{MSS} $(m^2 g^{-1})$	S.E. $(m^2 g^{-1})$	p-value	R^2 (%)
412	0.3178	0.0098	0.00	89.1
443	0.3479	0.0108	0.00	89.0
490	0.4389	0.0135	0.00	89.1
510	0.4403	0.0135	0.00	89.2
555	0.4514	0.0140	0.00	89.0
665	0.4079	0.0118	0.00	90.3

Table 4.2: Specific scattering coefficients for phytoplankton (b^*_C).

Wavelength (nm)	b^*_C $(m^2 mg^{-1})$	S.E. $(m^2 mg^{-1})$	p-value	R^2 (%)
412	0.0228	0.0051	0.00	77.2
443	0.0217	0.0046	0.00	80.5
490	0.0254	0.0045	0.00	85.6
510	0.0258	0.0046	0.00	86.2
555	0.0321	0.0049	0.00	86.9
665	0.0293	0.0049	0.00	85.9

In addition to measuring absorption, the AC-9 also gave an independent estimate of the total scattering coefficient and provided a comparison for those scattering coefficients estimated from the method of Kirk (1984). By measuring both the absorption and attenuation coefficients, the total scattering coefficient could be estimated from AC-9 results simply by subtraction (b = c-a). Figure 4.4 shows the comparison of scattering coefficients as derived from both the AC-9 measurements and the expressions from Kirk (1984) applied to the PRR600 data. As with the absorption coefficients, these two methods result in scattering coefficients that are in close agreement, therefore, there can be some confidence in the scattering coefficients used in this study, particularly in the 665 nm waveband.
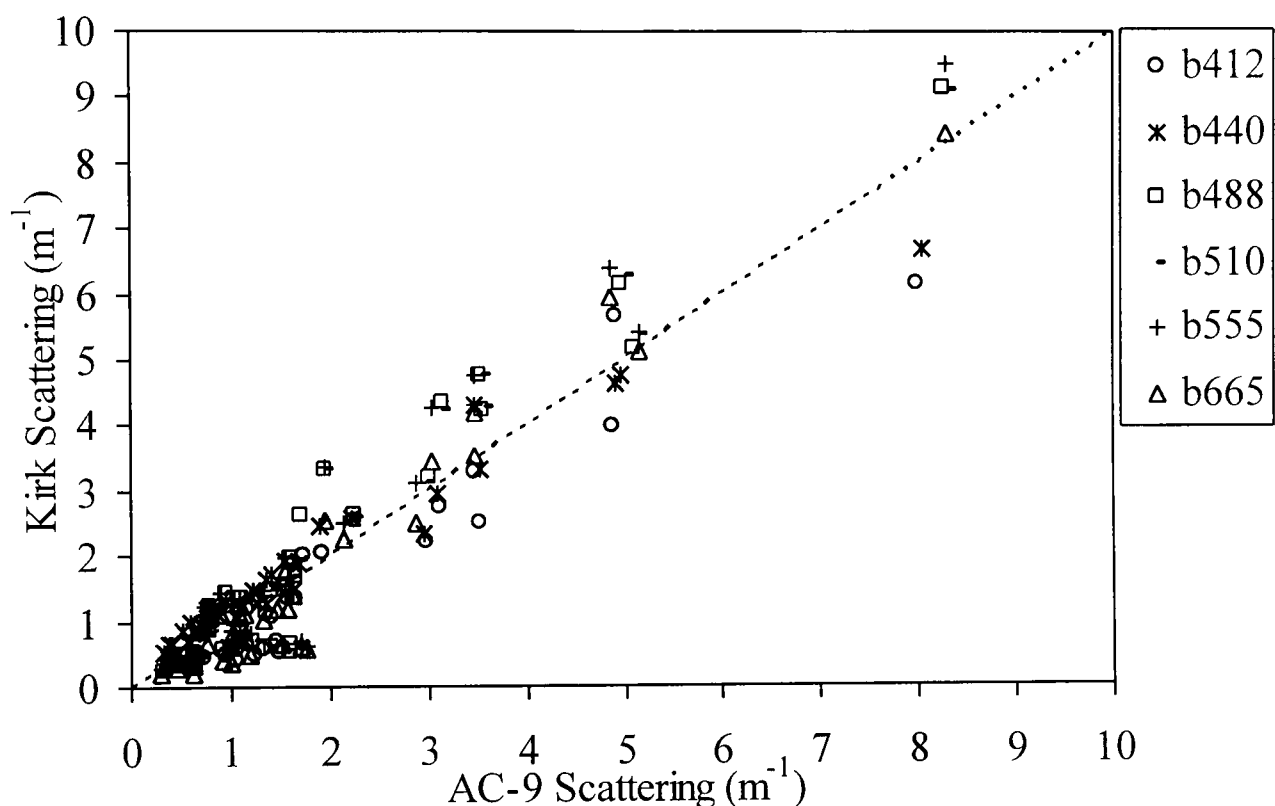
Figure 4.4: Comparison of scattering coefficients as estimated from the method of Kirk (1984) and as measured using the AC-9.

4.3   Irradiance Reflectance Spectra

Figure 4.5 presents the spectral variation of irradiance reflectance, R, as a function of MSS concentration. Reflectance was averaged over categories of MSS concentration, and showed an increase in average reflectance at all wavelengths with increasing sediment load, up to a maximum of 13% at 550 nm for MSS between 10 and 15 mg l^{-1}. The spectral variation in R showed a peak at green wavelengths for all sediment categories, with depressed reflectance in the blue due to the strong blue-absorption by all materials as shown in figure 4.1 and in the red by the strong

absorption by water itself.
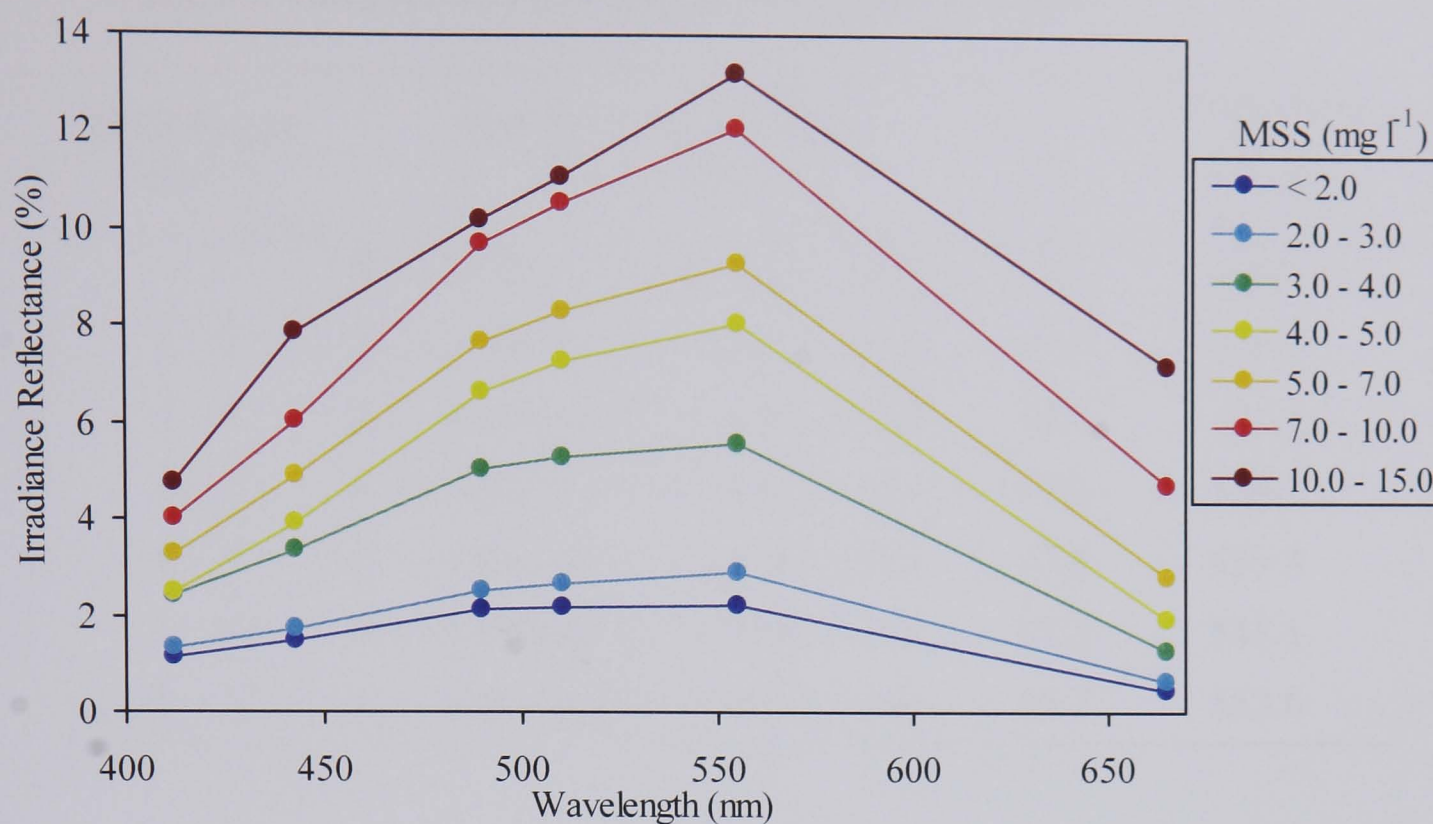
Figure 4.5: **Spectral variation of irradiance reflectance, (R, %) averaged over categories of Mineral Suspended Sediment concentrations (MSS, mg l⁻¹). Lines joining data points do not imply spectral interpolation but are added for presentation only.**

Closer analysis of the reflectance spectra in figure 4.5 identified a shift of the dominant wavelength towards the red with increasing sediment load. This shift in the reflectance peak with increasing MSS is quantified in table 4.3. A 2nd order polynomial relationship was fitted to the average spectral reflectance for each MSS category and the wavelength of the peak reflectance (λ_{PeakR}) was calculated where

$\dfrac{dR}{d\lambda} = 0$. Table 4.3 and figure 4.6 show the gradual increase in λ_{PeakR} from 526 nm

for MSS less than 2 mg l⁻¹ up to 553 nm for MSS ranging from 10 to 15 mg l⁻¹. This observation confirmed the role of the MSS absorption spectra as measured in section 4.2.1 in which increasing absorption by MSS at shorter wavelengths resulted in the gradual shift in the reflectance peak towards longer wavelengths.

Table 4.3:   Determination of the wavelength of peak reflectance, λ_{PeakR}, for categories of increasing MSS concentration.

MSS Range (mg l^{-1})	Spectral Variation of R (R=aλ^2+bλ+c)	R^2 (%)	λ (nm) when $\dfrac{dR}{d\lambda} = 0$
< 2	R = -0.0000091λ^2 + 0.096λ - 23.0	98.7	525.5
2 – 3	R = -0.000116 λ^2 + 0.123 λ - 29.8	97.5	529.7
3 – 4	R = -0.000230 λ^2 + 0.245 λ - 59.5	98.6	531.3
4 – 5	R = -0.000351 λ^2 + 0.378 λ - 94.2	97.6	538.5
5 – 7	R = -0.000369 λ^2 + 0.398 λ - 98.6	97.8	539.3
7 – 10	R = -0.000448 λ^2 + 0.489 λ - 122	97.3	545.1
10 – 15	R = -0.000388 λ^2 + 0.429 λ - 106	96.7	552.6

For the case of pure water, using the optical properties in Smith and Baker (1981), the peak reflectance was calculated to occur at λ = 472 nm. In agreement, Jerlov (1976) reported clear oceanic values of 470-473 nm. A clear water value have been added to figure 4.6 to show the potential behaviour at low MSS concentrations. Although not included in table 4.3 because of the shortage of data for category averaging, two stations with MSS concentrations over 15 mg l^{-1} showed the continuing rise in peak wavelength with increasing MSS; concentrations of 15.3 and 23.1 mg l^{-1} resulted in peak wavelengths of 570.5 and 578.8 nm respectively. These results are in agreement with studies based on hyperspectral analyses; Bukata et $al.$ (1997) observed a peak wavelength of 560 nm for an MSS concentration of 10 mg l^{-1} whereas Han (1997) revealed an increase from 578 nm at 25 mg l^{-1} to 592 at 175 mg l^{-1} and 646 nm at sediment concentrations of 500 mg l^{-1}.
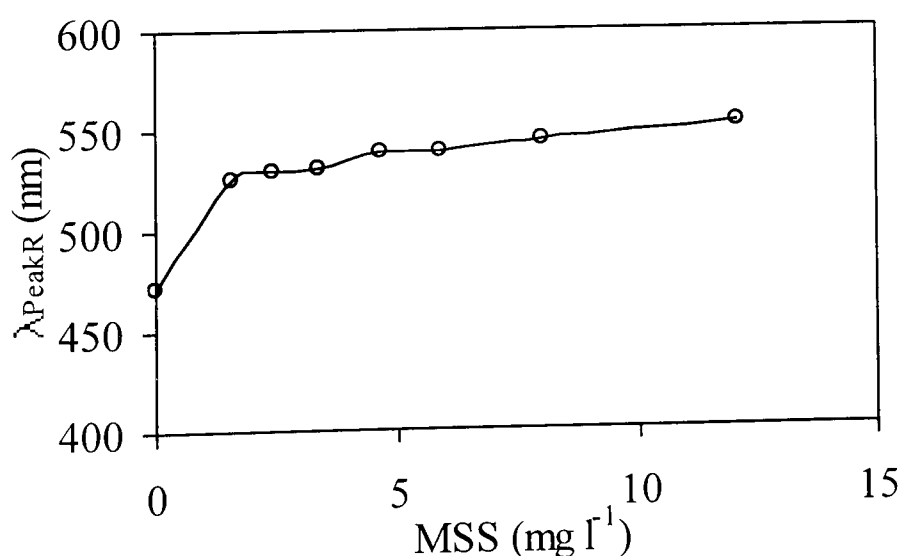
Figure 4.6: Average wavelength of peak reflectance against MSS for categories assessed in table 4.3.

Whilst figure 4.6 shows that the wavelength of peak reflectance is dependent. to some extent, on the concentration of MSS, figure 4.7 presents the peak wavelength against MSS measured for all stations individually and highlights the degree of variability in this relationship. Points in figure 4.7 are categorised according to the measured phytoplankton pigment concentrations (C) and show the trend to vary systematically with increasing C.
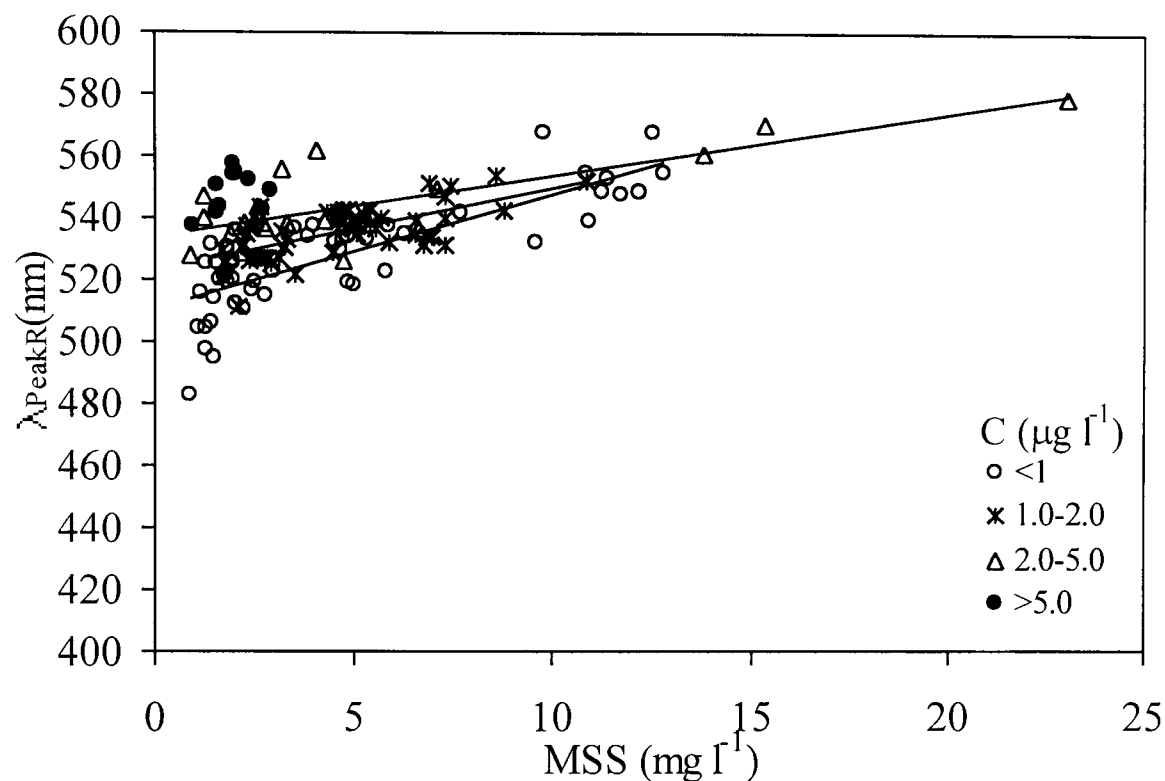
Figure 4.7: Wavelength of peak irradiance reflectance for all stations, categorised according to concentrations of phytoplankton pigments.

Table 4.4 shows the best-fit linear relationship between MSS and peak wavelength for each category of C and shows the peak wavelength at zero MSS to increase systematically with increasing C and the gradient of the relationship decreasing with increasing C. No trend was established for C greater than 5 μg l^{-1} because of the limited range of MSS within this category, however, the clustering of stations with high C suggests that this trend of decreasing gradient may continue.

Table 4.4: Relationship between peak wavelength and MSS concentration for categories of increasing pigment concentrations.

C ($\mu g \, l^{-1}$)	Relationship between peak wavelength (y) and MSS (x)	R^2 (%)
<1	y = 3.73x + 510.5	64.9
1.0-2.0	y = 2.65x + 523.4	44.8
2.0-5.0	y = 1.99x + 534.0	63.7

These results show that for a fixed concentration of MSS (particularly at low concentrations), increasing concentrations of C can result in considerable shifts in the wavelength of peak reflectance. This may result in large errors in sediment algorithms that are based on colour ratios, as was discussed in Binding *et al.* (2003) using early results involving colour ratio algorithms in the Irish Sea. This result also emphasises the difficulty that suspended sediments introduce into chlorophyll-retrieval algorithms; the fact that the three regression lines appear to merge shows that at high sediment loads, any spectral shifts due to phytoplankton are obscured by the effects of sediments.

4.4   Algorithm Development

The first step in algorithm development was to identify which of a variety of reflectance parameters best represented the observed spectral response to increasing MSS.   Table 4.5 presents a range of reflectance parameters, in terms of both reflectance and colour ratios, and their respective relationships with MSS. Analysis of colour ratios showed the strongest relationships between MSS and the ratios of reflectance in the red to one other wavelength. These ratios reflect the observed shift in reflectance towards longer wavelengths such that the $R_{665}/R_{(\lambda)}$ ratio increases with increasing sediment load. The relationship between this ratio and MSS improves as the wavelength of the denominator increases such that MSS explains around 65% of the variance in the ratio R_{665}/R_{555}. Traditionally, the red to green reflectance ratio is expected to be strongly correlated with MSS, reflecting the shift of the peak in the reflectance spectra from green to red with increasing MSS concentrations. Early results in this study (Binding *et al.*, 2003) showed that there was a strong correlation between the red to green colour ratio and MSS concentrations only at those stations

where the optical properties were dominated by MSS.

For those stations with the greatest dominance of MSS, there was a strong relationship ($R^2 = 87.0\%$) between MSS and R_{665}/R_{555}. With increasing influence of phytoplankton pigments and yellow substance, this relationship was found to break down, with increasingly greater spread in the data points. Consequently, an algorithm based on colour ratios using these wavelengths has limited potential, applicable only to waters that are optically dominated by suspended sediments.

Table 4.5: Details of the relationships between MSS concentration and various reflectance parameters.

Reflectance Parameter	Relationship with MSS	R^2 (%)
R_{665}/R_{412}	$= 0.0002MSS^2 + 0.101MSS + 0.3195$	41.8
R_{665}/R_{443}	$= 0.0004MSS^2 + 0.048MSS + 0.287$	36.8
R_{665}/R_{490}	$= 0.0007MSS^2 + 0.029MSS + 0.189$	47.0
R_{665}/R_{510}	$= 0.0006MSS^2 + 0.028MSS + 0.171$	52.2
R_{665}/R_{555}	$= -0.0001MSS^2 + 0.029MSS + 0.143$	64.9
R_{412}	$= -0.0225MSS^2 + 0.691MSS + 0.035$	59.7
R_{443}	$= -0.0365MSS^2 + 1.180MSS - 0.5039$	67.6
R_{490}	$= -0.0595MSS^2 + 1.702MSS - 0.431$	68.1
R_{510}	$= -0.0625MSS^2 + 1.83MSS - 0.562$	73.1
R_{555}	$= -0.065MSS^2 + 2.062MSS - 0.916$	77.2
R_{665}	$= -0.0051MSS^2 + 0.6893MSS - 0.880$	91.8

Figure 4.5 showed reflectance to increase with increasing MSS for all wavelengths and this is confirmed in the relationships in table 4.5. This relationship, however, is weaker for blue wavelengths, improving substantially with increasing wavelength with a greater proportion of explained variability in the regression equations. This may be caused by preferential absorption at short wavelengths by all particulate and dissolved materials. The influence of yellow substance on reflectance will be most pronounced in the blue region of the spectrum and least pronounced in the red. Phytoplankton would also have greatest influence on reflectance at 443 nm. The minimal influence of yellow substance at longer wavelengths suggests that an

algorithm may have a greater probability of success if the wavelengths were selected from the red region of the spectrum.

The strongest relationship was found between MSS and reflectance in the red waveband (665 nm). Figure 4.8 shows the observed relationship between MSS concentrations and irradiance reflectance at 665 nm measured at all optical stations. A quadratic function of the form described in table 4.6 describes nearly 92% of the variability in R_{665}.
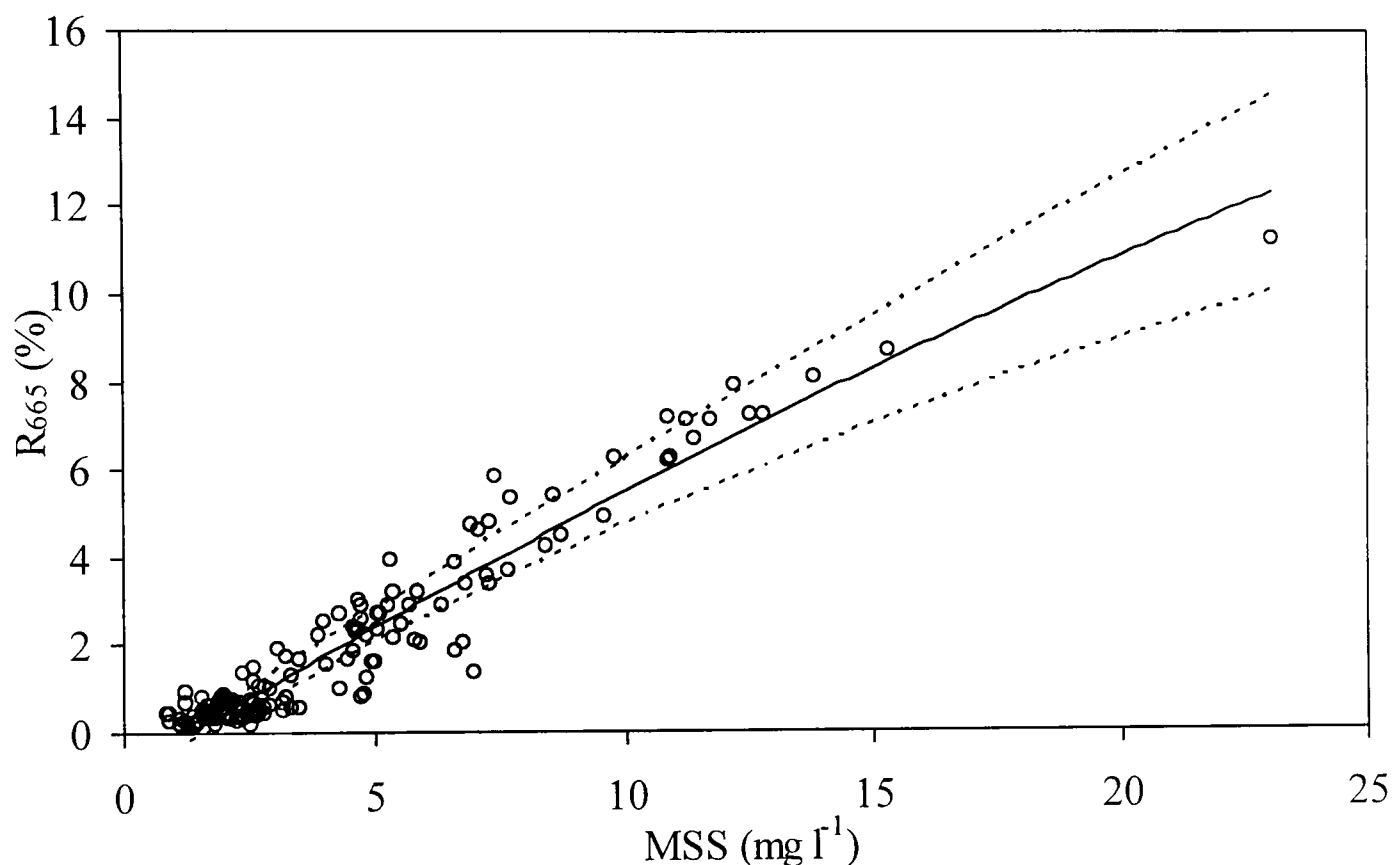
Figure 4.8: **Relationship between Mineral Suspended Sediment concentrations (MSS) and irradiance reflectance at 665 nm (R_{665}). Dashed line gives ± 1 S.E. of predicted R_{665}. Least squares best fit obeys the form $R_{665} = \alpha MSS^2 + \beta MSS + \gamma$.**

Table 4.6: **Statistics relevant to the regression analysis between R_{665} and MSS.**

$R_{665} = \alpha MSS^2 + \beta MSS + \gamma$	
$R^2 = 91.8\%$, $p = 0.00$, $n = 144$	
$\alpha \pm$ S.E.	-0.00508 ± 0.0023
$\beta \pm$ S.E.	0.689 ± 0.0396
$\gamma \pm$ S. E.	-0.880 ± 0.124

Inverting the regression equation enables the estimate of MSS concentrations from any given R_{665}. An average percentage error in predicted MSS was calculated as the mean difference between measured and predicted MSS as a proportion of the measured MSS (equation 4.3)

$$\% \text{ Error} = \left[\sum \left(\frac{\sqrt{(MSS_{Meas} - MSS_{Pred})^2}}{MSS_{Meas}} \right) \right] \Big/ n \qquad (4.3)$$

where MSS_{Meas} and MSS_{Pred} are the measured and predicted MSS concentrations respectively and n is the total number of observations. This method leads to an average percentage difference between predicted and observed MSS concentrations of 21.3%. For comparison, the direct gravimetric measurement of MSS concentrations in this study resulted in an average percentage standard error of the mean of triplicate observations of 12.4%.

Assuming no effect from other constituents and negligible scattering by water at this wavelength, R_{665} can be expressed simply in terms of the optical properties of MSS and absorption by water, a_W (equation 4.4).

$$R_{665} \approx \frac{b_b^*{}_{MSS}[MSS]}{(a_W + a^*{}_{MSS}[MSS])} \qquad (4.4)$$

where $b_b^*{}_{MSS}$ and $a^*{}_{MSS}$ are the MSS specific backscattering and absorption coefficients respectively. At small concentrations of MSS, equation 4.4 is dominated by the effect of water. As MSS increases, so does the contribution of a_{MSS} to total absorption, therefore reducing the gradient of the relationship between R and MSS. If MSS continues to rise, the absorption term will be dominated by a_{MSS} and R can be written as:

$$R_{665} \approx \frac{b_b^*{}_{MSS}[MSS]}{a^*{}_{MSS}[MSS]} \approx \frac{b_b^*{}_{MSS}}{a^*{}_{MSS}} \qquad (4.5)$$

Consequently, at high MSS concentrations, reflectance becomes independent of the

concentration of MSS and the relationship between R_{665} and MSS saturates. This trend can be seen in figure 4.8, where the gradient reduces with increasing MSS. For the conditions presented in table 4.6, the relationship between R_{665} and MSS would saturate at $\dfrac{d R_{665}}{d MSS} = 0$, when MSS = 59.4 mg l^{-1}, producing a reflectance of 20.1%. This represents the upper limit of MSS concentrations that this algorithm could potentially be valid for, although care should be taken in interpreting results above the range of MSS used in its development (up to 23 mg l^{-1}).

Two important observations should be noted from figure 4.8; firstly, the large spread in the data points, particularly at reflectances lower than around 2% and secondly, the presence of a significant x-axis intercept, suggesting that a baseline MSS concentration of 1.36 mg l^{-1} exists. This observed offset is physically unrealistic; according to the theory, reflectance at red wavelengths should approach zero in the absence of all particulate matter. An attempt was made to constrain the relationship by forcing it through the origin but this considerably reduced the percentage of the variance explained by the relationship. Initially it was suggested that these two features were simply the result of measurement errors. However, results presented in Chapter Five will show them to have greater significance in the underlying relationship between MSS and R_{665}.

4.5   A Simple Reflectance Model

4.5.1   Model Parameter Definitions

In an effort to re-create the relationship between R_{665} and MSS from theory, and to further understand the effects of dissolved and particulate matter on R_{665}, a simple reflectance model was constructed. The model was derived from the Gordon *et al.* (1975) solution to the radiative transfer equation which allows reflectance to be described in terms of its inherent optical properties, absorption and backscattering according to equation 4.6 (Gordon *et al.*,1975; Morel and Prieur, 1977; Kirk, 1981; Kirk, 1984). The model, therefore, incorporates the absorption and scattering spectra derived in section 4.2.

$$R(0^-,\lambda) = f \frac{b_b(\lambda)}{a(\lambda)}$$

(4.6)

The contribution of different materials to the total absorption and scattering coefficients is additive, therefore equation 4.6 can be re-written in terms of the specific absorption (a^*) and backscattering coefficients (b_b^*) for the individual dissolved and particulate materials where

$$a = a_W + a^*_{YS}[YS] + a^*_{MSS}[MSS] + a^*_C[C] \qquad (4.7)$$

and

$$b_b = b_b^*{}_W + b_b^*{}_{MSS}[MSS] + b_b^*{}_C[C] \qquad (4.8)$$

The subscripts W, MSS, YS and C refer to water, mineral suspended sediments, yellow substance and phytoplankton respectively and the square brackets represent the concentrations of each substance.

Backscattering was not measured and was therefore calculated from the total scattering coefficients by assuming a backscattering efficiency factor, b_b/b. This relationship between scattering and backscattering varies for each of the in-water constituents. For MSS, the Petzold function for turbid waters was assumed (see Kirk, 1981), whereas for pure water, the backscattering coefficient is simply half of the total scattering because of the symmetrical nature of the volume scattering function. The backscattering ratio for phytoplankton is known to be considerably lower than that for mineral sediments and for this model, was given a value of 0.005, which was taken from a range of values in Bricaud *et al.* (1983).

The model is a simple one that only deals with elastic scattering (that is scattering where there is no wavelength (energy) change upon scattering). Inelastic scattering (such as fluorescence and Raman scattering), where the scattered photons have longer wavelengths than the incident photon, is not considered in this study because it is assumed to be negligible compared with the scattering by mineral particles. It is emphasised, however, that it may play a significant part in determining reflectance in open ocean optics.

The factor f relating reflectance to absorption and backscattering is re-written here as $C(\mu_0)$, and is a function of μ_0, the average cosine of the angle the photons make with the vertical beneath the water after Kirk (1981):

$$C(\mu_0) = 0.975 - 0.629\mu_0 \tag{4.9}$$

Values of μ_0 were calculated for each optical station from details of the solar zenith angle and the local atmospheric conditions at the time of sampling according to the method described in Chapter Three. Results are presented both for direct light, assuming clear skies, and for more realistic atmospheric conditions based on the observed cloud cover at the time on station. With knowledge of μ_0, the factor $C(\mu_0)$ can be estimated for each station to see how seasonal and geographical variations in sun angle may influence the measured R_{665}. Table 4.7 provides details of the parameters calculated, showing the range of values observed over all stations. The parameter $C(\mu_0)$ is considerably different from the value of 0.33 commonly adopted in optical studies which assumes the sun to be at zenith and therefore $\mu_0 = 1$ (Gordon et al., 1975; Morel and Prieur, 1977).

In this study, the maximum observed solar elevation was 61° which resulted in a value of $C(\mu_0)$ of 0.389. For small solar elevations, with the sun low in the sky, photons travel more obliquely as represented by the lower values of μ_0. The latitude at which this study was carried out means that the sun was never at zenith and therefore the factor $C(\mu_0)$ never reached its minimum of 0.33. Furthermore, frequent overcast conditions also acted to reduce the range of $C(\mu_0)$ compared with those values calculated assuming clear skies and direct light.

Table 4.7: Summary of calculated μ_0 and $C(\mu_0)$ for all optical stations under both direct light conditions and those based on cloud cover observations.

	Solar Elevation (degrees)	Direct Light		Observed Light	
		μ_0	Resulting $C(\mu_0)$	μ_0	Resulting $C(\mu_0)$
Average	42.44	0.833	0.451	0.835	0.450
Maximum	61.02	0.9313	0.389	0.885	0.419
Minimum	15.06	0.688	0.543	0.763	0.495

For general model use with unspecified daylight conditions, an average μ_0 for the study period was taken, resulting in a value of $C(\mu_0)$ of 0.45 (see table 4.7). When reproducing reflectances at each station, μ_0 was calculated specifically and the adapted relationship between R and absorption and backscattering was used.

The complete reflectance model is that presented in equation 4.10. A Fortran programme was written to run the model; required inputs were the concentrations of MSS, C and YS and skylight parameters for the calculation of $C(\mu_0)$.

$$R = (0.975 - 0.629\mu_0)\frac{0.5b_W + 0.019b^*_{MSS}[MSS] + 0.005b^*_C[C]}{a_W + a^*_{YS}[YS] + a^*_{MSS}[MSS] + a^*_C[C]} \qquad (4.10)$$

where each of the inherent optical properties took the values derived in section 4.2 and presented in table 4.8 for 665 nm.

Table 4.8: Reflectance model parameter definitions and sources. All values at 665 nm.

Model Parameter	Source
$b^*_{MSS} = 0.411$ m^2 g^{-1}	Derived from PRR600 and measured MSS
$b^*_C = 0.0293$ m^2 mg^{-1}	Derived from PRR600 and measured C
$b_W = 0.0008$ m^{-1}	Smith and Baker (1981)
$a^*_C = 0.01987$ m^2 mg^{-1}	Derived from PRR600 and measured MSS
$a^*_{MSS} = 0.0108$ m^2 g^{-1}	Derived from PRR600 and measured C
$a_W = 0.415$ m^{-1}	Smith and Baker (1981)
$a^*_{YS} = 0.0244$	Measured using spectrophotometry
b_b/b (MSS) = 0.019	Petzold (1972)
b_b/b (C) = 0.005	Taken from range of values in Bricaud *et al.* (1983)
b_b/b (W) = 0.5	Morel (1974)

4.5.2 Model Results

The reflectance model was first used in the forward modelling mode; calculating reflectance on the basis of known concentrations of the optically active constituents (YS, C and MSS) and the skylight properties. Figure 4.9 presents a plot of measured

versus modelled reflectance at 665 nm. The average percentage difference between measured and modelled R_{665} is 165%, although this is dominated by the variability at small R_{665} (decreases from 287% for measured R_{665} < 1% to 46% for R_{665} >1%). Care should be taken in interpreting these percentage errors, since reflectance is also expressed as a percentage. For clarity, a 10% error in a reflectance of 5% is 0.5%.

Although at low reflectances the model predictions are in considerable error, it was felt that for the full range of observed R_{665}, there was a good overall agreement, with points close to a 1:1 relationship. Whilst this level of uncertainty may not be satisfactorily small for predictive purposes, it was felt that the reasonable 1:1 agreement was sufficient to allow the qualitative interpretation of model simulations.
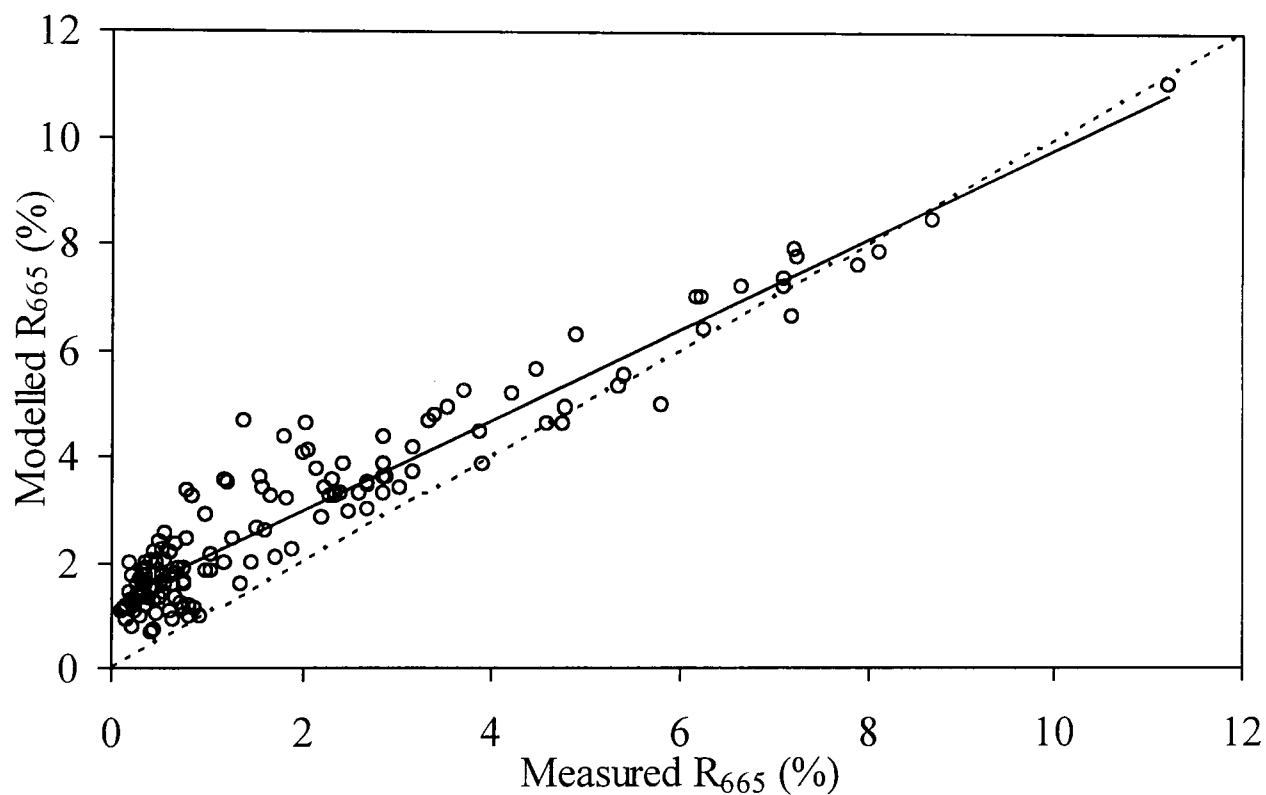
Figure 4.9: Relationship between modelled R_{665} and R_{665} as measured by the PRR600 for all stations.

The model was therefore used to gain further understanding of how the presence of phytoplankton and yellow substance may influence the relationship between R_{665} and MSS and thus give an idea of the robustness of the algorithm in table 4.6. Whilst the waters sampled for the development of the MSS algorithm only contained MSS up to 25 mg l^{-1}, it was thought to be of value to model the behaviour of R_{665} for MSS up to 100 mg l^{-1}. It is acknowledged that this may not be wholly appropriate on the basis that the IOPs used in the model were obtained on water samples with MSS below

25 mg l^{-1} and thus the results above this limit should be interpreted with caution.

The model was used to determine the relationship between R_{665} and MSS for a hypothetical water column in which concentrations of C and YS were varied. The model was run firstly for conditions of zero YS with C ranging from zero to 20 μg l^{-1} (figure 4.10). Because of the chlorophyll absorption band evident near 665 nm (figure 4.1), it was expected that phytoplankton would cause considerable variability in the relationship between mineral sediments and reflectance. The series of curves in figure 4.10 reveal that for a fixed concentration of MSS, increasing concentrations of C result in a decrease in R_{665}, representing the increasing absorption by phytoplankton pigments at 665 nm. Figure 4.10b shows the same data on a log plot which highlights the variability at low reflectances. Figure 4.10b shows that at zero MSS, R_{665} actually increases with increasing C, a counter-intuitive trend since phytoplankton pigments are strong absorbers of light at this wavelength. This trend occurs simply because of the dominance of absorption by water, as demonstrated in the positive numerator of equation 4.11. The rate of change in reflectance decreases as C increases as a result of the increasing role of absorption by C relative to absorption by water, as indicated by the denominator in equation 4.11.

$$\frac{dR}{dC} = \frac{C(\mu_0)a_w b_b{}^* c - C(\mu_0) b_{bw} a^* c}{a_w{}^2 + a^*{}_c{}^2 [C]^2 + 2 a_w a^*{}_c [C]} \tag{4.11}$$

This trend continues at very low concentrations of MSS up to a point where the relationship reverses and reflectance begins to decrease with increasing C. The cross-over of the curves in figure 4.10b occurs as a consequence of an equilibrium having been established among the optical properties of W, MSS and C, such that any change in C causes no variation in reflectance. For these model conditions, this pivot point occurs at a concentration of MSS of 0.344 mg l^{-1}, calculated as the value of MSS at $\frac{dR}{dC} = 0$ (equation 4.12).

$$\frac{dR}{dC} = 0 \text{ when MSS} = \frac{b_{bw} a^* c - a_w b_b{}^* c}{a^*{}_{MSS} b_b{}^* c - b_b{}^*{}_{MSS} a^* c} \tag{4.12}$$
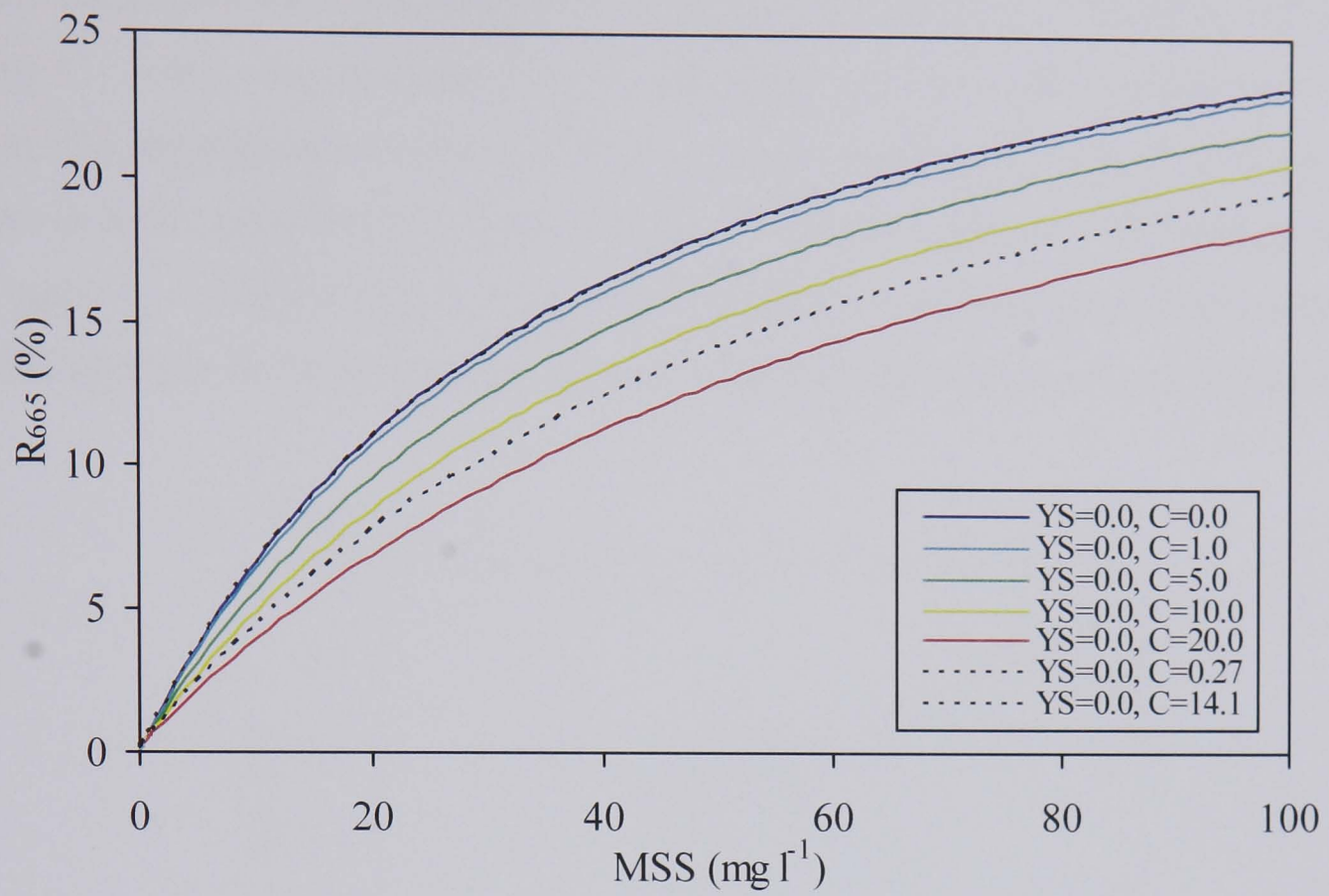
Figure 4.10a and b: Relationship between modelled R_{665} and MSS illustrating the effect of increasing concentrations of phytoplankton pigments (C). Dashed lines indicate maximum and minimum C observed in this study.

Figure 4.11 shows the relationship between R_{665} and C for stations dominated by C (MSS:C < 0.2) and confirms the tendency for R to increase with C, although with the *in situ* data, the trend of increasing R with increasing C is evident for MSS as high as 2 mg l^{-1}. This suggests there may be uncertainty in the model parameters; most likely the phytoplankton optical properties. This uncertainty could be because of errors in either experimental procedures or assumptions made in the determination of a^*_C and b^*_C, or simply because of natural variability in the absorption and scattering coefficients due to variations in, for example, phytoplankton species and cell size.
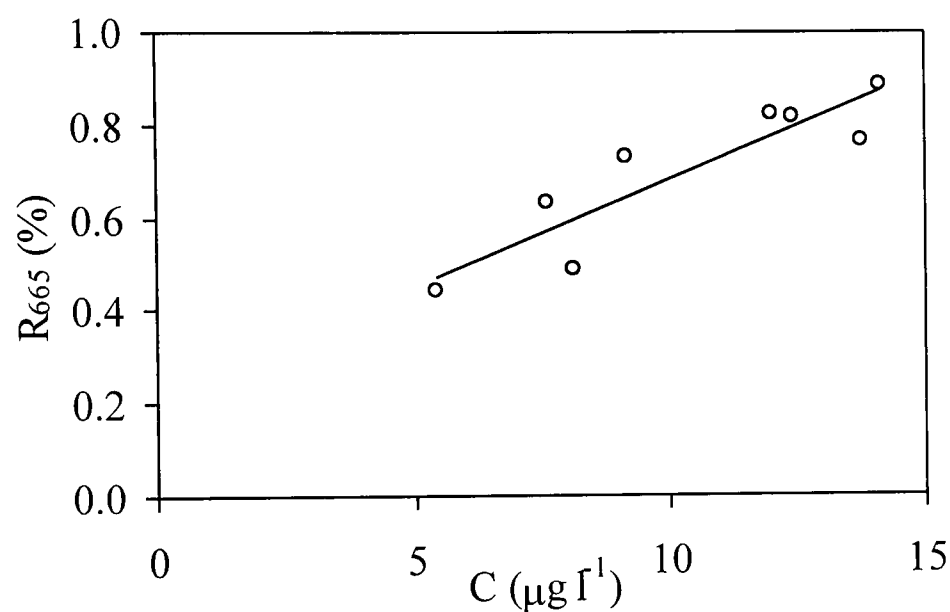
Figure 4.11: Relationship between R_{665} and C, for stations where MSS:C is less than 0.2. Best fit relationship is given by: $R_{665} = 0.0456C + 0.2262$ ($R^2 = 80.1\%$) .

To see whether or not these modelled trends were apparent in the data used in the MSS algorithm, the relationship between MSS and R_{665} was studied with data points categorised according to the concentration of C measured at each station (figure 4.12). Stations with the highest pigment concentrations tended to have the lowest reflectance, although these also had the lowest MSS concentration. For any single concentration of MSS, there did not appear to be a systematic decrease in reflectance with increasing C, as might be expected due to enhanced absorption.
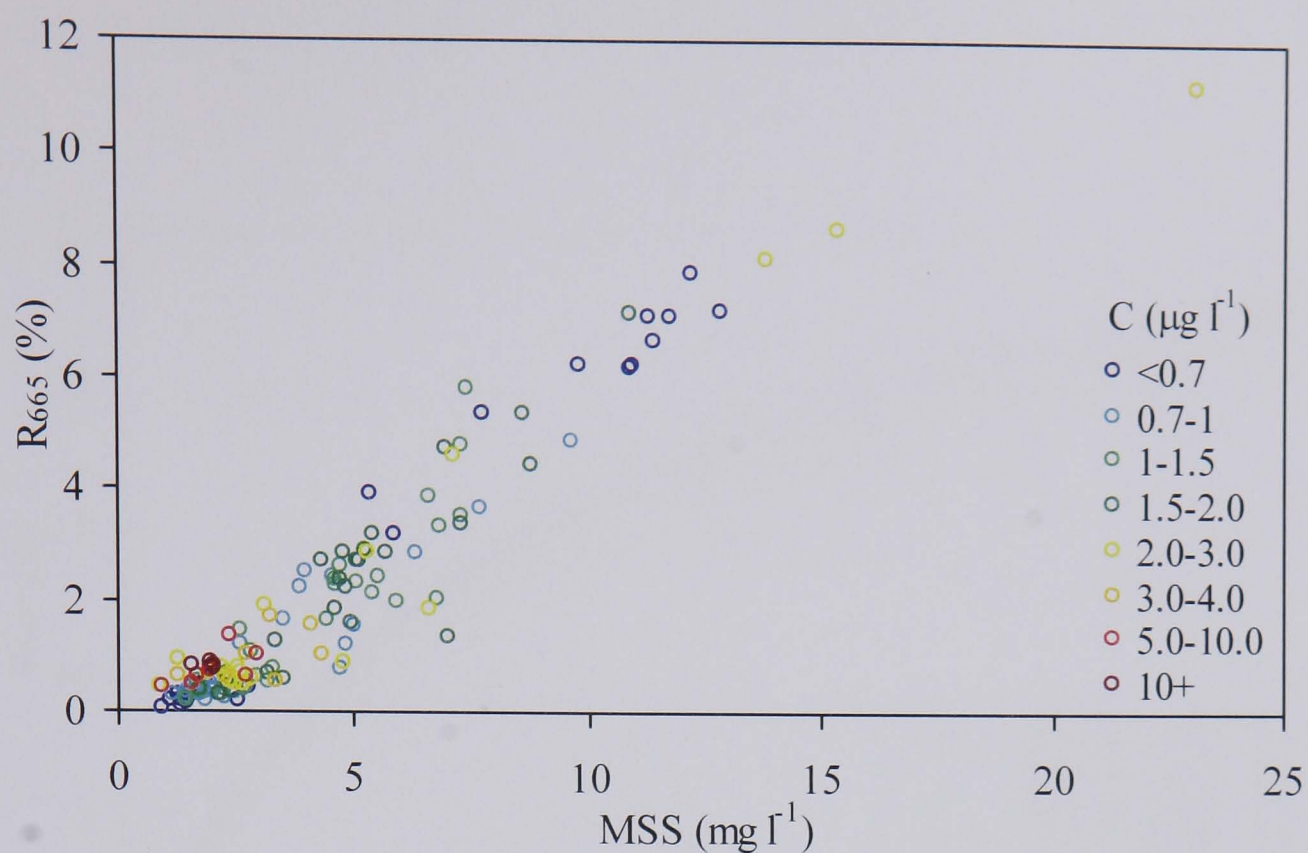
Figure 4.12: Relationship between MSS and R_{665} categorised according to the measured pigment concentration at each station.

Although it appears that for moderate phytoplankton populations in a scattering dominated environment, the simple reflectance algorithm may still work, it is expected that the algorithm may fail if concentrations of C exceed those observed in this study. Furthermore, the algorithm may fail when phytoplankton such as coccolithophores are abundant. Detached coccoliths are very efficient scatterers and the enhanced backscatter results in highly reflective water in both visible and NIR wavelengths (Moore *et al.*, 1999). A simple reflectance algorithm would overestimate sediment concentrations under these circumstances.

Figure 4.13 shows the model results for conditions of zero C with YS ranging from zero to 5 m^{-1}. This series of curves highlight the minimal impact of yellow substance on reflectance at 665 nm, with very little deviation from the line of zero concentration. Increasing YS causes a small decrease in the reflectance at any particular concentration of MSS. This is a consequence of the known spectral absorption properties of yellow substance, being strongest in the shorter blue wavelengths and with almost negligible absorption in the red portion of the spectrum. The insensitivity of these longer wavelengths to dissolved organic material provides greater potential for the accurate estimation of particulate matter than shorter wavelengths.
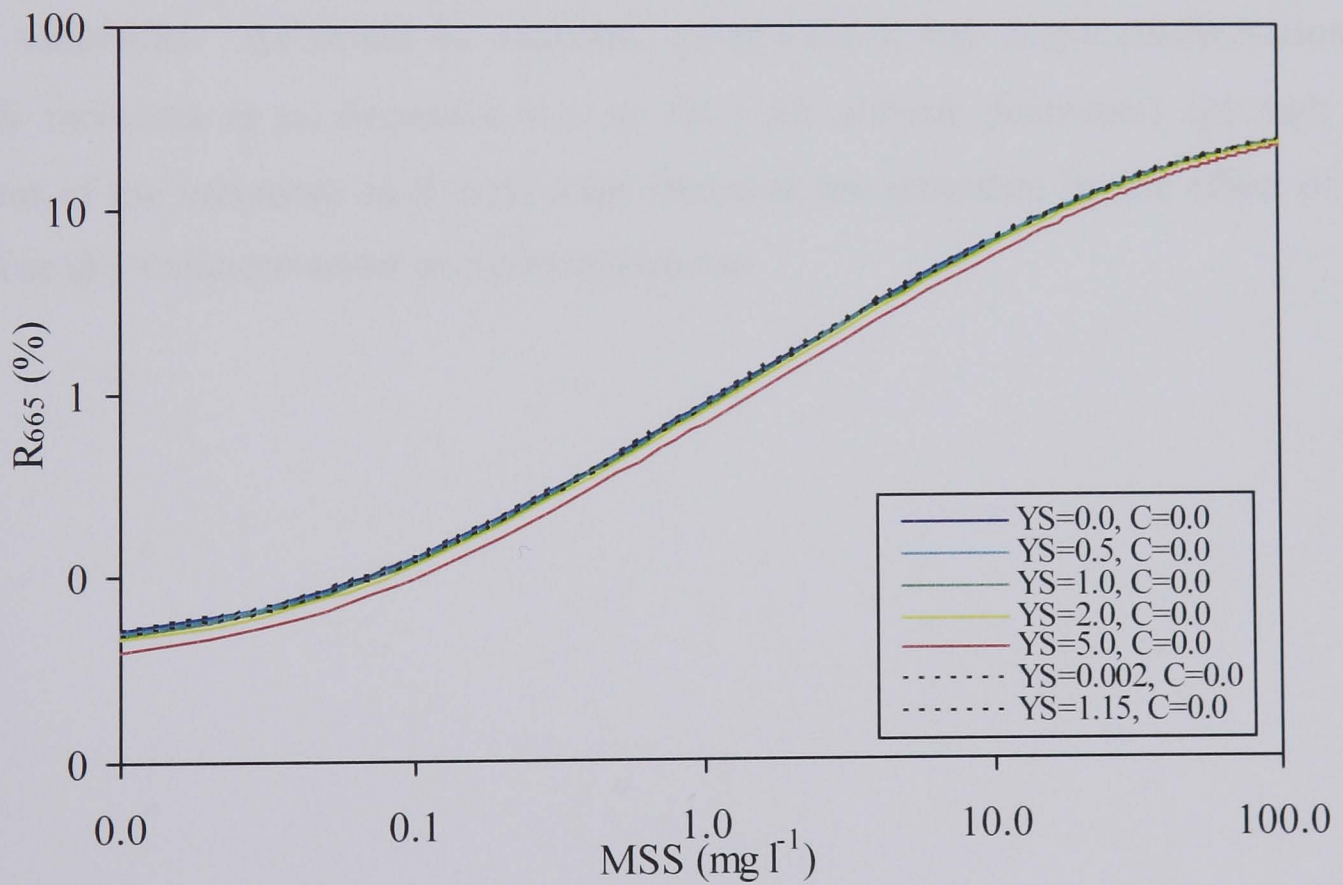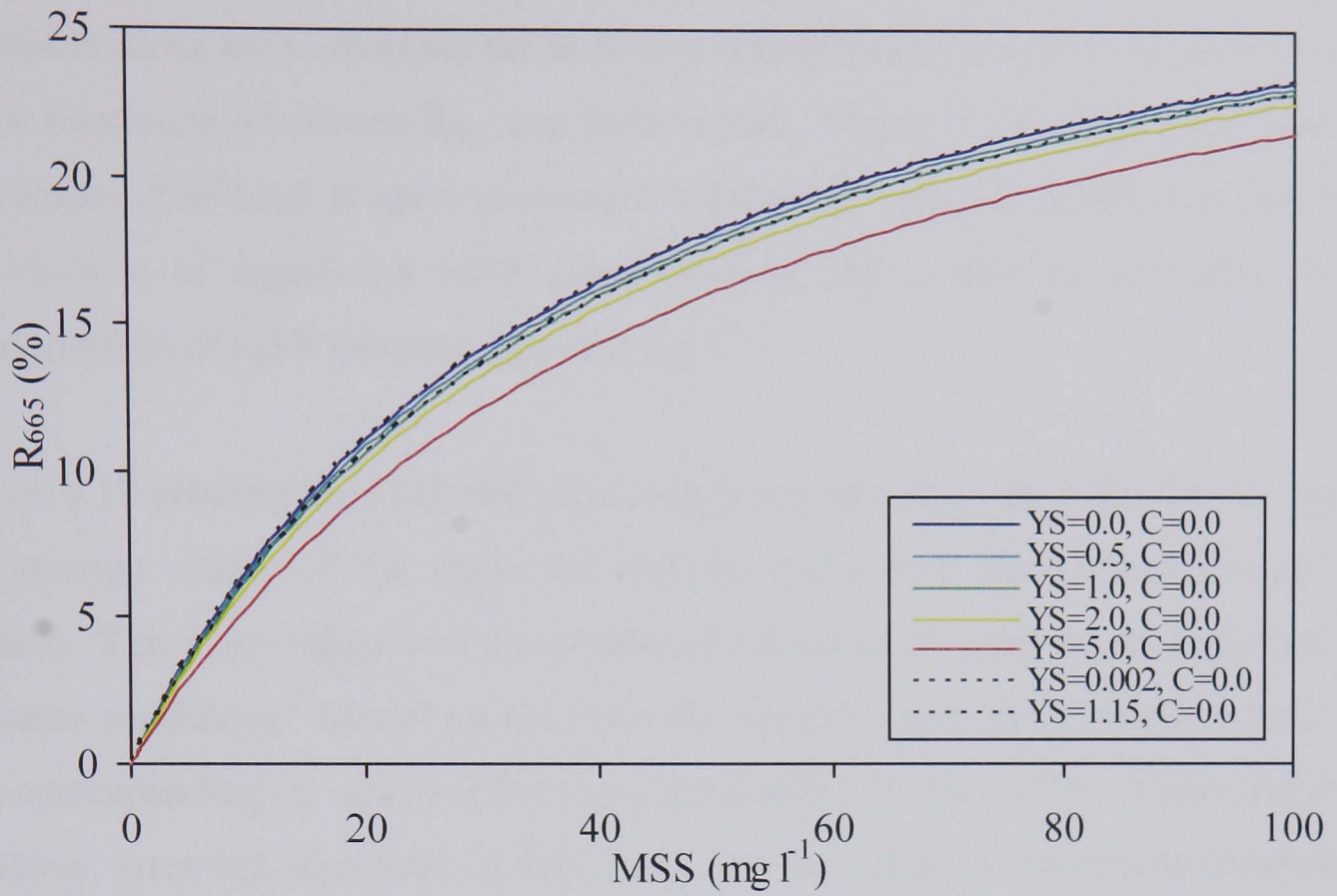
Figure 4.13a and b: Relationship between modelled R$_{665}$ and MSS, illustrating the effect of increasing concentrations of yellow substance (YS). Dashed lines indicate maximum and minimum YS observed in this study.

Figure 4.14 shows the response of R_{665} to the combination of both C and YS, for a range of concentrations. Whilst yellow substance was shown to have only a small effect on reflectance at this wavelength, it can be seen that its contribution to absorption does act to increase the sediment concentration at which the pivotal point in the relationship between R_{665} and MSS occurs. Figure 4.13b shows that although reflectance at 665 nm is quite sensitive to changes in optically active constituents in the absence of significant MSS concentrations, the sensitivity decreases as the concentration of MSS increases above 2 mg l^{-1}.

Figure 4.15 presents the modelled relationship between R_{665} and MSS for varying μ_0, the average cosine of the angle the photons make with the vertical beneath the surface. This is an indicator of the combined effects of the solar zenith angle and sky radiance conditions. Model results show the variation in R for μ_0 ranging from 1 to 0.6, corresponding to values of the $C(\mu_0)$ parameter of 0.346-0.598. These extremes, however, were not measured in this study; the full range of conditions observed in the Irish Sea is indicated by the dashed lines in figure 4.15 and show considerably less variability. As would be expected, reflectance at any single concentration of MSS increases as μ_0 decreases (i.e. as the solar altitude decreases) although the extent of the variations in R with solar elevation are smoothed by the effect of the diffuse sky radiation under overcast conditions.
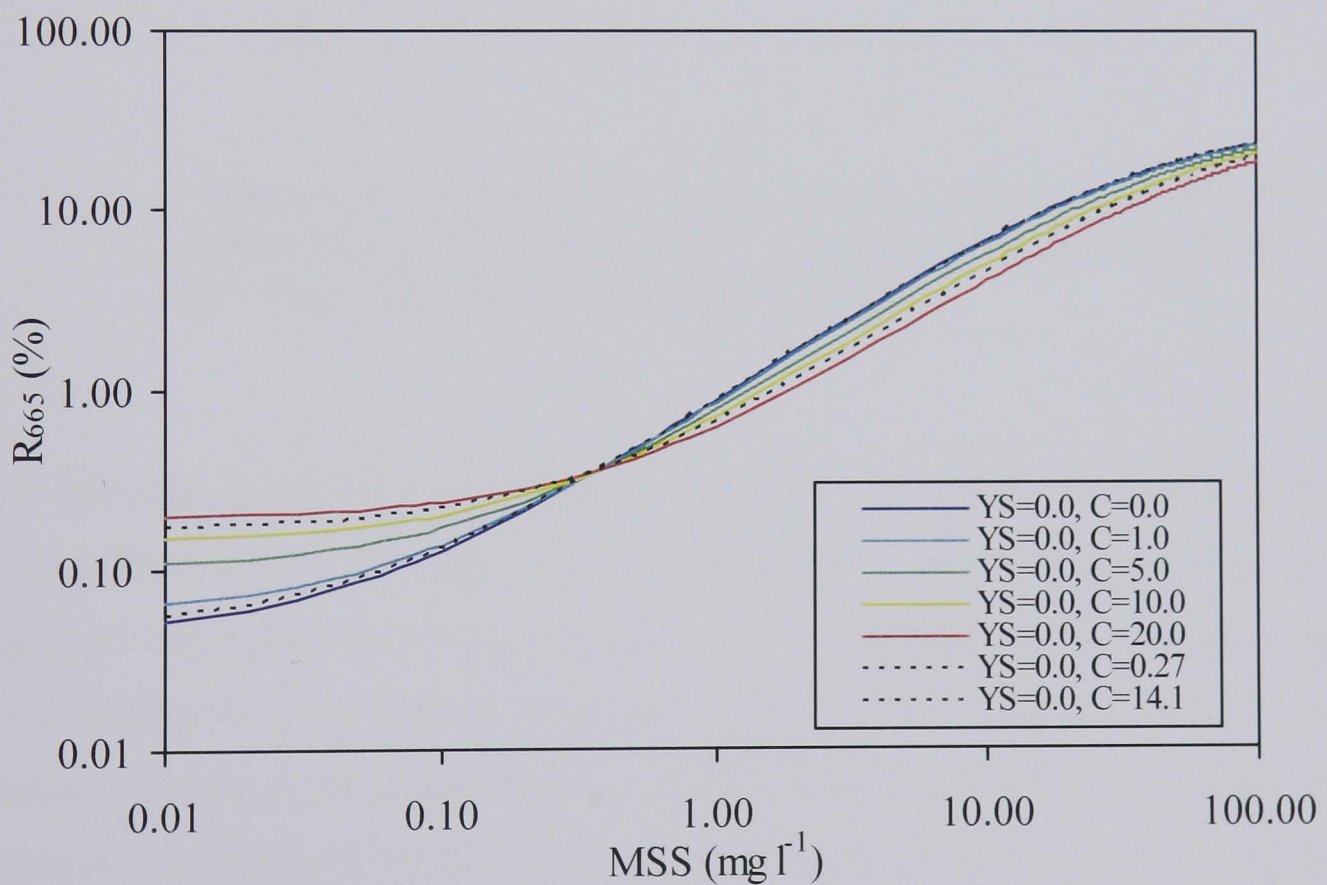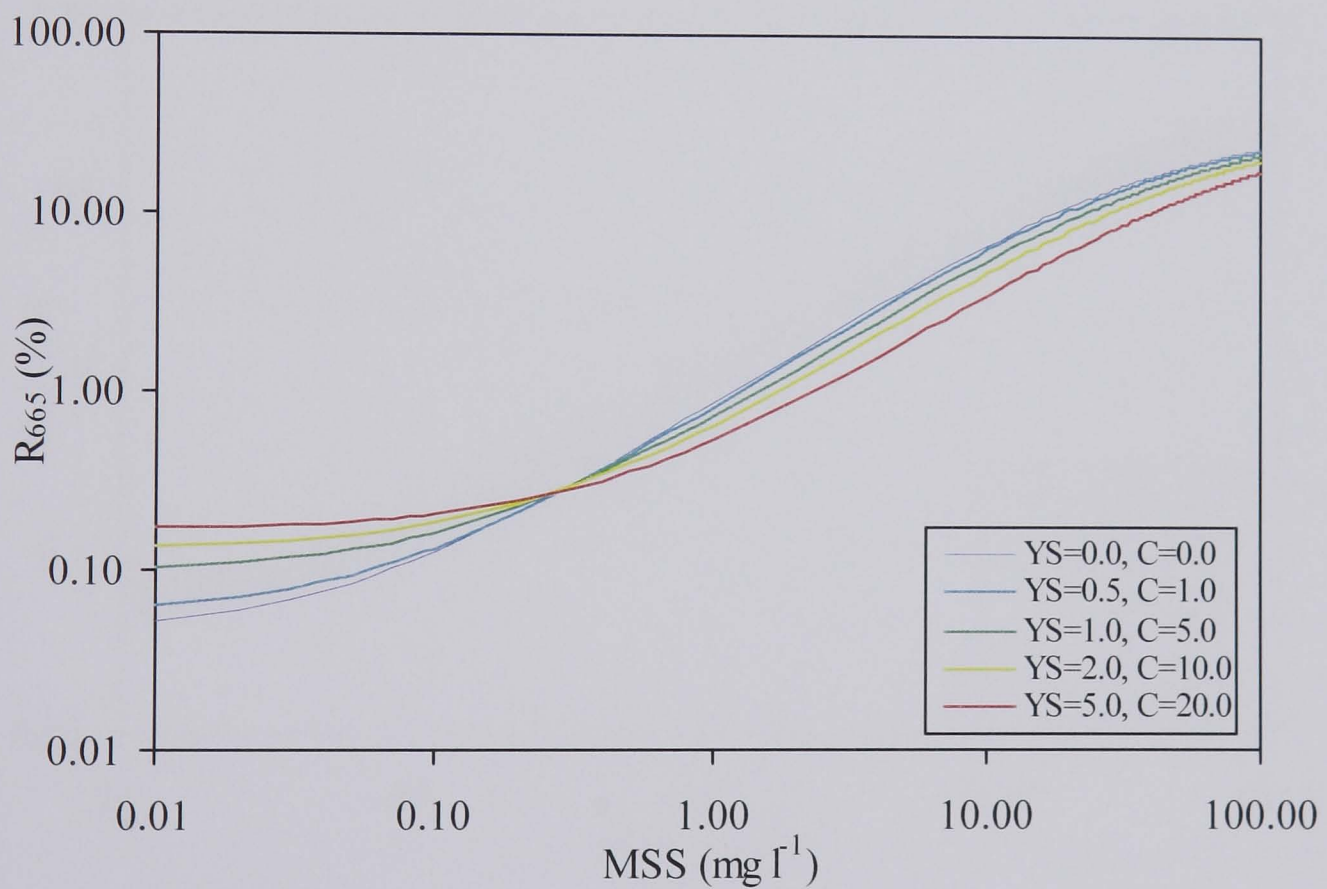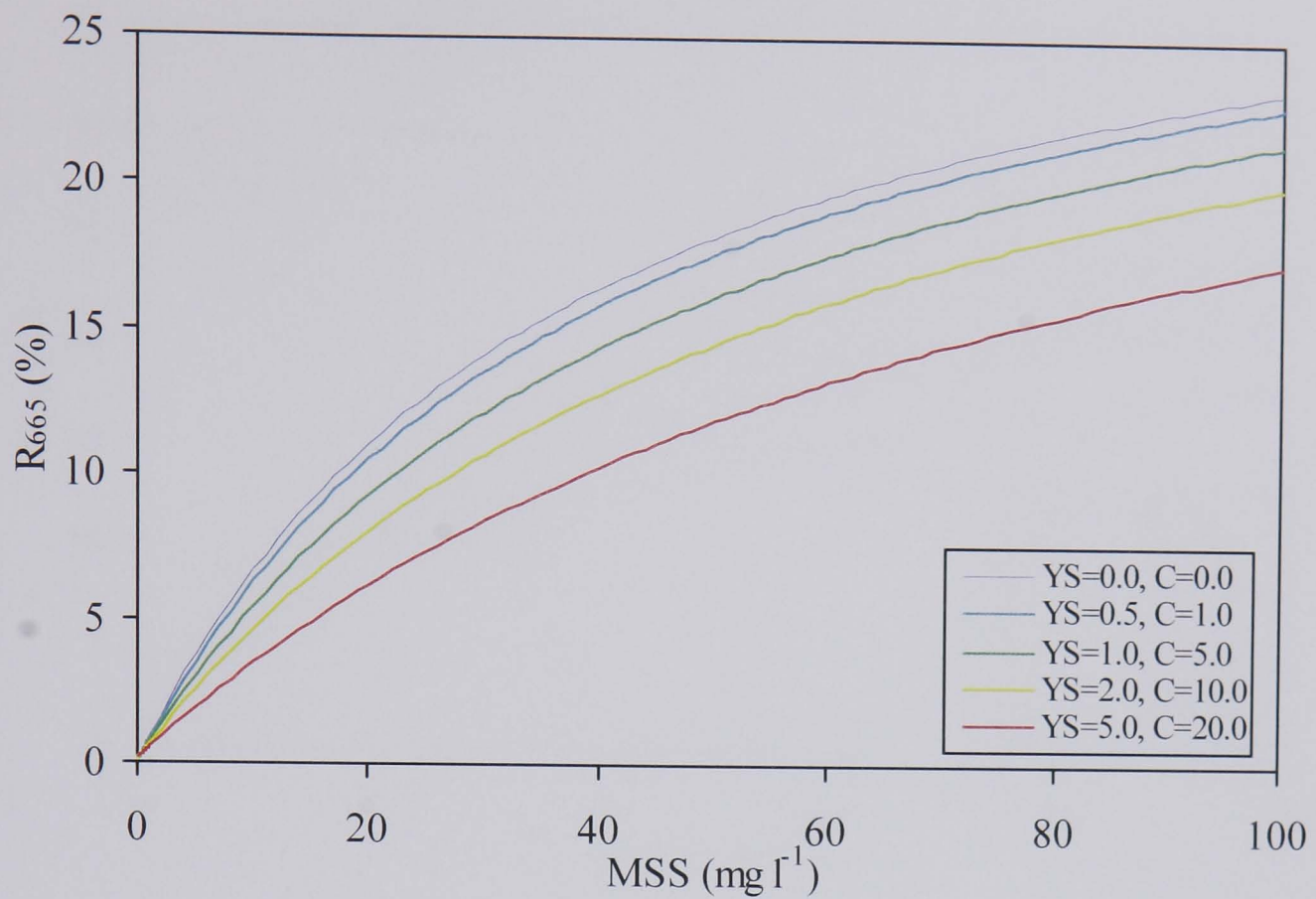
Figure 4.14a and b: Relationship between modelled R$_{665}$ and MSS, illustrating the combined effect of increasing concentrations of both phytoplankton pigments and yellow substance.
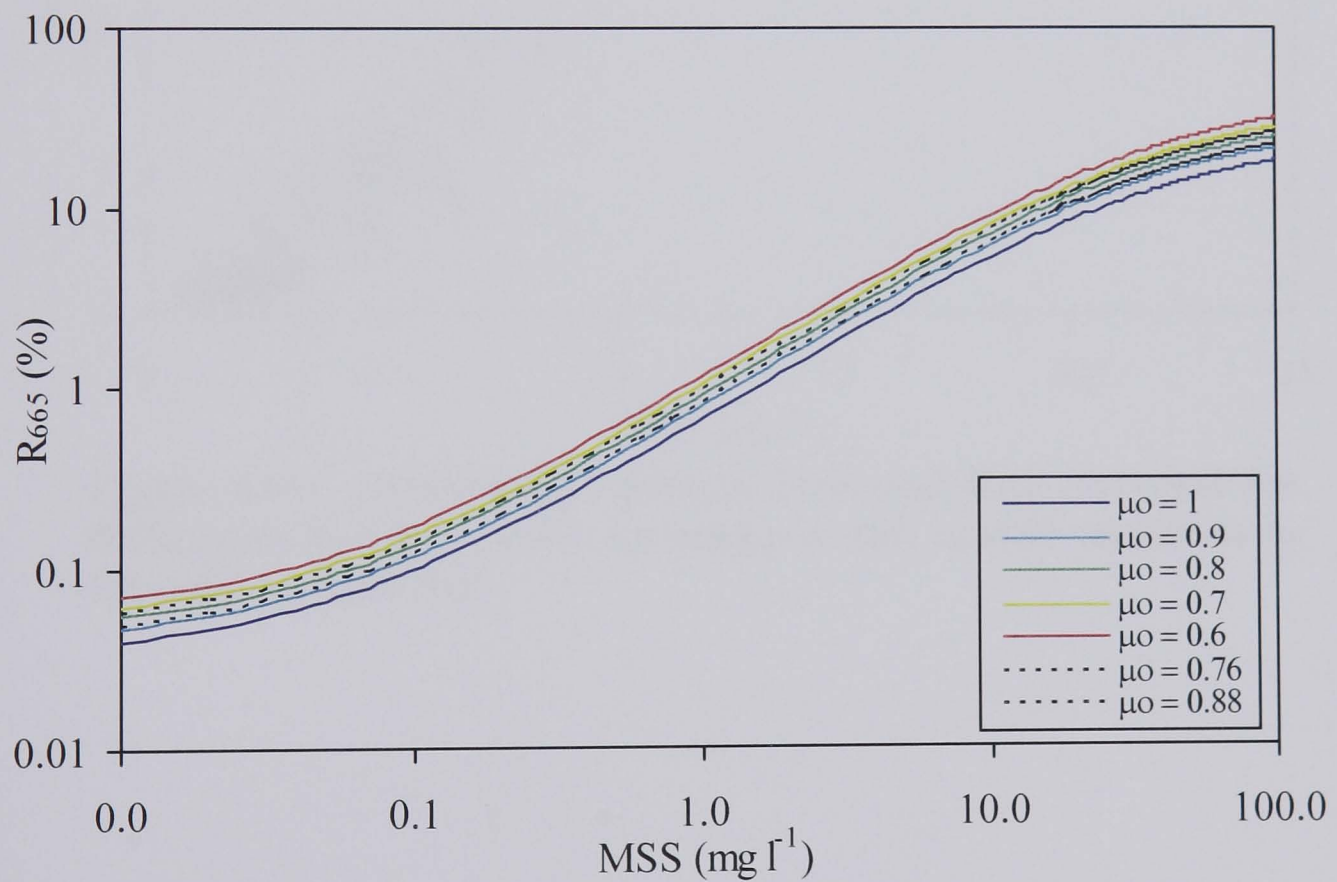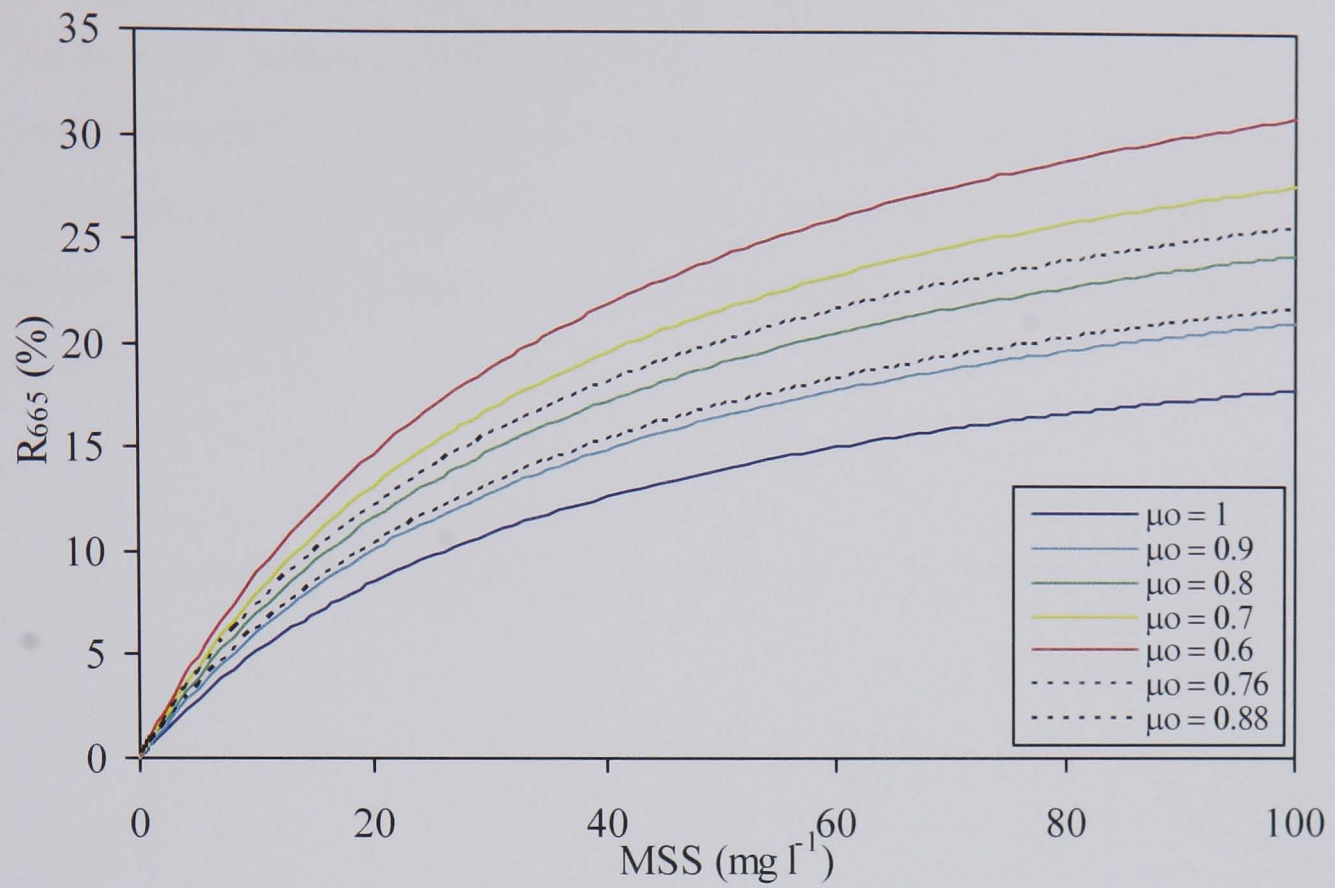
Figure 4.15a and b: Relationship between modelled R_{665} and MSS, illustrating the effect of varying μ_0. Dashed lines indicate maximum and minimum μ_0 observed in this study.

Figure 4.16 shows a plot of $R_{665}/C(\mu_0)$ (i.e. b_b/a according to the relationship R = $C(\mu_0)b_b/a$) against MSS. This figure shows no reduction in the spread in the data points, suggesting that the factor $C(\mu_0)$ is not the primary source of the variability in the relationship between reflectance and MSS. The fact that there is still considerable variability in the data points in a plot of IOPs against MSS suggests that the inconsistencies may be caused by intrinsic variations in the inherent optical properties. This is the subject of the following chapter and will not be investigated further here.
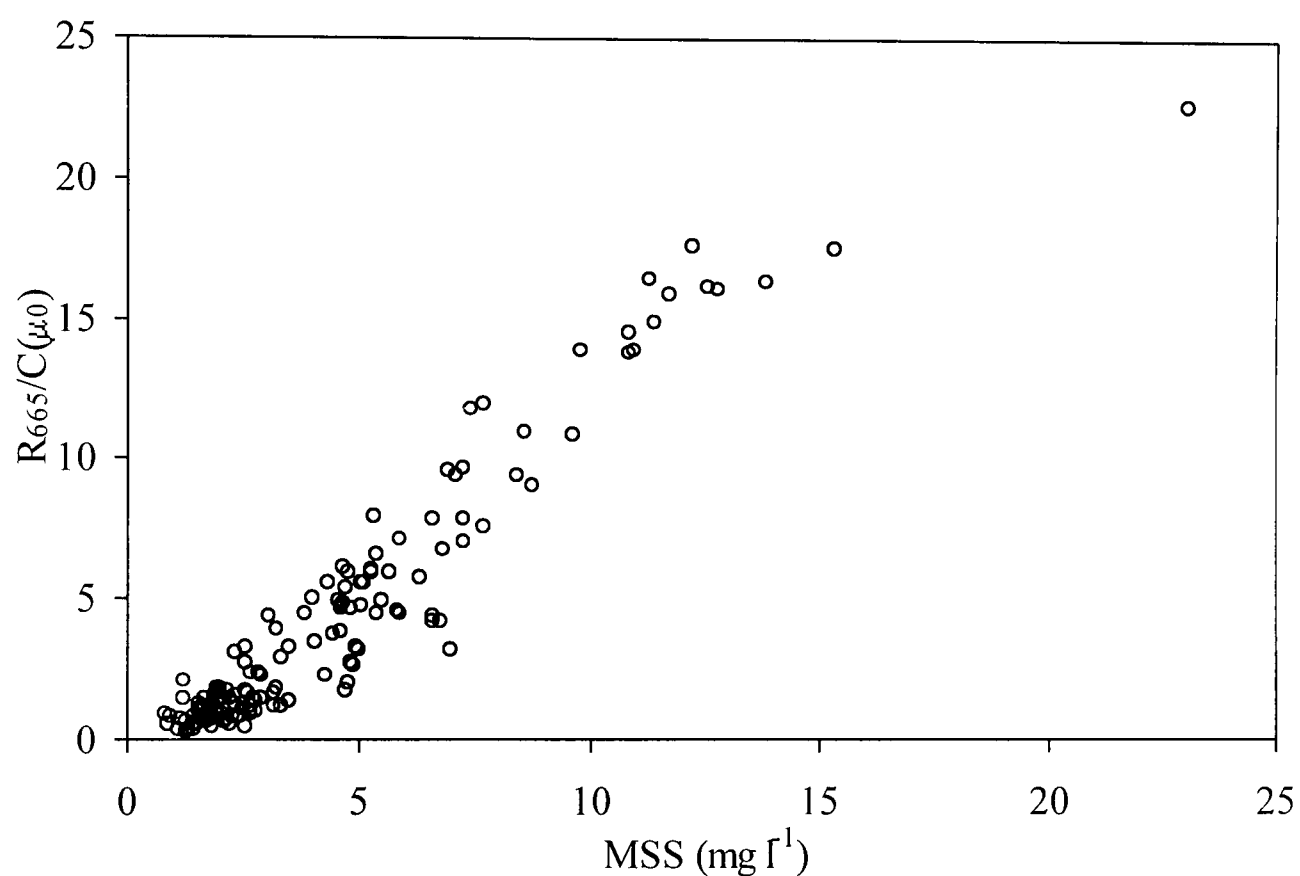
Figure 4.16: Relationship between MSS and R_{665} corrected for differences in $C(\mu_0)$ caused by temporal and spatial variations in the incident light flux.

4.6   Discussion

4.6.1   Inherent Optical Properties in Optical Modelling

Optical models similar to the one used in this study have been used by, for example, Carder and Steward (1985), Sathyendranath *et al.* (1989), Lee *et al.* (1994), Bukata *et al.* (1995) and Kutser *et al.* (2001). The models differ both in the number of optically active constituents used in the calculation of absorption and scattering and the numerical values of the concentration-specific IOPS. Many of the published reflectance models have been derived for Case 1 waters and therefore the absorption and scattering of yellow substance and total suspended matter are often expressed as a function of chlorophyll concentration (Carder and Steward, 1985; Sathyendranath *et al.*, 1989). This is acceptable in oceanic Case 1 waters where these components co-vary but not in coastal and inland waters where components are not in correlation with chlorophyll (or this correlation changes with space and time). The variability of the Irish Sea IOPs is discussed below with respect to those properties found in the literature for the same and other regions.

Inherent optical properties of MSS, C and YS have been presented that are in reasonable agreement with both independent measurements of absorption and scattering and with values in the literature. Absorption due to yellow substance has been studied extensively in waters ranging from open ocean to estuarine and freshwater lakes (e.g. Bricaud *et al.*, 1981; Carder *et al.*, 1989). For a wide range of seawaters, the coefficient describing the slope of the absorption coefficient, S, has been shown to vary from 0.01 to 0.02 with most lying between 0.012 and 0.015 (Kirk, 1994). The exponent obtained in this study (S=0.0165) is, therefore, in close agreement with many in the literature. The small standard error of the mean associated with this coefficient (± 5.45%) highlights the stability of the absorption properties of yellow substance in this region. The low concentrations that were measured in the Irish Sea (maximum of 1.15 m^{-1} but the majority below 0.4 m^{-1}) combined with its known absorption qualities show that yellow substance plays a relatively minor role in the optical properties of this region, particularly at longer wavelengths.

In contrast to yellow substance, little work has been published on the absorption properties of inorganic particles. Of those which are available, many suggest an

exponential decrease in absorption with increasing wavelength (Gallegos *et al.*, 1990; Bowers *et al.*, 1996; Bowers *et al.*, 1998). Results here are in qualitative agreement with those in the literature, however, quantitative comparisons are difficult since previous work has often assumed zero absorption at 750 nm (e.g. Bowers *et al.*, 1996). Whilst this assumption is certainly true for phytoplankton, it may not be the case for inorganic material (see Chapter Three).

The absorption due to organic material on the filters provided typical chlorophyll absorption spectra, with absorption peaks at approximately 670 and 430 nm. Absorption reached a maximum of 0.092 m^2 mg^{-1} at 440 nm. Bricaud *et al.* (1995) observed values of a^*_C spanning over more than one order of magnitude (0.01 to 0.18 m^2 mg^{-1}) on 185 samples from different regions. The absorption of the organic samples in this study, because of the method of combusting rather than bleaching filters, contained contributions from non-algal detrital matter and thus a^*_C may be greater than would be expected for phytoplankton pigments only. This variability may have been minimised by the process of normalising a^*_C at 750 nm. It may also be this normalisation process that resulted in the larger standard error observed in a^*_C at shorter wavelengths. It is thought that organic detritus has an exponential absorption spectrum (Bricaud and Stramski, 1990). By normalising to 750 nm, it is simply a constant factor that is removed and, therefore, any resulting error would increase as wavelength decreased, as was exhibited in this study.

Some of the inconsistency in absorption spectra measured in this study may also be natural variability in the samples, suggesting there may be both temporal and spatial variations in a^*_C. Absorption due to phytoplankton is known to be species-dependent, influenced by the size, shape and physiological state of the phytoplankton cells (Bricaud and Stramski, 1990; Mitchell and Kiefer, 1988; Bidigare *et al.*, 1990). Although for modelling purposes in the past, a^*_C has often been assumed as constant, it is now widely accepted as varying not only for individual species but also for natural phytoplankton assemblages. Nevertheless, in turbid waters, such variability may have only minimal effect on the observed reflectance, therefore, for simplicity, this study adopted an average value of a^*_C from observations in the Irish Sea. In order to improve the accuracy of model determinations in the presence of high chlorophyll concentrations, it may be necessary to carry out further work on the

absorption properties of phytoplankton in the Irish Sea, in relation to cell size and cellular chlorophyll concentrations (Bricaud *et al.*, 1995).

The average specific scattering coefficient for MSS derived in this study was 0.41 m^2 g^{-1}. Published values of scattering coefficients for mineral sediments range from 0.29 to 2.41 m^2 g^{-1} (Di Toro, 1978; Gallegos *et al.*, 1990; Vant, 1990; Whitlock *et al.*, 1981). The observed variability in published b$^*_{MSS}$ may be attributed to variations in factors such as particle size, shape and refractive index (Jerlov, 1976). These variations in particle scattering and their relevance in algorithm development will be discussed in more detail in Chapter Five. The specific scattering coefficients for phytoplankton in this study ranged from 0.022 to 0.032 m^2 mg^{-1}. Using the same technique, Weidemann and Bannister (1986) found an average chlorophyll-specific scattering coefficient of 0.08 m^2 mg^{-1} in Irondequoit Bay, whereas Bricaud *et al.* (1983) reported values ranging from 0.09 to 0.6 m^2 mg^{-1} for four marine phytoplankton species. Morel (1987) tabulated b$^*_C$ ranging from 0.04 m^2 mg^{-1} to 0.595 m^2 mg^{-1} for 22 species. The higher scattering coefficients of both Bricaud *et al.* (1983) and Morel (1987) were for a coccolithophore species which are renowned for their high scattering efficiency. Coefficients derived here are at the lower end of the determinations of b$^*_C$ found in the literature which may imply the dominance of large cells or high intracellular pigment concentrations.

Whilst in the past, optical models have concentrated on Case 1 waters, more recent effort has been directed at the modelling of the more complex turbid waters (Forget *et al.*, 1999; Woodruff *et al.*, 1999; Kutser *et al.*, 2001; Doxaran *et al.*, 2002a). In these sediment dominated Case 2 waters, scattering by phytoplankton is comparatively small such that it is frequently assumed negligible (e.g. Hakvoort *et al.*, 2002). In extreme turbidities, further simplification may be possible; Forget *et al.* (1999) neglected absorption by sediments, phytoplankton and detritus, as well as scattering by phytoplankton whilst modelling reflectance in turbid waters with sediment loads up to 234 mg l^{-1}. Sydor and Arnone (1997) showed no significant differences in turbid water reflectance spectra obtained using scattering coefficients from a range of phytoplankton species, despite differences in cell size of an order of magnitude. These observations highlight the insensitivity of the reflectance model to scattering by phytoplankton under scattering dominated conditions in turbid waters.

4.6.2 An algorithm for the determination of MSS

Algorithms for the determination of MSS concentrations have traditionally been based either on colour changes (through reflectance ratios) or brightness (through single-band reflectance). In this study, it was found that the measurement of single-band reflectance, rather than variations in colour through reflectance ratios, was the most reliable method for the derivation of suspended sediments in the Irish Sea. Early results published in Binding *et al.* (2003) and results concerning the wavelength of peak reflectance in this chapter showed that MSS algorithms based on colour ratios in the visible spectrum are susceptible to failure due to the presence of other optically active constituents. The level of success of colour ratios in the Irish Sea was shown to be strongly influenced by the degree to which mineral sediments dominated the inherent optical properties of the water body under study (Binding *et al.*, 2003). This limitation was not as clearly evident in a single-band reflectance algorithm, provided that the wavelength adopted was in the red portion of the spectrum.

The strong empirical relationship between MSS and R_{665} enabled predictions of MSS concentrations from irradiance reflectance with an average uncertainty of less than 22%. To put this into context, the main objective of the SeaWiFS project was to estimate chlorophyll concentrations in Case 1 waters within 35% error (Hooker *et al.* 1992). A similar level of accuracy for any in-water constituent in the more complex Case 2 waters is, therefore, assumed satisfactory.

The inherent optical properties (IOPs) of the main constituents contributing to ocean colour were used in a simple reflectance model to study the robustness of the MSS algorithm under varying environmental conditions. Comparison between modelled and measured reflectance showed that the adopted IOPs, although approximate, were a realistic starting point. Modelled reflectance highlighted the insensitivity of the proposed algorithm to variations in yellow substance concentrations. Model simulations also suggested an algorithm based on R_{665} may break down in the presence of high chlorophyll concentrations, although there was little evidence of this in the *in situ* observations.

Although the general nature of the R-MSS association is well documented, there is

little evidence in the literature of precise relationships between R and MSS that are directly comparable with results in this study. This is primarily because of differences in wavelength selections, bandwidths or reflectance parameters (R_{rs} rather than R) used over a period spanning the lifetime of many satellite colour sensors. A relationship was found between irradiance reflectance and total mineral suspended solids measured by Bukata *et al.* (1988) in Lake Ontario. The gradient of the relationship between reflectance and MSS was greater than that observed in this study; reflectance reached 11% for MSS concentrations of 9 mg l^{-1} compared with concentrations greater than 15 mg l^{-1} in this study.

At high suspended sediment loads, the sensitivity of a reflectance algorithm to changing sediment concentrations decreases and eventually saturates. This has been observed in the field by Doxaran *et al.* (2002a), in tank experiments by Moore *et al.* (1999) and in model results by Bukata *et al.* (1995). The algorithm in this study was shown to be of value only for concentrations of MSS less than 60 mg l^{-1}, which although is a reasonable range for shelf sea applications, would be of limited value in highly turbid environments. The study by Moore *et al.* (1999) suggested the use of near infra-red (NIR) wavelengths to determine higher sediment concentrations. However, Doxaran *et al.* (2002b) showed that at 850 nm, reflectance saturated for concentrations over 250 mg l^{-1} and concluded that single wavelength reflectance measurements in the visible and NIR would not allow the accurate estimation of suspended sediment concentrations.

The use of colour ratios has been successful in the estimation of suspended sediment concentrations in, for example, the Bay of Fundy (Amos and Topliss, 1985; Topliss, 1986) and the Humber Estuary (Robinson *et al.*, 1998). Topliss (1986) applied multiple algorithms to Landsat imagery for the determination of sediment concentrations up to 1000 mg l^{-1}, adopting progressively longer wavelengths in colour ratios as concentrations increased. The locations of these studies, however, provided conditions under which mineral sediments were likely to be the predominant factor controlling colour. In addition, radiometric observations were calibrated against suspended sediment concentrations at specific localities and dates, therefore, variability in the factors producing changes in the R-MSS relationship may have been small.

Reflectance ratios containing wavelengths in the NIR have also been shown to work well in extremely turbid environments (Moore *et al.*, 1999; Doxaran *et al.*, 2002b). Doxaran *et al.*(2002a, 2002b) showed a strong relationship between the reflectance ratio of wavebands centred on 850 and 555nm and concentrations of total suspended matter ranging from 13 mg l^{-1} to 985 mg l^{-1}. These studies confirm that colour ratios adopting NIR wavelengths can be used successfully in highly turbid waters where there is sufficient scattering to overcome the strong absorption by water at these wavelengths (>2 m^{-1} at 800 nm, Smith and Baker (1981)). Nevertheless, reflectance in the band 700-900 nm was shown to be close to zero for sediment concentrations below 50 mg l^{-1} (Doxaran *et al.*, 2002b). The effectiveness of reflectance ratios incorporating NIR wavebands is, therefore, limited to these extreme turbidity levels and would not be applicable to the more moderate concentration ranges measured in shelf seas. In moderately turbid waters such as the Irish Sea, enhanced reflectance in response to increasing sediment loading does not extend appreciably into the NIR, therefore, discounting the possible use of long wavelength colour ratios. As was discussed earlier, colour ratios at shorter, visible wavelengths are too sensitive to other optically active constituents.

With the wavelength selection currently available on the SeaWiFS colour sensor, it is therefore maintained that for moderate sediment concentrations typical of shelf seas, single-band reflectance algorithms are the most suitable method of retrieving accurate sediment concentrations from ocean colour. Consequently, improvements in the accuracy of concentration estimates will require better understanding of the factors causing variability in the MSS-Reflectance relationship.

Figure 4.16 implies that the source of much of this variability lies in the inherent optical properties of the constituents under consideration. Changes in sediment characteristics such as grain size and refractive index are known to influence the way in which light is scattered by particles (Van de Hulst, 1957) and have been shown to directly influence reflectance through both laboratory experiments (Moore *et al.*, 1999) and modelling (Doxaran *et al.*, 2002a). It is this variability in particle scattering properties and its influence on reflectance algorithms that will be investigated in the following chapter.

Chapter Five

The Effect of Variable Particle Scattering Properties on Single Wavelength Reflectance Algorithms

CHAPTER FIVE: THE EFFECT OF VARIABLE PARTICLE SCATTERING PROPERTIES ON SINGLE WAVELENGTH REFLECTANCE ALGORITHMS

5.1 Introduction

In Chapter Four, a simple reflectance-based algorithm was presented that resulted in estimates of mineral suspended sediment (MSS) concentrations from *in situ* ocean colour measurements with an average accuracy of 22% over a range of concentrations up to 25 mg l^{-1}. Although there was a strong relationship between reflectance at 665 nm and MSS, there was significant error at low concentrations that could not be explained through variations in the ambient light conditions, or through the presence of other in-water constituents. Results in this chapter present evidence that this variability was caused by natural variability in the particle scattering efficiency brought about by inherent differences in particle size and/or composition. A method is presented that enables a first-estimate of the specific scattering coefficient to be obtained from details of the spectral variation of irradiance.

5.2 The Effect of Variable Particle Scattering

As described in Chapter Four, the waters sampled in this study were, for the most part, scattering dominated waters (b/a>1). Consequently, reflectance was determined almost entirely by scattering, as illustrated in figure 5.1. There was, however, an increase in the spread in the data points at high R_{665}, which may have resulted from the simultaneous increase in sediment absorption with increasing scattering. From the algorithm presented in Chapter Four, it was clear that variability was introduced when relating MSS to R_{665}, therefore, it was concluded that the source of this variability must have been in the relationship between MSS and scattering. This is confirmed in figure 5.2, showing the degree of variability in the relationship between the total scattering coefficient at 665 nm (b_{665}) and MSS concentration.

Previous studies have shown that reflectance is influenced by variations in particle size, shape and composition, all of which affect the way in which particles scatter incident light (Moore *et al.*, 1999; Woodruff *et al.*, 1999; Doxaran *et al.*, 2002a). The observed variability in the relationship between b_{665} and MSS could, therefore, have been caused by geographical or temporal variations in these particles characteristics, resulting in changes in the particle scattering efficiency. This hypothesis was

assessed by studying the differences in the estimated MSS-specific scattering coefficient (b^*_{MSS}) at all stations.
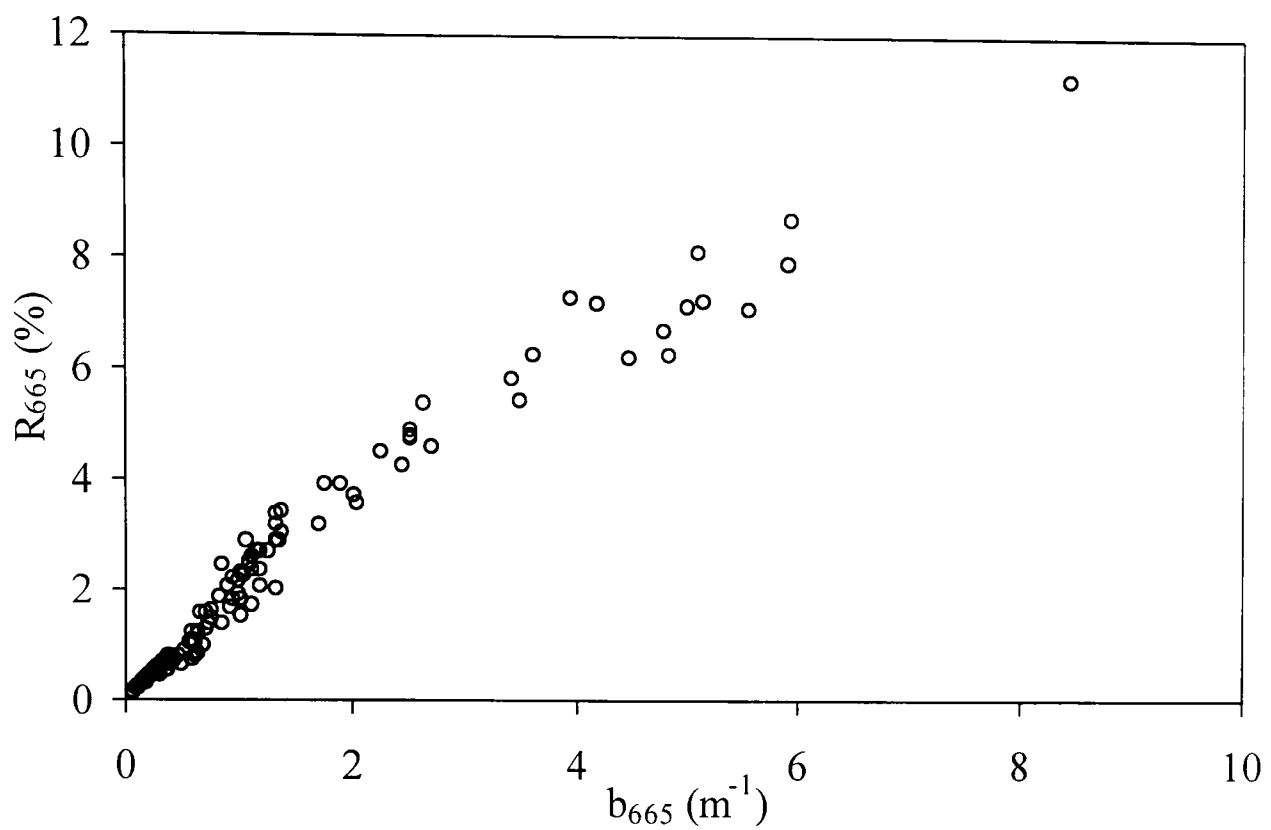
Figure 5.1: Relationship between measured reflectance at 665 nm, R_{665} (%) and the total scattering coefficient at 665 nm, b_{665} (m^{-1}).
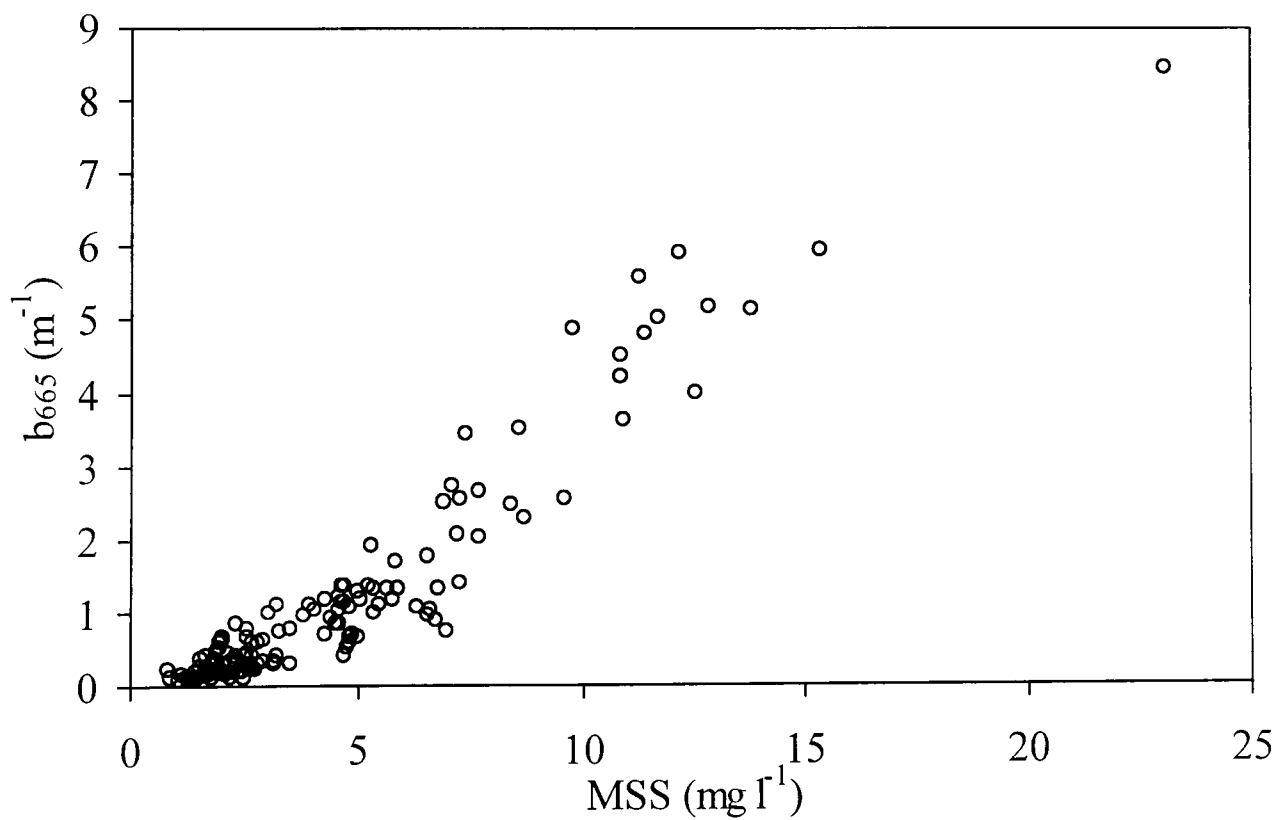
Figure 5.2: Relationship between the total scattering coefficient at 665 nm, b_{665} (m^{-1}) and MSS concentration (mg l^{-1}).

Rather than assuming a single scattering coefficient for all mineral particles as in Chapter Four, particle scattering coefficients were determined individually for each station. Assuming that the scattering by phytoplankton was small compared with that of mineral particles, b^*_{MSS} was calculated according to equation 5.1. Molecular and inelastic scattering were assumed to be negligible in these sediment-dominated waters.

$$b^*_{MSS\,(665)} = \frac{b_{T(665)}}{[MSS]}$$ (5.1)

where $b_{T(665)}$ is the total scattering coefficient at 665 nm and [MSS] denotes the concentration of MSS in mg l^{-1}. Calculated b^*_{MSS} ranged from 0.04 to 0.49 m^2 g^{-1} for all stations. The effect of this variability in b^*_{MSS} on the algorithm presented in Chapter Four could be seen clearly when all stations were categorised according to the calculated b^*_{MSS}; for each category of b^*_{MSS}, a new relationship was formed between R_{665} and MSS (figure 5.3). For the same mass-concentration of MSS, the associated reflectance increased with increasing particle scattering efficiency. At low scattering efficiencies, the relationship between R_{665} and MSS was linear whilst at higher b^*_{MSS}, the relationship appeared to saturate at higher concentrations of MSS.
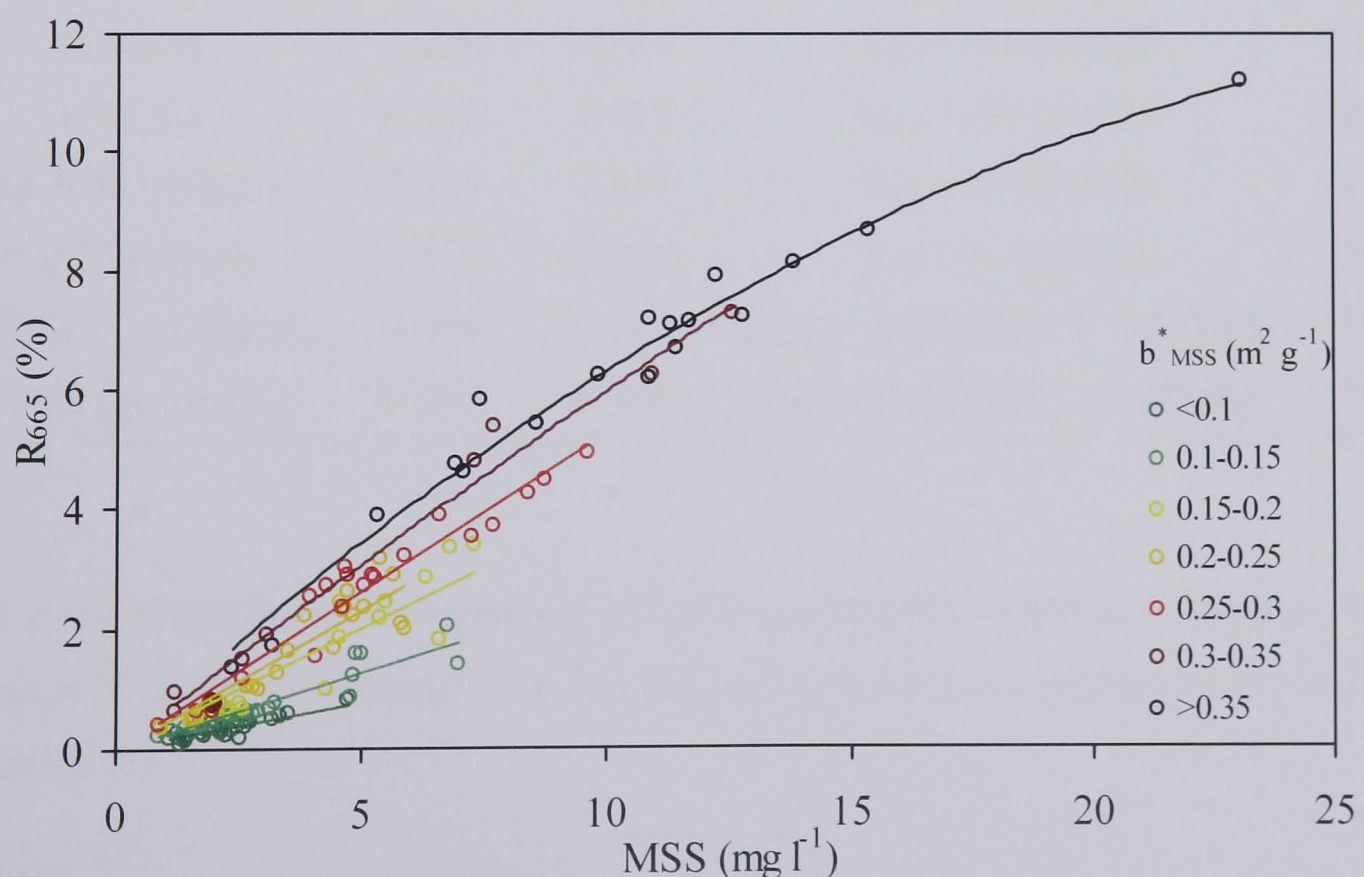
Figure 5.3: Relationships between MSS and R_{665} for categories of the MSS-specific scattering coefficient, b^*_{MSS}.

Table 5.1 provides results of regression analyses between R_{665} and MSS for each category of b^*_{MSS} as shown in figure 5.3. The slope of the linear relationships increased from 0.150 for b^*_{MSS} less than 0.1 m^2 g^{-1} to 0.625 for b^*_{MSS} greater than 0.35 m^2 g^{-1}. When separated into categories of b^*_{MSS}, MSS explained a minimum of 82% of the variability in R_{665}, increasing up to 97.7% for higher scattering efficiencies. In Chapter Four, two features were highlighted in the plot of R_{665} against MSS (figure 4.6); a significant positive intercept in the y-axis, suggesting a baseline MSS concentration existed, and an increase in the variability of R_{665} at low MSS concentrations. These two features can be explained by the results presented in figure 5.3; the variability at low reflectances is a consequence of variations in the particle scattering efficiency and the fact that the relationships in figure 5.3 pivot around the origin forces a positive intercept from a best fit line for the entire data set.

Table 5.1: Variation in the relationship between MSS and R_{665} for categories of b^*_{MSS}

b^*_{MSS} Category $(m^2\ g^{-1})$	Average b^*_{MSS} $(m^2\ g^{-1})$	St. Dev. b^*_{MSS} $(m^2\ g^{-1})$	Relationship between R_{665} and MSS	R^2 (%)
< 0.1	0.076	0.014	$R_{665} = 0.150MSS$	82.7
0.1-0.15	0.125	0.014	$R_{665} = 0.250MSS$	88.8
0.15-0.2	0.177	0.015	$R_{665} = 0.406MSS$	84.5
0.2-0.25	0.226	0.014	$R_{665} = 0.458MSS$	81.9
0.25-0.3	0.267	0.015	$R_{665} = 0.525MSS$	94.4
0.3-0.35 (linear)	0.324	0.017	$R_{665} = 0.598MSS$	97.7
> 0.35 (linear)	0.415	0.049	$R_{665} = 0.625MSS$	93.5
0.3-0.35 (quadratic)	0.324	0.017	$R_{665} = -0.004MSS^2 + 0.64MSS$	97.8
> 0.35 (quadratic)	0.408	0.047	$R_{665} = -0.01MSS^2 + 0.75MSS$	97.4

The slope of the linear relationship between R_{665} and MSS varied as a function of the average b^*_{MSS} for each category as depicted in figure 5.4 and could be estimated from equation 5.2.

$$slope = -2.53b^{*}_{MSS}{}^2 + 2.60b^{*}_{MSS} \qquad (R^2 = 97.9) \qquad (5.2)$$
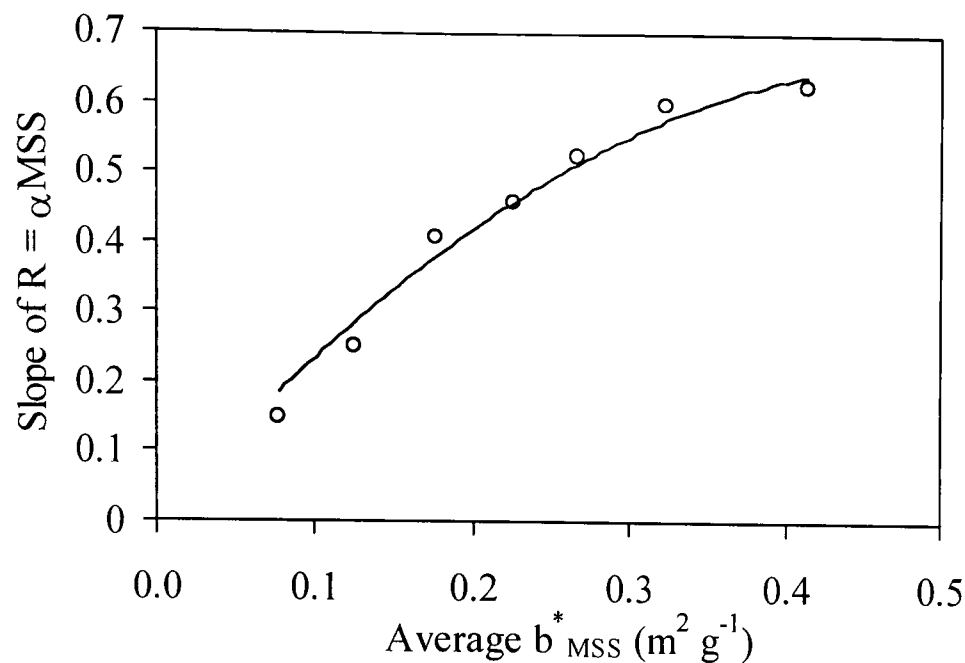
Figure 5.4: Slope (α) of the relationship R = αMSS for categories of b^*_{MSS} as in table 5.1.

Although figure 5.4 shows that the rate of change in the slope decreases with increasing b^*_{MSS}, this is considered to simply be an artefact of the type of regression used in table 5.1; it is suggested that the relationship between the slope and b^*_{MSS} should be a linear one. In figure 5.3, whilst the smaller b^*_{MSS} displayed a linear relationship between R_{665} and MSS, the same relationship for higher b^*_{MSS} started to saturate at high MSS concentrations. For the largest b^*_{MSS} categories, regressions were limited to data points before the tendency to saturate. However, it appears that the regression analysis may still have underestimated the slope of the linear section of the curve for these higher b^*_{MSS}.

With this understanding of the way in which the relationship between R_{665} and MSS varied as a function of b^*_{MSS}, it was possible, with prior knowledge of the scattering efficiency of the particles under study, to obtain more accurate estimates of MSS concentrations from R_{665}. Using the b^*_{MSS} estimated from equation 5.1, the relevant relationship between R_{665} and MSS was estimated from equation 5.2 at each optical station and an improved prediction of MSS was obtained. These corrected MSS predictions are presented in figure 5.5 plotted against the measured MSS concentrations. This figure highlights the improved accuracy of the method, removing much of the uncertainty in predicted MSS concentrations, particularly at low concentrations. The percentage difference between observed and predicted MSS is reduced from 21.3% for predicted MSS based on simple reflectance to 15.3% when taking into account variations in b^*_{MSS}.
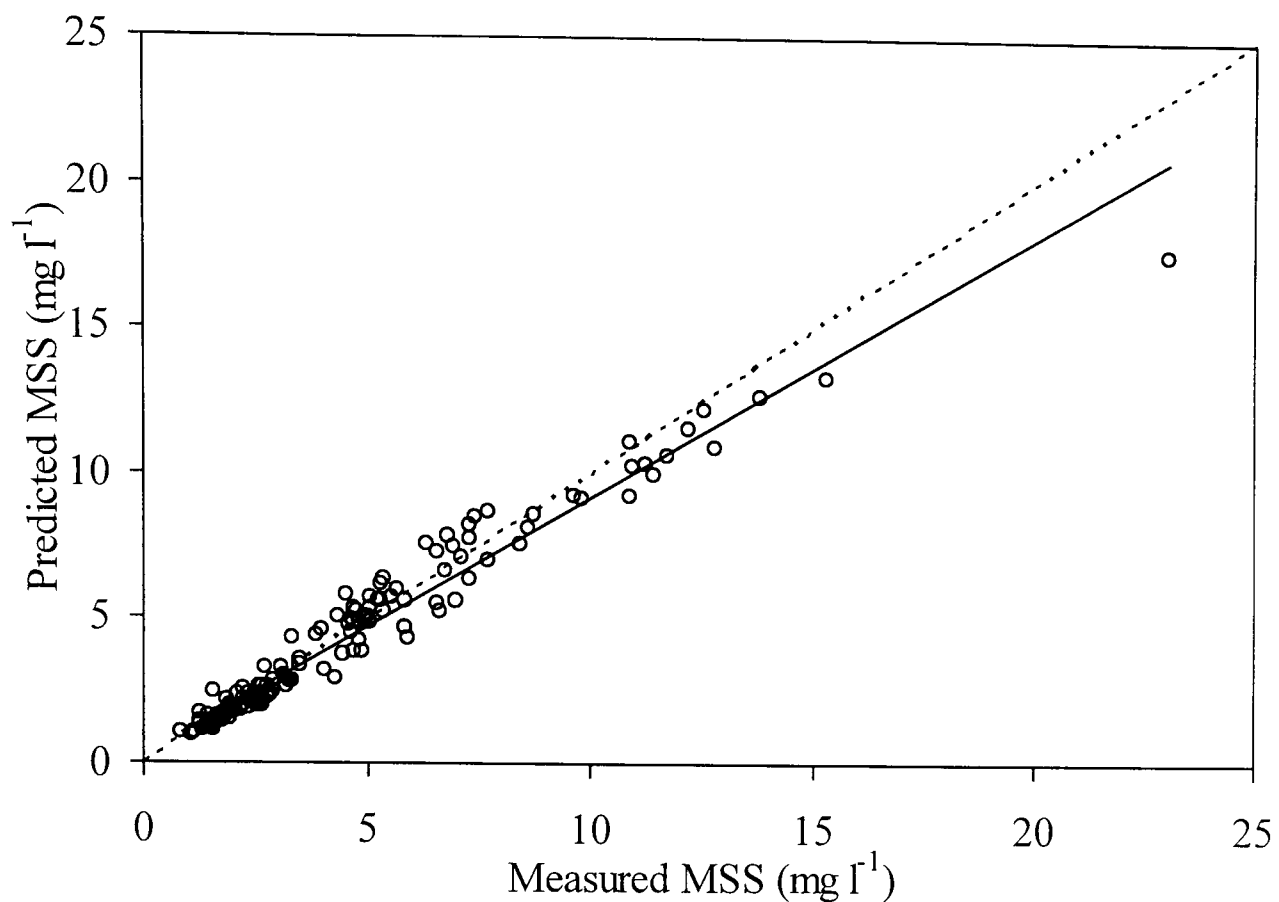
Figure 5.5: Measured MSS versus MSS concentration predicted from R_{665} and corrected for variations in b^*_{MSS}. Dashed line represents the 1:1 relationship.

Although this correction provided a more accurate estimate of MSS concentration, it is evident in figure 5.5 that predicted MSS trailed off from the 1:1 relationship (dashed line in figure 5.5) at high concentrations. This was simply a result of the use of linear relationships between R_{665} and MSS for each b^*_{MSS} category, resulting in the underestimation of MSS at high concentrations.

5.3   Reflectance Model Results

In order to further understand the effect of particle scattering efficiency, the reflectance model presented in Chapter Four was used again to try to reproduce observations. The model was first run to reproduce the reflectance at each station from the known concentrations of MSS, C and YS and the individual particle scattering coefficients b^*_{MSS} as derived from equation 5.1. The agreement of modelled reflectance with measured reflectance was improved considerably compared with that presented in Chapter Four when particle scattering was taken as constant (figure 5.6). The percentage difference between modelled and measured R_{665} was reduced from 165%, when b^*_{MSS} variability was neglected, to just 9%. In particular, the retrieval accuracy was improved at the lower reflectances (R<1%)

where the percentage difference between modelled and measured R_{665} decreased from 287% to 8.6% by including variations in b^*_{MSS}. This considerable improvement in predicted reflectance emphasises the importance of accounting for variations in particle scattering efficiency in reflectance models.
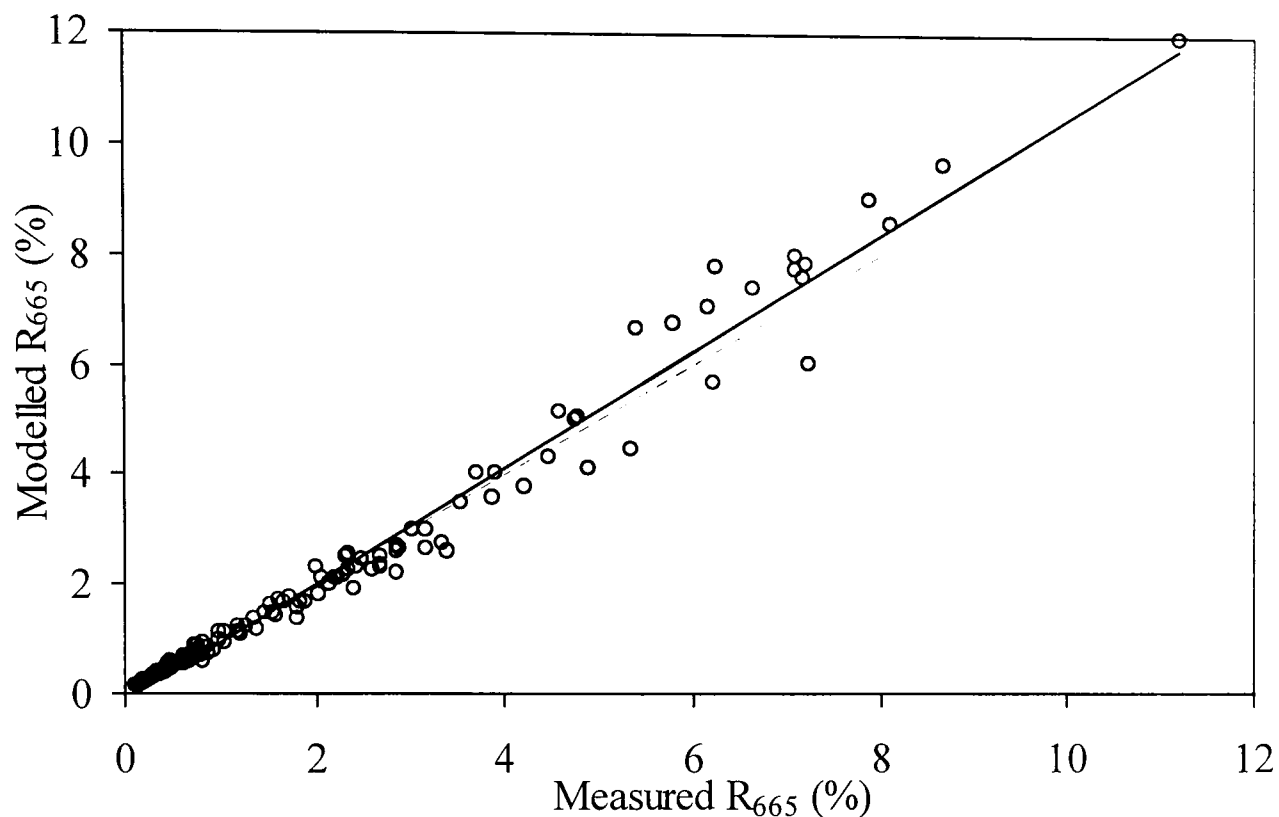
Figure 5.6: **Relationship between modelled R_{665} corrected for variations in b^*_{MSS} and R_{665} as measured by the PRR600 for all stations. Dashed line represents the 1:1 relationship.**

Figure 5.6 proves that the reflectance model worked well in the forward mode (predicting reflectance from concentrations of in-water constituents) and, therefore, that the chosen inherent optical properties were accurate. Nevertheless, to use this model in the inverse mode to estimate MSS concentrations, it would first be necessary to account for the optical properties of both YS and C. In order to avoid this, the model was simplified further to a two-parameter model based solely on the optical properties of water and MSS. Modelled versus measured R_{665} for this simple case are presented in figure 5.7 for all stations. The percentage difference between modelled and measured reflectance was increased to 16%, still only a fraction of the uncertainty of the model results in Chapter Four when a fixed b^*_{MSS} was assumed. A least squares best fit linear regression highlighted the strong 1:1 relationship ($y = 1.003x - 0.005$, $R^2 = 96.5\%$). The good agreement between the modelled and measured reflectances, despite neglecting the optical properties of YS and C, re-

emphasised the dominance of mineral sediments in controlling the optical properties in this region.
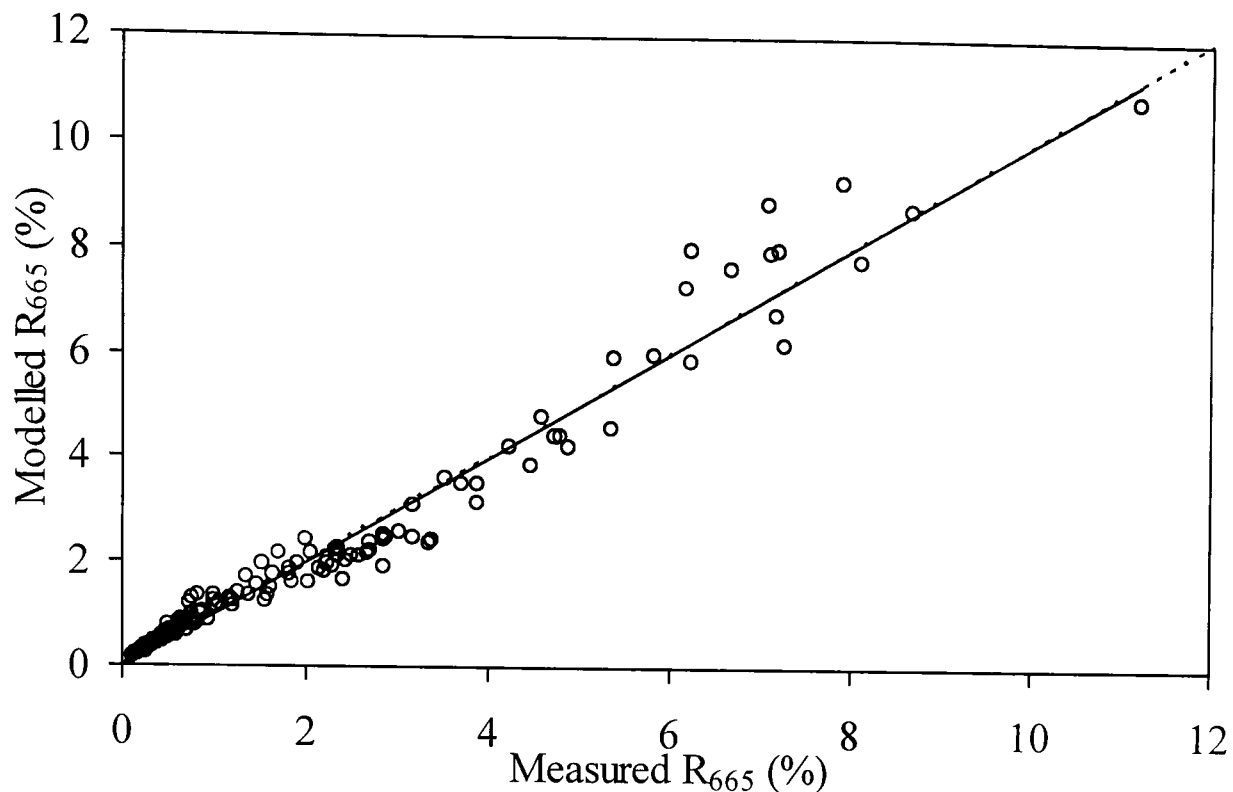
Figure 5.7: Modelled versus measured R_{665}. Model predictions based on a simple 2-parameter model (water and MSS). Dashed line represents the 1:1 relationship.

For the simple case where the optical properties of constituents other than MSS were neglected, the reflectance model was run to study the effect of variations in b^*_{MSS} on the relationship between R_{665} and MSS. Figure 5.8 presents the modelled reflectance for b^*_{MSS} ranging from 0.1 to 0.45 m^2 g^{-1} with the *in situ* observations categorised according to estimated b^*_{MSS} superimposed for comparison. Model results showed that for any concentration of MSS reflectance increased with increasing b^*_{MSS}. Furthermore, for each category of b^*_{MSS} reflectance saturated as MSS concentration increased. It was then clear that the linear relationships observed in figure 5.3 were simply the linear section of what would develop into a saturating curve at sufficiently high MSS concentration. The saturation point of each of the modelled curves was arbitrarily taken as the point where R_{665} increased by less than 0.1% per unit increase in MSS concentration and was found to occur at an MSS concentration of 179 mg l^{-1} irrespective of the value of b^*_{MSS}. This is considerably larger than the proposed saturation point of the reflectance algorithm presented in Chapter Four. This is attributed simply to methodology; whereas the quadratic function allowed an algebraic solution to the saturation point, the modelled curves require a point to be selected at which any increase in reflectance will not allow the accurate determination

of any increase in MSS. This, of course, will depend on the sensitivity of the colour sensor in use. Table 5.2 contains details of the modelled saturation reflectances; for the selected range of b^*_{MSS}, the saturating reflectance ranged from 6.5% to 29%. A simple linear relationship (equation 5.3) enabled the determination of the saturating reflectance for any given value of b^*_{MSS}.

$$Saturating\ R = 64.98b^*_{MSS} + 0.0039 \hspace{4cm} (5.3)$$
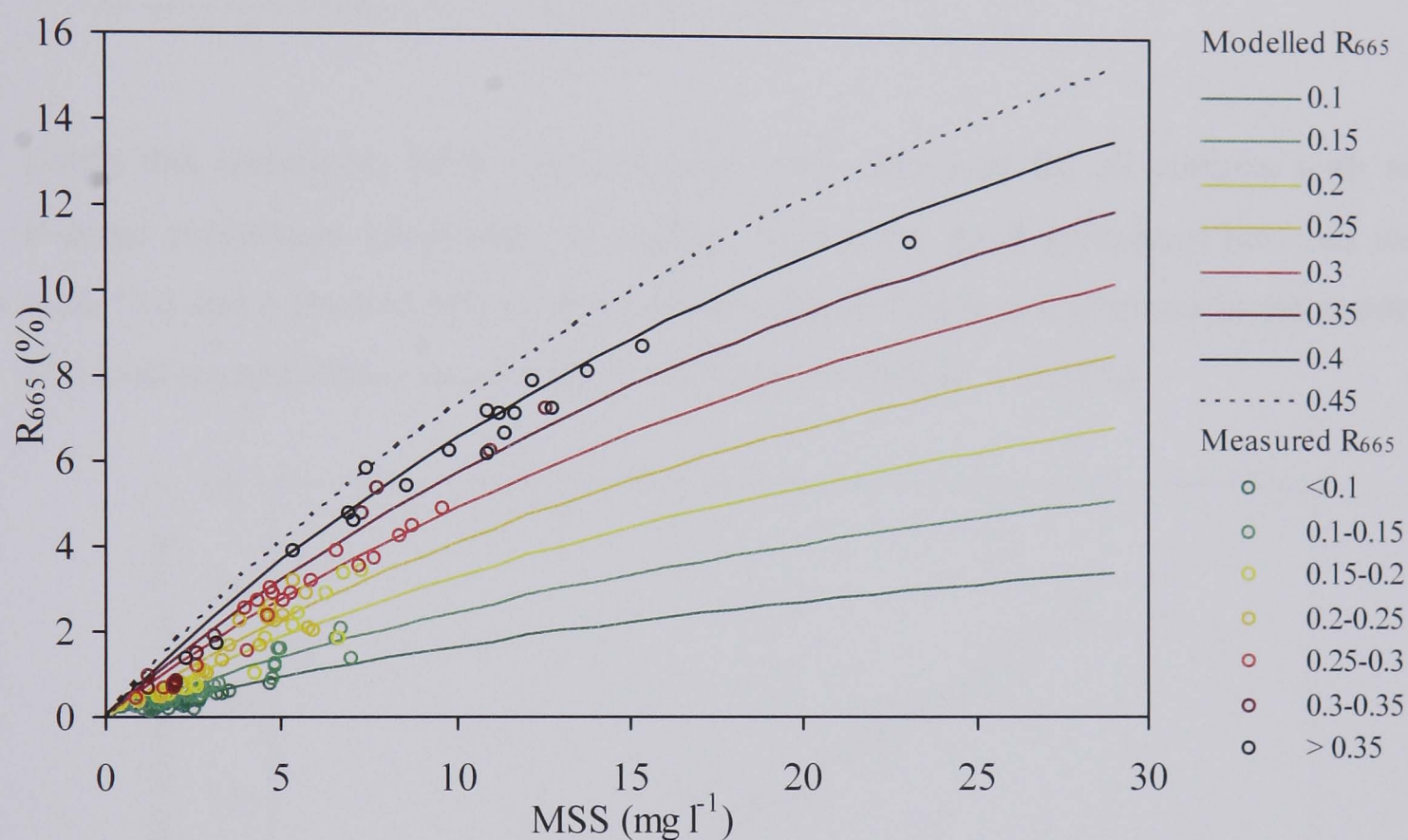
Figure 5.8: **Relationship between R_{665} and MSS for varying b^*_{MSS}, open circles represent observed R_{665} and lines represent modelled R_{665}.**

b^*_{MSS} (m^2 g^{-1})	R_{665} (%)
0.45	29.24
0.4	25.99
0.35	22.75
0.3	19.50
0.25	16.25
0.2	13.00
0.15	9.75
0.1	6.50

Table 5.2: **Reflectance at the saturation point of the R-MSS relationship (MSS=179 mg l^{-1}) for varying b^*_{MSS}.**

Because reflectance at 665 nm could be modelled successfully when neglecting the contribution from YS and C, with only a limited increase in the retrieval uncertainty, it was possible to use the model in the inverse mode for the purpose of predicting MSS concentrations (equation 5.4).

$$MSS = \frac{R \ a_w}{C(\mu_0) \ \frac{b_b}{b} \ b^*_{MSS} - R \ a^*_{MSS}}$$

(5.4)

Using this technique, MSS concentrations were estimated for all stations with an average percentage uncertainty of 13.9%. Again, the good agreement between the modelled and measured MSS concentrations (figure 5.9) was confirmed in the results of a least squares linear regression ($y = 1.043x + 0.016$, $R^2 = 92.4\%$).
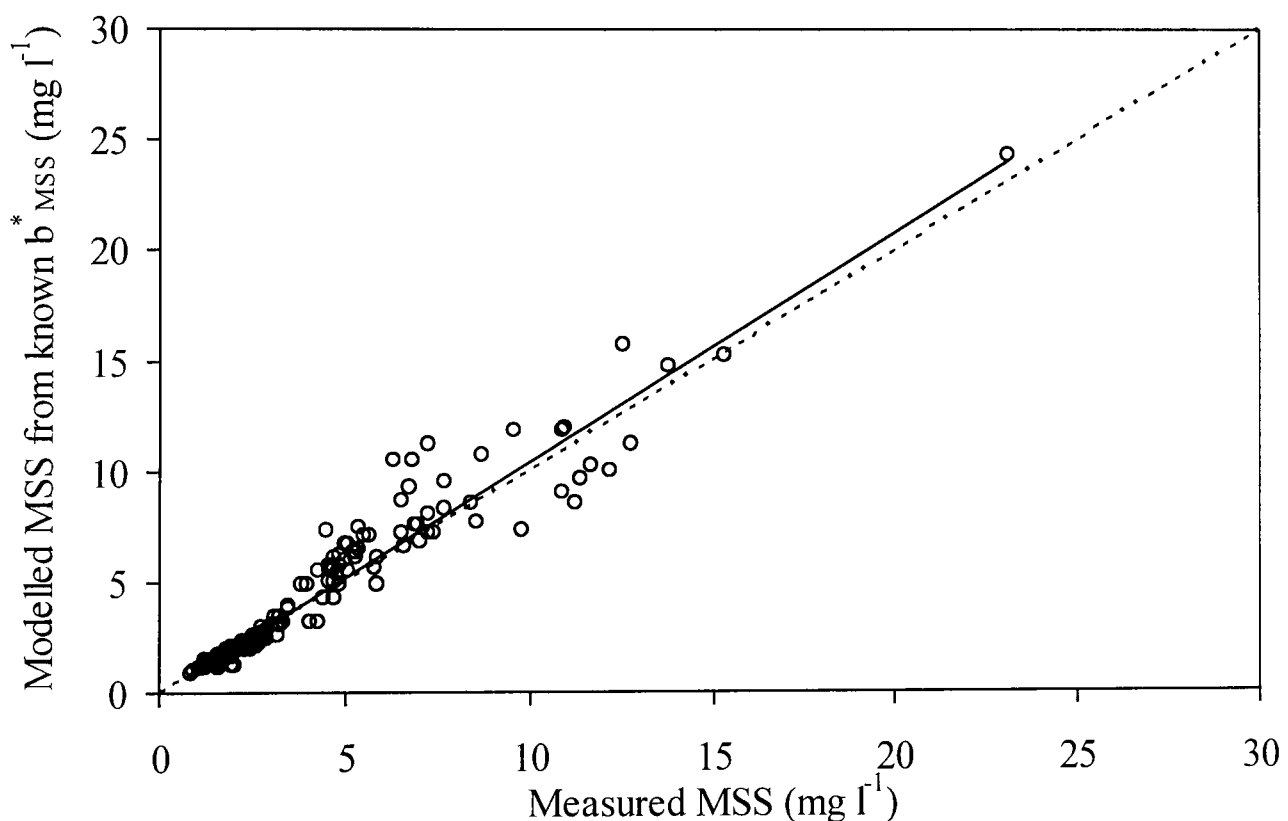
Figure 5.9: Modelled versus measured MSS concentrations for all stations based on a simple 2-parameter inverse model. Dashed line represents the 1:1 relationship.

5.4   Factors Affecting Particle Scattering Efficiency

It was expected that the observed variations in particle scattering efficiency would be due to differences in particle properties such as grain size, shape and composition. Whilst no direct measurements of these parameters were routinely obtained, some

basic inferences were initially made based on the ratio of MSS/TSS, a measure of the amount of inorganic matter present in a sample of suspended material relative to the total suspended matter.

There was a positive correlation between b^*_{MSS} and MSS/TSS ($R = 0.51$), although there remained a great deal of unexplained variability. By looking at the average b^*_{MSS} for selected categories of MSS/TSS (figure 5.10) it was found that, on average, waters with the largest fraction of mineral particles (MSS/TSS = 80-90%) resulted in the most efficient particle scattering. With increasing organic content the particle scattering efficiency decreased, although for the largest organic fractions, b^*_{MSS} appeared to increase again. Even though there was some uncertainty in this increase due to the large error in the < 40% category, such an increase may have been caused by the so far unaccounted contribution to scattering from organic matter. For high concentrations of organic suspended material, total scattering would be enhanced and while b^*_{MSS} was calculated as $b_T/[MSS]$, this would result in small increases in b^*_{MSS} that were not related to the scattering by mineral particles themselves. Such a contribution to scattering from organic matter and the associated overestimate in the true b^*_{MSS} would cause an underestimate of the total MSS concentrations predicted from the inverse modelling technique. Whilst there was some suggestion of this occurring in the model results (MSS concentrations were underestimated by up to 20% at stations where C was greater than 5 µg l^{-1}), this is considered to be a small increase in the prediction uncertainty.
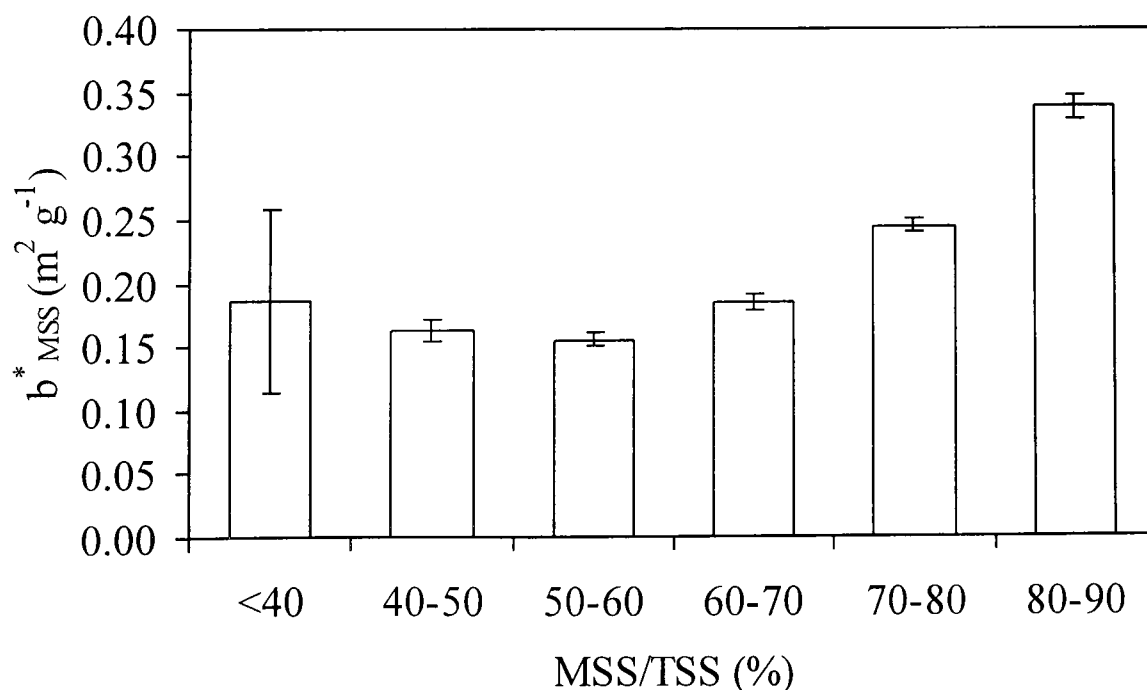
Figure 5.10: Variation of b^*_{MSS} for selected categories of MSS/TSS. Error bars represent ± 2 standard errors.

Figure 5.11 presents the sediment scattering coefficient for total suspended particulate concentrations (calculated as $b_T/[TSS]$ rather than $b_T/[MSS]$) which altered the trend by accounting for the increase in organic matter. The correlation between b^*_{TSS} and MSS/TSS was significantly greater than b^*_{MSS} (Pearson Correlation = 0.73). Although when studying b^*_{TSS} the uncertainty in the validity of the scattering coefficient at low MSS/TSS is removed, it is not possible to incorporate b^*_{TSS} into the optical model without then estimating TSS concentrations. Furthermore, if this was the case, the absorption coefficient would be difficult to quantify correctly without prior knowledge of the pigment concentrations or organic content. Therefore, whilst b^*_{TSS} may give a more logical representation of the behaviour of scattering with respect to particle characteristics, it is b^*_{MSS} that is required for modelling purposes.
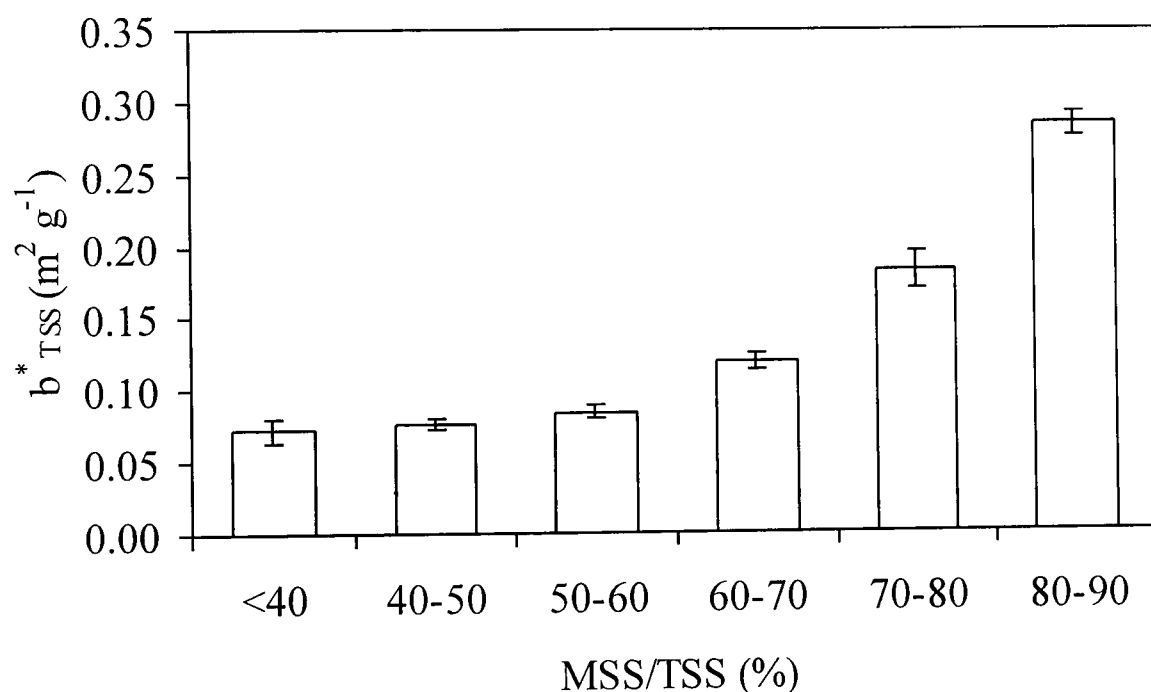
Figure 5.11: Variation of b^*_{TSS} for selected categories of MSS/TSS. Error bars represent ± 2 standard errors.

There are numerous potential causes of a decrease in particle scattering efficiency with increasing organic matter. These are summarised below as three principal hypotheses for the causes of the trends visible in figures 5.10 and 5.11.

   1) The decrease in average b^*_{TSS} was caused by increasing particle sizes due to particle flocculation associated with increasing organic matter.

2) The scattering efficiency of mineral particles did not change but the decrease in average b^*_{TSS} was the result of lower scattering efficiency of the organic matter itself. By combining the scattering effects of organic and inorganic fractions, the larger the organic content, the lower the average b^*_{TSS}.

3) The decrease in average b^*_{TSS} results from the smaller refractive index of organic relative to inorganic matter. Although not significantly affecting total scattering, changes in refractive indices would affect backscattering and thus the backscattering probability, b_b/b. Since the total scattering coefficient was computed with the assumption of a constant b_b/b (=0.019), it could be that observed variations in b^*_{MSS} were in fact caused by variations in b_b/b.

Whilst the above hypotheses describe inherently different processes, they may all occur as a consequence of increasing organic suspended matter. A distinct seasonal cycle of b^*_{MSS} (or b^*_{TSS}) might therefore be expected, with lower scattering efficiencies in the summer months when there would be more organic material available, increasing to higher values in the winter where phytoplankton populations are minimal and increased wind stirring re-suspends mineral particles from the bottom. Despite the fact that in this dataset, there was considerable variability in b^*_{MSS} during any single cruise, there appeared to be a minimum in the average b^*_{MSS} during the summer months (figure 5.12), which lends support to all of the above hypotheses. This seasonal cycle in b^*_{MSS} can be written as a co-sinusoidal curve such that $b^*_{MSS} = 0.2352 + 0.0977\cos\omega t$ ($R^2 = 49\%$, p = 0.00) where ω is the angular frequency of the annual cycle and is given by $2\pi/T$. T is the number of days in the year and t is the day of the year (t = 1 on January 1st).
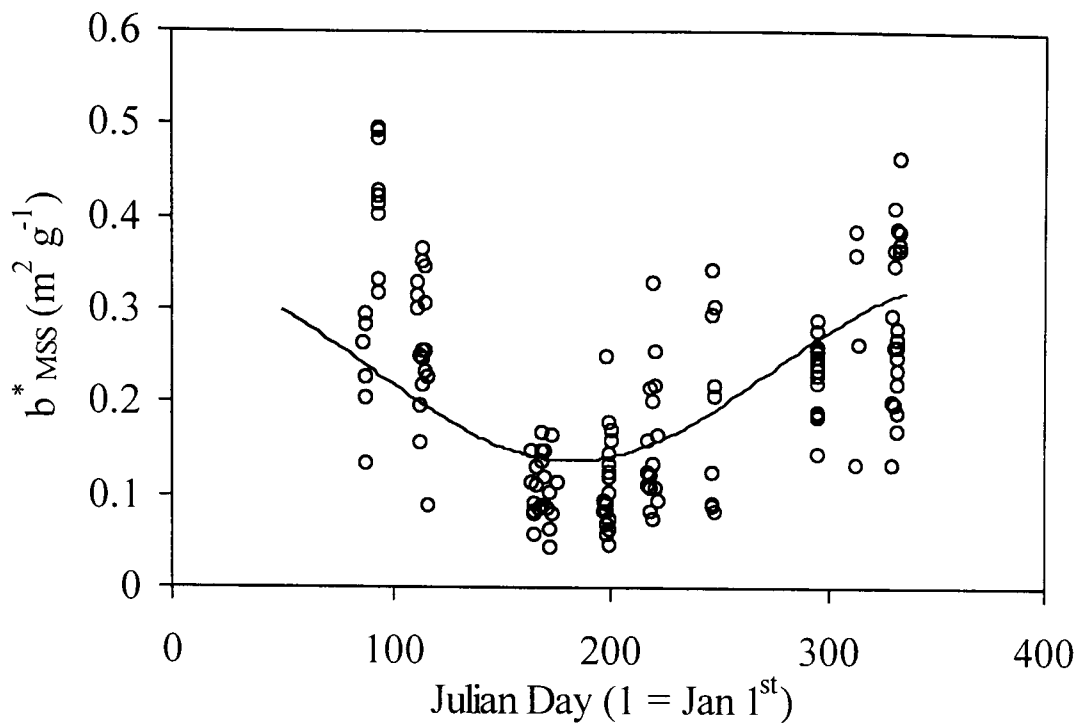
Figure 5.12: Seasonal cycle of b*$_{MSS}$ observed for all stations.

During the Celtic Sea cruise in June 2000, a LISST-100 (Sequoia Scientific Inc.) was available to provide grain size information. The LISST uses laser diffraction and a series of ring detectors to measure forward-scattering at 32 angles, giving a size distribution for the particles in suspension (Traykovski *et al.*, 1999). At each station the measured mean grain size was averaged over the upper 10 m of the water column. Although only a few observations were obtained, b*$_{MSS}$ was found to correlate strongly with grain size (Pearson Correlation = -0.90) with mean particle diameters (δ) ranging from 25 to 80 μm. Least squares linear regression provided a predictive expression for b*$_{MSS}$, with grain size explaining over 80% of the variability in b*$_{MSS}$ (equation 5.7)

$$b*_{MSS} = 0.159 - 0.00132\delta \qquad (p= 0.016, R^2 = 80.3\%, n = 7) \qquad (5.7)$$

During two other cruises (Clyde Sea 2, 2001 and Irish Sea 4, 2001), the AC-9 (WET Labs) and Hydroscat-2 (HOBI Labs) were available and provided independent measurements of the total scattering and backscattering coefficients. As described in Chapter Four, the AC-9 determines scattering by measuring absorption and attenuation coefficients (b = c - a). The Hydroscat-2 is an *in situ* optical backscattering sensor that measures backscattering at two predetermined wavelengths

(in this case 470 nm and 676 nm). For these two cruises, the backscattering ratios at both 470 and 676 nm were calculated (table 5.3) and showed that on average, Clyde Sea particles resulted in lower backscattering ratios compared with the Irish Sea. The derived backscattering ratios of 0.011 in the Clyde Sea and 0.022 in the Irish Sea are in good agreement with those in the literature for phytoplankton (Bricaud *et al.*, 1983) and mineral sediments (Herlevi, 2002) respectively. Herlevi (2002) measured b_b/b functions fluctuating between 0.015 and 0.022 in mineral-dominated lake waters.

Table 5.3: Backscattering probabilities (b_b/b) at 470 nm and 676 nm measured with the Hydroscat-2 in the Clyde Sea and Irish Sea.

	b_b/b @ 470 nm		b_b/b @ 676 nm	
	Clyde Sea	Irish Sea	Clyde Sea	Irish Sea
Average	0.010	0.024	0.011	0.022
Min	0.005	0.019	0.006	0.018
Max	0.018	0.027	0.020	0.025

The particle refractive indices, n_p, were estimated using a model presented by Twardsowski *et al.* (2001) (equations 5.5 and 5.6) which incorporates values of b_b/b and the spectral variation of the beam attenuation coefficient, c, into Mie scattering theory.

$$c = A\lambda^{-\gamma} \tag{5.5}$$

where γ is the hyperbolic slope of the attenuation spectrum and A is constant.

$$n_p = 1 + \frac{b_b}{b}^{(0.5377+0.4867\gamma^2)}[1.4676 + 2.2950\gamma^2 + 2.3113\gamma^4] \tag{5.6}$$

Derived refractive indices for the Clyde and Irish Seas (table 5.4) agree with expected values for algal cells and inorganic minerals respectively (Twardowski *et al.*, 2001). This is supported by the measured organic content of suspended particulate material during each of these sampling periods. The Clyde Sea was visited during the spring

and exhibited a dominance of organic material (MSS/TSS = 49%, $C = 6.9\,\mu g\,l^{-1}$) compared with Irish Sea conditions (MSS/TSS = 82% and $C = 1.4\,\mu g l^{-1}$). The maximum refractive indices observed in the Clyde Sea were those obtained from the Clyde Estuary where there was significant inorganic suspended material.

Table 5.4: Estimated particle refractive indices for the Clyde and Irish Seas.

Refractive index, n_p	Clyde Sea	Irish Sea
Average	1.076	1.177
Max	1.110	1.195
Min	1.009	1.157

Chapter Four compared scattering coefficients as estimated from Monte Carlo expressions after Kirk (1984) with those measured by the AC-9. Whilst the calculated scattering coefficients were in good agreement with those measured by the AC-9, there was some uncertainty in the lower scattering coefficients observed in the Clyde Sea. This can be explained now by the observed differences in the backscattering probability. Kirk's expressions assumed a b_b/b of 0.019 whereas in the Clyde Sea, the average measured b_b/b was 0.0126 decreasing to a minimum of 0.006. Using these measured b_b/b values to re-calculate the total scattering coefficient from Kirk's equations highlighted the effect this had on the derived coefficients (figure 5.13). The scattering coefficients at both wavelengths shifted markedly towards the 1:1 line when compared with the scattering coefficients determined from the AC-9.

The same was not observed for the Irish Sea (figure 5.14). During this cruise, the measured b_b/b did not change greatly from the 0.019 assumed by Kirk and, therefore, the previous estimated scattering coefficients were a good approximation.
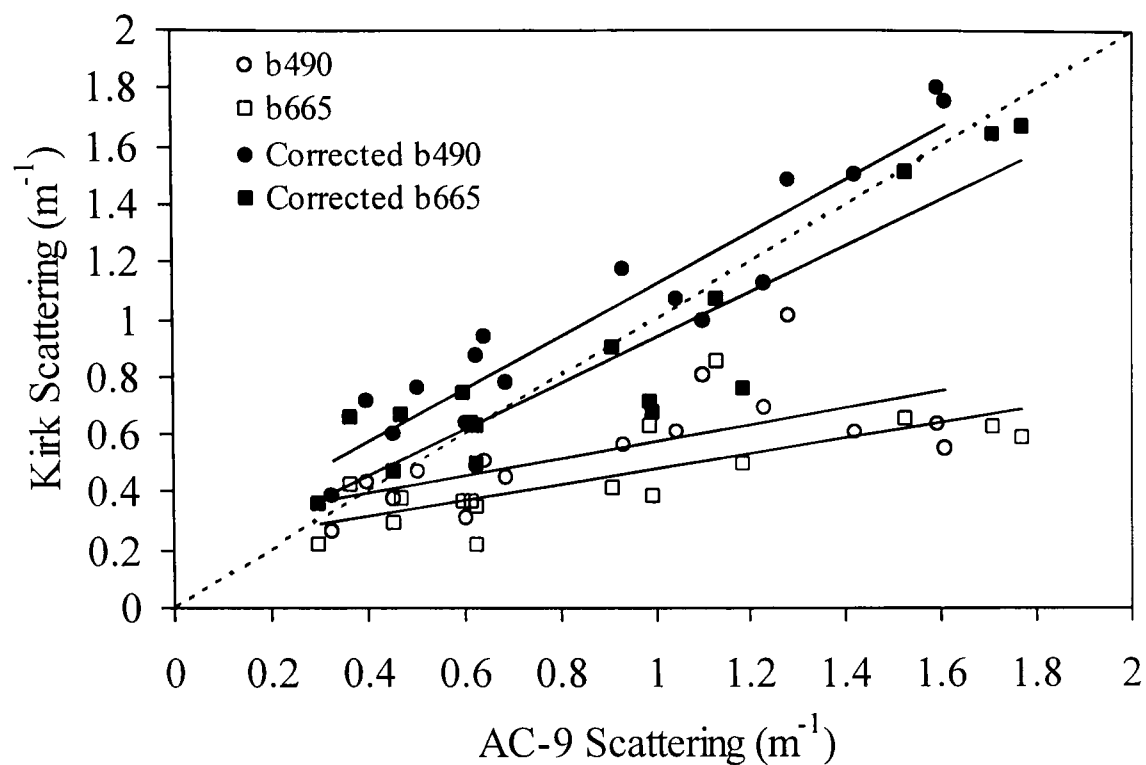
Figure 5.13: Plot of scattering coefficients derived from Kirk's expressions (open symbols assuming a fixed b_b/b = 0.019, closed circles corrected for b_b/b as measured by the Hydroscat) against scattering coefficients as measured by the AC-9 in the Clyde Sea, May 2001. Dashed line represents the 1:1 relationship.
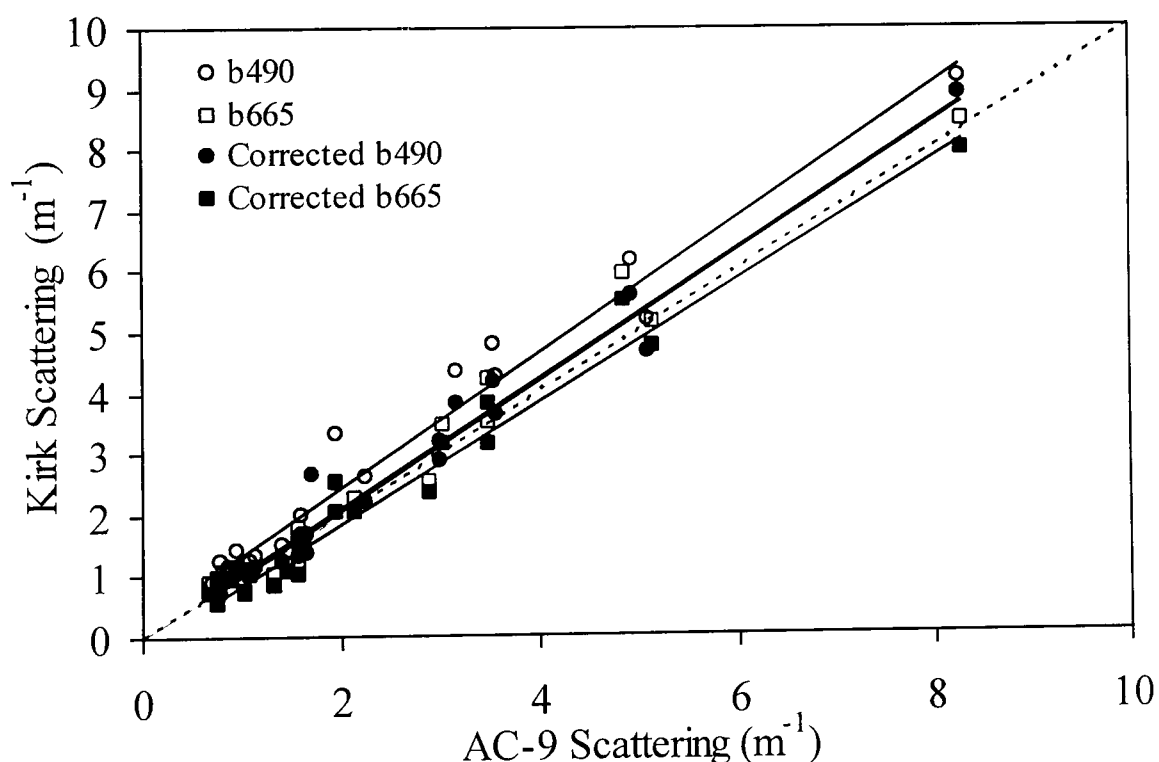
Figure 5.14: Plot of scattering coefficients derived from Kirk's expressions (open symbols assuming a fixed b_b/b = 0.019, closed circles corrected for b_b/b as measured by the Hydroscat) against scattering coefficients as measured by the AC-9 in the Irish Sea, November 2001. Dashed line represents the 1:1 relationship.

It is apparent from figures 5.13 and 5.14 that large variations in the backscattering probability have a significant effect on the observed total scattering coefficients. However, results from this section support the conclusion that it is in fact a combination of the processes described in the three hypotheses that lead to the observed variations in the particulate scattering efficiencies. Without a further detailed investigation including the coincident measurement of all the above-mentioned parameters, it is difficult to separate the effects of each process independently. Nevertheless, for the purpose of this study, the requirement is to estimate the magnitude of b^*_{MSS} in order to improve predictions of MSS concentrations; isolating and fully understanding the factors affecting b^*_{MSS} is beyond the scope of this study with the data available.

5.5   Estimating b^*_{MSS} from Spectral Reflectance

A method was developed whereby the value of b^*_{MSS} could be estimated from a factor combining the wavelength of peak reflectance and the magnitude of a single waveband reflectance. The choice of this factor can be justified by referring back to results in Chapter Four. The wavelength of peak reflectance was found to increase not only with increasing MSS concentration but also with increasing pigment concentration. However, waters dominated by inorganic sediments (small grain sizes and high refractive indices resulting in efficient scattering), would have higher reflectance than those dominated by organic material (large grain sizes and low refractive indices resulting in low scattering coefficients). Accounting for both variations in peak wavelength (colour changes) and reflectance (brightness changes), through the factor [λ_{PeakR}/R_{665}], provided a method for estimating the particulate scattering coefficient, b^*_{MSS} (figure 5.15). This factor explained 71% of the variability in b^*_{MSS} through a power function ($b^*_{MSS} = 2.83[\lambda_{PeakR}/R_{665}]^{-0.45}$). The large spread in the data at intermediate b^*_{MSS} may have been the consequence of the unaccounted scattering from organic matter as suggested by the points in figure 5.15 where C was greater than 5 μg l^{-1}, causing an unrealistic increase in the estimated b^*_{MSS} (as for figure 5.10).
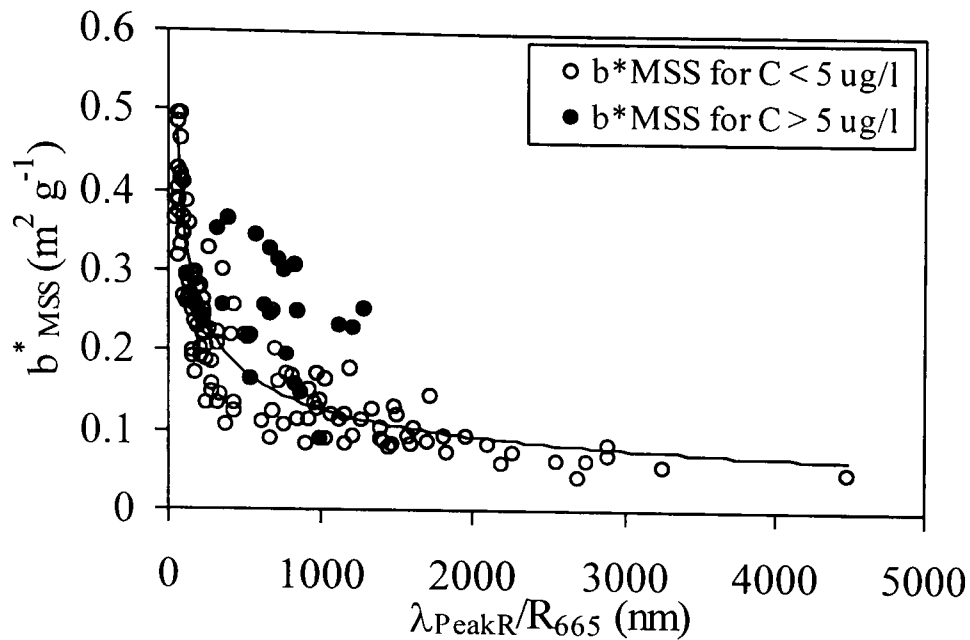
Figure5.15: Relationship between b^*_{MSS} and the factor $[\lambda_{PeakR}/R_{665}]$.
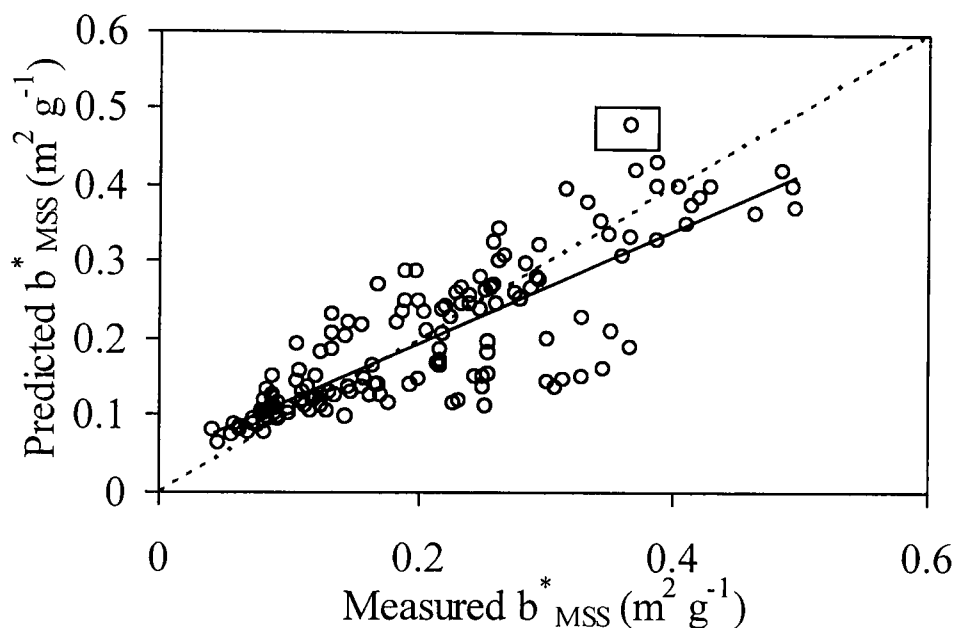
Figure 5.16: Predicted versus measured b^*_{MSS}. Dashed line represents the 1:1 relationship.

This technique resulted in predictions of b^*_{MSS} accurate to within 24%, although there was a tendency to underestimate the higher b^*_{MSS} values (figure 5.16). The retrieval accuracy was improved considerably when estimating b^*_{TSS} since (as for figure 5.11), the scattering coefficient then accounted for the contribution from organic material. The spread in the data around the intermediate scattering coefficients was considerably reduced (figure 5.17) such that 86% of the variability in b^*_{TSS} was explained by $[\lambda_{PeakR}/R_{665}]$. A power function ($b^*_{TSS} = 4.57[\lambda_{PeakR}/R_{665}]^{-0.61}$) enabled the prediction of b^*_{TSS} with an uncertainty of 21% and decreased the tendency to underestimate high values of b^*_{TSS} (figure 5.18).
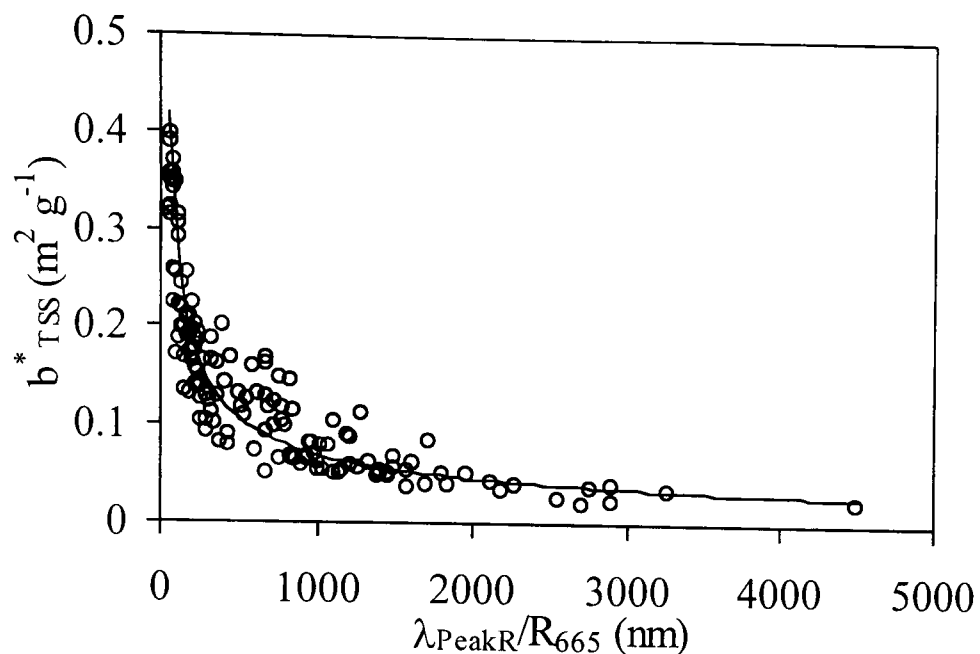
Figure 5.17: Relationship between b^*_{TSS} and the factor [Peak λ/R_{665}].
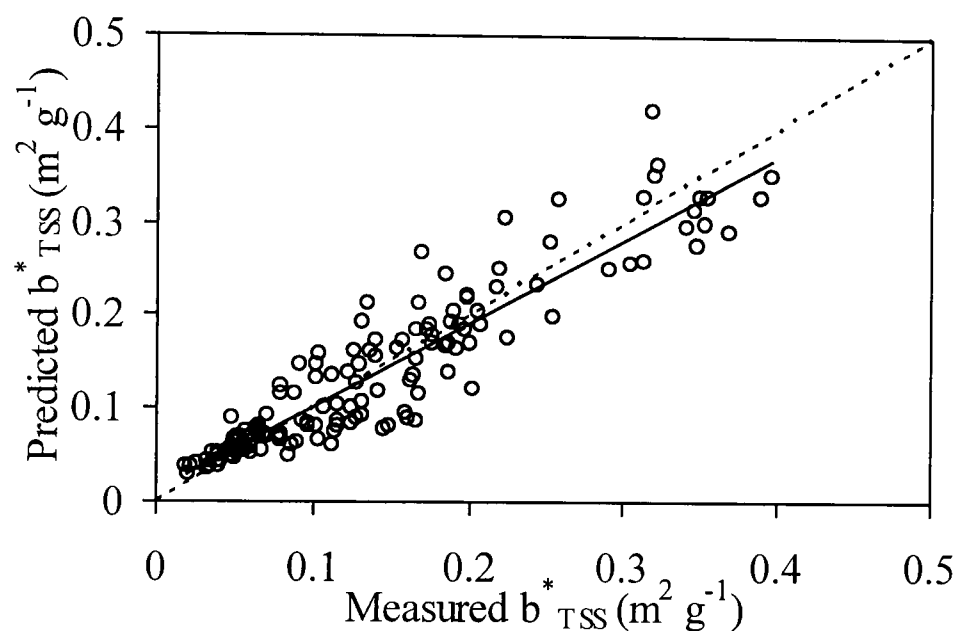
Figure 5.18: Predicted versus Measured b^*_{TSS}. Dashed line represents the 1:1 relationship.

Using this technique for the prediction of particle scattering coefficients from the spectral reflectance would, in theory, enable improved estimates of MSS concentrations from reflectance. Although the technique predicted b^*_{TSS} with greater accuracy than b^*_{MSS}, it is the mineral fraction of the suspended load that can be modelled easily from optical theory.

Figure 5.19 shows that although the resulting MSS predictions were in good agreement with measured concentrations, there was a tendency to underestimate higher concentrations. This contradicts expectation since the trend in figure 5.16 would underestimate b^*_{MSS} at high values, therefore it would be expected that modelled MSS concentrations would be overestimated. On further investigation it

became apparent that the tendency of the relationship in figure 5.19 to veer off the 1:1 agreement at high concentrations was driven by a single station (where MSS = 23 mg l^{-1}), where b$^*_{MSS}$ was actually overestimated, as highlighted on figure 5.16. The average percentage error in the estimated MSS concentrations was 23%, which is not significantly different from the uncertainty associated with predictions based in the simple reflectance algorithm in Chapter Four. This technique will be tested further in the next chapter when it will be applied to independent data sets of ocean colour.
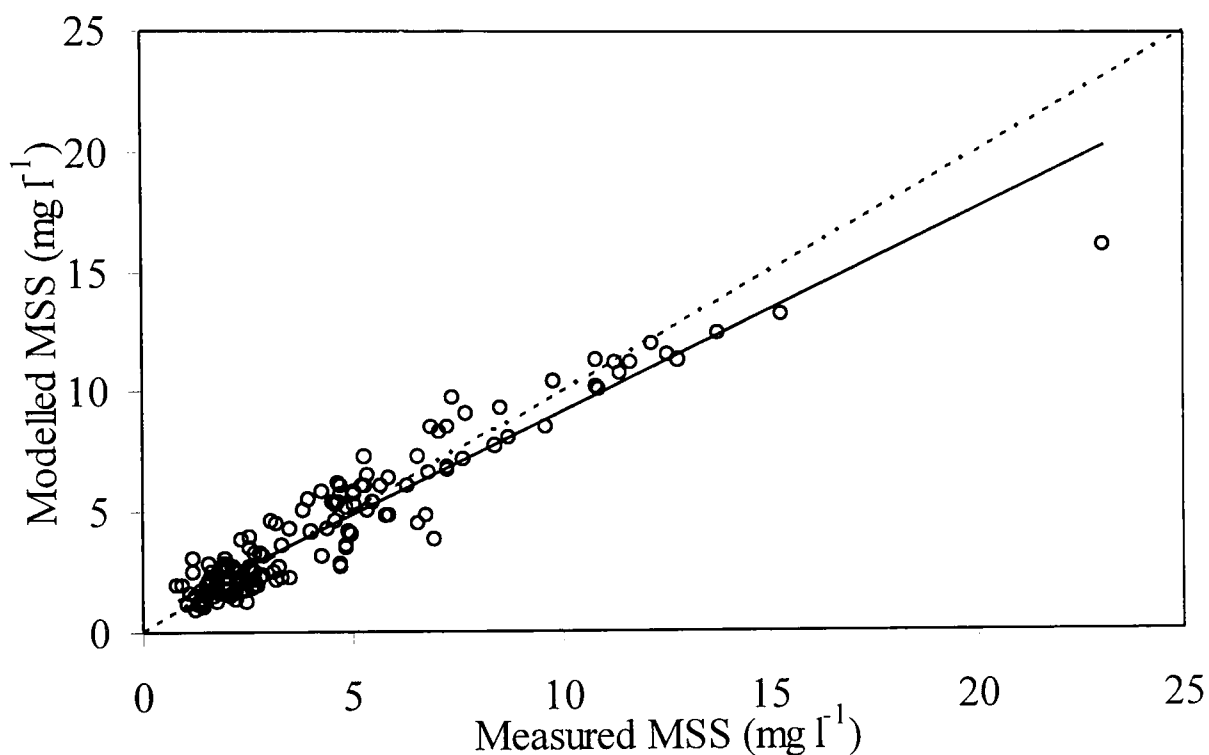
Figure 5.19: Modelled versus measured MSS concentration following correction for variations in particle scattering. Dashed line represents the 1:1 relationship.

5.6   Discussion

Variability in the Reflectance-MSS relationship in the Irish Sea has been shown to be the consequence of changes in mass-specific scattering coefficients brought about by differences in particle properties such as grain size and refractive index. These observations testify to the potential difficulty of remotely sensing suspended sediment concentrations from waters in which particle properties can vary considerably in both space and time. For distinct categories of particle scattering coefficients, a robust relationship has been found between reflectance at 665 nm and mineral suspended sediment concentrations. The systematic increase in the slope of the Reflectance-MSS relationship with increasing b^*_{MSS} may go some way to explaining the differences in previously published sediment algorithms. The obvious discrepancy between results of Bukata *et al.* (1988) and those presented in this study was highlighted in Chapter Four, where a reflectance of 11% measured by Bukata corresponded to an MSS concentration of 9 mg l^{-1}, compared with 15 mg l^{-1} in this study. This may be explained now by the fact that Bukata's measurements were of lake sediments which, because of reduced turbulence, may have been finer particles (therefore enhancing scattering). In an earlier study, Bukata *et al.* (1983) presented mineral scattering coefficients, for the same lake, ranging from 0.4 to 0.6 m^2 g^{-1} which are greater than the average Irish Sea b^*_{MSS} used in Chapter Four.

The importance of the accurate determination of particle scattering properties is highlighted in results of the optical model. When used in the forward mode to predict reflectance from concentrations of the optically active constituents, the error in predicted reflectance is reduced from 165% to 9% by accounting for variations in b^*_{MSS}. With knowledge of the particle scattering coefficient, b^*_{MSS}, concentrations of MSS can be predicted from this model, used in the inverse mode, with an average uncertainty of 14% compared with 22% for a simple single-band reflectance algorithm. The difficulty lies in the estimation of b^*_{MSS} and/or b_b/b. This has been partially overcome by using an empirical relationship between the factor λ_{peakR}/R_{665} and b^*_{MSS}, which enables the prediction of b^*_{MSS} with an average uncertainty of 24%. Whilst the use of λ_{peakR}/R_{665} gives a reasonable approximation of the value of b^*_{MSS}, there is substantial spread in the data that needs to be resolved so as to reduce the error incurred in the derived sediment concentrations. The use of hyperspectral ocean colour observations may improve the b^*_{MSS} estimated from the peak wavelength

technique, although this has limited applications in satellite remote sensing until sensors with hyperspectral capabilities are in routine use.

The values of b^*_{MSS} observed in this study are comparable with other studies in the Irish Sea (Bowers et al., 1996; Bowers and Mitchelson-Jacob, 1996; Harker, 1997) and also fall within the ranges found in the literature as estimated from other techniques. In this study, b^*_{MSS} ranged from 0.04 to 0.49 m^2 g^{-1} at 665 nm. Models using anomalous diffraction theory (Van de Hulst, 1957) showed specific scattering coefficients for particles to vary from 0.238 to 0.006 m^2 g^{-1} (at 750 nm) as particle diameters increased from 5.5 to 100 μm. A study by Doxaran et al. (2002a) showed the spectral variation of reflectance up to 900 nm, for different sediment loads, and showed that following a peak in reflectance between 600 and 700 nm, there was a consistent trough at 750 nm before increasing again further into the infra-red. It is feasible, therefore, that b^*_{MSS} at 665 nm may be larger than that calculated by Van de Hulst (1957) at 750 nm, which would be in agreement with those found here.

Inversion of IOPs from tank experiments measuring reflectance of turbid waters produced particle scattering coefficients ranging from 0.032 to 0.295 m^2 g^{-1} (Moore et al., 1999). Again, these are lower than found in the present study, which may be explained by the fact that Moore et al. (1999) used a backscattering efficiency factor (b_b/b) of 0.025, compared with the 0.019 used in this study. Furthermore, it is not made clear in Moore et al. (1999) if the scattering coefficients are based on total SPM, or the mineral fraction.

Scattering by sediments is dependent on the sediment type through variations in both grain size and the refractive index. By combining Mie theory and reflectance modelling, Forget et al. (1999) showed that, as would be expected, for a fixed mass of sediment reflectance is enhanced by increasing the relative number of small particles and lowered by increasing the number of large particles. In agreement, Moore et al. (1999) showed, using tank experiments, that the relationship between reflectance and the concentration of particles varied between different sediment types and between size-fractionated sediments of the same type, with the smaller fraction of each sediment having a greater reflectance for the same mass-concentration. Scattering, and therefore reflectance, are dependent on the optical cross-sectional area of the

particles (d^2). Suspended particle concentrations, however, are a volumetric quantity (d^3), so this suggests that a Reflectance-MSS relationship would indeed be sensitive to changes in grain size. Woodruff *et al.* (1999) found a strong relationship between reflectance in the red (580-680 nm) from the broad-band satellite sensor AVHRR (the Advanced Very high Resolution Radiometer) and K_{PAR}, the diffuse attenuation coefficient for PAR, under varying environmental conditions including changes in grain size. Since both K_d and R are dependent on the cross sectional area of particles, this relationship would be independent of grain size.

In this study, a limited data set showed a strong negative correlation between b^*_{MSS} and grain size, where b^*_{MSS} coefficients up to 0.15 m^2 g^{-1} were observed for particles diameters in the range 25-80 μm. This is in reasonable agreement with those scattering coefficients derived by Van de Hulst (1957) for a similar range of grain sizes. Although in this study, grain size measurements were only available for one of the cruises, a study by Jones *et al.* (2000) in the Celtic Sea showed clear increases in particle grain sizes during the summer months from LISST measurements, thus supporting the suggestion that scattering coefficients decrease in the summer months due to particle flocculation associated with increasing organic matter. Results in Jones *et al.* (2000) showed the mean particle diameters in the middle of St George's Channel to vary from approximately 35μm in March and September 2000 to over 70 μm in June 2000.

In addition to grain size, the scattering properties are controlled by the refractive index (n_p) of the particles in suspension, which is a function of particle composition and can, therefore, be related to the backscattering coefficient. The index of refraction typically ranges from 1.14 - 1.26 for mineral particles and from 1.02 - 1.07 for phytoplankton (Zaneveld *et al.*, 1974; Twardowski, *et al.*, 2001). Living cells are at the low end of the range because of their relatively high water content (40-80%). Baker and Lavelle (1984) showed that if particle size and shape were held constant, particulate scattering coefficients increased with increasing refractive index. Using the models of Twardowski *et al.* (2001), refractive indices of particles were estimated for two cruises in this study; the Irish Sea in November 2001 and the Clyde Sea in April 2001. The derived n_p are realistic and fall within a range of indices found in the

literature for similar particle types, with average values of 1.08 for the phytoplankton-dominated waters of the Clyde Sea and 1.18 for the predominantly mineral particles of the Irish Sea in winter.

Results presented in this chapter are in overall agreement with those of Doxaran *et al.* (2002a), who, whilst having no observations of scattering coefficients, modelled the effect of variations in the refractive index of particles on reflectance. They showed that particles of greater refractive index, for example mineral sediments, produce larger reflectance than a lower refractive index associated with organic matter. Forget *et al.* (1999), by incorporating Mie theory into a reflectance model, also found reflectance to be highly sensitive to variations in refractive index.

In some studies, it has been suggested that the variability in reflectance induced by changes in particle characteristics can be reduced by studying reflectance ratios (Moore *et al.*, 1999; Doxaran *et al.*, 2002a, 2002b), based on the assumptions that scattering by minerals is sufficient to assume negligible scattering by any other parameter and that there is no spectral variation in the scattering parameters. These studies, however, have been based on either laboratory experiments (Moore *et al.*, 1999) in which there is only one variable sediment characteristic or on *in situ* observations based on a single survey or single season in extremely turbid waters (Doxaran *et al.*, 2002a), in which case there may be little variation in b^*_{MSS} or b_b/b.

The present study covers the annual variability in sediment scattering properties from different regions of the Irish, Celtic and Clyde Seas, therefore sampling a wide range of b^*_{MSS} and b_b/b. Contrary to the above assumptions, this study found that b^*_{MSS} and b_b/b not only change with particle composition, but could also exhibit significant variation with wavelength.

Chapter Six

Algorithm Validation in the Menai Strait and Results from SeaWiFS Satellite Imagery

CHAPTER SIX: ALGORITHM VALIDATION IN THE MENAI STRAIT AND RESULTS FROM SEAWIFS SATELLITE IMAGERY

6.1   Introduction

The previous two results chapters have dealt with the development of a technique for determining suspended sediment concentrations from *in situ* ocean colour measurements. This next results chapter shows how those techniques were applied to two independent ocean colour data sets as an algorithm validation exercise. Section 6.2 presents a time series of *in situ* reflectance observations obtained during a period of sampling in the Menai Strait between March and October 2001. This provided a data set that was used to test the accuracy of the algorithm in determining MSS concentrations from reflectance measurements that were not used in the initial algorithm development. The validation process was taken one step further in section 6.3 by applying the same techniques to SeaWiFS ocean colour imagery of the Irish Sea. A moored transmissometer provided a time series of suspended sediment concentrations for comparison with the algorithm results.

6.2   Menai Strait Time Series

6.2.1   Measured Optically Active Constituents

Measured concentrations of phytoplankton pigments (chlorophyll *a* and phaeopigments) in the Menai Strait identified a double phytoplankton bloom in the spring of 2001, with maximum concentrations of chlorophyll in March/April and May/June (figure 6.1). This double peaked spring phytoplankton bloom is a common feature in the Menai Strait also observed by Blight *et al.* (1995) and Kratzer *et al.* (2000). Maximum phaeopigment concentrations occurred shortly after the peak in chlorophyll concentrations, reflecting the successive breakdown of the blooms. Pigment concentrations were minimal over the summer months from late June onwards and remained low for the rest of the year. Phytoplankton species counts identified the beginning of a *Phaeocystis* bloom in May (Shon, pers. comm.) as indicated by the arrow in figure 6.1.
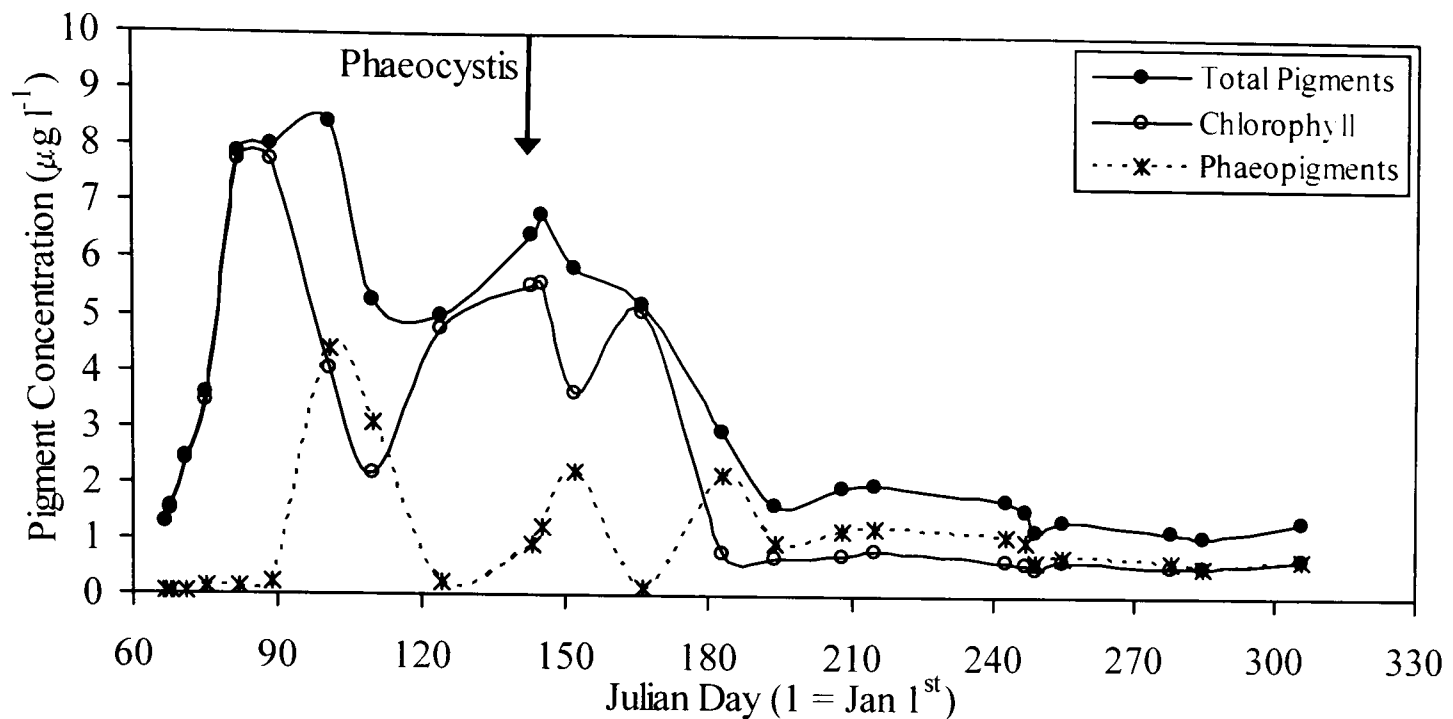
Figure 6.1: Time series of phytoplankton pigment concentrations in the Menai Strait during 2001.

Total suspended sediment (TSS) concentrations ranged from 6 to 16 mg l^{-1} over the sampling period, whilst MSS concentrations reached a maximum of 12 mg l^{-1} in February (figure 6.2). This is considerably lower than that found in previous studies in the Menai Strait by Buchan *et al.* (1967) and Kratzer *et al.* (2000), who observed maximum concentrations of 50 mg l^{-1} in December 1962 and 25 mg l^{-1} in November 1996 respectively, although it is acknowledged that measurements in this study were not taken between November and January.

The largest proportions of organic suspended material (minimum MSS/TSS) coincided with the timing of the spring bloom through April and May. Ratios of MSS/TSS were as little as 40% until May and then increased to 70-80% from June through to October. The MSS/TSS ratio was high even towards the end of the spring bloom and particularly when there was *Phaeocystis* present. *Phaeocystis pouchetii* has two stages of growth; a unicellular flagellate phase and a secondary gelatinous colonial phase (Van de Hoek *et al.*, 1995). When nutrients in the water column become scarce, the single cells aggregate into a colony, surrounded by a sticky, mucous membrane, within which they are able to store nutrients. *Phaeocystis* may, therefore, result in the enhanced flocculation of mineral suspended sediment, which, with a resulting decrease in average density, would enable increasing concentrations of MSS to remain in

suspension, thus increasing the observed MSS/TSS ratio.
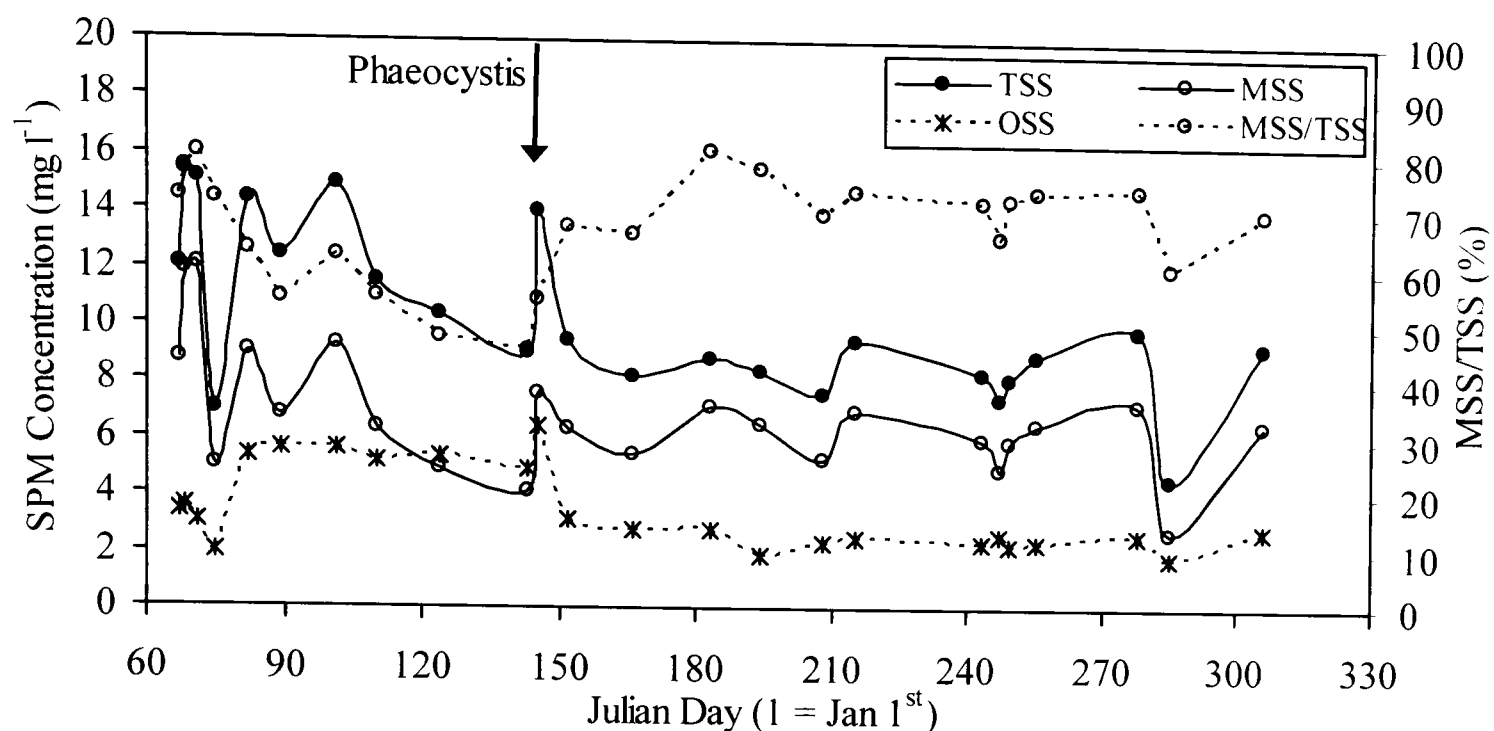
Figure 6.2: Time series of suspended particulate matter concentrations in the Menai Strait during 2001.

Whilst sediment concentrations were not as high as previously measured in the Menai Strait, this was still a scattering dominated environment, with the average ratio of scattering to absorption (b/a) reaching as high as 13.33 at 555 nm (table 6.1). Even at 665 nm, where absorption by water is high, optical properties were still dominated by scattering.

Table 6.1: Scattering to absorption ratios (b/a) in the Menai Strait for all wavebands, as derived from the PRR600.

	b/a 412	b/a 443	b/a 490	b/a 510	b/a 555	b/a 665
Average	3.00	4.22	6.03	6.57	7.71	2.70
Maximum	6.03	8.20	11.26	12.05	13.33	6.55
Minimum	1.02	1.40	2.18	2.57	3.69	1.07

6.2.2   Reflectance Algorithm Results

The simple reflectance algorithm (quadratic function of R_{665}) was applied to the Menai Strait reflectance measurements to predict MSS concentrations (figure 6.3). The

algorithm reproduced the trends in MSS concentrations over the year with reasonable accuracy, particularly in the winter months, although the concentrations were consistently underestimated (figure 6.4). The average percentage difference between the observed and predicted MSS concentrations over the whole sampling period was 31.4%. In the summer months (June-August), however, the algorithm underestimated MSS concentrations by an average of 50%.
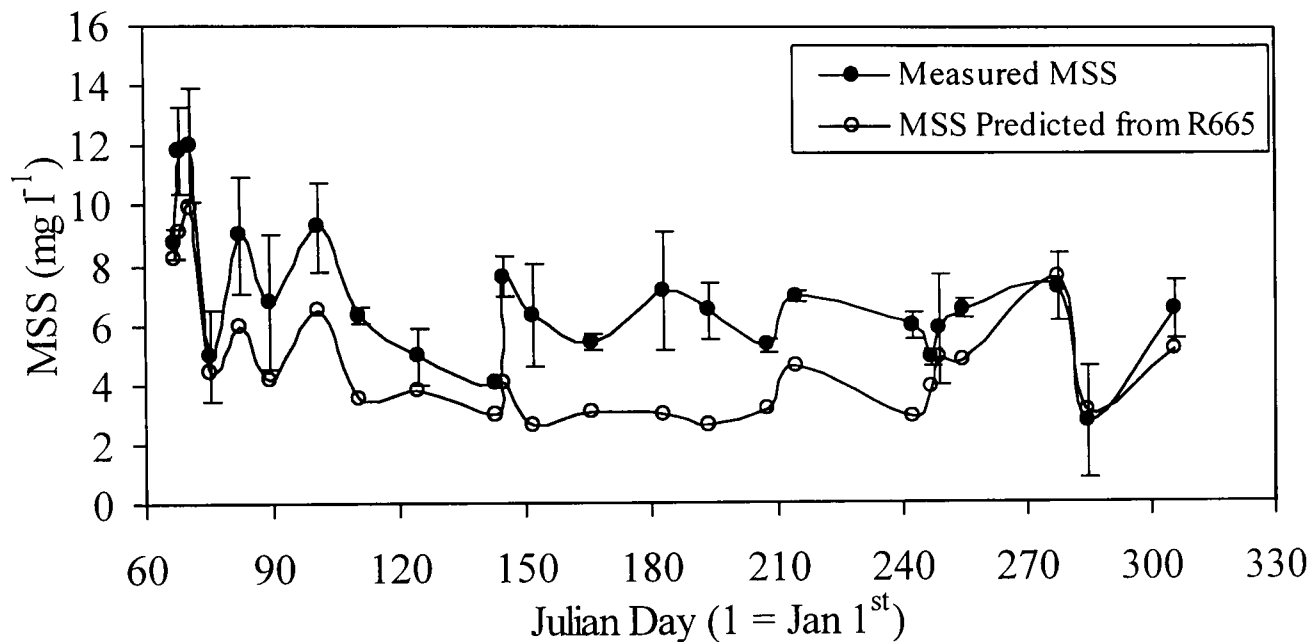
Figure 6.3: Time series of MSS concentrations predicted from R_{665} compared with measured MSS concentrations.
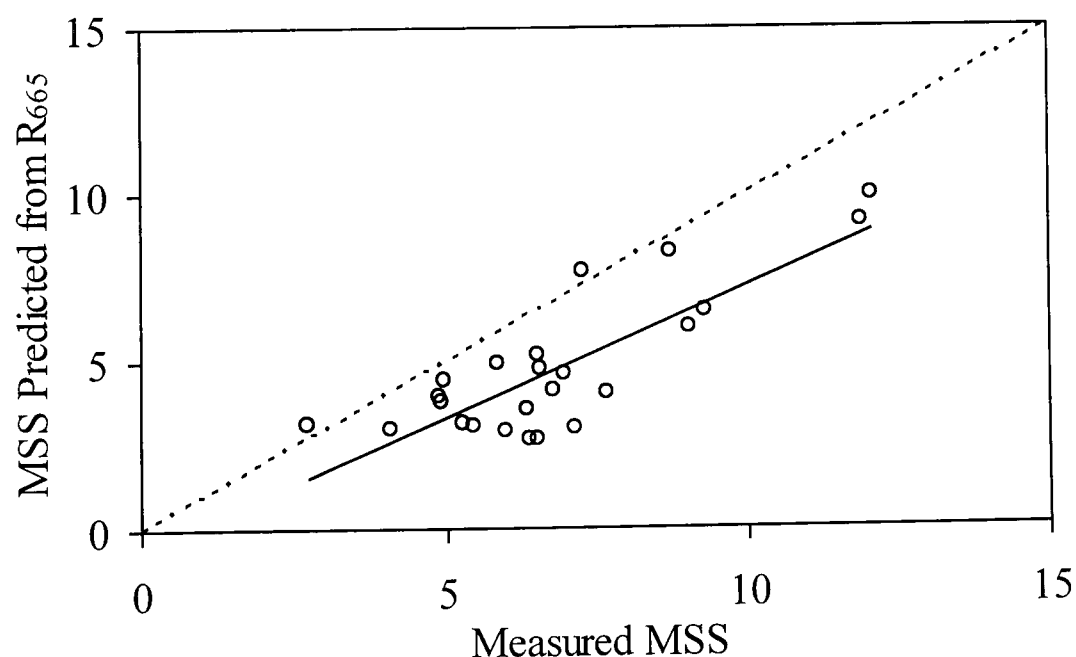
Figure 6.4: MSS concentrations measured in the Menai Strait versus concentrations predicted from R_{665}. Dashed line represents the 1:1 relationship.

The underestimation of the MSS concentrations over the year suggests that suspended particles in the Menai Strait may have been less efficient scatterers (lower b^*_{MSS}) than the particles in the rest of the Irish Sea where the algorithm had been developed. The role of variable b^*_{MSS} in the accuracy of algorithm predictions and factors controlling b^*_{MSS} in the Menai Strait will be discussed in the following sections.

6.2.3 The Effect of Variable Particle Scattering on Predicted MSS

In order to test the dependence of the algorithm results on the scattering efficiency of the particles in suspension, the MSS-specific scattering coefficients were estimated using methods described in earlier chapters. Values of b^*_{MSS} ranged from a minimum of $0.08 \, m^2 \, g^{-1}$ in mid July to $0.38 \, m^2 \, g^{-1}$ in March. This compares with a range of $0.04 \, m^2 \, g^{-1}$ to $0.49 \, m^2 \, g^{-1}$ observed throughout the Irish Sea and shows that, on average, particles in suspension in the Menai Strait are indeed less efficient scatterers than those held in suspension in the Irish Sea. Figure 6.5 shows the variation of the derived b^*_{MSS} over the year plotted with the ratio Predicted MSS/Measured MSS from the simple reflectance algorithm results. The similarity in pattern over the year, suggests that the variations in particle scattering have a key influence on the success of the reflectance algorithm in deriving MSS concentrations. This is confirmed in figure 6.6 where 56% of the variation in the ratio Predicted MSS/Measured MSS is attributed to variations in b^*_{MSS}.
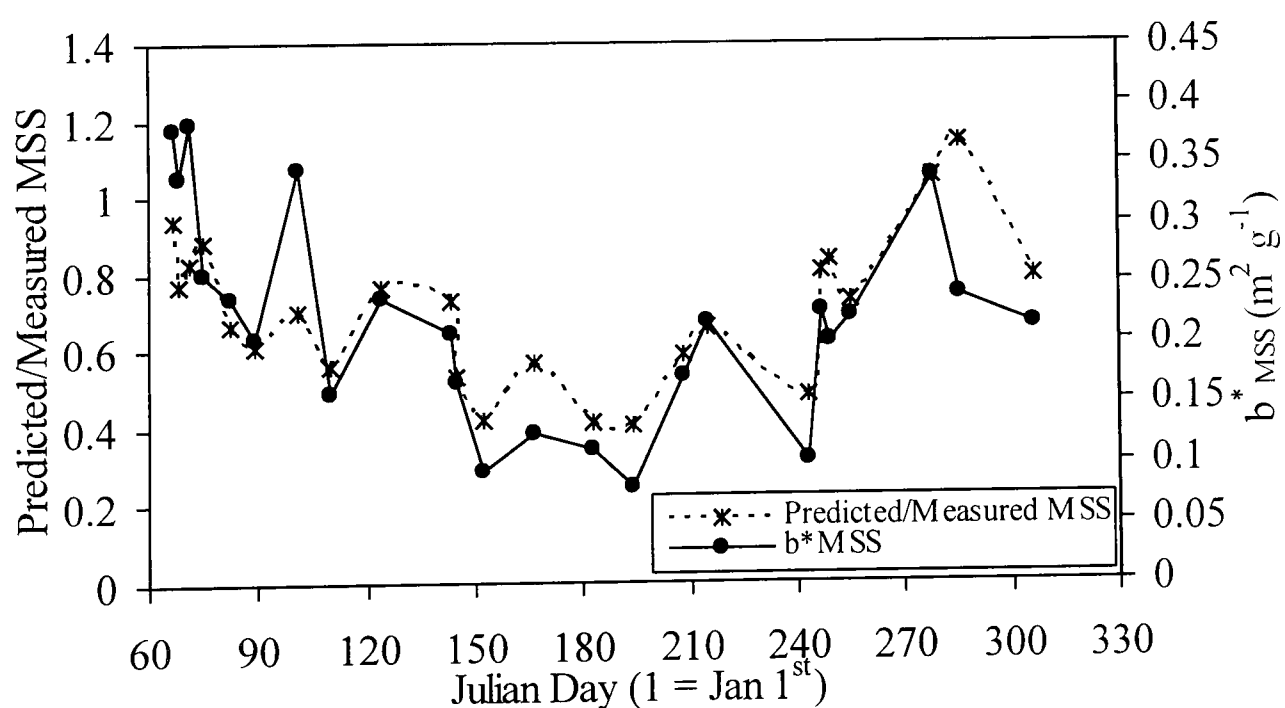
Figure 6.5: Variation of b^*_{MSS} in the Menai Strait over the year compared with the ratio Predicted/Measured MSS.
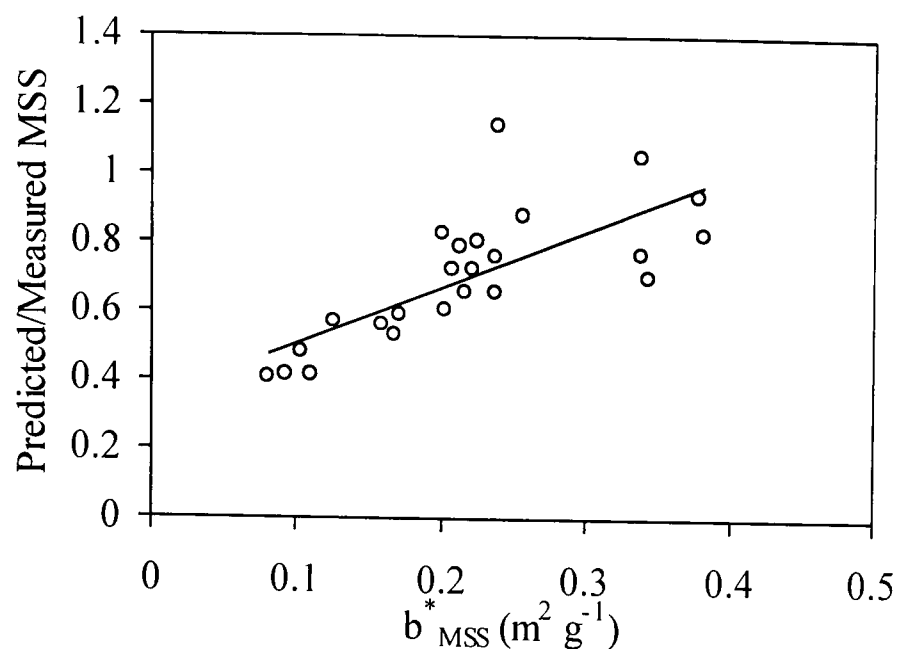
Figure 6.6: **The ratio of MSS predicted from R$_{665}$ to measured MSS against measured b*$_{MSS}$ for all sampling occasions in the Menai Strait.**

6.2.4 Factors Affecting Particle Scattering Properties

Values of b*$_{MSS}$ estimated from the Menai Strait data series display a pronounced seasonal cycle, with a minimum in the summer months, which can be expressed as a co-sinusoidal curve such that

$$b^{*}_{MSS} = (0.258 \pm 0.014) + (0.128 \pm 0.024)\cos\omega\, t \tag{6.1}$$

$$(R^2 = 56\%, p = 0.00)$$

where ω is the angular frequency of the annual cycle and is given by $2\pi/T$. T is the number of days in the year and t is the day of the year (t = 1 on January 1st).

The relationship between b*$_{MSS}$ and the ratio MSS/TSS that was found in the Irish Sea (as presented in Chapter Five) was not seen in the Menai Strait (Pearson Correlation = 0.1). As was mentioned earlier, the phytoplankton species *Phaeocystis* is known to play a significant role in the aggregation of suspended particles. *Phaeocystis* may result in the accumulation of mineral sediment, which, by increasing the average particle grain size and decreasing the refractive index, would result in a lower scattering efficiency as suggested by figure 6.7.
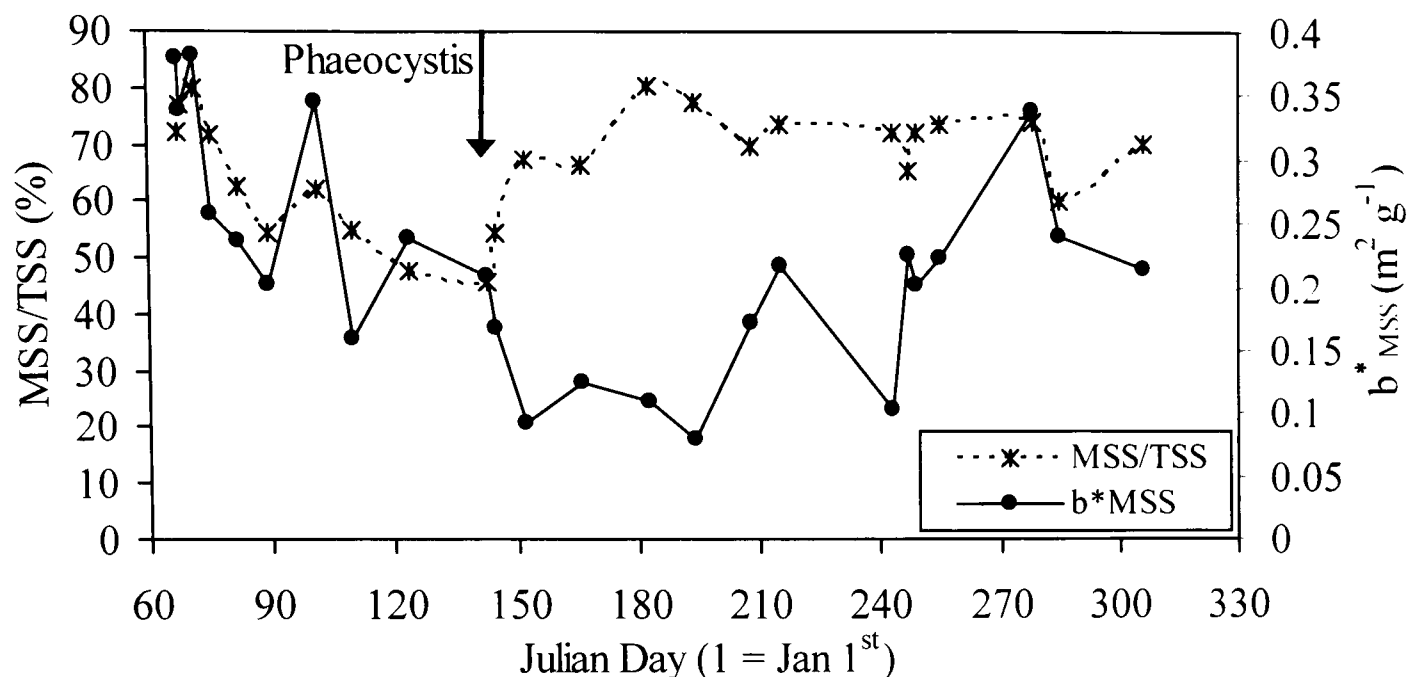
Figure 6.7: Time series of b*$_{MSS}$ and MSS/TSS in the Menai Strait during 2001.

It might be expected that b*$_{MSS}$ may have an inverse relationship with tidal range based on the fact that stronger tidal currents during spring tides would suspend larger particles than in weaker currents during neap tides. This, however, does not appear to be the case (figure 6.8), with a positive correlation found between the two parameters (Pearson Correlation = 0.58).
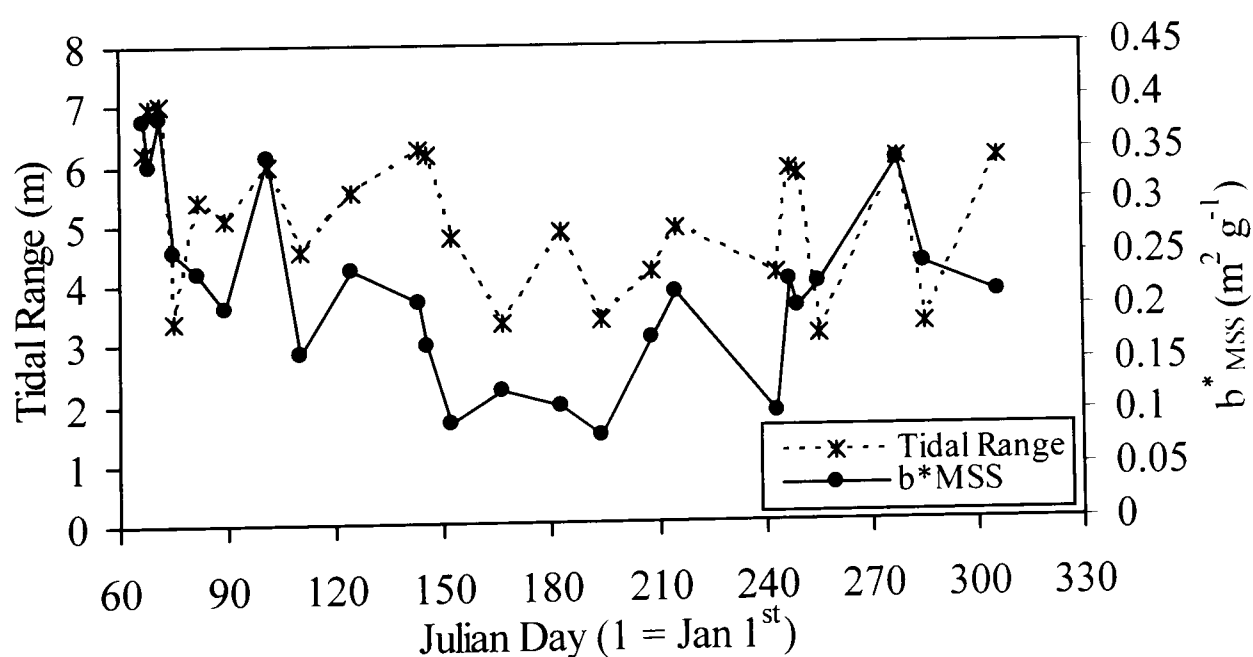
Figure 6.8: Time series showing tidal range at Menai Bridge and the variation of b*$_{MSS}$ in the Menai Strait during 2001.

It is suggested, therefore, that the observed seasonal cycle may be a consequence of a number of processes working to both bind and break apart sediment aggregates (thus altering particle size and refractive index). Although not a strong relationship, figure 6.9 suggests that at small tidal ranges (and inferring from this, low tidal stirring), b^*_{MSS} begins to increase. This observation is in agreement with suggestions that particle size variations due to flocculation have a two-way dependence on turbulence. Mixing is firstly required to create collision occurrences between particles up to a threshold where too much turbulence then tears the particles apart again (Jones, Pers. Comm.). Therefore, at low tidal energies, fine particles may result in high b^*_{MSS}, whereas at intermediate tidal energies, increased particle collision may aid flocculation sufficiently to decrease b^*_{MSS}. At high tidal energies, turbulence may act to tear the flocs apart, reducing again to finer particles and thus increasing b^*_{MSS}.
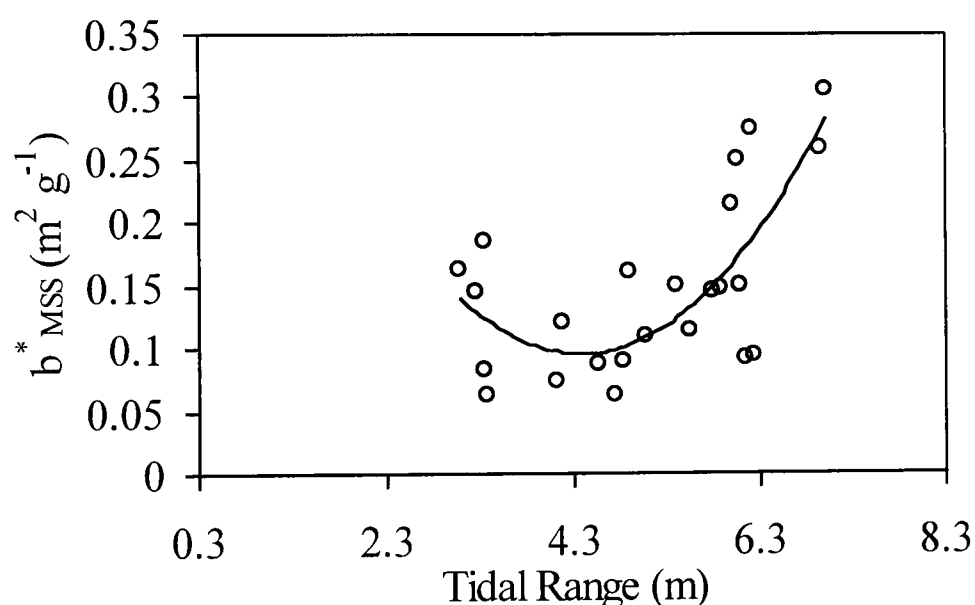
Figure 6.9: Relationship between tidal range at Menai Bridge (as a proxy for tidal stirring intensity) and b^*_{MSS}. ($y = 0.027x^2 - 0.237x + 0.61$, $R^2 = 53.9\%$, p=0.0).

Values of b^*_{MSS} were estimated from the peak wavelength technique described in Chapter Five and are presented in figure 6.10 plotted against the measured b^*_{MSS}. Although there was a strong correlation (Pearson Correlation = 0.90) between measured and predicted values, the method overestimated b^*_{MSS} at low values and underestimated at high values.
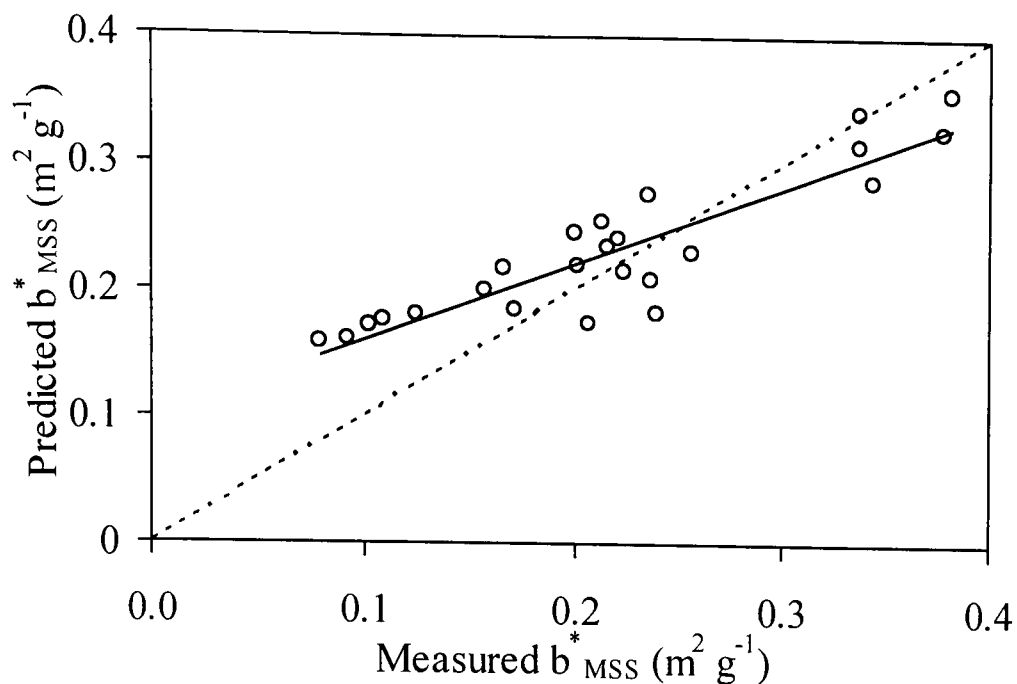
Figure 6.10: b^*_{MSS} predicted from the peak wavelength technique versus measured b^*_{MSS}. Dashed line represents the 1:1 relationship.

This offset in the predicted b^*_{MSS} has a clear effect on the estimated seasonal cycle of b^*_{MSS} as indicated in figure 6.11, by overestimating summer mass-specific scattering coefficients by as much as 60%. This can be explained by returning to the method by which b^*_{MSS} is predicted. Figure 6.12 shows the λ_{peakR}/R_{665} versus b^*_{MSS} relationship presented in Chapter Five with observations from the Menai Strait time series superimposed. The Menai Strait data points can be seen to follow the line of those Irish Sea stations least influenced by organic matter. Because of the large spread in the data points at mid scattering coefficients, the best fit line is drawn away from the lower scattering coefficients in the Menai Strait data, thus resulting in the overestimated scattering coefficients seen in figures 6.10 and 6.11.

| x | Menai Strait Measured b*MSS | ------ Best Fit to Measured Menai b*MSS |
| o | Menai Strait Predicted b*MSS | ——— Best Fit to Predicted Menai b*MSS |
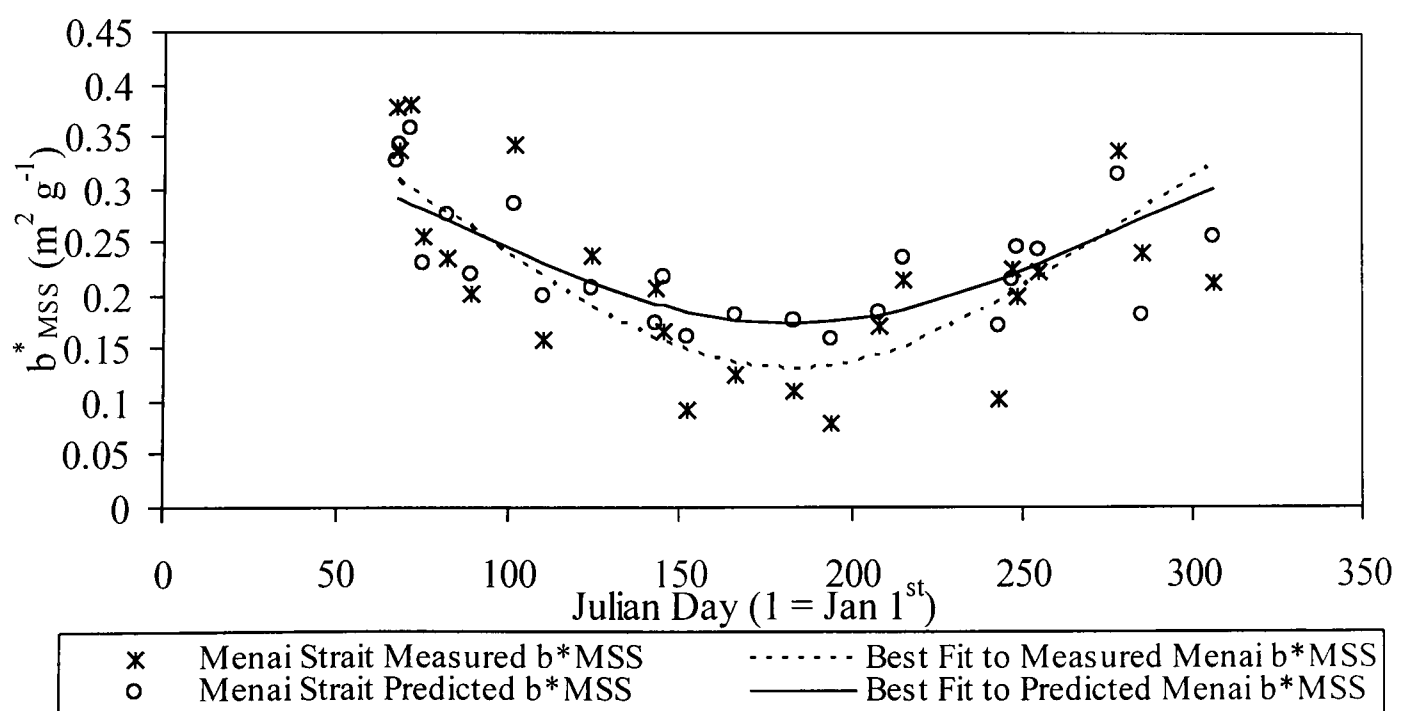
Figure 6.11: Seasonal cycle of b^*_{MSS} as measured from *in situ* observations and predicted from λ_{peakR}/R_{665}.
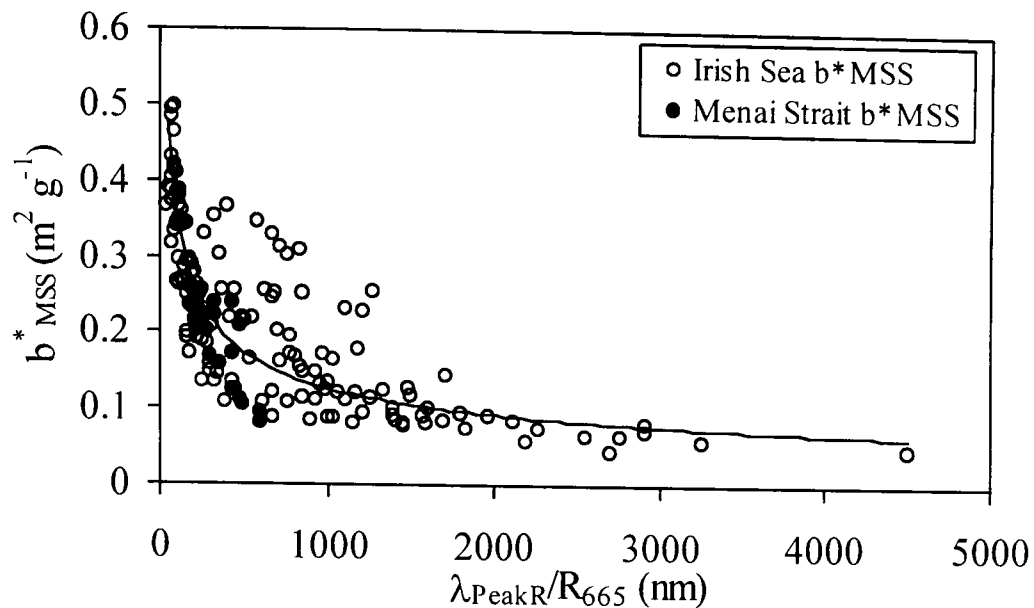
Figure 6.12: The relationship between b*$_{MSS}$ and λ_{peakR}/R$_{665}$ for all Irish Sea stations, with data from the Menai Strait superimposed.

6.2.5 Reflectance Model Results

The reflectance model, developed in Chapters Four and Five, was applied, in the forward modelling mode, to the Menai Strait data set. By inputting the measured concentrations of MSS, C and YS, the measured b*$_{MSS}$ and the inherent optical properties of each other constituent as previously derived for the Irish Sea, the reflectance at 665 nm was reproduced with an average difference between modelled and measured reflectances of 9.5% (figure 6.13).
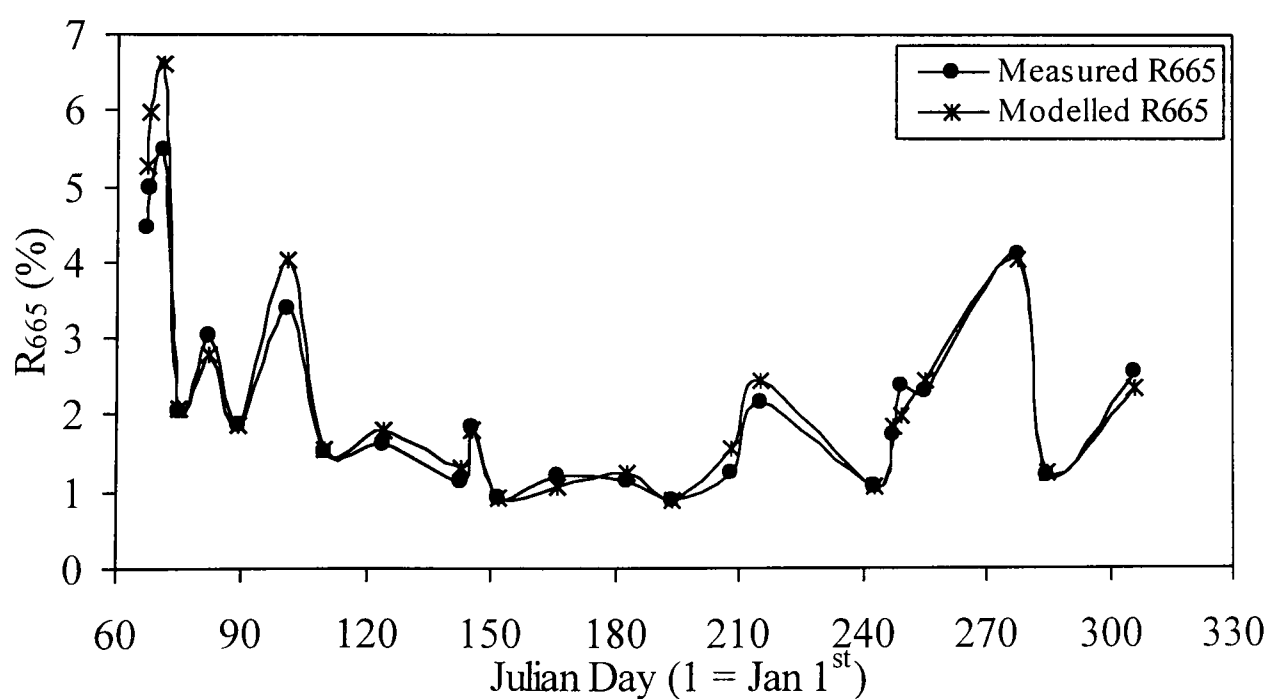
Figure 6.13: R$_{665}$ modelled from known concentrations of MSS, C and YS.

The correct reproduction of measured reflectance in this independent experiment confirms the accuracy of the inherent optical properties adopted in the reflectance model. Furthermore, it suggests that whilst b^*_{MSS} has been shown to be significantly different in the Menai Strait than in the Irish Sea, the remaining IOPs cannot vary all that much since little error is introduced into the predicted reflectances by using average IOPs for the Irish Sea. By removing the influences of YS and C from the optical model such that R_{665} is determined solely by water and MSS, the average difference between modelled and observed reflectance is increased to 20.5%. Whilst the difference between modelled and measured R_{665} is most pronounced during the spring bloom (figure 6.14), reflectance is still reproduced well for the rest of the year.
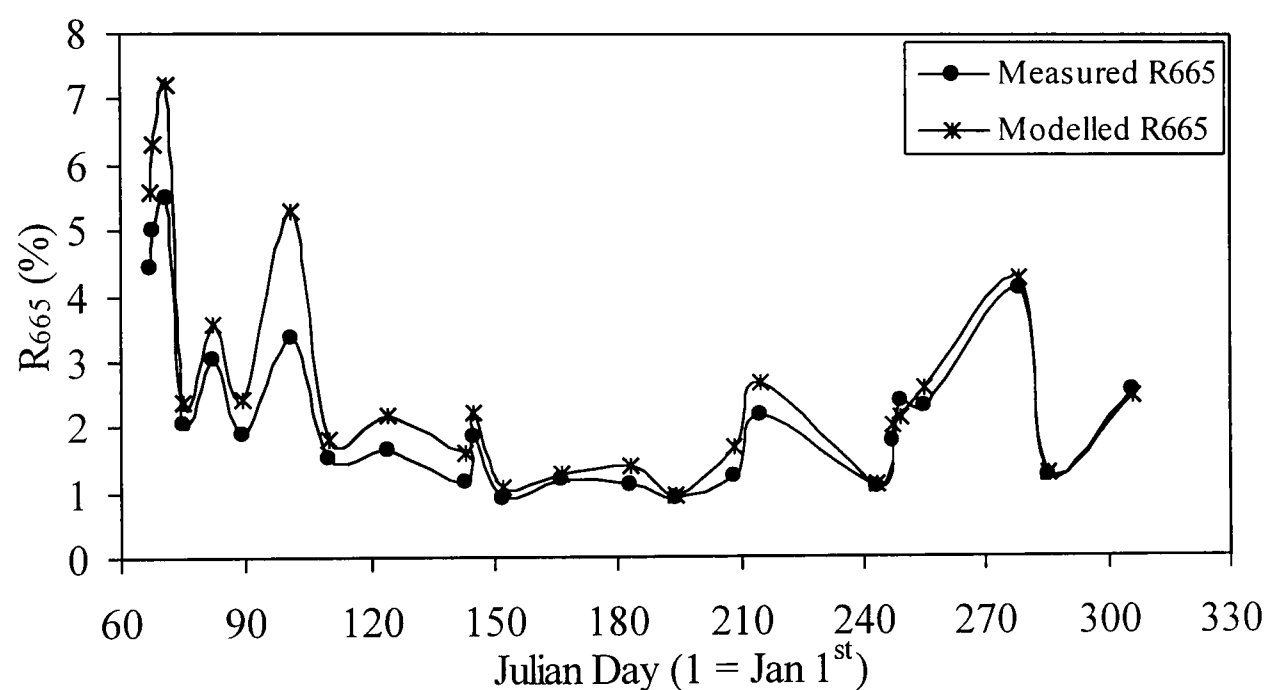
Figure 6.14: R_{665} modelled using a simple 2-parameter optical model neglecting the effects of C and YS.

The same reflectance model was used in the inverse mode, as described in Chapter Five, to predict MSS concentrations from the measured reflectance according to equation 6.2.

$$MSS = \frac{R\,a_w}{C(\mu_0)\,\frac{b_b}{b}\,b^*_{MSS} - R\,a^*_{MSS}}$$

(6.2)

Absorption coefficients and the backscattering probability were assumed to be the same as those used in Chapters Four and Five. A time series of MSS concentrations in

the Menai Strait predicted from this modelling technique is presented in figure 6.15 along with both gravimetrically measured concentrations and MSS predicted from the simple reflectance algorithm. Predicted MSS concentrations resulting from this inverse modelling are improved considerably compared with the results of the simple reflectance algorithm, with the percentage difference between observed and predicted MSS reduced from 31.4% to 12.8% and the predicted concentrations lying reasonably on the 1:1 line against the measured MSS in figure 6.16 ($R^2 = 76.3\%$). The improved predictions are most pronounced in the summer months where the simple algorithm underestimated MSS by as much as 60%.
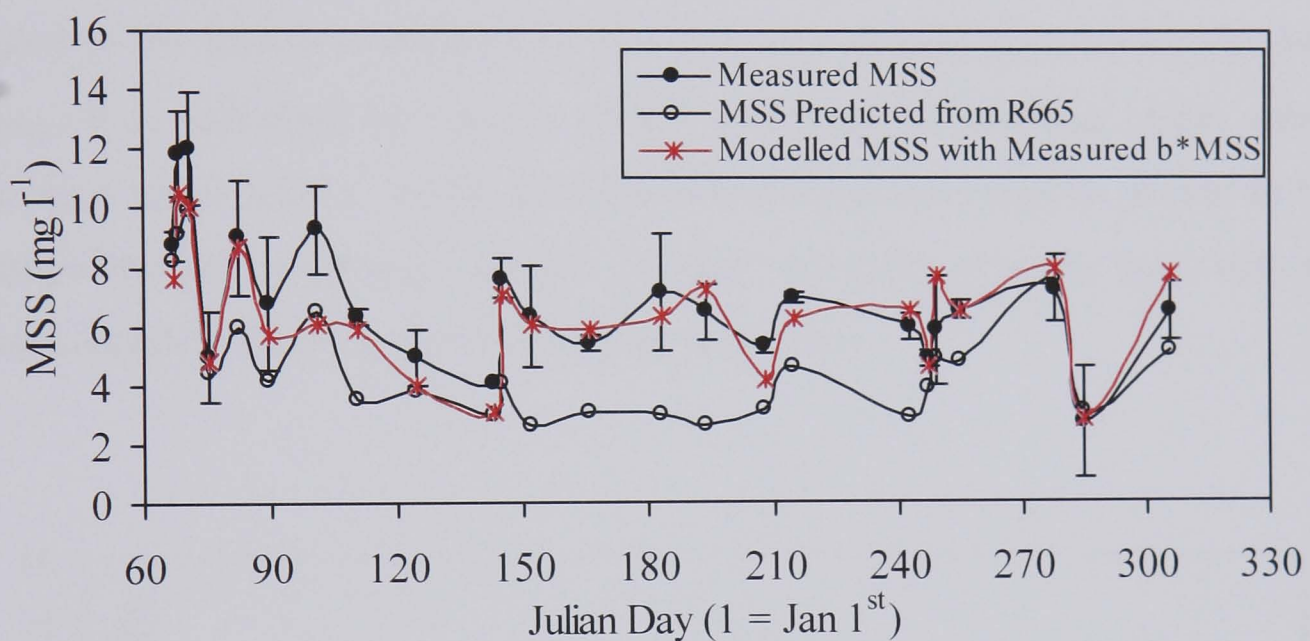
Figure 6.15: **Improvement in predicted MSS concentrations after correcting for variations in b^*_{MSS} using a simple 2-parameter reflectance model.**
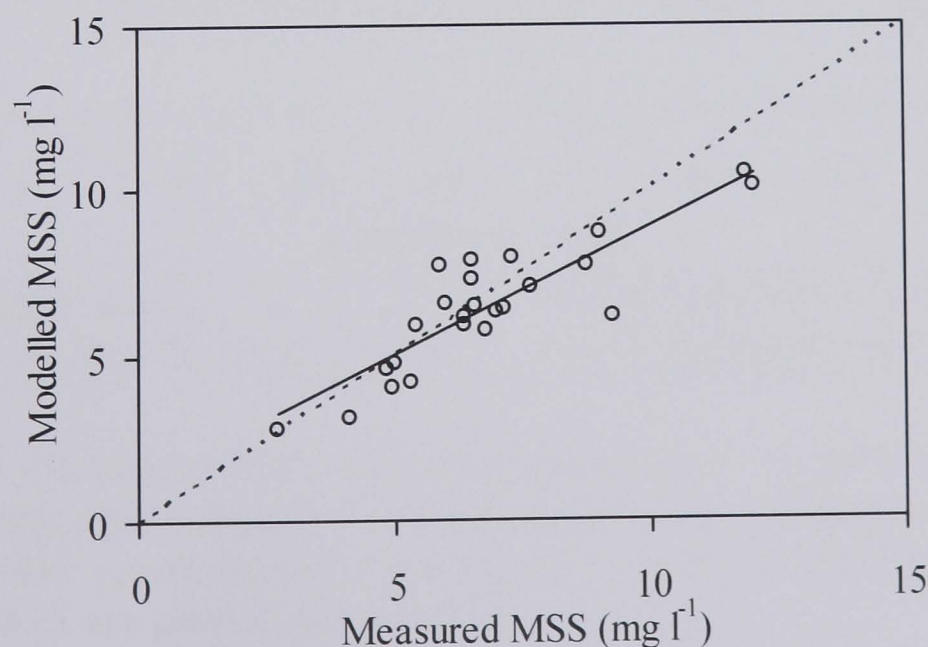
Figure 6.16: MSS concentrations measured in the Menai Strait versus concentrations modelled from known R_{665} and b^*_{MSS}. Dashed line represents the 1:1 relationship.

Figure 6.15 and 6.16 highlight the improved accuracy in MSS determinations when values of b^*_{MSS} are known. However, when not known, it is necessary to predict b^*_{MSS} from the techniques previously described. Predictions of MSS concentrations were obtained (figure 6.17) through inverse modelling using values of b^*_{MSS} predicted both from the parameter λ_{PeakR}/R_{665} and from a simple seasonal cycle (equation 6.1). A summary of the uncertainty in each of the methods of predicting MSS (table 6.2) shows that on average, using the λ_{PeakR}/R_{665} method to obtain b^*_{MSS} values reduces the uncertainty in predicting MSS concentrations by 10% compared with results of the simple reflectance algorithm. MSS concentrations are, nevertheless, still underestimated in the summer months (by an average of 38%), which can now be attributed to the known overestimates of low b^*_{MSS} brought about by interference in the λ_{PeakR}/R_{665} technique by organic matter scattering. A seasonal cycle, although producing a lower error in predicted MSS over the summer months, proves to be an oversimplification, producing a greater average variability over the year, with some unreliable predictions towards the end of the time series.
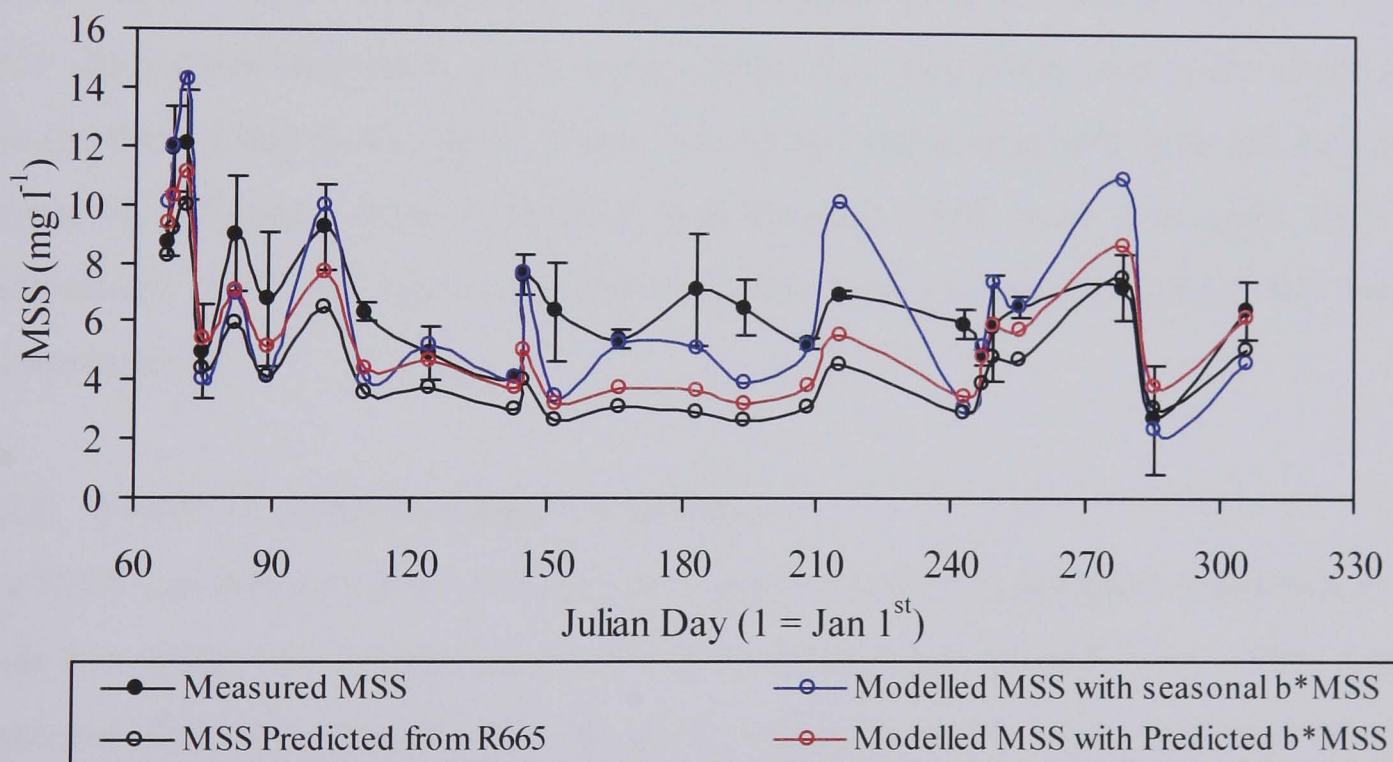
Figure 6.17: Modelled MSS concentrations using b^*_{MSS} predicted from the λ_{peakR} technique (in red) and b^*_{MSS} predicted from a simple seasonal cycle (in blue). MSS predicted from the simple reflectance algorithm and true measured MSS are plotted for reference.

Table 6.2: Average percentage difference between measured and predicted MSS concentrations using the various predictive techniques discussed in the text.

	Simple R_{665} Algorithm	Reflectance model with known b^*_{MSS}	Reflectance model with seasonal b^*_{MSS}	Reflectance model with b^*_{MSS} predicted from peak λ/R_{665}
All Dates	31.35	12.78	33.58	21.97
Summer Only	49.51	10.92	25.12	38.47

6.3   SeaWiFS Imagery Validation in the Irish Sea

Taking the algorithm validation one step further, the same techniques were applied to a series of SeaWiFS satellite images of the Irish Sea. A total of 78 SeaWiFS images were processed from 1999 and 2000 for the completion of this work. Image processing models were written in order to produce further daily maps of spectral reflectance (R), MSS concentrations as estimated from the simple quadratic function of R_{665}, peak wavelength, b^*_{MSS}, and a revised MSS concentration corrected for variations in b^*_{MSS}. In addition, chlorophyll maps were produced from the NASA OC4 chlorophyll algorithm. Only those images that were clear over most of the Irish Sea (or those clear in the region where the moored transmissometer was located) were processed. Images from September and October 1999 were processed only for comparison with the transmissometer results and are not presented for further interpretation.

6.3.1   SeaWiFS Satellite Image Processing

SeaWiFS satellite imagery was used to produce maps of suspended sediments in the Irish Sea using the techniques described in Chapters Four and Five. This section describes how the imagery was obtained, which products were used and how the images were processed to obtain maps of MSS concentrations. The stages of image processing are shown in the flow chart in figure 6.18 and are described in more detail in the following pages.

SeaWiFS ocean colour satellite imagery was obtained from the NERC Remote Sensing Data Analysis Service (RSDAS), Plymouth. The RSDAS group receive real-

time imagery from the NERC-supported Dundee Satellite Receiving Station (DSRS) and undertake secondary data processing, including atmospheric correction, to produce level 2 geophysical and biological products. Once provided with these level 2 products, further image processing was carried out using a combination of the NASA SeaWiFS Data Analysis System (SeaDAS, v.4) and the image processing software ERDAS Imagine 8.4.

Preliminary search for clear imagery on the
RSDAS quick-look database
(http://www.npm.ac.uk/rsdas)

RSDAS carry out initial data processing
to level 2A imagery including
atmospheric corrections

Raw imagery obtained as HDF files
containing L_w and E_s for all wavebands

Extraction of files and conversion to binary
format using SeaDAS v.4

ERDAS Imagine models written to:

Calculate R_{rs} from L_w/E_s

Calculate R from R_{rs}

Calculate MSS from
quadratic function of R_{665}

Calculate λ_{peakR}

Calculate b^*_{MSS} from λ_{peakR}

Calculate MSS from optical
model corrected for
variations in b^*_{MSS}

Calculation of statistics on
imagery; max/min values, daily,
weekly, monthly means, time
series etc.

Image processing using ERDAS,
including image sub-setting,
application of colour palettes and
legends, and final image presentation

Figure 6.18: Flow chart illustrating SeaWiFS image processing procedure.

SeaWiFS data was received as water-leaving radiance $(L_w^{(0+,\lambda)})$ and incident downwelling irradiance at sea-level, $(E_s^{(0+,\lambda)})$ at all visible wavelengths. These two parameters enabled the calculation of remote sensing reflectance $R_{rs}^{(0+)} = L_w/E_s$, above the surface. Since *in situ* observations of ocean colour were recorded as irradiance reflectance $(R^{(0-)} = E_u/E_d)$, below the surface, some manipulation of the satellite data was required to obtain comparable satellite reflectances. Remote sensing reflectance can be expressed as a function of irradiance reflectance according to:

$$R_{rs}^{(0+)} = \frac{(1-\rho)\,(1-\bar{\rho})}{n^2(1-\bar{r}\,R^{(0-)})}\,\frac{R^{(0-)}}{Q} \qquad (6.3)$$

where ρ is the internal Fresnel reflectance for upwelling radiance at the water-air interface, $\bar{\rho}$ is the Fresnel reflection at the air-water interface for the downwelling irradiance above the surface, n is the refractive index of sea water, $\bar{r}$ is the water-air interface reflection for the upwelling irradiance and is of the order of 0.48 (Morel and Gentili, 1996; Doxaran *et al.*, 2002a) and $Q = E_u/L_u$ and is frequently taken to be equal to π (Kirk, 1994), assuming complete isotropy of the underwater radiance field. This, however, is a considerable oversimplification of the properties of the light field; Loisel and Morel (2001) found that, even in very turbid water, the upward radiance field is not isotropic and remains sun-angle dependent. In the literature, the Q factor was found to span the range 1 to 7 but, for simplicity, a more realistic value of Q was taken as 5, after Austin (1974).

In equation 6.3, the ratio $\dfrac{(1-\rho)\,(1-\bar{\rho})}{n^2\,(1-\bar{r}R^{(0-)})}$ accounts for the effects of reflection and refraction at the air-water interface. As the upwelling light flux passes through the water-air interface, it undergoes refraction that increases its angle to the vertical. Therefore, the flux contained within a small solid angle beneath the surface spreads out to a larger solid angle above the surface. The Fresnel reflection at the air-water interface, $\bar{\rho}$, for vertically incident light, is approximately 0.02. That is to say that around 2% of the light incident on the sea surface is reflected back into the atmosphere. Austin (1974) showed that $\dfrac{(1-\rho)\,(1-\bar{\rho})}{n^2}$ was approximately equal to

0.54 for conditions under zenith sun. In Case 1 waters $R^{(0-)}$ is often small enough to allow the term $(1 - \bar{r} R^{(0-)})$ in equation 6.3 to be discarded. However, in Case 2 waters, where R can be greater than 0.1, this term should be accounted for (Doxaran *et al.*, 2002a), giving:

$$R_{rs}^{(0+)} = \frac{0.54}{(1 - \bar{r}\, R^{(0-)})} \frac{R^{(0-)}}{Q} \tag{6.4}$$

This equation shows the dependence of R_{rs} on both the IOPs (since $R \propto b_b/a$) and the directional properties of the light field (through Q). A model was written within ERDAS Imagine incorporating equation 6.4 to enable the conversion of SeaWiFS-measured L_w/E_s to daily images of irradiance reflectance, $R^{(0-)}$.

6.3.2   Estimating λ_{peakR} from SeaWiFS Imagery

As was described in Chapter Four, the wavelength of peak reflectance (λ_{peakR}) was estimated by fitting a quadratic function to plots of the spectral reflectance. With the *in situ* measured spectral reflectance, a multiple regression was carried out using the statistical package Minitab. However, the image processing package ERDAS Imagine has only limited statistical functions. In order to derive the wavelength of peak reflectance from SeaWiFS imagery, a model was written within ERDAS to calculate the regression equation according to the description of multiple regressions given in Snedecor and Cochran (1967), as outlined below.

For simplicity, the regression equation $R = a + b\lambda + c\lambda^2$ as first presented in Chapter Four is expressed as $\tilde{Y} = a + b_1 X_1 + b_2 X_2$, where $\tilde{Y}$ is the predicted reflectance, X_1 is λ, X_2 is λ^2, and a, b_1 and b_2 are the regression coefficients. The values of a, b_1 and b_2 are chosen so as to minimise $\sum (Y - \tilde{Y})^2$, the sum of the squares of the differences between the actual (Y) and the predicted ($\tilde{Y}$) reflectances.

The value of the coefficient a is given by equation 6.5 (where the bars indicate mean values) and the coefficients b_1 and b_2 are determined from equations 6.6 and 6.7 respectively.

$$a = \overline{Y} - b_1\overline{X}_1 - b_2\overline{X}_2$$

(6.5)

$$b_1 = \frac{(\sum x_2^2)(\sum x_1 y) - (\sum x_1 x_2)(\sum x_2 y)}{D}$$

(6.6)

$$b_2 = \frac{(\sum x_1^2)(\sum x_2 y) - (\sum x_1 x_2)(\sum x_1 y)}{D}$$

(6.7)

where $D = (\sum x_1^2)(\sum x_2^2) - (\sum x_1 x_2)^2$

(6.8)

In equations 6.5–6.8, $x_1 = X_1 - \overline{X}_1$ (and $x_2 = X_2 - \overline{X}_2$), the differences between each wavelength and the mean wavelength (or wavelength^2). The calculated values of x_1 and x_2 for the central wavelengths of the SeaWiFS visible bands are given in table 6.3. Equations 6.5–6.8 sum each of the functions of x_1 and/or x_2 across all those wavelengths in table 6.3.

Table 6.3: Calculated values of x_1 and x_2 for the visible wavebands of a SeaWiFS image.

Wavelength (nm)	x_1	x_2
412	-101.333	-100776
443	-70.3333	-74270.7
490	-23.3333	-30419.7
510	-3.33333	-10419.7
555	41.66667	37505.33
670	156.6667	178380.3

The equations above result in the determination of the multiple regression of the form $R = a + b_1\lambda + b_2\lambda^2$. The wavelength of peak reflectance is then given by that point where $dR/d\lambda = 0$ (i.e. at $-b_1/2b_2$).

6.3.3   Chlorophyll Predictions

Chlorophyll concentrations, in $\mu g \ l^{-1}$, were calculated according to equation 6.9, the NASA OC4 chlorophyll algorithm, version 4 (O'Reilly *et al.*, 2000).

$$[\text{Chl a}] \ = \ 10^{(0.366-3.067R+1.93R^2+0.649R^3-1.532R^4)} \tag{6.9}$$

where $R = \log_{10}(R_{555}^{443} > R_{555}^{490} > R_{555}^{510})$. The term in brackets denotes the maximum of the three reflectance ratios.

This algorithm was derived empirically based on a pigment database comprising over 2800 *in situ* measurements, with chlorophyll concentrations up to 64 $\mu g \ l^{-1}$.

Whilst this algorithm has been shown to work well in Case 1 waters, some caution should be adopted when interpreting chlorophyll concentrations derived in more turbid Case 2 waters. Mineral sediments have been shown to considerably reduce the sensitivity of the blue/green ratio to changes in chlorophyll, leading to erroneously high derived chlorophyll concentrations (Bowers *et al.*, 1996).

6.3.4   *In situ* TSS from a Moored Transmissometer

Total suspended sediment concentrations (TSS) were obtained from a calibrated transmissometer during the INTERREG Project 'Irish Sea Southern Boundary Study' (Jones *et al.*, 2000). A moored transmissometer was located at 52° 18.6' N, 6° 11.24' W (see figure 6.24 for location). The instrument was held at 23m above the seabed in a total water depth of around 30m. Resulting sediment concentrations were assumed to be representative of surface concentrations as measured by the satellite since these waters were vertically well mixed year-round. The transmissometer provided TSS concentrations averaged into half-hour bins for three periods; September 5th to October 5th 1999, March 31st to June 15th and June15[th] to September 5th 2000. Not all of this data, however, was suitable for use in this validation exercise as there was evidence of considerable errors in beam transmittance as a consequence of bio-fouling on the optical lenses. Only results when there were no obvious signs of fouling were used in the validation procedure. Full calibrations of beam transmittance against total suspended particulate concentrations were carried out on four occasions

during 3-monthly research cruises. During each cruise, the instruments were cleaned, therefore allowing a period of reliable data at the beginning of each measurement period.

6.3.5   Comparing Algorithm Results with Transmissometer Observations

Figure 6.19 shows a time series of MSS concentrations at the transmissometer mooring site as derived from inverse modelling applied to SeaWiFS imagery and corrected for variations in particle scattering. For comparison, the total suspended sediment (TSS) concentrations as obtained from the transmissometer at the mooring site at the times of image acquisitions, are also presented. The satellite-derived concentrations show the expected seasonal cycle in concentrations; highest concentrations in the winter, with a minimum in the summer months. A peak in concentrations in April 2000 corresponds to a period of strong winds combined with extreme spring tides. Whilst the two data series represent different fractions of SPM, it is encouraging that they show agreement in temporal variations over the year.
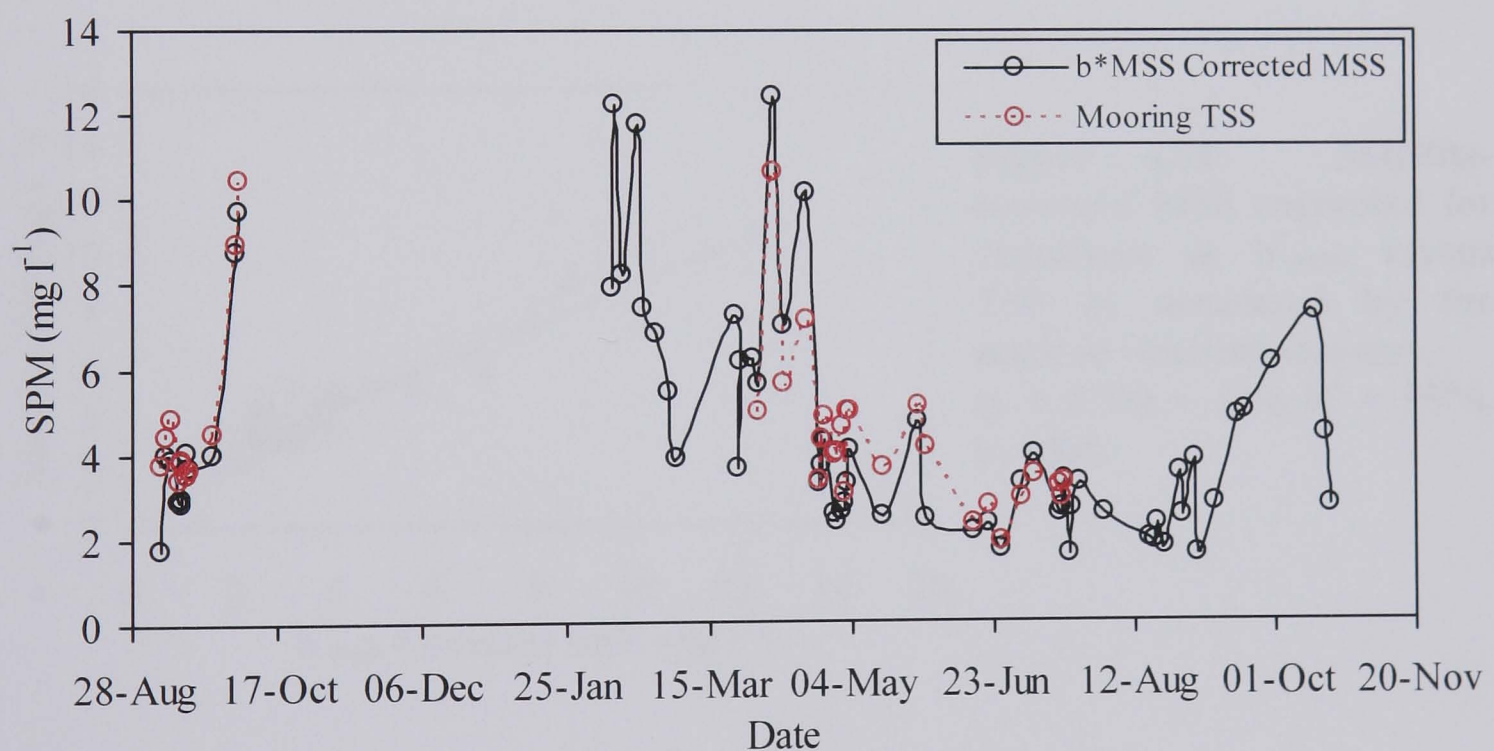
Figure 6.19:   Time series of satellite-derived MSS concentrations compared with observations of TSS concentrations from a moored transmissometer.

Figures 6.20 and 6.21 show plots of predicted MSS concentrations (before and after corrections for particle scattering) against observed concentrations of TSS at the mooring site. Concentrations of MSS were first estimated from the simple reflectance

model (quadratic function of R_{665}) and are shown to be in agreement with observed TSS with a percentage difference between observed and predicted concentrations of 25% (figure 6.20). By correcting for variations in particle scattering, the difference between predicted and observed concentrations was reduced to 18% (figure 6.21), with points lying more closely to the 1:1 relationship (indicated by the dashed line in figures 6.20 and 6.21).
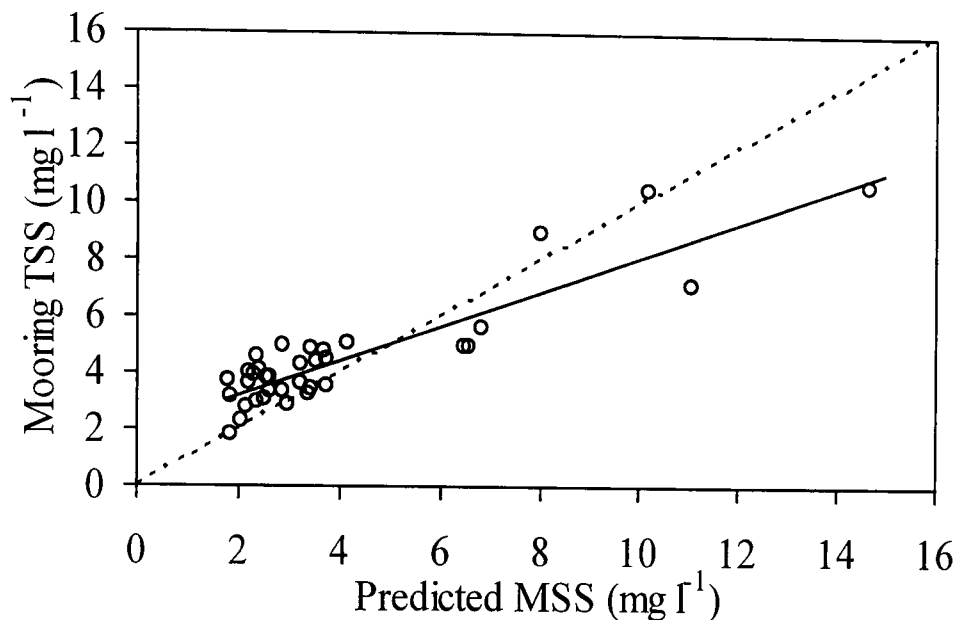
Figure 6.20: Satellite-retrieved MSS versus TSS measured by the moored transmissometer.
(y = 0.61x + 1.97, R^2 = 80%, p =0.0).
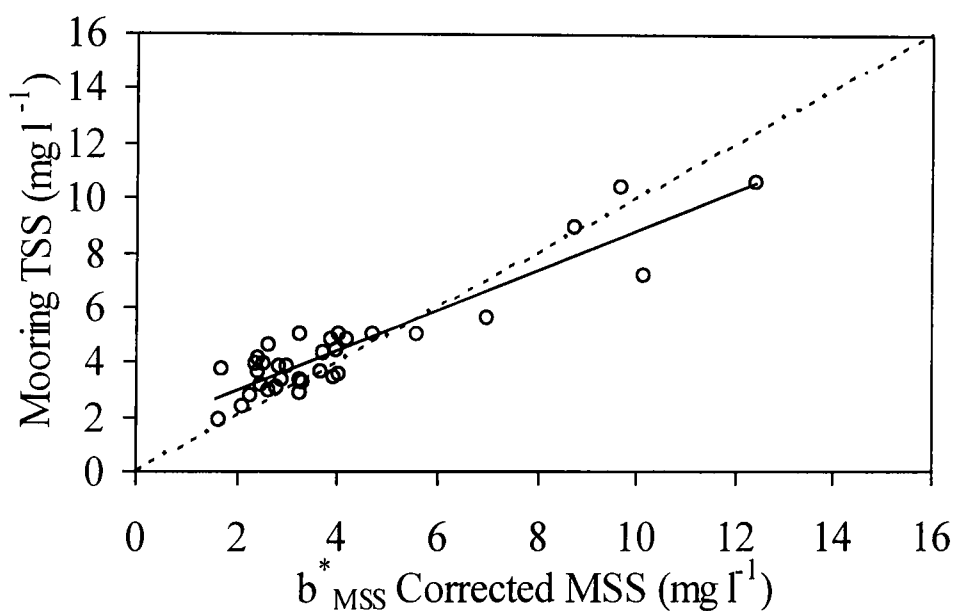
Figure 6.21: Satellite-retrieved MSS corrected for variations in b^*_{MSS} versus TSS as measured by the moored transmissometer.
(y = 0.73x + 1.46 R^2 = 85%, p = 0.0)

Observed versus predicted concentrations show a close agreement with the 1:1 line in figures 6.20 and 6.21 but demonstrate a clear tendency for the algorithm to predict MSS concentrations lower than observed TSS at low concentrations and higher than observed TSS at high concentrations. This may be explained by the differences in the parameters being measured; at low concentrations of MSS (usually observed in the summer months), it might be expected that TSS may contain significant concentrations

of organic suspended sediment (OSS), whilst for the higher sediment concentrations (usually the winter months) it might be expected that TSS would consist almost entirely of MSS. Nevertheless, MSS concentrations are still overestimated since, on occasions, predicted MSS is higher then the measured TSS concentration. Possible sources of error in the satellite-derived MSS concentrations which may explain this discrepancy will be discussed in section 6.3.7.

6.3.6 Seasonal Variability in b^*_{MSS}

The imagery was processed using the λ_{peakR} technique to obtain values of b^*_{MSS}, and for consistency, results at the mooring site were analysed. The values of b^*_{MSS} estimated at the mooring site varied between 0.097 and 0.434 m^2 g^{-1}, with a minimum in the summer months in agreement with those observations in the Irish Sea in Chapter Five and in the Menai Strait in this Chapter. The seasonal variation in b^*_{MSS} as derived from λ_{peakR}/R_{670} is in surprisingly good agreement with observations in the Menai Strait (figure 6.22). Observations of b^*_{MSS} suggested that particles in the Menai Strait were generally less efficient scatterers than the rest of the Irish Sea, therefore, figure 6.22 may imply that the λ_{peakR}/R_{670} method underestimates b^*_{MSS} from the Irish Sea SeaWiFS imagery.
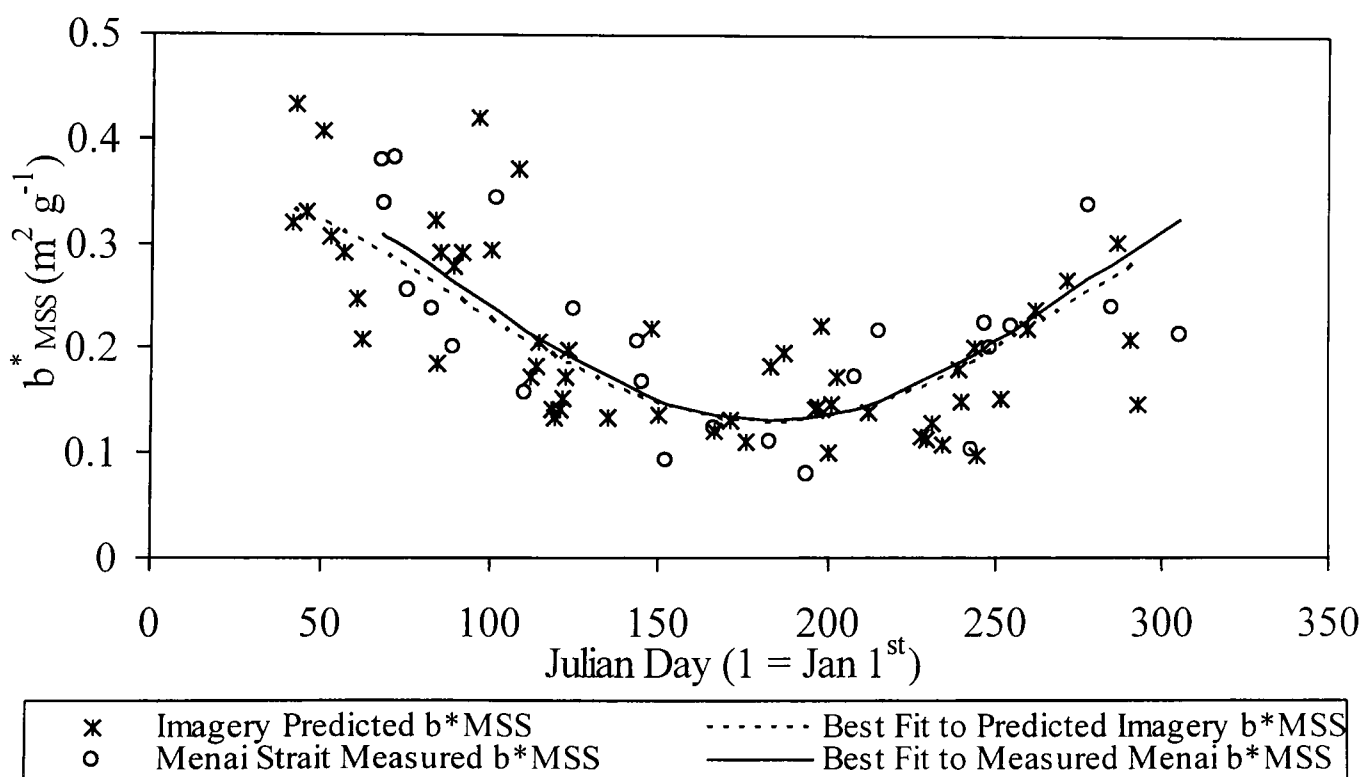
Figure 6.22:   Seasonal cycle of b^*_{MSS} as derived from SeaWiFS imagery from λ_{PeakR}/R_{670} and measured in the Menai Strait.

In the Irish Sea, a trend was evident between b^*_{MSS} and the ratio of MSS/TSS. Whilst there was no way of estimating OSS from SeaWiFS imagery, the ratio MSS Chl showed a significant negative correlation with b^*_{MSS} (Pearson correlation = -0.51) at the mooring site. Although care should normally be taken in interpreting results from the OC4 algorithm in Case 2 waters, the derived chlorophyll concentrations (figure 6.23) appear to produce a realistic seasonal variation, with a spring bloom in May.
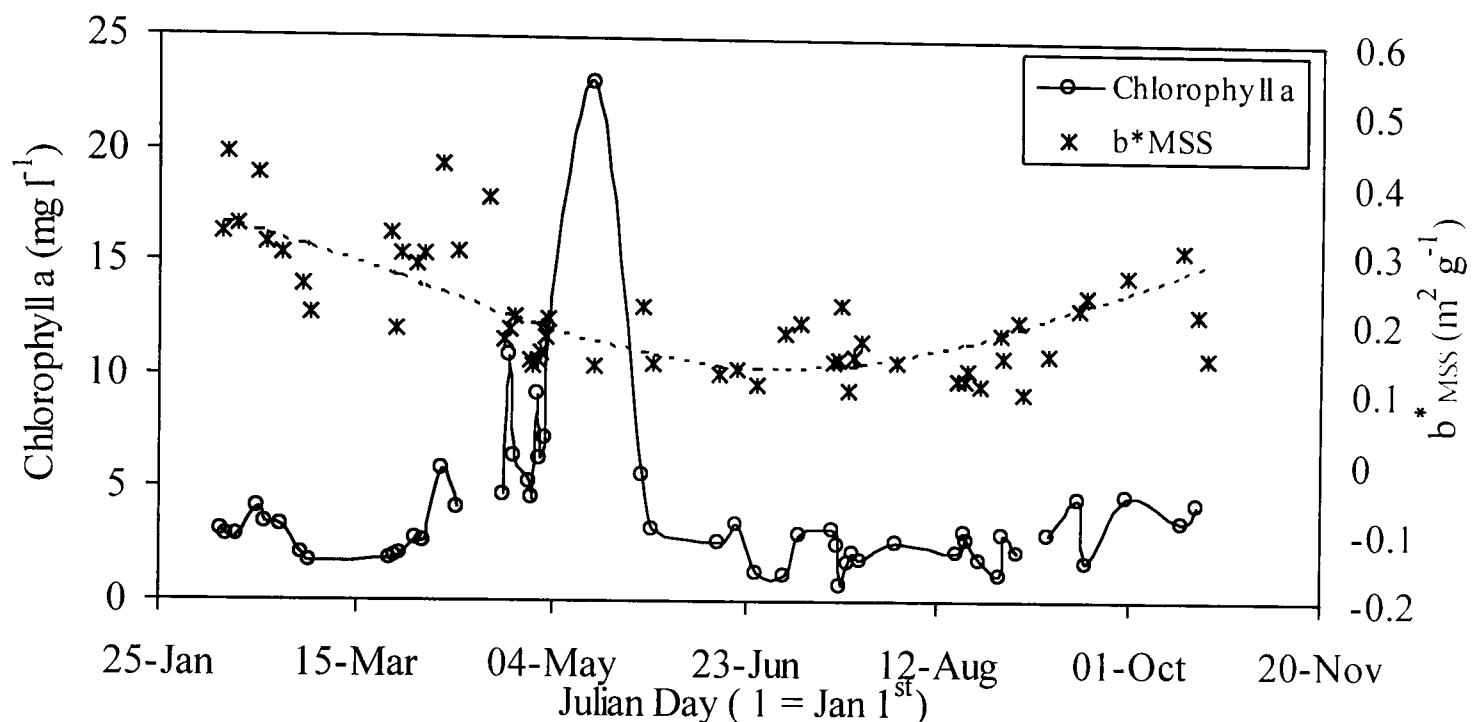
Figure 6.23: Seasonal cycle of satellite-retrieved chlorophyll concentration and b^*_{MSS} at the mooring site.

6.3.7 MSS Distributions in the Irish Sea

The annual mean and range of MSS concentrations in the Irish Sea for the year 2000 were calculated from 62 SeaWiFS images and are presented in figure 6.24 and 6.25 respectively. A number of interesting features in the spatial distribution of MSS in this region are evident. In particular, the region is characterised by pronounced areas of high turbidity off Anglesey and Arklow Bank that remain persistent features of the surface suspended sediment distribution in the Irish Sea throughout the year. High concentrations also occur in the shallow regions of Liverpool Bay, Morecambe Bay, Solway Firth and the Severn Estuary (see figure 3.1, Chapter Three, for locations). The annual mean MSS concentration varies spatially from a minimum of 0.01 mg l^{-1} in the Celtic Sea to a maximum of 66.8 mg l^{-1} within the Severn Estuary.

Annual MSS Range (mg/l)

0.0 - 1.99	
2.0 - 3.99	
4.0 - 5.99	
6.0 - 7.99	
8.0 - 9.99	
10.0 - 11.99	
12.0 - 13.99	
14.0 - 15.99	
16.0 - 17.99	
18.0 - 19.99	
20.0 - 24.99	
25.0 - 29.99	
>30.0	

Figure 6.25: Range of MSS concentrations (mg/l) over the year 2000.
* marks the location of the moored transmossometer.

Annual Average MSS (mg/l)

<1.5	
1.5 - 1.99	
2.0 - 2.49	
2.5 - 2.99	
3.0 - 3.49	
3.5 - 3.99	
4.0 - 4.49	
4.5 - 4.99	
5.0 - 5.49	
5.5 - 5.99	
6.0 - 6.49	
6.5 - 6.99	
7.0 - 7.99	
8.0 - 8.99	
9.0 - 9.99	
10.0 - 10.99	
11.0 - 11.99	
12.0 - 14.99	
15.0 - 19.99	
>20.0	

Figure 6.24: Average MSS concentrations (mg/l) corrected for variations in b*MSS over the year 2000.
* marks the location of the moored transmissometer.

The spatial distribution of MSS concentration correlates strongly with the tidal stirring parameter h/u^3 as was noted by Simpson and Brown (1991) and Bowers *et al.* (1998), emphasising the role of the turbulent kinetic energy (TKE) in keeping sediments in suspension. Fast currents in excess of 1 m s^{-1} are found near Arklow and off Anglesey, whilst weaker currents are observed in the western Irish Sea and Celtic Sea (refer to figure 3.2 in Chapter Three). There are abrupt changes in MSS concentrations associated with the transition from vertically mixed to stratified waters such as the western Irish Sea and the Celtic Sea frontal regions.

The annual range in MSS concentrations at any one position varied from less than 0.1 mg l^{-1} to 106 mg l^{-1}, although the majority of pixels showed an annual variation of less than 40 mg l^{-1}. The speckled appearance in figure 6.25 is the consequence of pixels bordering cloud in the daily images. Regularly, these pixels considerably overestimate reflectance (and consequently overestimate MSS concentrations) due to the inaccuracy of atmospheric correction procedures near cloud edges. The largest true annual variations in MSS concentrations were apparent in the Severn Estuary and the shallow Cardigan and Liverpool Bays and Solway Firth. This is in agreement with Bowers *et al.* (1998) who found the greatest annual variation in MSS in the eastern Irish Sea, off Anglesey, Wicklow and Cardigan Bay from a time series of AVHRR visible reflectance in the 1980s.

Figures 6.26a-i present monthly mean MSS concentrations for the year 2000 (February to October) as derived from reflectance at 670 nm and corrected for variations in b*$_{MSS}$. There is noticeable seasonality in the distribution of MSS in these images which has been summarised by calculating spatially-averaged (over the entire Irish Sea image) monthly mean concentrations (figure 6.27). These monthly mean concentrations vary approximately cosinusoidally with time, with highest concentrations in February (4.51 mg l^{-1}) decreasing to a minimum of 2.09 mg l^{-1} in July before increasing again in towards the end of the year. The monthly averages are in reasonable agreement with Bowers *et al.* (1998), who found that for the Irish Sea as a whole over the period 1982 to 1988, the surface concentration of MSS in the winter was 5.39 mg l^{-1}, reducing to 2 mg l^{-1} in the summer.

MSS (mg/l)

<1.5
1.5-1.99
2.0-2.49
2.5-2.99
3.0-3.49
3.5-3.99
4.0-4.49
4.5-4.99
5.0-5.49
5.5-5.99
6.0-6.49
6.5-6.99
7.0-7.99
8.0-8.99
9.0-9.99
10.0-10.99
11.0-11.99
12.0-14.99
15.0-19.99
>20.0
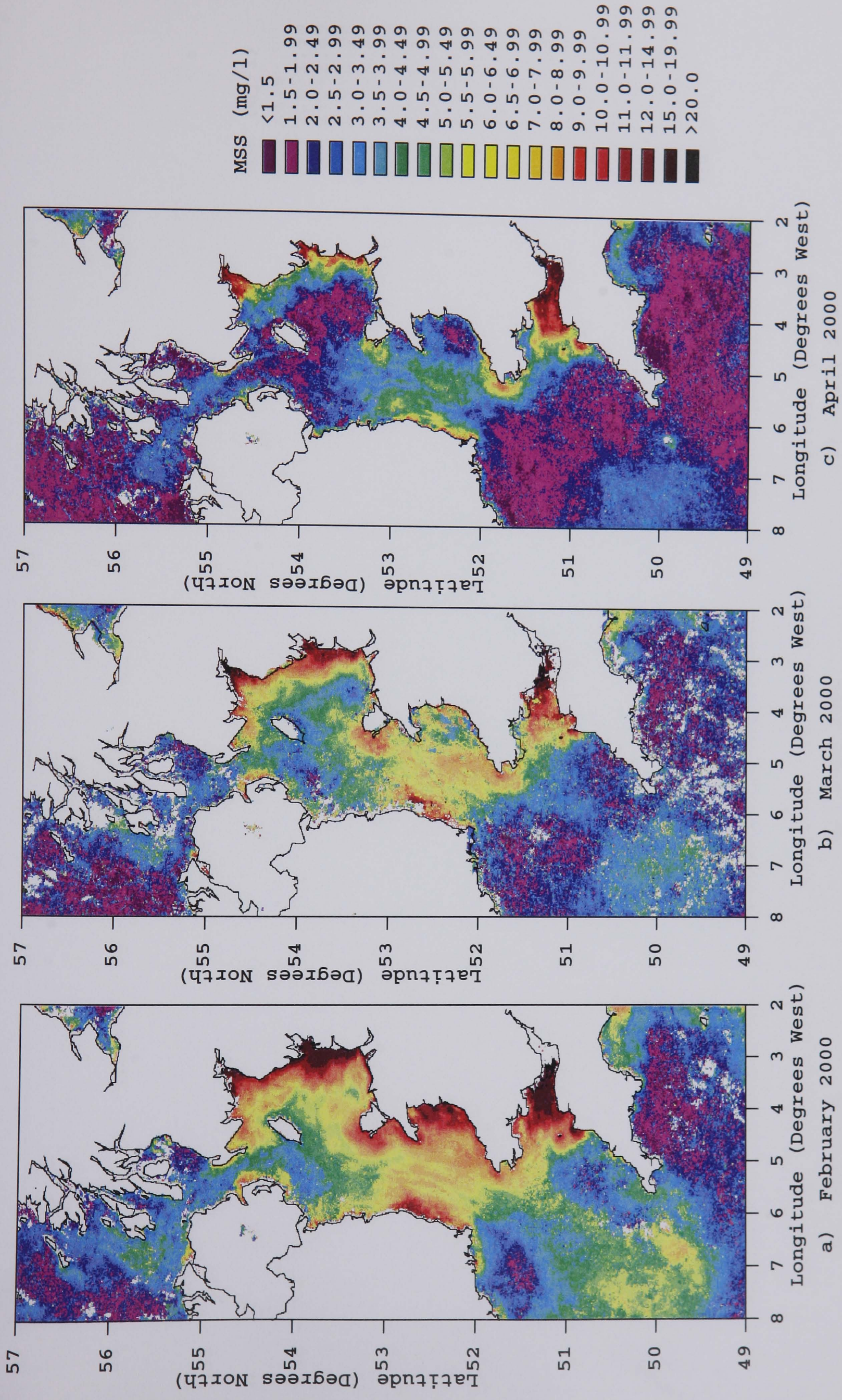
Figure 6.26: Monthly mean Mineral Suspended Sediment (MSS) concentrations derived from SeaWiFS R665 and corrected for variations in particle scattering (b*MSS)

a) February 2000   b) March 2000   c) April 2000

Figure 6.26cntd: Monthly mean Mineral Suspended Sediment (MSS) concentrations derived from SeaWiFS R665 and corrected for variations in particle scattering (b*MSS)

MSS (mg/l)

<1.5
1.5-1.99
2.0-2.49
2.5-2.99
3.0-3.49
3.5-3.99
4.0-4.49
4.5-4.99
5.0-5.49
5.5-5.99
6.0-6.49
6.5-6.99
7.0-7.99
8.0-8.99
9.0-9.99
10.0-10.99
11.0-11.99
12.0-14.99
15.0-19.99
>20.0

g) August 2000

h) September 2000

i) October 2000
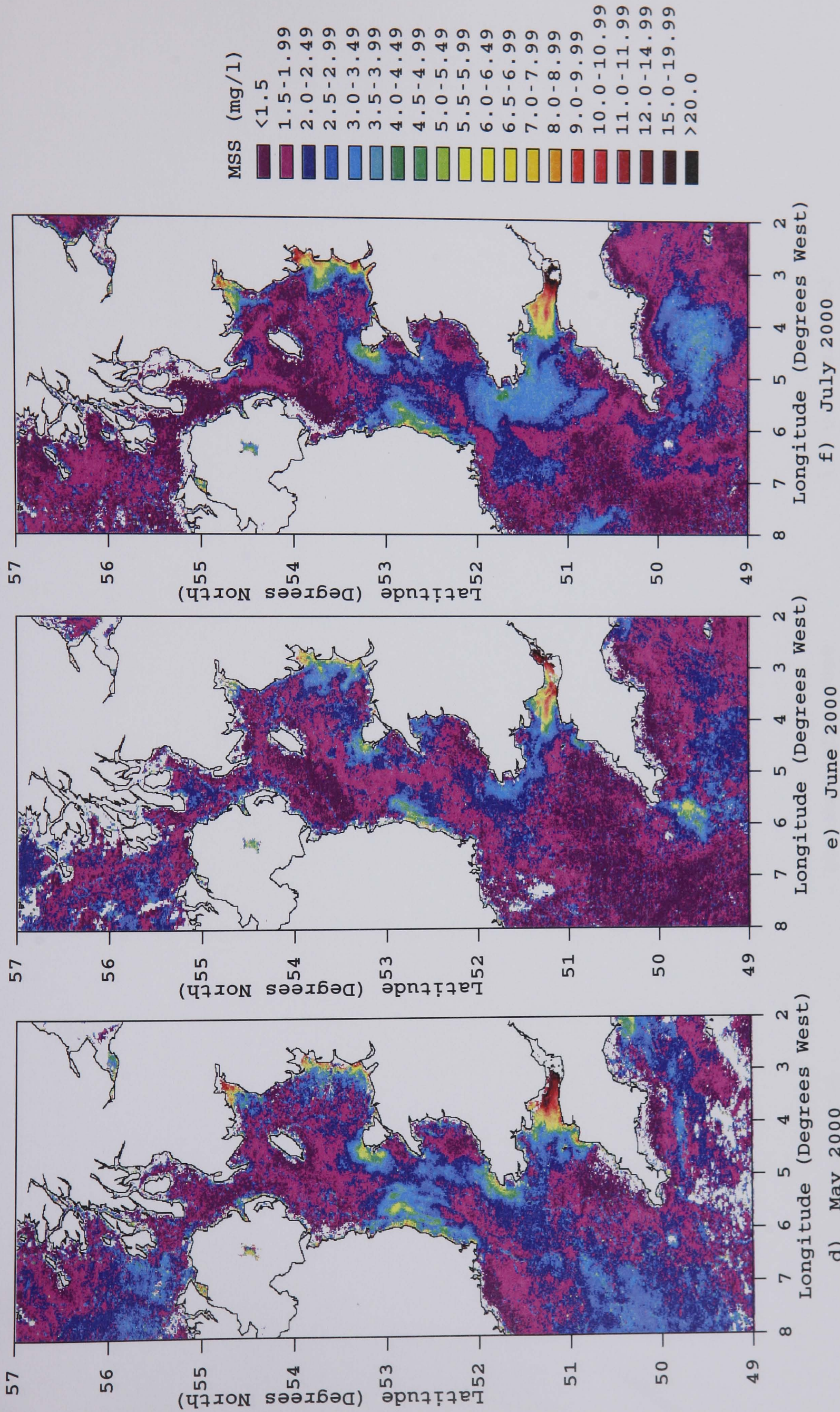
Figure 6.26 cntd: Monthly mean Mineral Suspended Sediment (MSS) concentrations derived from SeaWiFS R665 and corrected for variations in particle scattering (b*MSS)
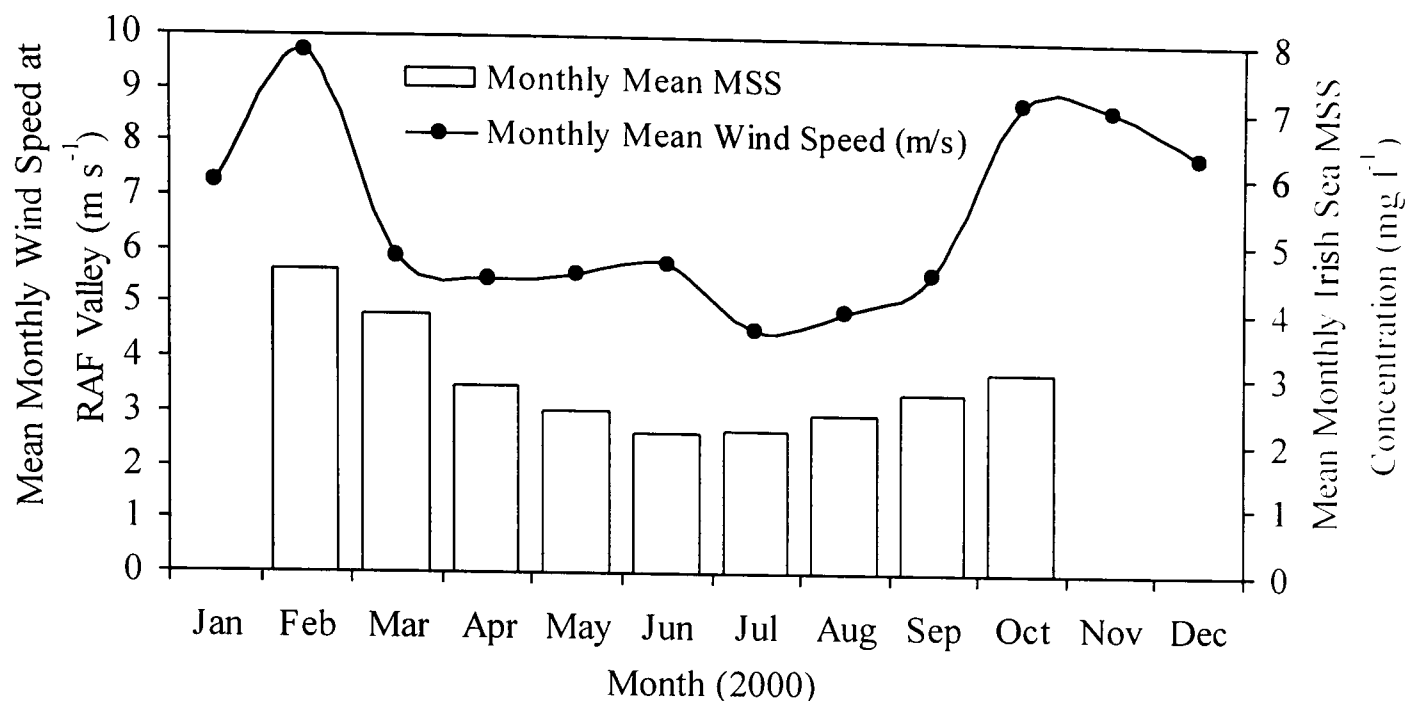
Figure 6.27: Monthly mean MSS concentrations for the Irish Sea plotted with monthly mean wind speeds measured at RAF Valley, Anglesey (provided by the British Atmospheric Data Centre, BADC).

The seasonality in MSS concentrations at the mooring site appears to be driven, at least in part, by seasonal variations in wind stress (being stronger in the winter than the summer, figure 6.27). Observing correlations between imagery results and known forces that drive sediment suspension in the Irish Sea is promising support that it is true variations in MSS concentrations that the images are representing. These satellite imagery results suggest that it is tidal stirring that determines a 'background' spatial distribution of MSS, resulting in the fixed nature of many of the turbidity features observed. The temporal distribution of MSS, on scales larger than the spring-neap cycle, appears to be determined by wind-induced stirring, at least for shallow waters at the mooring site.

A feature evident in the June average MSS images (figure 6.26e) that requires some discussion is the anomalous increase in MSS concentrations off the south coast of Cornwall. On further investigation, this apparent increase in monthly mineral sediments is actually a Coccolithophore bloom that can be identified in daily imagery from June 16th onwards, appearing to break down towards the end of July. Figure 6.28a shows a subset of the region of interest from an image of MSS concentrations from June 26th 2000 (13:03) and, in addition, the results of the SeaWiFS Coccolithophore flag (figure 6.28b). A true colour composite image of the Brittany and Cornwall coasts (figure 6.28c) for the same date highlights the increase in

reflectance over all wavelengths resulting in a milky white appearance to the surface waters. The SeaWiFS Coccolithophore algorithm (Robinson, 2000; Gordon *et al.*, 2001) was developed by empirical determinations of the spectral signatures of Coccolithophore blooms in relation to various non-bloom conditions. A number of conditions were set relating to the spectral water-leaving radiances that allow blooms to be distinguished from other conditions.

Although the presence of Coccolithophores in the surface waters causes erroneously high predicted MSS concentrations, the apparent success of the SeaWiFS Coccolithophore flag at highlighting the occurrence of such blooms means that such problem areas can simply be removed from image analysis.
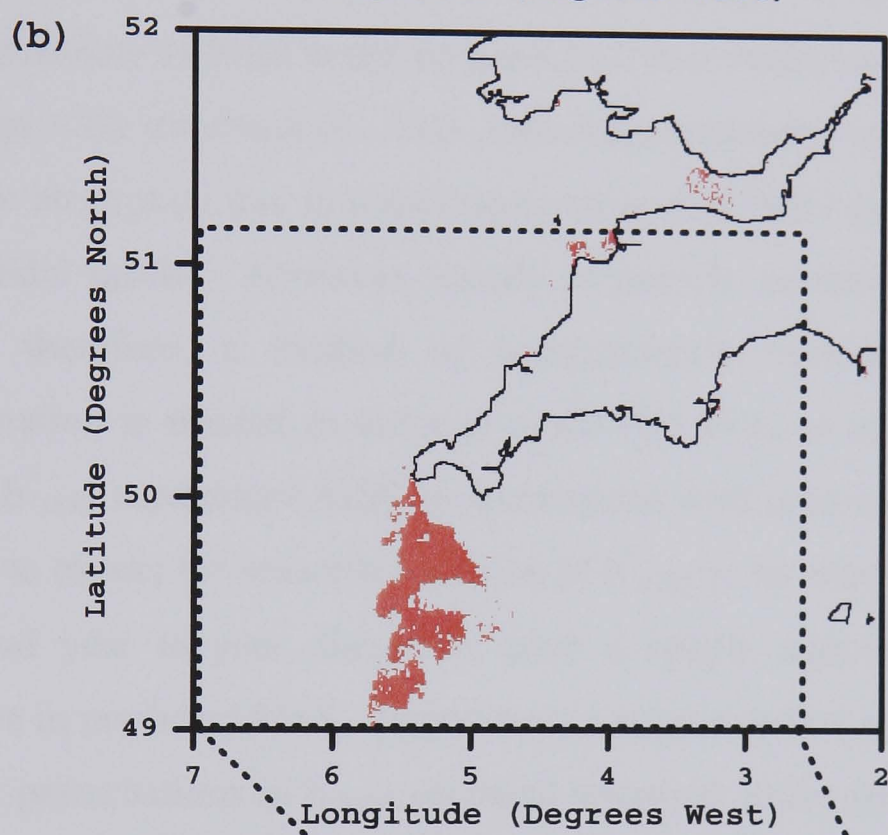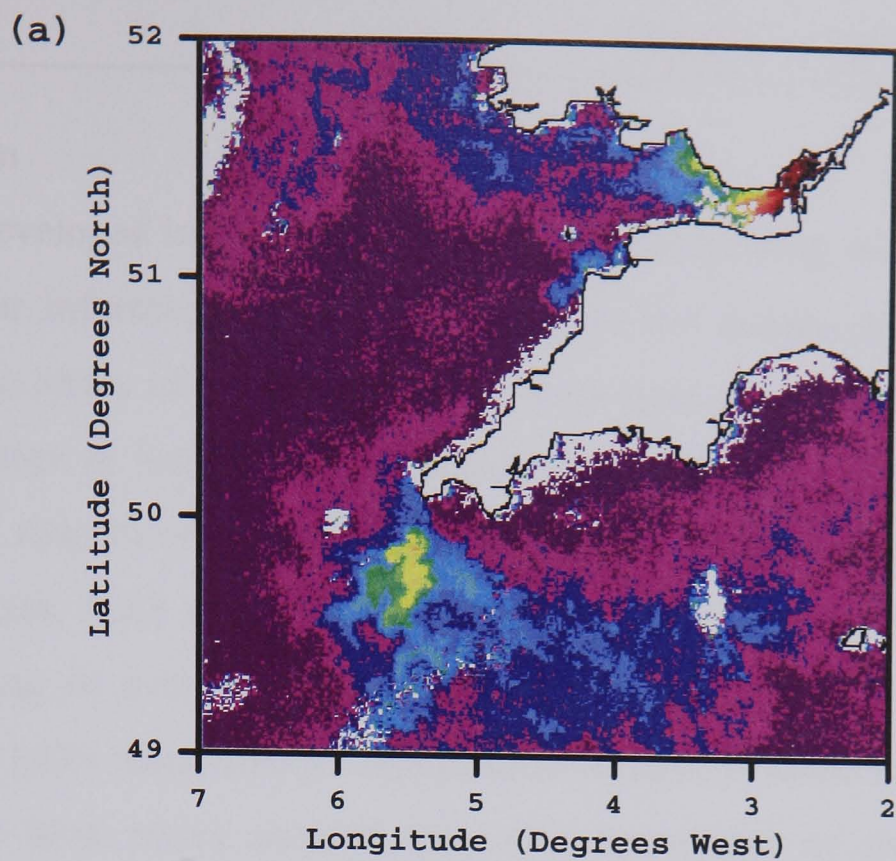
Figure 6.28a: MSS concentration (mg/l) as derived from R670 and corrected for variability in b*MSS for 26 June 2000, 13:03.

Figure 6.28b: Results of the SeaWiFS Coccolithophore flag for 26 June 2000, 13:03.

Figure 6.28c: True colour composite SeaWiFS image off Brittany and Cornwall on 26 June 2000. (Provided by the SeaWiFS Project, NASA/Goddard Space Flight Center)

6.4   Discussion

The techniques developed in Chapters Four and Five for deriving MSS concentrations from ocean colour information have been tested on two independent data sets; one concerning a time series of *in situ* radiometer data from the Menai Strait, the other being the application to SeaWiFS satellite imagery of the Irish Sea, with coincident measurements of suspended sediment concentrations. Without prior knowledge of scattering properties, MSS concentrations were retrieved using a simple reflectance algorithm, resulting in average uncertainties of 31% and 25% for the *in situ* and satellite-retrieved MSS respectively. Application of inverse modelling techniques to the Menai Strait time series showed that with knowledge of particle scattering properties, concentrations of MSS could be predicted from reflectance with increased accuracy (less than 13% uncertainty). The scattering-dominated environment meant that neglecting the absorption due to constituents other than MSS and water had little impact on the model results. However, details of particle scattering properties are rarely available, therefore, a method of independently estimating b^*_{MSS} from reflectance information is needed in order to reach this level of accuracy. Using a seasonal trend in b^*_{MSS} reproduced MSS concentrations with reasonable accuracy but there is no reason to expect the seasonal variation of b^*_{MSS} to be exactly the same from place to place and year to year, therefore, such a simple approach may lead to considerable errors in predicted MSS. In addition, a simple annual cycle would make no corrections for perturbations in b^*_{MSS} on small temporal scales such as the spring-neap tidal cycle, in response to isolated storm activity or unexpected phytoplankton blooms.

The use of λ_{peakR}/R_{665} to estimate values of b^*_{MSS} appears to give reasonable results, enabling the prediction of MSS concentrations with an average uncertainty of 22% from *in situ* optical properties in the Menai Strait and 18% for satellite imagery of the Irish Sea. Although at present, the improvements to MSS concentration predictions brought about by accounting for b^*_{MSS} in this way are only small, results are promising and further work with this technique would be beneficial. With the now common use of hyperspectral *in situ* radiometry (and increasingly so from space), it will be possible to obtain more accurate determinations of the wavelength of peak reflectance.

Results in this study suggest that the scattering properties of suspended sediments are

affected both by the amount of organic matter and the degree to which turbulence may aid or inhibit particle aggregation. Much of the particulate matter in the oceans exists in the form of flocs that continuously aggregate and disaggregate, thus altering their sizes, effective densities, surface areas and consequently their optical properties (Lick *et al.*, 1993). The processes of aggregation and disaggregation depend on collisions between particles; for flocs to form, particles must collide and then stick together. Lick *et al.*, (1993) showed experimentally that the removal of organic matter from sediment suspensions led to a decrease in the resulting floc sizes. Burban *et al.* (1989) showed that the average floc size under fixed turbulent conditions decreased with increasing sediment concentration since the disaggregation process is partially dependent on the number of particle collisions. The processes of particle aggregation and disaggregation of marine particles are complex and yet to be fully understood (Lick *et al.*, 1993), but these observations go some way to explaining the scattering behaviour of suspended particles in the Menai Strait.

The temporal variations of suspended sediment concentrations in both the Menai Strait and the Irish Sea in 2000 were in general agreement with previous observations. Buchan *et al.* (1967) and Kratzer *et al.* (2000) observed strong seasonality in suspended sediment concentrations in the Menai Strait, with much greater sediment loads in the winter than the summer. This trend was also apparent in seasonal studies of SPM in the Irish Sea (Mitchelson, 1983; Weeks, 1989). Whilst a strong seasonal cycle in suspended sediments was not observed in the Menai Strait study because data was not collected between November and February, the Irish Sea imagery results suggested a strong seasonal variation in MSS. Sediment concentrations in the Menai Strait also showed the typical increase in concentrations during spring tides compared with neap tides, confirming that more sediment was carried during periods of stronger tidal stirring.

Buchan *et al.* (1967) ascribed the seasonal cycle to biological activity; either to the binding of bottom sediments by micro-organisms, making them less susceptible to erosion in the summer months, or to the filter feeding organisms that remove sediment from suspension in the summer months. Results in this study suggest that the seasonal cycle of MSS in the Irish Sea may be a consequence of wind-induced stirring. This is in agreement with Boudjelas (1994) who attributed the annual cycle of beam

attenuation in the Irish Sea to seasonal changes in wind stress. Others, however, have attributed seasonal cycles in SPM to seasonal changes in particle size and type (Jones *et al.*, 1998), which is also apparent in this data set, suggesting that it may be a combination of processes, both physical and biological that determine the seasonal cycle in sediment concentrations in the Irish Sea.

Whilst the temporal variability of MSS over the year was in agreement with previous observations, absolute concentrations of suspended sediments observed in the Menai Strait during the year 2000 were noted to be considerably lower than previous years observed by Kratzer *et al.* (2000) and Buchan *et al.* (1967). Kratzer *et al.* (2003) proposed that a noticeable downward trend in turbidity in the Menai Strait may be a response to long term changes in wind forcing. Recently published observations of the long term trends in NW Europe storminess have shown that wind strength increased over the 1960s, 70s and 80s (during which time there was a corresponding increase in turbidity) but decreased during the 1990s (Alexandersson *et al.*, 2000). Results from this study may, therefore, be further evidence for the suggestion that the Menai Strait has been becoming clearer in recent years.

The spatial distribution of suspended sediments in the Irish Sea derived from the inverse modelling technique is in good agreement with previous studies, and is strongly correlated with the tidal stirring parameter h/u^3. Relationships between remote sensing reflectance (and therefore suspended sediment concentrations) have been inferred previously from CZCS imagery (Weeks and Simpson, 1991) and AVHRR imagery (Bowers *et al.*, 1998).

Chapters Four and Five confirmed that there is strong evidence for the use of visible reflectance for estimating MSS concentrations from ocean colour measurements in moderately turbid shelf sea environments. This chapter has taken these observations one step further to show that these relationships do indeed allow accurate reproductions not only from *in situ* colour information but also that remotely sensed from satellites. Algorithm development studies frequently reach the stage where a statistically significant relationship is used to interpret satellite imagery in terms of suspended sediment distributions, but few take it to the final stage to assess the accuracy of sediment concentration retrieval. This has been carried out in this Chapter

using a moored transmissometer to provide an independent data set of suspended sediment concentrations. Such a comparison, although appearing to confirm the accuracy of the algorithm, requires some discussion. Comparing single spot samples obtained from a transmissometer with satellite imagery introduces uncertainties due to inhomogenous sediment distributions within scales similar to the pixel size of the image (so called sub-pixel variability). This may lead to errors in the ground truth samples in regions of strong sediment gradients. The site under study here, however, does not appear to be a region of strong horizontal sediment gradients; where possible, pixels immediately surrounding the mooring site were analysed to give an indication of this variability. Over the year, MSS concentrations in the 8 pixels immediately surrounding the mooring site showed less than 15% variability with respect to that measured at the centre pixel. Although this suggests that this is an area of limited horizontal gradient, it does not give an indication of the variability on scales smaller than a single pixel.

Uncertainty is also introduced by the fact that the transmissometer measures total suspended sediment whereas the optical model has been developed to measure the mineral fraction only. Whilst the comparison shows clearly that the two follow similar trends, there is still an unknown quantity relating to the organic fraction of TSS. Furthermore, attenuation coefficients measured from transmissometers are known to be influenced by particle properties. The beam attenuation coefficient depends not only on the particle concentration but also particle size, shape and index of refraction (Baker and Lavelle, 1984) and thus estimated concentrations may be biased in a similar manner to the reflectance model. Particle size has been suggested as the most influential variable (Ulloa *et al.*, 1994), although particle shape can also be important (Pollack and Cuzzi, 1980).

A survey of published field transmissometer calibrations showed a trend of decreasing calibration slopes from environments with fine particles to those with larger particles. The transmissometer readings presented in this study were calibrated against TSS on several occasions during the mooring deployment and therefore much of the variability in derived concentrations due to changing particle optical properties may have been removed. Furthermore, any response of optical properties to changes in sediment properties will be more clearly represented in the radiometer measurements

because of the large volumes of water contained in their measurement fields compared with the small volume of water sampled by a transmissometer (10 cm pathlength).

Aside from the uncertainties in *in situ* measurements, there are a number of sources of error in satellite-derived reflectances which may also adversely affect the derived MSS concentrations. The use of absolute values of reflectance in remote sensing algorithms depends on precise knowledge of sensor calibration, atmospheric correction, sea surface interactions and wind effects. Reflectance ratios have been used in the past specifically to minimise these influences but it has been shown in this study that, given the limited choice of wavelengths available with the SeaWiFS sensor, band ratios are not suitable for retrieving suspended sediment concentrations in this region. Consequently, effort is now required to improve the measurement accuracy of satellite retrieved radiances through precise atmospheric correction schemes.

The standard NASA atmospheric correction scheme for SeaWiFS assumes negligible water-leaving radiance in the near infra-red part of the spectrum (Gordon and Wang, 1994). Termed the 'dark pixel' atmospheric correction procedure, this assumption works well in Case 1 waters where absorption at these wavelengths is sufficient to remove all significant water-leaving radiance. In contrast, when high concentrations of suspended sediments are present, strong backscatter results in significant water leaving-radiance in the atmospheric correction bands at 765 nm and 865 nm and negates the standard Case 1 water 'dark pixel' procedure (Moore *et al.*, 1999). Assumption of zero water-leaving radiance in the near infra-red leads to an overestimate in the aerosol scattering which will be amplified towards shorter wavelengths. This results in an excessive atmospheric correction for the visible bands and frequently yields negative water-leaving radiance values in turbid Case 2 waters, particularly in bands 1 (412 nm) and 2 (443 nm). This was observed on occasions during image processing for this study, an example of which is given in figure 6.29. The extent of the negative pixels clearly increases in the shorter wavelengths, resulting in considerable loss of data.
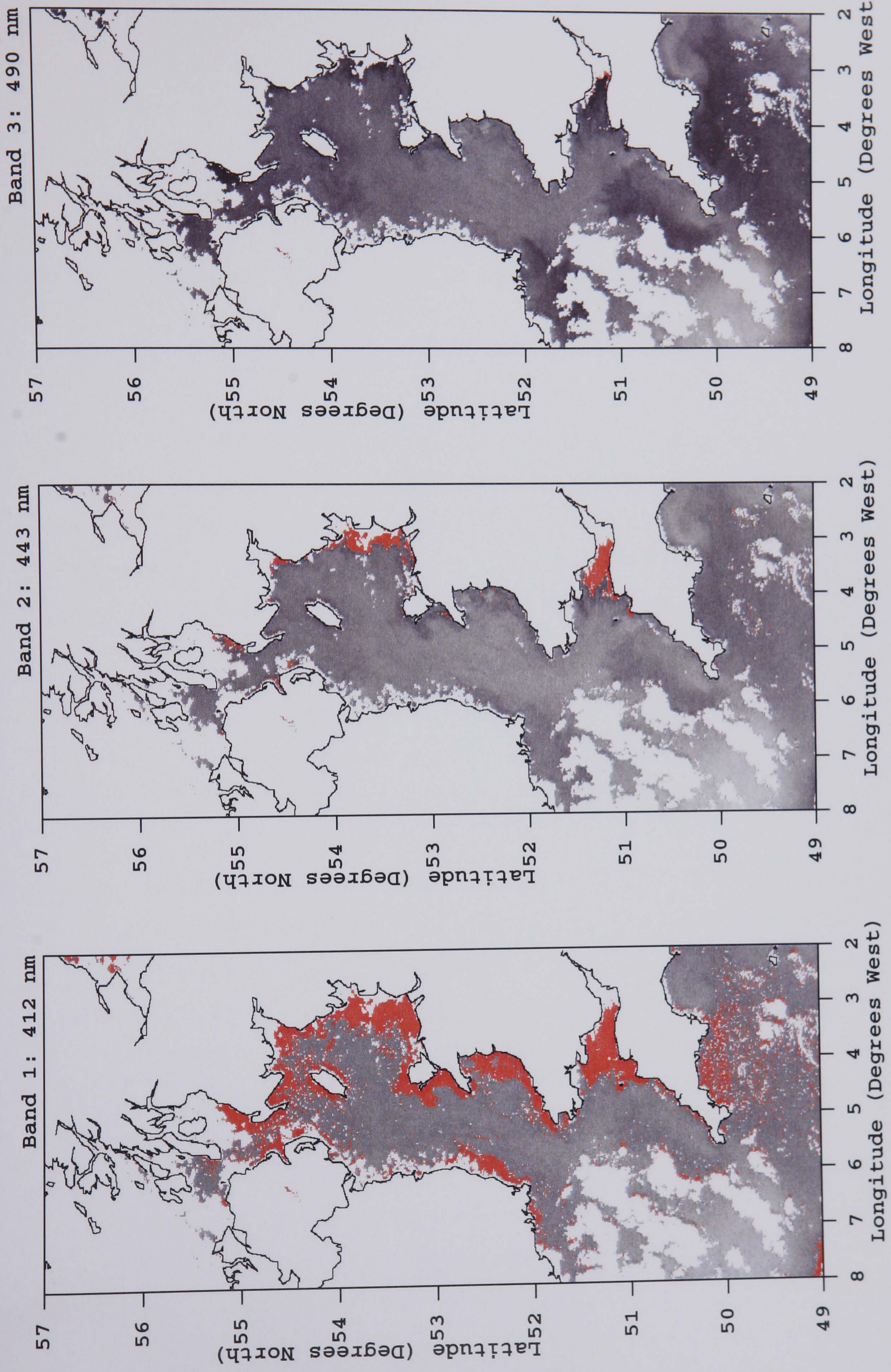
Figure 6.29: SeaWiFS water-leaving radiance, Lw for bands 1-6 (centred on 412, 443, 490, 510, 555, 670 nm) from 25th February 2000, 13:14. Red regions highlight pixels with negative radiance.
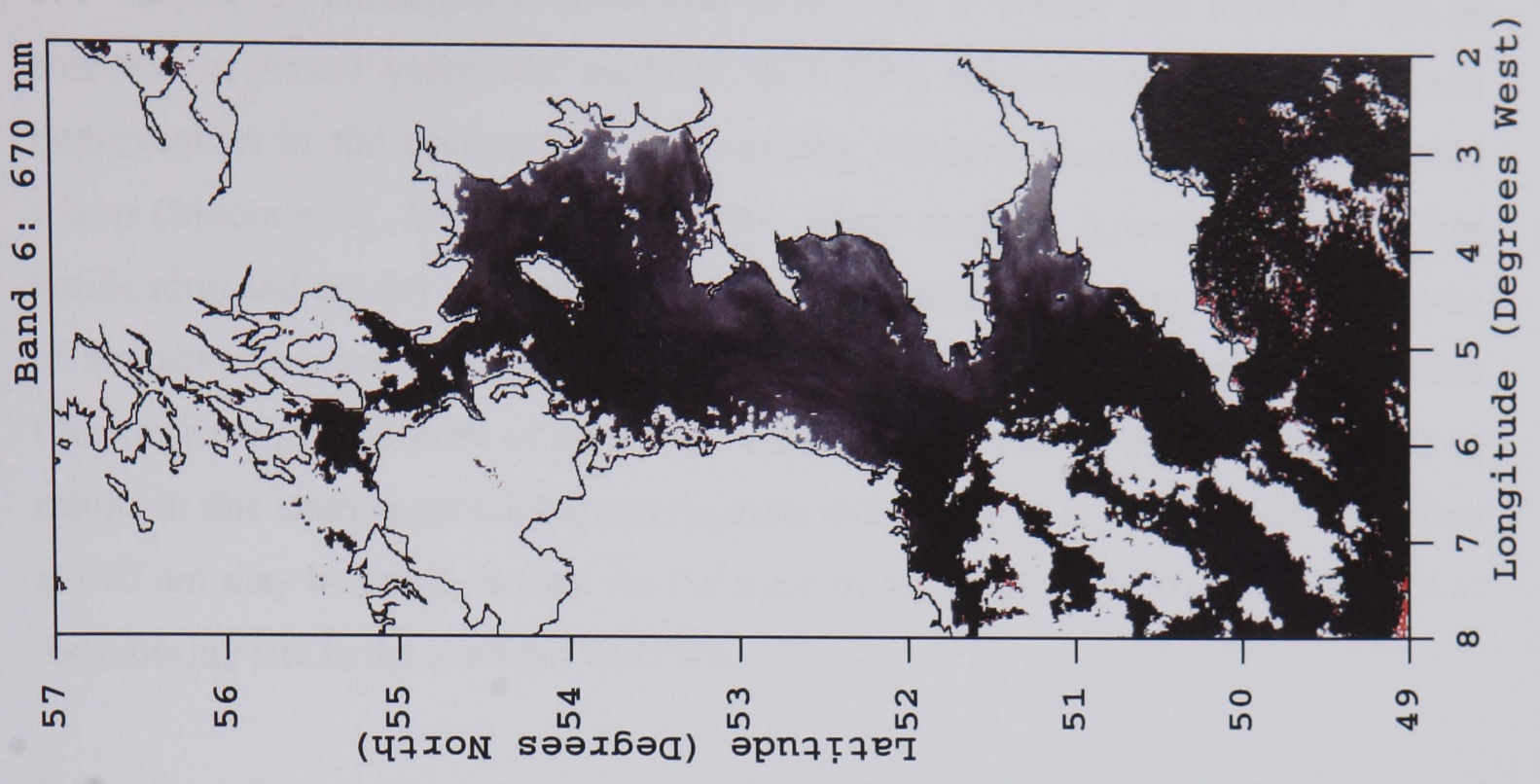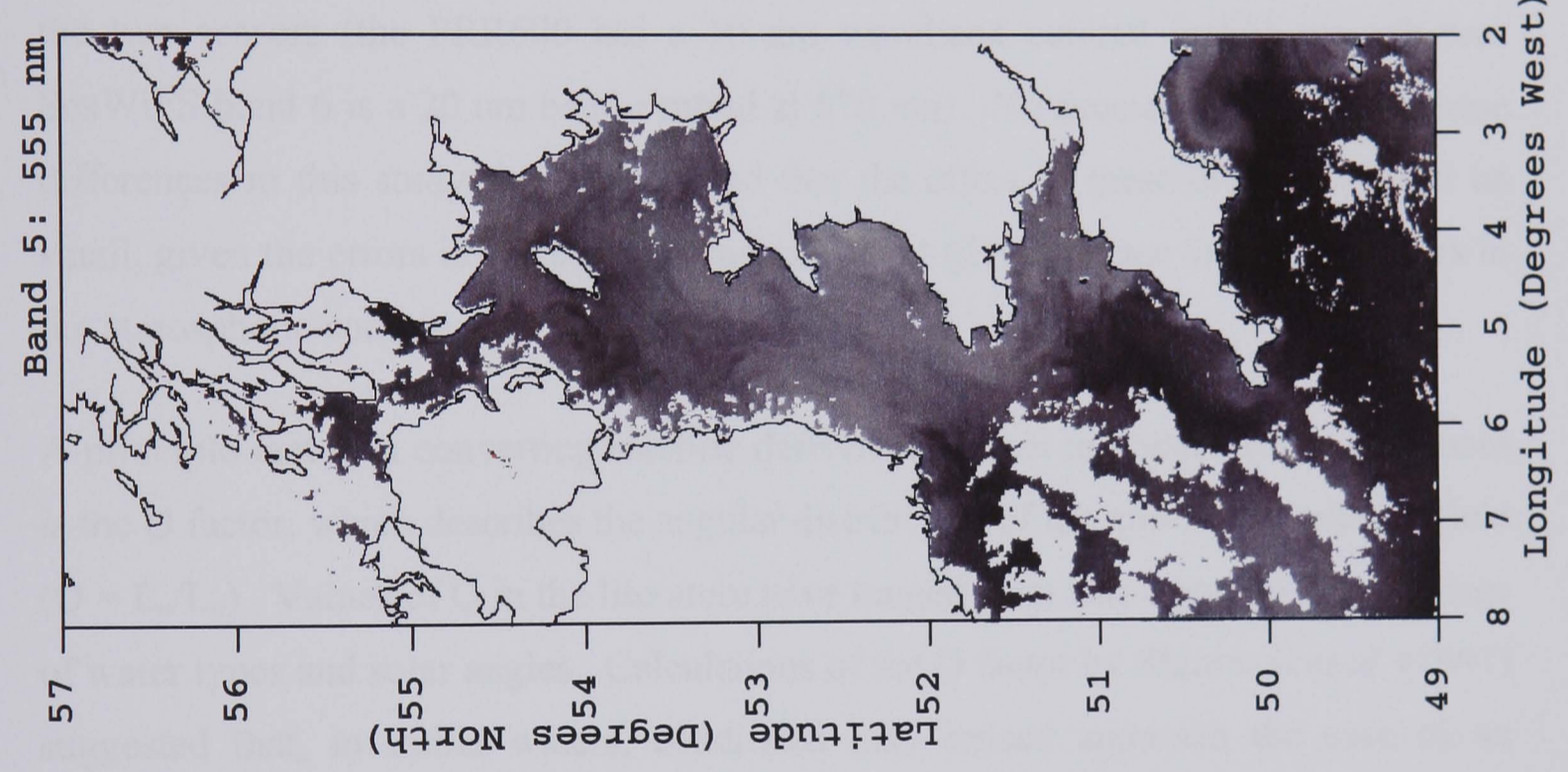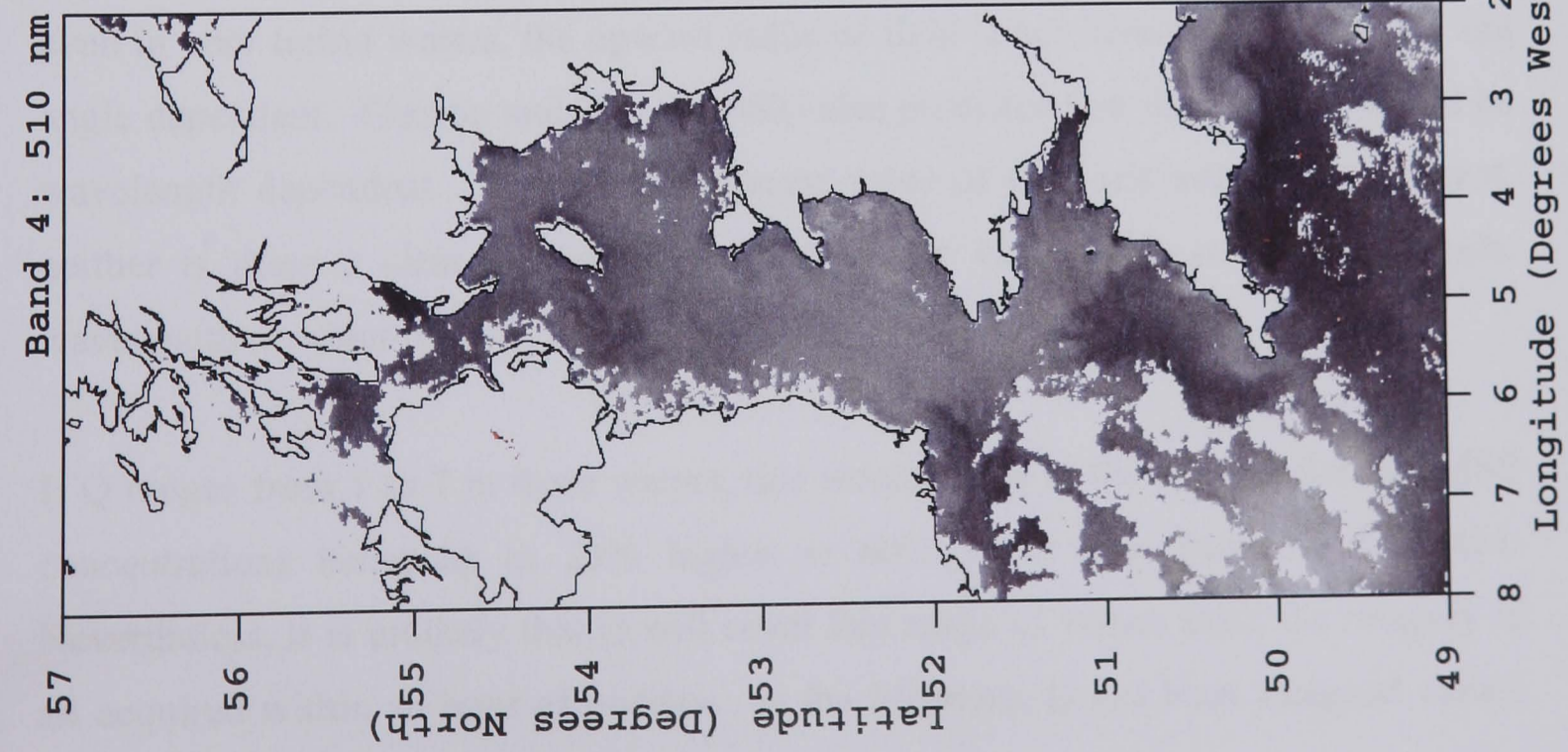
Figure 6.29 cntd: SeaWiFS water-leaving radiance, Lw for bands 1-6 (centred on 412, 443, 490, 510, 555, 670 nm) from 25th February 2000, 13:14. Red regions highlight pixels with negative radiance.

The subject of atmospheric correction over Case 2 waters has received special attention in recent years and methods have been recommended that show some improvement in the accuracy of water-leaving radiance measurements over turbid waters (Moore *et al.*, 1999; Hu *et al.*, 2000). These methods, however, require further verification and are not yet routinely available for image processing. Whilst the issue of atmospheric correction is still to be fully resolved, satellite imagery results in this Chapter have proved to be of significant value. The success of the inverse modelling results in this study is promising and suggests that the errors in atmospheric correction at 670 nm may be small, at least for the range of sediment concentrations observed at the mooring site in the southern Irish Sea.

It is acknowledged that there are some differences between the band characteristics of the two sensors (the PRR600 has a 10 nm waveband centred at 665 nm whereas SeaWiFS band 6 is a 20 nm band centred at 670 nm). No account was taken of these differences in this study; it is anticipated that the effect of these differences will be small, given the errors involved in the measurement of reflectance *in situ* and errors in the atmospheric correction of SeaWiFS.

A principle factor in converting satellite-derived radiances to underwater reflectances is the Q factor, which describes the angular distribution of the upwelling radiance field ($Q = E_u/L_u$). Values of Q in the literature have ranged from less than 1 to 7 for a range of water types and solar angles. Calculations of the Q factor by Shimwell *et al.* (1997) suggested that, in turbid waters, conditions may indeed approach the case of an isotropic light field whereby $Q = \pi$. In contrast, Loisel and Morel (2001) showed that even in very turbid waters, the upward radiance field is not isotropic and remains sun angle dependent. Gordon and Morel (1983) also predicted that the Q factor would be wavelength dependent. Therefore, a precise value of Q is not available at present, neither is there a clear idea of how the Q factor varies with solar zenith angle, wavelength or water type.

If Q ranges from 1 to 7 in these waters, this would result in the satellite-derived MSS concentrations being up to 23% higher or 60% lower than currently predicted. Nevertheless, it is unlikely that Q will cover this range of values since the imagery is all acquired within an hour of midday. In the literature, Q has been assigned values

between 3 and 5 for those sun and viewing angles typically involved in remote sensing studies. This study adopted a value of 5. Therefore, assuming a full range of 3 to 5, derived concentrations could be up to 27% lower than currently estimated. This may be possible since at present, MSS concentrations appear to be overestimated. Nonetheless, whilst there are other sources of error to account for it is difficult to say if this is true, but it is clear that further work is necessary in determining values of Q in order to accurately interpret single wavelength colour imagery (and indeed colour ratios if Q is wavelength dependent).

Chapter Seven

Summary and Conclusions

CHAPTER SEVEN: SUMMARY AND CONCLUSIONS

7.1 Summary of Findings and Implications for Future Research

The primary aim of this study was to develop a technique to derive suspended sediment concentrations in the Irish Sea from SeaWiFS ocean colour imagery. To attain this, *in situ* measurements of irradiance reflectance were collected at wavelengths coincident with the SeaWiFS sensor, enabling an assessment of the way in which suspended sediments and other optically active constituents affect ocean colour in the region.

It was found that the measurement of single band reflectance, rather than variations in colour through reflectance ratios, was the most reliable method for the derivation of suspended sediments in the Irish Sea. Results published in Binding *et al.* (2003), as well as observations concerning the wavelength of peak reflectance in Chapter Four, highlighted that MSS algorithms based on colour ratios in the visible spectrum are susceptible to failure due to the presence of other optically active constituents. The success of previously published algorithms based on visible wavelength colour ratios has been restricted to regions where mineral sediments are likely to dominate the optical signal such as the Bay of Fundy (Amos and Topliss, 1985; Topliss, 1986) and the Humber Estuary (Robinson *et al.*, 1998). Reflectance ratios containing wavelengths in the NIR have been shown to work well in extremely turbid environments with sediment concentrations up to 1000 mg l^{-1} (Moore *et al.*, 1999; Doxaran *et al.*, 2002a, 2002b). The successful use of NIR wavelengths, however, is dependent on the fact that in highly turbid waters there is sufficient scattering to overcome the strong absorption by water at these wavelengths. Results of Doxaran *et al.* (2002b) showed that reflectance in the band 700-900 nm was close to zero for sediment concentrations below 50 mg l^{-1}. Therefore, the effectiveness of reflectance ratios incorporating NIR wavebands is limited to these extreme turbidity levels and would not be applicable to the more moderate concentration ranges measured in shelf seas.

In agreement with many previous optical studies (e.g. Robinson, 1985; Bukata *et al.*, 1995), reflectance in the Irish Sea increased at all wavelengths with increasing sediment loading. A strong empirical relationship was identified between MSS and

R_{665} enabling predictions of MSS concentrations from irradiance reflectance with an average uncertainty of less than 22%. Nevertheless, the large spread in the data points at low MSS concentrations combined with a significant x-axis intercept (suggesting that a baseline MSS concentration of 1.36 mg l^{-1} exists) would result in large errors, particularly at low concentrations.

The observed variability in the Reflectance-MSS relationship was found to be the consequence of changes in mass-specific scattering coefficients (b^{*}_{MSS}) brought about by differences in particle properties such as grain size and refractive index. A systematic increase in the slope of the Reflectance-MSS relationship with increasing b^{*}_{MSS} was identified and formed the basis of a more robust technique for estimating MSS concentrations through inverse modelling.

A detailed study of the inherent optical properties of the optically active constituents enabled the development of a simple reflectance model. Using this model in the forward mode, it was possible to gain a more thorough understanding of the way in which phytoplankton and yellow substance affect the Reflectance-MSS relationship. With knowledge of variations in b^{*}_{MSS}, the reflectance model used in the forward mode enabled the reproduction of R_{665} from known concentrations of MSS, YS and C with an uncertainty of just 9%. This confirms that our understanding of the way the inherent optical properties determine ocean colour in the Irish Sea is accurate. Omitting the optical properties of YS and C from the reflectance calculations had little impact on the retrieval accuracy of the model, confirming the predominant role of scattering by MSS in the region. When used in the inverse mode, this simplified optical model predicted MSS concentrations from R_{665} with an average uncertainty of less than 14%.

An investigation was carried out to determine the factors causing the observed variations in b^{*}_{MSS}. With limited direct measurements of particle properties such as grain size, refractive indices and backscattering properties, it was suggested that the observed variability in the scattering coefficients resulted from the large diversity of grain sizes and particle compositions present in the Irish Sea over two years of sampling. The large variations in particle properties and their effect on scattering have implications for the values of scattering coefficients and backscattering ratios

chosen in optical models developed for dynamic systems such as shelf seas. Most optical models applied to turbid waters have been carried out under conditions where such scattering properties may not vary considerably with space or time, either because the study was restricted to a single geographical position or a single season, or because the dynamics of the environment meant that there would be little variation in the scattering properties under study (Moore *et al.*, 1999; Doxaran *et al.*, 2002a).

The effect of particle scattering properties (incorporating particle size distribution and refractive indices) on reflectance has been studied through theoretical considerations (e.g. Forget *et al.*, 1999) and laboratory experiments (Novo *et al.*, 1989; Moore *et al.*, 1999). However, no examples could be found in the literature describing similar observations of *in situ* variations in particle characteristics linking scattering properties to variations in reflectance in the context of ocean colour algorithms. Neither has a technique been proposed for the measurement of b^*_{MSS} from ocean colour measurements to improve estimates of suspended sediment concentrations in shelf seas.

In this study, a method was proposed to estimate values of b^*_{MSS} from a factor combining the wavelength of peak reflectance and the magnitude of a single waveband reflectance. This enabled the prediction of b^*_{MSS} in the Irish Sea accurate to within 24%. Whilst this technique appeared to give reasonable first estimates of b^*_{MSS}, there was considerable spread in the data due to the influence of scattering by organic particles. The estimation of b^*_{TSS} removed this variance by accounting for the organic content of the suspended particles. However, until some method is available to determine the proportions of organic to inorganic fractions of SPM, it is not possible to utilise b^*_{TSS} in the optical model presented here. Some error is foreseen in the technique used here for determining the wavelength of peak reflectance since it is dependent on the accurate fit of a quadratic function to only six data points. This technique may be improved with the increasing use of hyperspectral *in situ* and remote sensing colour sensors.

Curran and Novo (1988) highlighted a number of stages in the development of algorithms for the estimation of suspended sediment concentrations (SSC) from remotely sensed ocean colour. Most studies have followed the stages below:

1. Simultaneous measurement of SSC and spectral radiance or reflectance.

2. Derivation of an empirical relationship between SSC and the spectral radiance or reflectance.

3. Use of the spectral radiance or reflectance and the relationship in (2) to estimate SSC.

4. Determination of the accuracy of SSC estimation using an independent set of SSC and ocean colour data.

Curran and Novo (1988) highlighted that the majority of studies in the literature terminate at stage 2 or 3 on the assumption that a statistically significant correlation between SSC and the ocean colour parameter is sufficient basis for an accurate estimation of SSC from ocean colour imagery. Even now, algorithm development research rarely proceeds to the final stage where the retrieval accuracy can be determined by testing on an independent data set. Although an acceptable retrieval accuracy was obtained in this study based on the data set from which the algorithms were derived, a more thorough error analysis was performed on two independent data sets of ocean colour with coincident measurements of suspended sediment concentrations.

The time series of optical and water quality observations in the Menai Strait showed that the scattering efficiency of particulate matter exhibited a seasonal pattern, with a minimum in the summer months. This seasonality in b^*_{MSS} was attributed to the flocculation of particles in the summer months as a result of both an increase in the organic content of the suspended matter and a decrease in wind-induced turbulence. Application of the simple reflectance algorithm (quadratic function of R_{665}) to the Menai Strait data set consistently underestimated MSS concentrations (by as much as 60%) suggesting that the particles here were less efficient scatterers than those in the Irish Sea. By accounting for variations in particle scattering efficiencies through inverse modelling, the uncertainty in predicted MSS concentrations was reduced to 13%, with improved accuracy being most evident in the summer months.

The application of the reflectance model to SeaWiFS imagery of the Irish Sea accurately reproduced known regions of high turbidity with MSS concentrations that were in good agreement with those measured *in situ* from a moored transmissometer.

Average percentage uncertainties in sediment concentrations were reduced from 25% when applying the simple reflectance algorithm, to 18% when accounting for variations in particle scattering through inverse modelling. Images provided a valuable time series of maps detailing the seasonal distributions of suspended sediment in the Irish Sea.

The SeaWiFS project specifications called for an uncertainty of less than ±35% in the retrieval of chlorophyll *a* concentrations in Case 1 waters (Hooker *et al.*, 1992) and, although deriving suspended sediment concentrations was not a specific objective of the SeaWiFS project, a similar uncertainty for sediment concentrations should be a realistic goal in sediment-dominated waters. Despite the well publicised problems of atmospheric correction over Case 2 waters, the uncertainty in predicted sediment concentrations in the Irish Sea are well within the goals set out by the SeaWiFS project. Any further improvements in the accuracy of algorithms utilising single band reflectance will necessitate advances in atmospheric correction procedures over Case 2 waters. A number of methods have been recommended in recent years that show some improvement in the accuracy of water-leaving radiance measurements over turbid waters (Moore *et al.*, 1999; Hu *et al.*, 2000). These methods, when routinely available for image processing, should be evaluated to see if any further improvements can be made in the study of suspended sediments in the Irish Sea.

Although the algorithms presented in this study maintain reasonable levels of accuracy during phytoplankton bloom periods, it is expected that the techniques would break down under conditions of extreme productivity or when phytoplankton such as coccolithophores are abundant. Coccolithophore blooms are known to be highly reflective due to the enhanced backscatter from detached coccoliths (Balch *et al.*, 1996) and it has been shown in this study that this results in anomalous increases in predicted MSS concentrations. Nevertheless, methods are now available, as was shown in Chapter Six, that enable affected pixels in an image to be flagged and removed from further processing (Robinson, 2000; Gordon *et al.*, 2001).

Remote sensing algorithms for suspended sediments in the Irish Sea are rare. Therefore, techniques developed in this study have great potential in the study of

coastal processes in this region. It must be emphasised, however, that this algorithm may, at present, only be used for regional applications. Further work will be required testing the applicability of these algorithms to other regions. Nevertheless, the water masses studied here incorporate a range of physical environments, from strongly tidal (and therefore turbid) coastal waters to clearer stratified waters and phytoplankton-dominated sea lochs. The strength of the relationship between R_{665} and MSS under these contrasting conditions is promising, suggesting the algorithm may be applicable to a wide range of water types throughout the year in this region.

Satellite-measured reflectance has been used in previous studies to infer the distribution of suspended sediments in the Irish Sea (Simpson and Brown, 1987; Weeks and Simpson, 1991; Bowers *et al.* 1998). Single waveband reflectance algorithms utilising the AVHRR visible band (580-680 nm) have been proposed, for example, in Delaware Bay (Stumpf and Pennock, 1989), the North Sea (Aguirre-Gomez, 2000), the Bay of Biscay (Froidefond *et al.*, 1998) and the Irish Sea (Bowers *et al.*, 1998) with varying degrees of success. The advantage of obtaining a suitable algorithm applicable to ocean colour sensors such as SeaWiFS, MODIS or MERIS, with numerous narrow wavebands, rather than broad band sensors such as Landsat, SPOT and AVHRR, is that there is then potential to use the remaining spectral wavebands to obtain the remaining optically active constituents; yellow substance and phytoplankton pigments. Furthermore, it would be valuable to be able to obtain further information on the nature of the suspended matter, for instance, successfully deriving the contributions of both organic and inorganic material to the total SPM. This may then enable the observation of a whole suite of water quality parameters from a single satellite image.

Whilst the SeaWiFS objective to derive chlorophyll concentrations to within 35% has been met with some degree of success in Case 1 waters, this is not so in Case 2 waters, where sediments are known to interfere with the retrieval accuracy of standard colour ratio algorithms. The need for improved accuracy in chlorophyll determination is critical in shelf seas which are some of the most productive regions of the world's oceans (Mann and Lazier, 1991). Brown and Simpson (1990) showed empirically that the relationship between the blue/green reflectance ratio and chlorophyll changed as the concentration of MSS increased. In a study of absorption

properties of inorganic particles, Bowers *et al.* (1996) showed that the blue green ratio becomes less sensitive to changes in chlorophyll if inorganic sediments are present. Bowers *et al.* (1996) claimed that in order to use a blue/green ratio to determine chlorophyll in Case 2 waters, it would first be necessary to obtain an independent estimate of suspended sediment concentrations. Figure 7.1 shows the impact of mineral sediments on the retrieval accuracy of the current NASA OC4 chlorophyll algorithm applied to the *in situ* measured ocean colour data from the Irish Sea. In the most turbid waters studied, the OC4 algorithm overestimated chlorophyll concentrations by up to 1000%. Results in this study, enabling the accurate determination of suspended sediments in shelf seas, may go some way to improving chlorophyll estimates in turbid waters.
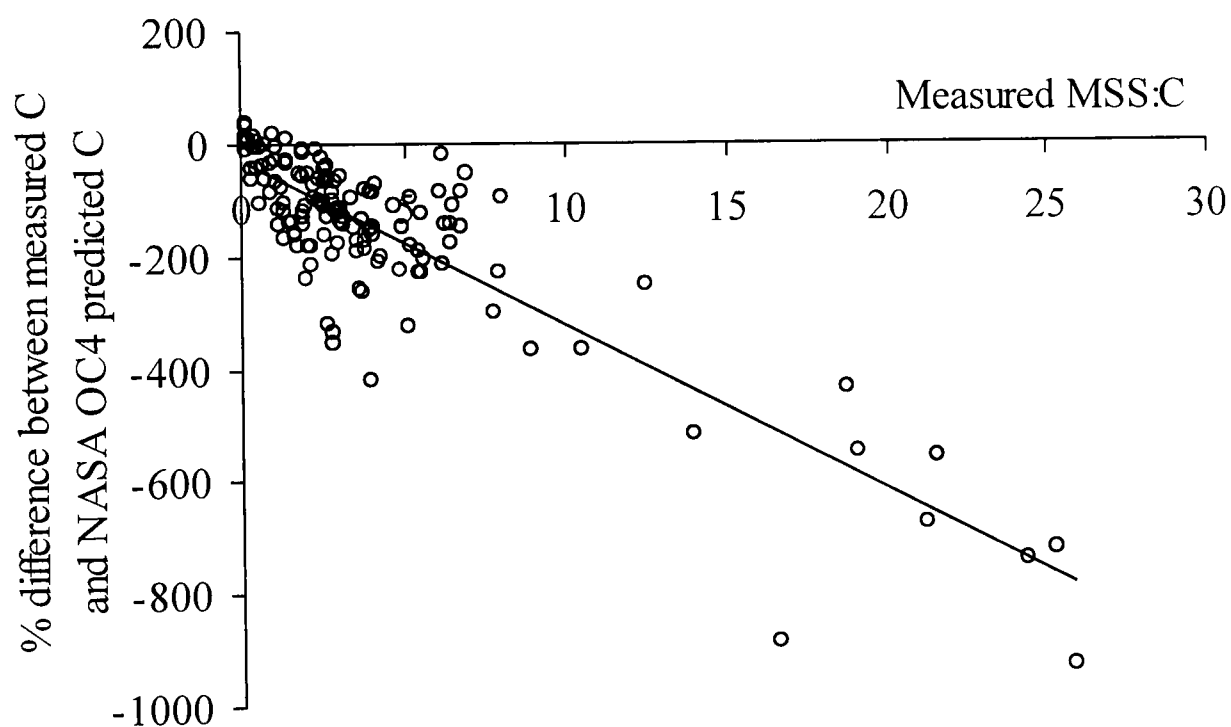
Figure 7.1: The effect of mineral sediments on the retrieval accuracy of the NASA OC4 chlorophyll algorithm in the Irish Sea. $(y = -29.6x - 30.7, R^2 = 75\%, p = 0.00)$

7.2   Conclusions

- The measurement of single band reflectance, rather than variations in colour through reflectance ratios, is shown to be the most reliable method for the derivation of suspended sediments in the Irish Sea. Suspended sediment algorithms based on colour ratios in the visible spectrum are susceptible to failure due to the presence of other optically active constituents.

- A strong empirical relationship between reflectance at 665 nm and MSS enables the prediction of MSS concentrations from *in situ* reflectance measurements with an average uncertainty of less than 22%.

- The variability in the relationship between MSS and R_{665} can be attributed to variations in the particle scattering efficiency, b^*_{MSS}, brought about by changes in factors such as particle grain size, refractive index and the backscattering probability.

- Measured particle scattering properties are combined with optical theory to develop a reflectance model, which, when used in the inverse mode, enables the prediction of MSS concentrations from reflectance with an average uncertainty of less than 14%.

- Values of b^*_{MSS} can be estimated with an average uncertainty of 24% from the combined assessment of the colour and brightness of the water through the parameter λ_{PeakR}/R_{665}.

- The above techniques were applied to a time series of ocean colour measurements in the Menai Strait as an algorithm validation exercise and highlighted the improved accuracy of MSS predictions when accounting for variations in particle scattering properties.

- Application of inverse modelling to SeaWiFS ocean colour satellite imagery produces spatial distributions of MSS in agreement with those in the literature. Results from a moored transmissometer confirm the accuracy of the technique, predicting MSS concentrations with an uncertainty of 18%.

7.3 Recommendations for Further Work

- Further work is needed measuring reflectance in a range of turbidities with coincident observations of sediment characteristics such as grain size, refractive index and scattering properties. A detailed study of the factors affecting b^*_{MSS} and b_b/b and the way in which these parameters vary with geographical location, time and environmental conditions is essential if errors in estimating suspended sediment concentrations are to be reduced. There may be potential for measuring MSS/TSS and/or particle size from space if the factors affecting b^*_{MSS} can be determined more accurately.

- A detailed investigation of the method of estimating b^*_{MSS} from peak reflectance using hyperspectral radiometry is recommended. The present study estimated the wavelength of peak reflectance from information at just six wavelengths, therefore, more precise observations of peak wavelength will enable an accuracy assessment of this technique.

- The application of the same algorithms to other regions would test the applicability of these techniques outside the waters in which the algorithm was developed and will determine the extent to which these can be used as more general algorithms.

- Improvements are required in the atmospheric correction of SeaWiFS ocean colour imagery over Case 2 waters before the retrieval accuracy of the techniques presented in this study can be confirmed.

- Methods presented in this study should be applied to imagery from the recently launched MODIS and MERIS satellite sensors to assess the ongoing use of these techniques in ocean colour studies when SeaWiFS ceases operation.

Appendix I

List of Symbols and Abbreviations

LIST OF SYMBOLS

Symbol	Definition	Units	Page Introduced
β	Volume scattering function	$m^{-1}\,sr^{-1}$	18
β	Solar elevation	degrees	65
$\bar{\beta}$	Scattering phase function	sr^{-1}	18
δ	Solar declination	degrees	65
λ	Wavelength	nm	12
λ_{peakR}	Wavelength of peak reflectance	nm	77
Φ	Radiant flux	W	13
ρ	Fresnel reflectance	---	146
τ	Angular Day	degrees	66
ω	Solid angle	sr	13
θ	Zenith angle	degrees	13
ψ	Angular date	degrees	66
μ	Mean Underwater Cosine	---	21
(0^-)	Just beneath the surface	---	19
(0^+)	Just above the surface	---	19
(z)	At depth z	---	19
[MSS]	Mineral Suspended Sediment concentration	$mg\,l^{-1}$	17
[OSS]	Organic Suspended Sediment concentration	$mg\,l^{-1}$	59
[TSS]	Total Suspended Sediment concentration	$mg\,l^{-1}$	59
[YS]	Yellow Substance concentration	m^{-1}	17
a	Absorption coefficient	m^{-1}	16
A	Absorbance	---	16
$a^*_{W,MSS,YS,C}$	Specific absorption coefficient, where the subscripts W, MSS YS and C refer to water, mineral suspended sediments, yellow substance and phytoplankton pigments respectively.	$m^2\,g^{-1}$ $m^2\,mg^{-1}$	18
b	Scattering coefficient	m^{-1}	16
B	Scatterance	---	16
$b^*_{W,MSS,YS,C}$	Specific Scattering coefficient, where the subscripts W, MSS YS and C refer to water, mineral suspended sediments, yellow substance and phytoplankton pigments respectively.	$m^2\,g^{-1}$ $m^2\,mg^{-1}$	18
B_a	Acidified blank	---	56
b_b	Back-scattering coefficient	m^{-1}	18
B_b	Non-acidified blank	---	56
b_f	Forward-scattering coefficient	m^{-1}	18
c	Speed of light	$= 2.998 \times 10^8\,ms^{-1}$	12
c	Beam attenuation coefficient	m^{-1}	17
C	Phytoplankton pigments concentration	$\mu g\,l^{-1}$	17
$E_{u,d,s,0}$	Irradiance, where the subscripts u, d, s and 0 denote upwelling, downwelling, surface incident and scalar respectively	$\mu W\,cm^{-2}\,nm^{-1}$	13

f	Photon frequency	s^{-1}	12
f_a	Acidified Fluorescence	---	56
f_b	Non-acidified Fluorescence	---	56
h	Planck's constant	$= 6.626 \times 10^{-34}$ J s	12
h	Depth	m	46
I	Radiant Intensity	$W\ sr^{-1}$	13
K_d	Diffuse attenuation coefficient for downwelling light	m^{-1}	20
K_f and H_f	Fluorometer calibration constants	---	56
l_s	Absorption pathlength	m	61
$L_{u,d}$	Radiance, where the subscripts u and d denote upwelling and downwelling respectively	$\mu W\ cm^{-2}\ sr^{-1}\ nm^{-1}$	13
L_w	Water-leaving radiance	$\mu W\ cm^{-2}\ sr^{-1}\ nm^{-1}$	20
$N_{w,a}$	Refractive index of water, air	---	66
$OD_{s,f}$	Optical Density, where the subscripts s and f define in suspension and on filter	---	57
Q	$= E_u/L_u$	sr^{-1}	19
R	Irradiance reflectance $= E_u/E_d$	---	19
R	Range	---	56
R_{RS}	Remote sensing reflectance $= L_w/E_d$	sr^{-1}	20
S	Coefficient determining slope of yellow substance absorption	---	32
T	Transmittance	---	17
u	Tidal current amplitude	$cm\ s^{-1}$	46
V_{ex}	Volume extracted	ml	56
V_f	Volume filtered	l	56
W	Water	---	17
W_0	Initial weight	g	59
W_b	Burnt weight	g	59
W_d	Dry weight	g	59

LIST OF ABBREVIATIONS AND ACRONYMS

ADEOS	Advanced Earth Observation Satellite
AOPs	Apparent Optical Properties
ATM	Advanced Thematic Mapper
AVHRR	Advanced Very High Resolution Radiometer
C	Phytoplankton Pigments
CASI	Compact Airborne Spectrographic Imager
CTD	Conductivity, Temperature and Depth
CZCS	Coastal Zone Colour Scanner
DOM	Dissolved Organic Matter
DSRS	Dundee Satellite Receiving Station
ERTS	Earth Resources Technology Satellite
FOV	Field of View
FWHM	Full Width at Half Maximum
GAC	Global Area Coverage
HPLC	High Performance Liquid Chromatography
IOPs	Inherent Optical Properties
LAC	Local Area Coverage
MERIS	Medium Resolution Imaging Spectrometer
MODIS	Moderate Resolution Imaging Spectroradiometer
MSS	Mineral Suspended Sediment
MSS	Multispectral Scanner
NASA	National Aeronautics and Space Administration
NASDA	National Space Development Agency of Japan
NERC	Natural Environment Research Council
NIR	Near Infra Red
NIST	National Institute of Standards and Technology
OCTS	Ocean Colour and Temperature Sensor
OD	Optical Density
OSC	Orbital Sciences Corporation
OSS	Organic Suspended Sediment
PAR	Photosynthetically Available Radiation
PRR	Profiling Reflectance Radiometer
RSDAS	Remote Sensing Data Analysis Service
SeaDAS	SeaWiFS Data Analysis System
SeaWiFS	Sea-viewing Wide Field-of-view Sensor
SPM	Suspended Particulate Matter
SPOT	Satellite Pour l'Observation de la Terre
TM	Thematic Mapper
TSS	Total Suspended Sediment
YS	Yellow Substance

Appendix II

List of References Cited

LIST OF REFERENCES CITED

Alexandersson, H., Tuomenvirta, H., Schmith, T. and Iden, K. 2000. Trends of storms in NW Europe derived from an updated pressure data set. *Climate Research*, Vol. 14, No. 1, pp. 71-73.

Aguirre-Gomez, R. 2000. Detection of total suspended sediments in the North Sea using AVHRR and ship data. *International Journal of Remote Sensing*. Vol. 21. No. 8, pp. 1583-1596.

Amos, C. L. and Topliss, B. J. 1985. Discrimination of suspended particulate matter in the Bay of Fundy using the Nimbus-7 Coastal Zone Colour Scanner. *Canadian Journal of Remote Sensing*, Vol. 11, pp.85-92.

Austin, R. W. 1974. The remote sensing of spectral radiance from below the ocean surface. In: Jerlov, N. G. and Nielsen, E. S (Eds) *Optical Aspects of Oceanography* (Chapter 14, pp. 317-344). London: Academic Press. 494pp.

Baban, S. M. J. 1994. Mapping turbidity, surface temperature and water circulation patterns with the aid of satellite imagery. *Journal of the Institution of Water and Environmental Management*, Vol. 8, No. 2, pp. 197-204.

Baban, S. M. J. 1997. Environmental monitoring of estuaries estimating and mapping various environmental indicators in Breydon Water Estuary, UK, using Landsat TM imagery. *Estuarine, Coastal and Shelf Science*, Vol. 44, No. 5. pp. 589-598.

Baker, E. T. and Lavelle, J. W. 1984. The effect of particle size on the light attenuation coefficient of natural suspensions. *Journal of Geophysical Research*. Vol. 89, No. C5, pp. 8197-8203.

Balch, W. M., Drapeau, D. T., Cucci, T. L. and Vaillancourt, R. D. 1996. The 1991 coccolithophore bloom in the central North Atlantic. 1. Optical properties and factors affecting their distribution. *Limnology and Oceanography*. Vol. 41, No. 8, pp. 1669-1683.

Behrenfeld, M. J. and Falkowski, P. G. 1997. Photosynthetic rates derived from satellite based chlorophyll concentration. *Limnology and Oceanography*, Vol. 42, pp. 1-20.

Bidigare, R. R., Ondrusek, M. E., Morrow, J. H. and Kiefer, D. A. 1990. *In vivo* absorption properties of algal pigments. *Proceedings of SPIE Ocean Optics X*, Vol. 1302, pp. 290-302.

Binding, C. E. 1999. Optical classification of Irish Sea waters and the development of chlorophyll algorithms for use with ocean colour satellite imagery. *M.Sc. Thesis, University of Wales Bangor.* 115pp.

Binding, C. E. and Mitchelson-Jacob, E. G. 2000. SPM algorithms for SeaWiFS imagery of Case 2 waters. Poster presented at Oceans from Space, Venice 2000.

Binding, C. E. and Bowers, D. G. 2003. Measuring the salinity of the Clyde Sea from remotely sensed ocean colour. *Estuarine, Coastal and Shelf Science*. In press.

Binding, C. E., Bowers, D. G. and Mitchelson-Jacob, E.G. 2003. An algorithm for the retrieval of suspended sediment concentrations in the Irish Sea from SeaWiFS ocean colour satellite imagery. *International Journal of Remote Sensing*. In press.

Binding, C. E., Bowers, D. G. and Mitchelson-Jacob, E. G. 2002. The retrieval of suspended sediments from ocean colour satellite imagery. Paper presented at the Challenger Society for Marine Science, Plymouth, 9-13 Sept. 2002.

Blight, S. P, Bentley, T. L., Lefevre, D., Robinson, C., Rodrigues, R. Rowlands, J and Williams, P. J. leB. 1995. Phasing of autotrophic and heterotrophic plankton

metabolism in a temperate coastal ecosystem. *Marine Ecology Progress Series*. Vol. 128, pp. 61-75.

Bonsdorff, E., Blomqvist, E. M., Mattila, J. and Norkko, A. 1997. Coastal eutrophication: Causes, consequences and perspectives in the Archipelago areas of the northern Baltic Sea. *Estuarine, Coastal and Shelf Science*. Vol. 44. pp. 63-72.

Boudjelas, S. 1994. Temporal and Spatial variations in suspended sediments in the Irish Sea determined from AVHRR visible band and in situ data. *PhD thesis. University of Wales Bangor, UK.*

Bowers, D. G. and Mitchelson-Jacob, E. G. 1996. Inherent optical properties of the Irish Sea as determined from underwater irradiance measurements. *Estuarine, Coastal and Shelf Science*, Vol. 43, pp. 433-447.

Bowers, D. G., Harker, G. E. L. and Stephan, B. 1996. Absorption spectra of inorganic particles in the Irish Sea and their relevance to remote sensing of chlorophyll. *International Journal of Remote Sensing*, Vol. 17, No. 12. pp. 2449-2460.

Bowers, D. G., Boudjelas, S. and Harker, G. E. L. 1998. The distribution of fine suspended sediments in the Irish Sea and its dependence on tidal stirring. *International Journal of Remote Sensing*, Vol. 19, pp. 2789-2805.

Bowers, D. G., Harker, G. E. L., Smith, P. S. D and Tett, P. 2000. Optical properties of a region of freshwater influence (The Clyde Sea). *Estuarine, Coastal and Shelf Science*, Vol. 50, pp. 717-726.

Brakel, W. H. 1984. Seasonal dynamics of suspended-sediment plumes from the Tana and Sabaki Rivers, Kenya: Analysis of Landsat Imagery. *Remote Sensing of the Environment*, Vol. 16, pp. 165-173.

Bricaud, A., Morel, A. and Prieur, L. 1981. Absorption by dissolved organic matter of the sea (yellow substance) in the UV and visible domains. *Limnology and Oceanography*, Vol. 26, pp. 43-53.

Bricaud, A., Morel, A. and Prieur, L. 1983. Optical efficiency of some phytoplankters. *Limnology and Oceanography*, Vol. 28, No. 5, pp. 816-832.

Bricaud, A. and Stramski, D. 1990. Spectral absorption coefficients of living phytoplankton and non-algal biogenous matter; A comparison between the Peru upwelling area and the Sargasso Sea. *Limnology and Oceanography*, Vol. 35, pp. 562-582.

Bricaud, A., Babin, M., Morel, A. and Claustre, H. 1995. Variability in the chlorophyll-specific absorption coefficients of natural phytoplankton: analysis and parameterization. *Journal of Geophysical Research*. Vol. 100, No. C7, pp. 13,321-13,332.

Brown, J. and Simpson, J. H. 1990. The radiometric determination of total pigment and seston and its potential use in shelf seas. *Estuarine, Coastal and Shelf Science*, Vol. 31, pp. 1-9.

Buchan, S., Floodgate, G. D. and Crisp, D. 1967. Studies of the seasonal variation of the suspended matter of the Menai Strait: II the organic fraction. *Limnology and Oceanography*, Vol. 12, pp. 419-431.

Buiteveld, H., Hakvoort, J. H. M. and Donze, M. 1994. The Optical Properties of Pure Water. In: *Proceedings of SPIE Ocean Optics XII*, June 1994 Bergen. Norway. Vol. 2258, pp. 174-183.

Bukata, R. P., Bruton, J. E. and Jerome, J. H. 1983. Use of chromaticity in remote measurements of water quality. *Remote Sensing of Environment*. Vol. 13. pp. 161-177.

Bukata, R. P., Jerome, J. H., and Bruton, J. E. 1988. Relationships among secchi disk depth, beam attenuation coefficient and irradiance attenuation coefficient for Great lakes waters. *Journal of Great Lakes Research*, Vol. 14, pp. 347-355.

Bukata, R. P., Jerome, J. H., Kondratyev, K. Y. and Pozdnyakov, D. V. 1995. *Optical Properties and Remote Sensing of Inland and Coastal Waters*. CRC Press. Inc., Boca Raton, Florida, 362pp.

Bukata, R. P., Jerome, J. H., Kondratyev, K. Y., Pozdnyakov, D. V. and Kotykhov, A. A. 1997. Modelling the radiometric color of inland waters: implications to a) remote sensing and b) limnological color scales. *Journal of Great lakes Research*, Vol. 23, No. 3, pp. 254-269.

Burban, P. Lick, W. and Lick, J. 1989. The flocculation of fine-grained sediments in estuarine waters. *Journal of Geophysical Research*, Vol. 94. No. C6. pp. 8323-8330.

Butler, W. L. 1962. Absorption of light by turbid materials. *Journal of the Optical Society of America*, Vol. 52, pp. 292-299.

Carder, K.L. and Steward, R.G. 1985. A remote-sensing reflectance model of a red-tide dinoflagellate off west Florida. *Limnology and Oceanography*, Vol. 30, pp. 286-298.

Carder, K. L., Steward, R. G., Harvey, G. R. and Ortner, P. B. 1989. Marine humic and fulvic acids: their effects on remote sensing of ocean chlorophyll. *Limnology and Oceanography*, Vol. 34, pp. 68-81.

Chester, R. 1990. *Marine Geochemistry*. Unwin Hyman Ltd, London. 698pp.

Clark, D. K., Baker, E. T. and Strong, A. E. 1980. Upwelled spectral radiance distribution in relation to the particulate matter in sea water. *Boundary Layer Meteorology*, Vol. 18, pp. 286-298.

Cleveland, J. S. and Weidemann, A. D. 1993. Quantifying absorption by aquatic particles: A multiple scattering correction for glass-fibre filters. *Limnology and Oceanography*, Vol. 38, pp. 1321-1327.

Collins, M. and Pattiaratchi, C. 1984. Identification of suspended sediment in coastal waters using airborne thematic mapper data. *International Journal of Remote Sensing*, Vol. 5, No. 4, pp. 635-657.

Curran, P. J., Hansom, J. D., Plummer, S. E. and Pedley, M. I. 1987. Multi-spectral remote sensing of near-shore suspended sediments; a pilot study. *International Journal of Remote Sensing*, Vol. 8, pp. 103-112.

Curran, P. J. and Novo, E. M. M. 1988. The relationship between suspended sediment concentration and remotely sensed spectral radiance; a review. *Journal of Coastal Research*, Vol. 4, pp. 3541-368.

Davies-Colley, R. J. 1983. Optical properties and reflectance spectra of 3 shallow lakes obtained from a spectrophotometric study. *New Zealand Journal of Marine and Freshwater Research*, Vol. 17, pp. 445-459.

DiToro, D. M. 1978. Optics of turbid estuarine waters: Approximations and applications. *Water Research*, Vol. 12, pp. 1059-1068.

Doxaran, D., Froidefond, J., Lavender, S. and Castaing, P. 2002a. Spectral signature of highly turbid waters; Application with SPOT data to quantify suspended particulate matter concentrations. *Remote Sensing of Environment*. Vol. 81, pp. 149-161.

Doxaran, D. Froidefond, J. and Castaign, P. 2002b. A reflectance band ratio used to estimate suspended matter concentrations in sediment-dominated coastal waters. *International Journal of Remote Sensing*, Vol. 23, No. 23, pp. 5079-5085.

Duursma, E. K. and Smies, M. 1982. Sediments and transfer at and in the bottom interfacial layer. In: *Pollution transfer and transport in the sea.* Edited by G. Kullenberg (Boca Raton, Florida : C.R.C. Press).

Eisma, D. 1993. *Suspended Matter in the Aquatic Environment.* Springer-Verlag. Berlin. 315pp.

Elliott, A. J. 1991. EUROSPILL: Oceanographic processes and NW European databases. *Marine Pollution Bulletin,* Vol. 22, pp. 548-553.

Forget, P., Ouillon, S., Lahet, F., and Broche, P. 1999. Inversion of reflectance spectra of non-chlorophyllous turbid coastal waters. *Remote Sensing of Environment,* Vol. 68, pp. 264-272.

Froidefond, J. Castaign, P. and Prud'homme, R. 1998. Monitoring suspended particulate matter fluxes and patterns with the AVHRR/NOAA-11 satellite: application to the Bay of Biscay. *Deep-Sea Research Part II.* Vol. 46, pp. 2029-2055.

Gallegos, C. L., Correll, D. L. and Pierce, J. W. 1990. Modelling spectral diffuse attenuation, absorption and scattering coefficients in a turbid estuary. *Limnology and Oceanography,* Vol. 35, pp. 1486-1502.

Gordon, H. R. 1998. Vicarious calibration of ocean color sensors. *Remote Sensing of Environment,* Vol. 63, pp. 265-278.

Gordon, H.R., Boynton, G.C., Balch, W.M., Groom, S.B., Harbour, D.S. and Smyth T.J.. 2001. Retrieval of Coccolithophore Calcite Concentration from SeaWiFS Imagery. *Geophysical Research Letters,* Vol. 28, pp. 1587-1590.

Gordon, H. R, Brown, O. B. and Jacobs, M. M. 1975. Computed relationships between the inherent and apparent optical properties of a flat, homogenous ocean. *Applied Optics,* Vol. 14, pp. 417-427.

Gordon, H. R., Clark, D. K., Brown, J. W., Brown, O. B., Evans, R. H. and Broenkow, W. W. 1983. Phytoplankton pigment concentrations in the Middle Atlantic Bight: comparison of ship determinations and CZCS estimates. *Applied Optics,* Vol. 22, No. 1, pp. 20-36.

Gordon, H. R. and Ding, K. 1992. Self-shading of in-water optical instruments. *Limnology and Oceanography,* Vol. 37, No. 3, pp. 491-500.

Gordon, H. R. and McCluney, W. R. 1975. Estimation of the depth of sunlight penetration in the sea for remote sensing. *Applied Optics,* Vol. 14, No. 2, pp. 413-427.

Gordon, H. R. and Morel, A. 1983. *Remote assessment of ocean colour for interpretation of satellite visible imagery. A review.* New York: Springer. 114pp.

Gordon, H.R. and Wang, M. 1994. Retrieval of water-leaving radiance and aerosol optical thickness over the oceans with SeaWiFS: A preliminary algorithm. *Applied Optics,* Vol. 33, pp. 443-452.

Gould, R. W. and Arnone, R. A. 1998. Three-dimensional modelling of inherent optical properties in a coastal environment: coupling ocean colour imagery and *in situ* measurements. *International Journal of Remote Sensing,* Vol. 19. No. 11, pp. 2141-2159.

Hakvoort, H., Haan, J., Jordans, R.. , Vos, R., Peters, S. and Rijkeboer, M. 2002. Towards airborne remote sensing of water quality in the Netherlands – validation and error analysis. *Journal of Photogrammetry and Remote Sensing,* Vol. 57, No. 3, pp. 171-183.

Han, L. and Rundquist, D. C. 1996. Spectral characterization of suspended sediments generated from two texture classes of clay soil. *International Journal of Remote Sensing,* Vol. 17, No. 3, pp. 643-649.

Han, L. 1997. Spectral reflectance with varying suspended sediment concentrations in clear and algae-laden waters. *Photogrammetric Engineering and Remote Sensing*, Vol. 63, No. 6, pp. 701-705.

Harker, G. E. L. 1997. A comparison between optical measurements made in the field and in the laboratory, and the development of an optical model. *Ph.D. thesis*. University of Wales, Bangor, UK.

Harvey, J. G. 1968. The flow of water through the Menai Straits. *Geophysical Journal of the Royal Astronomical Society*, Vol. 15, pp. 517-528.

Herlevi, A. 2002. A study of scattering, backscattering and hyperspectral reflectance model for Boreal waters. *Geophysica*, Vol. 38, No. 1-2, pp. 113-132.

Hoepffner, N. and Sathyendranath., S. 1992. Bio-optical characteristics of coastal waters: absorption spectra of phytoplankton and pigment distribution in the western North Atlantic. *Limnology and Oceanography*, Vol. 37, No. 8, pp. 1660-1679.

Hollyer, R. J. 1978. Toward universal multispectral suspended sediment algorithms. *Remote Sensing of the Environment*, Vol. 7, pp.323-38.

Hooker, S. B., Esaias, W., E.., Feldman, G. C., Gregg, W. W. and McClain, C. R. 1992. An overview of SeaWiFS and ocean color. SeaWiFS Technical Report Series, Volume 1. NASA Technical Memorandum 104566. 25pp.

Hovis, W. A., Clark, D. K., Anderson, F., Austin, R. W., Wilson, W. H., Baker, E. T., Ball, D., Gordon, H. R., Mueller, J. L., El-Sayed, S. Z., Sturm, B., Wrigley, R. C. and Yentsch, C. S. 1980. Nimbus-7 coastal zone color scanner: system description and initial imagery. *Science*, Vol. 210, pp. 60-63.

Hu, C., Carder, K., and Muller-Karger, F. E. 2000. Atmospheric correction of SeaWiFS imagery over turbid coastal waters: a practical method. *Remote Sensing of Environment*, Vol. 74, pp. 195-206.

Hunter, J. R. 1972. An investigation into the circulation of the Irish Sea. *Ph.D. Thesis, university of Wales Bangor*. 166pp.

Irish Sea Study Group, 1990. *The Irish Sea - An Environmental Review: Part 1 Nature Conservation*. Liverpool University Press, Liverpool. 404pp.

Irish Sea Forum Report - Seminar 24, February 2000. Concerns about the Irish Sea Environment. http://www.liv.ac.uk/~isf1/isfhome.html

Jay, D. A., Geyer, W. R., Uncles, R. J., Vallino, J., Largier, J. and Boynton, W. R. 1997. A review of recent developments in estuarine scalar flux estimation. *Estuaries*, Vol. 20, pp. 262-280.

Jerlov, N. G. 1976. *Marine Optics*. Elsevier, Amsterdam. 231pp.

Jones, S., Simpson, J., McCandliss, R., Wallace, J., O'Kelly, C. and Trickett, P. 2000. *Irish Sea Southern Boundary Study*. INTERREG II Project Contract No. EU789/14/003. 25pp.

Jones, S. E., Jago, C.F., Balle, A. J., Chapman, D., Howland, R. J. M. and Jackson, J. 1998. Aggregation and resuspension of suspended particulate matter at a seasonally stratified site in the southern North Sea: physical and biological controls. *Continental Shelf Research*, Vol. 18, pp.1283-1309.

Kalle, K. 1966. The problem of Gelbstoff in the sea. *Oceanography and Marine Biology Annual Reviews*, Vol. 4, pp. 91-104.

Kiefer, D. A. and SooHoo, J. B. 1982. Spectral absorption by marine particles of coastal waters of Baja California. *Limnology and Oceanography*, Vol. 27, pp. 492-499.

Kirk, J. T. O. 1976. Yellow Substance (gelbstoff) and its contribution to the attenuation of photosynthetically active radiation in some inland and coastal

southeastern Australian waters. *Australian Journal of Marine and Freshwater Research*, Vol. 27, pp. 61-71.

Kirk, J. T. O. 1981a. A Monte Carlo study of the nature of the underwater light field in, and the relationships between optical properties of, turbid yellow waters. *Australian Journal of Marine and Freshwater Research*, Vol. 32, pp. 517-532.

Kirk, J. T. O. 1981b. Estimation of the scattering coefficient of natural waters using underwater irradiance measurements. *Australian Journal of Marine and Freshwater Research*, Vol. 32, pp. 533-539.

Kirk, J. T. O. 1984. Dependence of relationships between inherent and apparent optical properties of water on solar altitude. *Limnology and Oceanography*, Vol. 29, pp. 350-356.

Kirk, J. T. O. 1989. The upwelling light stream in natural waters. *Limnology and Oceanography*, Vol. 34, pp. 1410-1425.

Kirk, J. T. O. 1991. Volume scattering function, average cosines and the underwater light field. *Limnology and Oceanography*, Vol. 36, pp. 455-467.

Kirk, J. T. O. 1994. *Light and Photosynthesis in Aquatic Ecosystems, second edition*. Cambridge University Press. 509pp.

Kishino, M., Takahashi, M., Okami, N. and Ichimura, S. 1985. Estimation of the spectral absorption of phytoplankton in the sea. *Bulletin of Marine Science*, Vol. 37, pp. 634-642.

Kratzer, S., Bowers, D. G. and Tett, P. B. 2000. Seasonal changes in colour ratios and optically active constituents in the optical Case-2 waters of the Menai Strait, North Wales. *International Journal of Remote Sensing*. Vol. 21, No. 11. pp. 2225-2246.

Kratzer, S., Buchan, S. and Bowers, D. G. 2003. Testing long-term trends in turbidity in the Menai Strait, North Wales. *Estuarine, Coastal and Shelf Science*, Vol. 56, pp. 221-226.

Kullenberg, G. 1974. Observed and computed scattering functions. In: *Optical Aspects of Oceanography*, Jerlov, N. G. and Nielsen, E. S. (Eds.) Academic Press, London, pp. 25-49.

Kutser, T., Herlevi, A., Kallio, K., Arst, H. 2001. A hyperspectral model for interpretation of passive optical remote sensing data from turbid lakes. *Science of the Total Environment*. Vol. 268, pp. 47-58.

Lathrop, R. G., Lillesand, T. M. and Yandell, B. S. 1991. Testing the utility of simple multi-date Thematic Mapper calibration algorithms for monitoring turbid inland waters. *International Journal of Remote Sensing*, Vol. 12, No., 10, pp. 2045-2063.

Latimer, P. and Rabinowitch, E. 1959. Selective scattering of light by pigments *in vivo. Archives of Biochemistry and Biophysics*, Vol. 84, pp. 428-441.

Lee, Z. P., Carder, K. L., Hawes, S. K., Steward, R. G., Peacock, T. G. and Davis, C. O. 1994. Model for the interpretation of hyperspectral remote-sensing reflectance. *Applied Optics*, Vol. 33, pp. 5721-5732.

Lick, W., Huang, H. and Jepsen, R. 1993. Flocculation of fine-grained sediments due to differential settling. *Journal of Geophysical Research*, Vol. 98, No. C6, pp. 10279-10288.

Loisel, H. and Morel, A. 2001. Non-isotropy of the upward radiance field in typical coastal (Case 2) waters. *International Journal of Remote Sensing*, Vol. 22, No. 2, pp. 275-295.

Longhurst, A., Sathyendranath, S., Platt, T and Caverhill, C. 1995. An estimate of global primary production in the ocean from satellite radiometer data. *Journal*

of Plankton Research, Vol. 17, pp. 1245-1271.

Lyzenga, D. R. 1978. Passive remote sensing techniques for mapping water depth and bottom features. *Applied Optics,* Vol. 17, pp. 379-383.

Mann, K. H. and Lazier, J. R. N. 1991. *Dynamics of marine ecosystems: biological-physical interactions in the oceans.* Blackwell Scientific Publications. Boston. 466pp.

Mayo, M. A., Karnieli, A., Gitelson, A. and Benavraham, Z. 1993. Determination of suspended sediment concentrations from CZCS data. *Photogrammetric Engineering and Remote Sensing,* Vol. 59, No. 8, pp. 1265-1269.

Mitchelson, E. G. 1983. Phytoplankton and suspended sediment distributions in relation to physical structure and water leaving colour signals. *PhD Thesis. University College of North Wales, Bangor, Wales.*

Mitchelson-Jacob, E. G. 1999. Retrieval of suspended particulate matter concentrations from ocean colour imagery. *Unit for Coastal and Estuarine Studies report U99-2.* 64 pp.

Mitchelson, E. G., Jacob, N. J. and Simpson, J. H. 1986. Ocean colour algorithms from the Case 2 waters of the Irish Sea in comparison to algorithms from Case 1 waters. *Continental Shelf Research,* Vol. 5, No. 3, pp. 403-415.

Mitchell, B. and Kiefer, B. G. 1988. Chlorophyll a specific absorption and fluorescence excitation spectra for light-limited phytoplankton. *Deep Sea Research,* Vol. 35, No. 5, pp. 639-663.

Mobley, C. D. 1994. *Light and water; radiative transfer in natural waters.* Academic Press. 592 pp.

Moore, G. F., Aiken, J., and Lavender, S. J. 1999. The atmospheric correction of water colour and the quantitative retrieval of suspended particulate matter in case II waters: application to MERIS. *International Journal of Remote Sensing,* Vol. 20, pp. 1713-1733.

Moore, G. K. 1977. Satellite surveillance of physical water-quality characteristics. *Proceedings of the 12th International Symposium on Remote Sensing of the Environment,* Vol. 8, pp.445-461.

Morel, A. 1974. Optical properties of pure water and pure seawater. In Jerlov, N. G. and Nielsen, E. S. (Eds). *Optical aspects of oceanography.* Academic Press, London. pp. 1-24.

Morel, A. 1980. In-water and remote measurement of ocean color. *Boundary-Layer Meteorology,* Vol. 18, pp. 177-201.

Morel A. 1987. Chlorophyll-specific scattering coefficient of phytoplankton, a simplified theoretical approach. *Deep-Sea Research,* Vol. 34, pp. 1093-1105.

Morel, A. and Bricaud, A. 1981. Theoretical results concerning light absorption in a discrete medium, and application to specific absorption of phytoplankton. *Deep Sea Research,* Vol. 28A, No. 11, pp. 1375 - 1393.

Morel, A. and Gentili, B. 1996. Diffuse reflectance of oceanic waters. III. Implication of bidirectionality for the remote-sensing problem. *Applied Optics.* Vol. 35, pp. 4850-4862.

Morel, A. and Prieur, L. 1977. Analysis of variations in ocean colour. *Limnology and Oceanography,* Vol. 22, No. 4, pp. 709-721.

Mueller, J. L. and Austin, R. W. 1995. *Ocean Optics Protocols for SeaWiFS Validation, Revision 1,* SeaWiFS Technical Report Series, Vol. 25. S. B. Hooker. E. R. Firestone and J. G. Acker (eds.), NASA Technical Memorandum 104566, Greenbelt, Maryland.

Mueller, J. L and Fargion, G. S (Editors). 2002. Ocean Optics Protocols for Satellite Ocean Colour Validation, Revision 3, Volume 1&2. *NASA Technical Memorandum 21004.* Goddard Space Flight Centre, Greenbelt, Maryland. 308 pp.

Myers, V. I. and Allen, B. A. 1968. Electroptical remote sensing methods as non-destructive testing and measuring techniques in agriculture. *Applied Optics.* Vol. 7, pp. 1818-1838.

Novo, E. M. M., Hansom, J. D. and Curran, P. J. 1989. The effect of sediment type on the relationship between reflectance and suspended sediment concentration. *International Journal of Remote Sensing,* Vol. 10. No. 7. pp. 1283-1289.

Novo, E. M. M., Steffen, C. A. and Braga, C. Z. F. 1991. Results of a laboratory experiment relating spectral reflectance to total suspended solids. *Remote Sensing of Environment,* Vol. 36, No. 67-72.

O'Reilly, J. E., Maritorena, S., Siegel, D., O'Brien, M. C., Toole, D., Mitchell, B. G., Kahru, M., Chavez, F. P., Strutton, P., Cota, G., Hooker, S. B., McClain, C. R., Carder, K. L., Muller-Karger, F., Harding, L., Magnuson, A., Phinney, D., Moore, G. F., Aiken, J., Arrigo, K. R., Letelier, R., Culver, M. 2000. Ocean color chlorophyll a algorithms for SeaWiFS, OC2 and OC4: Version 4. In: *SeaWiFS Postlaunch Technical Report Series Volume 11*, edited by Hooker, S.B and Firestone, E.R. SeaWiFS Postlaunch Calibration and Validation Analyses, Part 3. NASA, Goddard Space Flight Center, Greenbelt, Maryland, pp. 9 -24.

Orford, J. D. 1989. A review of tides, currents and waves in the Irish Sea. In : *The Irish Sea; A resource at risk.* Sweeney, J. C. (Ed.). Geographical Society of Ireland. pp. 18-46.

Parslow, J., Hoepffner, N., Doerffer, R., Campbell, J. and Sathyendranath, S. 2000. Chapter 5. Case 2 Ocean-Colour Applications. In: *Remote Sensing of Ocean Colour in Coastal and other Optically Complex Waters.* Report No. 3 of the International Ocean Colour Coordinating Group, pp. 94-116. Edited by Sathyendranath, S.

Pegau, W. S. and Zanefeld, J. R. V. 1993. Temperature-dependent absorption of water in the red and near-infrared portions of the spectrum. *Limnology and Oceanography,* Vol. 38, pp. 188-192.

Petzold, T. J. 1972. Volume scattering functions for selected ocean waters. In: *Light in the Sea,* Edited by Tyler, J. E. Dowden, Hutchinson & Ross, Stroudsberg. pp. 150-174.

Phillips, D. M. and Kirk, J. T. O. 1984. Study of the spectral variation of absorption and scattering in some Australian coastal waters. *Australian Journal of Marine and Freshwater Research,* Vol. 35, pp. 635-644.

Pingree, R. D. and Griffiths, D. K. 1978. Tidal fronts on the shelf seas around the British Isles. *Journal of Geophysical Research.* Vol. 83, No. C9. pp. 4615-4622.

Piskozub, J., Flatau, P. J. and Zaneveld, J. V. R. 2001. Monte Carlo study of the scattering error of a quartz reflective absorption tube. *Journal of Atmospheric and Oceanic Technology,* Vol. 18, pp. 438-445.

Platt, T. and Sathyendranath, S. 1988. Oceanic primary production: Estimation by remote sensing at local and regional scales. *Science,* Vol. 241, pp. 1613-1620.

Pollack, J. B. and Cuzzi, J. N. 1980. Scattering by non-spherical particles of size comparable to a wavelength: a new semi-empirical theory and its applications to tropospheric aerosols. *Journal of Atmospheric Science* Vol. 37. pp. 868-881.

Poole, H. H. and Atkins, W. R. G. 1929. Photoelectric measurements of submarine illumination through the year. *Journal of the Marine Biological Association of the UK*, Vol. 16, pp. 297-324.

Pope, R. M. and Fry, E. S. 1997. Absorption spectrum (380-700nm) of pure water: II. Integrating cavity measurements. *Applied Optics*, Vol. 36, pp. 8710-8723.

Preisendorfer, R. W. 1961. Application of radiative transfer theory to light measurements in the sea. *Union Geodesique et Geophysique Internationale*. Vol. 10, pp. 11-30.

Prieur, L. and Sathyendranath, S. 1981. An optical classification of coastal and oceanic waters based on the specific spectral absorption curves of phytoplankton pigments, dissolved organic matter and other particulate materials. *Limnology and Oceanography*, Vol. 26, No. 4, pp. 671-689.

Ritchie, J. C., Schiebe, F. R. and McHenry, J. R. 1976. Remote Sensing of suspended sediments in surface waters, *Photogrammetric Engineering and Remote Sensing*, Vol. 42, No. 12, pp. 1539-1545.

Ritchie, J. C. and Cooper, C. 1988. Comparison of measured suspended sediment concentrations with suspended sediment concentrations estimated from Landsat MSS data. *International Journal of Remote Sensing*, Vol. 9, No. 3, pp. 379-387.

Robinson, I. S. 1979. The tidal dynamics of the Irish and Celtic Seas. *Geophysical journal of the Royal Astronomical Society*, Vol. 56, pp. 159-167.

Robinson, I. S. 1985. *Satellite Oceanography: An introduction for oceanographers and remote-sensing scientists*. Halsted Press, Chichester. 455pp.

Robinson, M. C., Morris, K. P. and Dyer, K. R. 1998. Deriving fluxes of suspended particulate matter in the Humber Estuary, UK, using airborne remote sensing. *Marine Pollution Bulletin*, Vol. 37, No. 3-7, pp. 155-163.

Robinson, W. D. 2000. The updated SeaWiFS Coccolithophore Algorithm. Chapter 7 in: *SeaWiFS Postlaunch Calibration and Validation Analyses, Part 1*. NASA Technical Memorandum. 2000-206892, Vol. 9, pp. 51-56. Edited by S. B. Hooker and E.R. Firestone. NASA Goddard Space Flight Center, 82 pp.

Sathyendranath, S., Prieur, L. and Morel, A. 1989. A three-component model of ocean colour and its application to remote sensing of phytoplankton pigments in coastal waters. *International Journal of Remote Sensing*, Vol. 10, pp.1373-1394.

Sathyendranath, S. 2000. *Remote sensing of ocean colour in coastal, and other optically-complex waters*. IOCCG Report Number 3, 2000. 140pp.

Shimwell, S. J., Wernand, M. R. and Boxall, S. R. 1997. Calculation of the Q factor for Case 2 waters. Proceedings of SPIE Ocean Optics XIII, Vol 2963. pp. 520-525.

Siddorn, J. R., Bowers, D. G. and Hoguanes, A. M. 2001. Detecting the Zambezi River plume using observed optical properties. *Marine Pollution Bulletin*, Vol. 42. No. 10, pp. 942-950.

Simpson, J. H. 1981. The shelf-sea fronts: implications of their existence and behaviour. *Philosophical Transactions of the Royal Society, London*. A302, pp. 531-546.

Simpson, J. H. and Brown, J. 1987. The interpretation of visible band imagery of turbid shallow seas in terms of the distribution of suspended particulates. *Continental Shelf Research*, Vol. 7, No. 11-12, pp. 1307-1313.

Simpson, J. H. and Hunter, J. R. 1974. Fronts in the Irish Sea. *Nature*. Vol. 250. pp. 404-406.

Smith, R. C. and Baker, K. 1981. Optical properties of the clearest natural waters. *Applied Optics*, Vol. 20, No. 2, pp. 177-184.

Snedecor, G. W. and Cochran, W. G. 1967. *Statistical Methods.* Sixth Edition. The Iowa State University Press, Iowa. 593pp.

Sogandares, F. M. and Fry, E. S. 1997. Absorption spectrum (340-640 nm) of pure water. I. Photothermal measurements. *Applied Optics,* Vol. 36. No. 33. pp. 8699-8709.

Spencer, J. W. 1971. Fourier series representation of the position of the sun. *Search,* Vol. 2, p. 172.

Stramski, D. and Morel, A. 1990. Optical properties of photosynthetic picoplankton in different physiological states as affected by growth irradiance. *Deep Sea Research,* Vol. 37, No. 2, pp. 245-266.

Strickland, J. D. H. and Parsons, T. R. 1972. *A Practical Handbook of Sea Water Analysis,* Fisheries Research Board of Canada. 300 pp.

Stumpf, R. P., and Pennock, J. R. 1989. Calibration of a general optical equation for remote sensing of suspended sediments in a moderately turbid estuary. Journal of Geophysical Research, Vol. 94, pp. 14,363-14,371.

Sydor, M. and Arnone, R. A. 1997. Effect of suspended particulate and dissolved organic matter on remote sensing of coastal and riverine waters. *Applied Optics,* Vol. 36, No. 27, pp. 6905-6912.

Tassan, S. 1988. The effect of dissolved 'yellow substance' on the quantitative retrieval of chlorophyll and total suspended sediment concentrations from remote measurements of water colour. *International Journal of Remote Sensing,* Vol. 9, No. 4. pp. 787-797.

Tassan, S. 1994. Local algorithms using SeaWiFS data for the retrieval of phytoplankton pigments, suspended sediment, and yellow substance in coastal waters. *Applied Optics,* Vol. 33, No. 12, pp. 2369-2378.

Tassan, S. 1997. Numerical model for the detection of sediment concentration in stratified river plumes using Thematic Mapper data. *International Journal of Remote Sensing,* Vol. 18, No. 12, pp. 2699-2705.

Tassan, S. and Sturm, B. 1986. An algorithm for the retrieval of sediment content in turbid coastal waters from CZCS data. *International Journal of Remote Sensing,* Vol. 7, No. 5, pp. 643-655.

Tett, P. 1990. The Photic Zone. In: Herring, P.J., Campbell, A.K., Whitfield. M. & Maddock, L. (Eds), *Light and Life in the Sea.* Cambridge University Press, Cambridge. pp. 59-87.

Topliss, B. J. 1986. Spectral variations in upwelling radiant intensity in turbid coastal waters. *Estuarine, Coastal and Shelf Science,* Vol. 22, pp. 395-414.

Topliss, B. J., Amos, C. L. and Hill, P. R. 1990. Algorithms for remote sensing of high concentration, inorganic suspended sediment. *International Journal of Remote Sensing,* Vol. 11, No. 6, pp. 947-966.

Traykovski, P., Latter, R. J. and Irish, J. D. 1999. A laboratory evaluation of the laser in situ scattering and transmissometry instrument using natural sediments. *Marine Geology,* Vol. 159, pp. 355-367.

Twardowski, M. S., Boss, E., Macdonald, J. B., Pegau, W. S., Barnard, A. H., Zaneveld, J. R. V. 2001. A model for estimating bulk refractive index from the optical backscattering ratio and the implications for understanding particle composition in case I and case II waters. *Journal of Geophysical Research.* Vol. 106, No. C7, pp. 14,129-14,142.

Ulloa, O., Sathyendranath, S. and Platt, T. 1994. Effect of particle-size distribution on the backscatter ratio in seawater. *Applied Optics.* Vol. 33. No. 30. pp. 7070-7077.

Van de Hoek, C., Mann, D. G. and Jahns, H. M. 1995. *Algae; An introduction to phycology*. Cambridge University Press, Cambridge. 627pp.

Van de Hulst, H. C. 1957. *Light scattering by small particles*. Wiley, New York. 470pp.

Vant, W. N. 1990. Causes of light attenuation in nine New Zealand estuaries. *Estuarine, Coastal and Shelf Science*, Vol. 31, pp. 125-137.

Wakeman, T. R., Peddicord, R. and Sustar, J. 1975. Effects of suspended solids associated with dredging operations on estuarine organisms. *Proceedings of the Ocean 75 Conference on Engineering in the Ocean Environment*. San Diego. CA. September 22-25, 1975. pp. 431-436.

Weeks, A. 1989. Seasonal and tidal cycles of suspended particulates in the Irish Sea. *P.hD. Thesis, University of Wales Bangor*. 245pp.

Weeks, A. R. and Simpson, J. H. 1991. The measurement of suspended particulate concentrations from remotely sensed data. *International Journal of Remote Sensing*, Vol. 12, pp. 725-737.

Weidemann, J. D. and Bannister, T. T. 1986. Absorption and scattering properties in Irondequoit Bay. *Limnology and Oceanography*, Vol. 31, No. 3, pp. 567-583.

Wernand, M. R., Shimwell, S. J., Boxall, S. and Van Aken, H. M. 1998. Evaluation of specific semi-empirical coastal colour algorithms using historic data sets. *Aquatic Ecology*, Vol. 32, pp. 73-91.

Whitlock, C. H., Poole, L. R., Usry, J. W., Houghton, W. M, Witte, W. G. Morris, W. D. and Gurganus, E. A. 1981. Comparison of reflectance with backscattering and absorption parameters for turbid waters. *Applied Optics*, Vol. 20, pp. 517-522.

Witte, W. G., Whitlock, C. H., Harris, R. C, Usry, J. W., Poole, L. R., Houghton, W. M., Morris, W. D. and Gurganus, E. A. 1982. Influence of dissolved organic materials on turbid water optical properties and remote sensing reflectance. *Journal of Geophysical Research*, Vol. 87, No. C1, pp. 441-446.

Woodruff, D. L., Stumpf, R. P., Scope, J. A. and Paerl, H. W. 1999. Remote estimation of water clarity in optically complex estuarine waters. *Remote Sensing of Environment*, Vol. 68, pp. 41-52.

Yentsch, C. S. 1962. Measurement of visible light absorption by particulate matter in the ocean. *Limnology and Oceanography*, Vol. 7, pp. 207-217.

Yentsch, C. S. and Menzel, D. W. 1963. A method for the determination of phytoplankton, chlorophyll and phaeophytin by fluorescence. *Deep Sea Research*, Vol. 10, pp. 221-231.

Zaneveld, J. R.V., Roach, D. M. and Pak, H. 1974. The determination of the index of refraction distribution of oceanic particulates. *Journal of Geophysical Research*, Vol. 79, No. 27, pp. 4091-4095.